Numerical and Analytical Studies of the Dynamics of Gaseous Detonations

Thesis by

Christopher A. Eckett

In Partial Fulfillment of the Requirements

for the Degree of

Doctor of Philosophy

California Institute of Technology

Pasadena, California

2001

(Submitted September 8, 2000)

Acknowledgements

There are several people who deserve thanks for the assistance they have given me over the years at Caltech. First and foremost, my advisor Joseph Shepherd has been a constant source of inspiration and insight in all aspects of detonation theory, modeling and experiments. His flexibility regarding my work location in the last couple of years was also greatly appreciated. James Quirk provided much of the framework for the numerical simulations with his software package Amrita, support for this software, and the flow solver used in the direct initiation simulations. I am grateful for his patience with me. I would also like to thank several other GALCIT researchers for their assistance with issues ranging from detonations and fluid mechanics to general computing – Marco Arienti, Joanna Austin, Patrick Hung, Michael Kaneshige, Chris Krok, Ashish Misra, Eric Morano, Martin Ross, Eric Schultz, and especially Mark Brady for his many hours of computing advice and assistance. Suzy Dake's secretarial talents were appreciated, as was the service of my thesis committee members Hans Hornung, Dale Pullin, Dan Meiron and Andrew Ingersoll.

The code used to produce the Arrhenius model detonation stability boundaries in chapter 2 was provided by Tom Jackson, at the time working at ICASE, and now with the University of Illinois at Urbana–Champaign. The development of the Intrinsic Low-Dimensional Manifold code in chapter 3 benefited from the advice of Ulrich Maas at Universitaet Stuttgart.

Finally, and most importantly, I am eternally grateful to my wife Debra for her years of moral support and patience, as well as my baby daughter Micaela who was the source of so much enjoyable distraction.

The first part of this research was supported by Los Alamos National Laboratory, subcontract 319AP0016-3L under DOE Contract W-7405-ENG-36. The second part was supported by the Caltech ASAP Center for Simulation of Dynamic Response of Materials, under the DOE Accelerated Strategic Computing Initiative (ASCI).

Abstract

This thesis examines two dynamic parameters of gaseous detonations, critical energy and cell size. The first part is concerned with the direct initiation of gaseous detonations by a blast wave and the associated critical energy. Numerical simulations of the spherically symmetric direct initiation event with a simple chemical reaction model are presented. Local analysis of the computed unsteady reaction zone structure identifies a competition between heat release rate, front curvature and unsteadiness. The primary failure mechanism is found to be unsteadiness in the induction zone arising from the deceleration of the shock front. On this basis, simplifying assumptions are applied to the governing equations, permitting solution of an analytical model for the critical shock decay rate. The local analysis is validated by integration of reaction zone structure equations with detailed chemical kinetics and prescribed unsteadiness. The model is then applied to the global initiation problem to produce an analytical equation for the critical energy. Unlike previous phenomenological models, this equation is not dependent on other experimentally determined parameters. For different fuel–oxidizer mixtures, it is found to give agreement with experimental data to within an order of magnitude. The second part of the thesis is concerned with the development of improved reaction models for accurate quantitative simulations of detonation cell size and cellular structure. The mechanism reduction method of Intrinsic Low-Dimensional Manifolds, originally developed for flame calculations, is shown to be a viable option for detonation simulations when coupled with a separate model in the induction zone. The agreement with detailed chemistry calculations of constant volume reactions and one-dimensional steady detonations is almost perfect, a substantial improvement on previous models. The method is applied to a two-dimensional simulation of a cellular detonation in hydrogen–oxygen–argon. The results agree well with an earlier detailed chemistry calculation and experimental data. The computational time is reduced by a factor of 15 compared with a detailed chemistry simulation.

Contents

List of Figures

List of Tables

Nomenclature

		SI Units[†]
Roman characters		
a	empirical stoichiometric coefficient [see page 43]	
A_j	energy integral constant for geometry integer j [see page 46]	
A_l	pre-exponential factor in reaction rate of elementary reaction l [see eq. (3.7)]	(various)
b	empirical stoichiometric coefficient [see page 43]	
B_j	energy integral constant for geometry integer j [see page 46]	
c	frozen sound speed	m/s
C	pre-exponential constant in global reaction rate [see page 43]	$\mathrm{s{\cdot}m^{3(a+b)}/mol^{a+b}}$
C_P	mixture specific heat at constant pressure	J/kg·K
C_v	mixture specific heat at constant volume	J/kg·K
C_{v_k}	specific heat at constant volume of species k	J/kg·K
d_c	critical tube diameter	m
D_n	normal shock velocity	m/s
$\boldsymbol{e}_k$	k-th right eigenvector of Jacobian $\partial \boldsymbol{F}/\partial \boldsymbol{W}$ [see page 178]	(various)
e	specific internal energy	J/kg

[†]SI units are listed here, although CGS units are often used in the text.

e_{cutoff}	cutoff value of internal energy for switching equation of state evaluation from freestream to ILDM [see page 133]	J/kg
e_k	specific internal energy of species k	J/kg
E_{a_l}	activation energy per unit mole in reaction rate of elementary reaction l [see eq. (3.7)]	J/mol
E_a	activation energy per unit mass	J/kg
E_c	critical energy	$\mathrm{J/m^{2-j}}$
E_{c1}	first critical energy	$\mathrm{J/m^{2-j}}$
E_{c2}	second critical energy	$\mathrm{J/m^{2-j}}$
E_{source}	initial energy release in blast initiation	$\mathrm{J/m^{2-j}}$
E_t	total energy per unit volume	$\mathrm{J/m^3}$
$\boldsymbol{f}$	rate vector [see eq. (3.17)]	(various)
$\bar{\boldsymbol{f}}$	vector of reaction rates for reduced reaction progress variables	mol/kg
$\boldsymbol{f}_{\boldsymbol{\psi}}$	Jacobian matrix $\partial \boldsymbol{f}/\partial \boldsymbol{\psi}$	(various)
f	overdrive factor [see eq. (3.11)]	
$\bar{f}_i$	reaction rate of reduced reaction progress variable i [see eq. (3.24)]	mol/kg·s
$\boldsymbol{F}$	convective flux vector in x or r direction	(various)
$\boldsymbol{F}_x$	convective flux vector in x direction [see eq. (3.30)]	(various)
$\boldsymbol{F}_y$	convective flux vector in y direction [see eq. (3.30)]	(various)
$\boldsymbol{g}$	vector of complete ILDM equations [see eq. (3.22)]	(various)

$\boldsymbol{g}_{\boldsymbol{\psi}}$	Jacobian matrix $\partial \boldsymbol{g}/\partial \boldsymbol{\psi}$	(various)
$\boldsymbol{G}$	geometry source term vector [see eq. (2.14)]	(various)
h	specific enthalpy	J/kg
H	specific total enthalpy	J/kg
j	geometry integer [see page 7]	
J^+	Riemann invariant of right-facing characteristics [see page 186]	m/s
k	pre-exponential factor in one-step reaction	1/s
k_{f_b}	backward rate coefficient of reaction l [see eq. (3.6)]	(various)
k_{f_l}	forward rate coefficient of reaction l [see eq. (3.6)]	(various)
$l_n^{(i)}$	co-ordinate (0 or 1) of interpolation bounding hyper-rectangle grid point i in co-ordinate direction n [see page 189]	
L	detonation cell length	m
M	flow Mach number in shock-attached reference frame	
n_e	number of atomic elements	
n_q	number of elementary reactions in detailed mechanism	
n_r	number of chemical degrees of freedom in reduced mechanism [see page 104]	
n_s	number of species	
$\boldsymbol{p}$	vector of auxiliary equations [see eq. (3.21)]	(various)
$\boldsymbol{p}_{\boldsymbol{\psi}}$	Jacobian matrix $\partial \boldsymbol{p}/\partial \boldsymbol{\psi}$	(various)
P	pressure	Pa

P_{CJ}	equilibrium pressure at rear of CJ detonation	Pa
P_e	partial derivative of pressure with respect to internal energy	kg/m^3
P_{vN}	post-shock (von Neumann) pressure for steady ZND detonation	Pa
P_{Z_k}	partial derivative of pressure with respect to chemical composition variable Z_k	(various)
P_ρ	partial derivative of pressure with respect to density	m^2/s^2
q_l	net rate of progress for reaction l [see eq. (3.6)]	mol/m^3·s
Q	heat of reaction	J/kg
Q	orthogonal matrix from real Schur decomposition of $\boldsymbol{f}_{\boldsymbol{\psi}}$ [see page 105]	
r	radial distance from co-ordinate origin	m
r_k	ratio of upwind to local wave strengths, in approximate Riemann solver [see page 179]	
$\mathcal{R}$	universal gas constant	J/mol·K
R	radius or axial position of shock	m
R_c	critical radius [see eq. (2.39)]	m
R_g	specific gas constant of mixture	J/kg·K
R_{source}	initial shock radius in blast initiation simulation	m
s	specific entropy	J/kg·K
$\boldsymbol{S}$	reaction source term vector	(various)
t	time	s
t_d	characteristic shock decay time [see eq. (2.29)]	s

$t_{d,c}$	critical shock decay time [see eq. (2.30)]	s
T	quasi-upper triangular matrix from real Schur decomposition of $\boldsymbol{f}_{\boldsymbol{\psi}}$ [see page 105]	(various)
T	temperature	K
$\hat{T}_1$	dimensionless first order term in temperature asymptotic expansion [see page 36]	
T_{CJ}	equilibrium temperature at rear of CJ detonation	K
T_{vN}	post-shock (von Neumann) temperature for steady ZND detonation	K
$\boldsymbol{u}$	vector flow velocity	m/s
u	flow velocity in x or r direction	m/s
U	velocity of shock or detonation front	m/s
U_{ave}	average propagation velocity of unsteady detonation	m/s
U_c	shock velocity at critical radius [see eq. (2.37)]	m/s
U_{CJ}	CJ detonation velocity	m/s
U_{ZND}	steady ZND detonation velocity	m/s
v	flow velocity in y direction	m/s
w	flow velocity in shock-attached reference frame	m/s
$\boldsymbol{W}$	conservative solution vector	(various)
W	mean molar mass of mixture	kg/mol
W_k	molar mass of species k	kg/mol
x	distance behind leading shock wave or axis co-ordinate in direction of detonation propagation	m

x_0	x co-ordinate of starting point of detonation cell [see page 153]	m
x_n	distance along co-ordinate direction n in multi-dimensional table – Appendix E [see page 189]	(various)
$x_{n,l}$	value of x_n for lower ($l = 0$) or upper ($l = 1$) edge of interpolation bounding hyper-rectangle [see page 189]	(various)
X_k	chemical symbol for species k	
y	transverse axis co-ordinate	m
$\boldsymbol{y}$	vector of species mass fractions	
y_k	mass fraction of species k	
$\boldsymbol{Z}$	vector of generic chemical composition variables Z_k	(various)
Z	reaction progress variable in one-step reaction	
Z_k	generic chemical composition variable k [see page 175]	(various)

Greek characters

α	initiation parameter [see eq. (2.26)]	
α_k	strength of k-th wave in approximate Riemann solver [see page 178]	(various)
β_l	temperature exponent in reaction rate of elementary reaction l [see eq. (3.7)]	
γ	ratio of mixture specific heats	
Δ	ZND induction length	m
Δ_{CJ}	ZND induction length for CJ detonation	m
Δ_H	hydrodynamic thickness	m

$\Delta_{1/2}$	ZND half-reaction length for CJ detonation	m
ζ	non-dimensional time [see page 37]	
ζ_{exp}	non-dimensional explosion time [see page 37]	
η	sonic parameter [see page 9]	
$\boldsymbol{\theta}$	vector of ILDM reaction progress variables	mol/kg
θ_i	ILDM reaction progress variable i	mol/kg
θ	activation energy normalized by post-shock temperature [see eq. (2.17)]	
$\boldsymbol{\vartheta}$	vector of conserved ILDM parameters [see page 106]	(various)
ϑ_e	ILDM parameter for internal energy [see page 106]	J/kg
ϑ_ρ	ILDM parameter for density [see page 106]	kg/m^3
ϑ_{χ_j}	constant ILDM parameter for specific element mole number of element j [see page 106]	mol/kg
κ	local front curvature	1/m
λ	detonation cell width	m
λ_k	k-th eigenvalue of Jacobian $\partial \boldsymbol{F}/\partial \boldsymbol{W}$ – Appendix B [see page 178]	m/s
λ_k	k-th eigenvalue of reaction system Jacobian $\boldsymbol{f}_{\boldsymbol{\psi}}$ [see page 121]	1/s
μ_{kj}	number of atoms of element j in species k	
ν	nonlinear greyscale shading function	
ν_k	CFL number of k-th wave in approximate Riemann solver [see page 179]	

ν'_{kl}	forward stoichiometric coefficient for species k in reaction l [see eq. (3.4)]	
ν''_{kl}	backward stoichiometric coefficient for species k in reaction l [see eq. (3.4)]	
π_n	interpolation weighting function for co-ordinate direction n [see page 189]	
ρ	density	kg/m^3
ρ_{cutoff}	cutoff value of density for switching equation of state evaluation from freestream to ILDM [see page 133]	kg/m^3
ϱ	arbitrary scalar	(various)
$\dot{\sigma}$	total thermicity [see page 8]	1/s
σ_k	thermicity coefficient of species k [see eq. (2.3)]	
τ	ZND induction time	m
$\boldsymbol{\phi}$	vector of specific mole numbers	mol/kg
ϕ_k	specific mole number of species k [see page 103]	mol/kg
ϕ_{cutoff}	cutoff mole number for switching chemical source step from induction manifold to ILDM [see page 123]	mol/kg
φ	nonlinear limiter function [see page 179]	
$\boldsymbol{\chi}$	vector of specific element mole numbers	mol/kg
χ_j	specific element mole number of element j [see page 104]	mol/kg
$\boldsymbol{\psi}$	state space vector [see page 103]	(various)
$\dot{\omega}_k$	net molar production rate of species k	mol/m^3·s

Ω_k	production rate of species k	1/s

Acronyms

AMR	adaptive mesh refinement
CDR	critical decay rate
CFD	computational fluid dynamics
CFL	Courant–Friedrichs–Lewy
CJ	Chapman–Jouget
CPU	central processing unit
CSP	computational singular perturbation
DDT	deflagration to detonation transition
GALCIT	Graduate Aeronautical Laboratories, California Institute of Technology
ILDM	intrinsic low-dimensional manifold
ODE	ordinary differential equation
PBT	point blast theory
PDE	partial differential equation
QSSA	quasi steady state approximation
ZND	Zel'dovich–von Neumann–Doering

Operators

Δ	difference
$\boldsymbol{\nabla}$	gradient operator
$\mathcal{L}_F$	convective operator [see page 70]

$\mathcal{L}_{FG}$	convective and geometry source operator [see page 14]	
$\mathcal{L}_{F_x}$	convective operator in x direction [see page 144]	
$\mathcal{L}_{F_y}$	convective operator in y direction [see page 144]	
$\mathcal{L}_S$	reaction source operator [see page 14]	
$[\,\cdot\,]$	molar concentration	$\mathrm{mol/m^3}$

Subscripts

$*$	at point of detonation failure [see page 47]
0	uniform freestream condition
1	initial right state in Riemann problem – Appendix C [see page 184]
2	state between shock wave and contact surface in Riemann problem – Appendix C [see page 184]
3	state between contact surface and expansion fan in Riemann problem – Appendix C [see page 184]
4	initial left state in Riemann problem – Appendix C [see page 184]
c	critical
cutoff	threshold cutoff for switching between numerical methods
CJ	pertaining to detonation traveling at CJ velocity [see page 16]
e	equilibrium
feature	numeric value of highlighted feature
i	at the time when the particle initially crosses the shock – Chapter 2
i	index of ILDM reaction progress variable – Chapter 3

j geometry integer – Chapter 2

j atomic element index – Chapter 3

k species index

k_i species index corresponding to ILDM reaction progress variable i

L left state – Appendix B

L lower sub-matrix [see page 105]

min minimum

max maximum

n co-ordinate direction of multi-dimensional table – Appendix E [see page 189]

ref reference quantity

R right state

s post-shock state

vN post-shock (von Neumann) state for steady ZND detonation

ZND pertaining to steady ZND detonation

Superscripts

(ϱ) pertaining to quantity ϱ – Appendix B [see page 181]

(i) grid point number of interpolation bounding hyper-rectangle – Appendix E [see page 189]

n timestep counter

T transpose

$*$	interpolant point – Appendix E [see page 189]

Accents

$\bar{}$	function in pressure partial derivative formulation [see page 181]
$\dot{}$	time derivative
$\hat{}$	Roe–average
$\tilde{}$	non-dimensional quantity [see page 14]

Chapter 1 Summary

A detonation is a form of high speed combustion in which a closely coupled shock wave and reactive wave propagate through a combustible mixture. The shock and reaction zone together are referred to as the detonation. The simplest model of a detonation treats the detonation wave as a discontinuity between an upstream state and a downstream thermochemical equilibrium state. Solution of the steady, inviscid, one-dimensional jump conditions between these states reveals a minimum velocity at which the detonation can propagate, the so called Chapman–Jouget (CJ) velocity (Fickett and Davis, 1979). Experimental evidence suggests this is the preferred velocity in nature for an unsupported detonation, and the CJ theory typically predicts the detonation velocity accurate to within a few percent. The downstream equilibrium state and composition, denoted as the CJ conditions, can also be solved from the jump relationships. The CJ velocity and CJ conditions are independent of the finite rate of the chemical reactions, so they are sometimes referred to as the static detonation parameters (Lee, 1984).

The next level of sophistication in a detonation model accounts for the fact that the detonation actually has some thickness by including finite rate chemical reactions. The Zel'dovich–von Neumann–Doering (ZND) model represents the detonation as a steady, one-dimensional flow with a shock discontinuity followed by a finite thickness reaction zone, ending with the CJ equilibrium conditions (Fickett and Davis, 1979).

Properties of a detonation that depend explicitly on the finite reaction rate are typically referred to as the dynamic parameters of detonation (Lee, 1984). The most commonly studied such parameters are:

Reaction length The length of the induction zone or recombination zone between the leading shock and some pre-defined identifier in the reaction zone.

Cell size The width or length of the characteristic cells seen in soot foil experiments

of real multi-dimensional detonations. The cells are the tracks of shock triple points formed by the intersection of the leading shock front with transverse waves that exist behind the front. The cell width is also the spacing of the transverse waves.

Critical tube diameter The minimum tube diameter from which a detonation can successfully diffract into an unconfined space and form a spherical detonation.

Critical energy The minimum energy of a point blast in a detonable mixture that will successfully initiate a spherical detonation. Similar definitions apply to energy per unit length or area of a line or plane blast to initiate a cylindrical or planar detonation.

Under the approximation of planar flow, the reaction length can be computed from the ZND model with an appropriate chemical reaction mechanism. However, no exact theories for the other parameters exist. Several empirical correlations between the parameters have been developed, along with some phenomenological models and approximate theoretical models. Discussions of cell size models and correlations with reaction length are presented by Fickett and Davis (1979), Westbrook (1982), Lee (1984) and Gavrikov et al. (2000). Reviews of critical diameter models are given by Lee (1984, 1996), and critical energy models by Lee (1977, 1984) and Lee and Higgins (1999). All of the models are approximate at best and none have become widely accepted as the final answer in detonation theory. The main reason highly successful models of the dynamic parameters have not been developed is an incomplete understanding of the underlying physics governing detonation dynamics. The small length scales and high speeds of detonation make detailed quantitative flow visualization difficult, so a complete understanding has not yet come from experiments. Numerical simulations offer an alternative for gaining such detailed descriptions of the flowfield.

In this work, we present numerical studies of two of the dynamic parameters of detonation, cell size and critical energy. The goal is to demonstrate the viability of numerical simulations for such detailed examination and to increase our understanding of the dynamic processes.

Chapter 2 examines the problem of direct detonation initiation and critical energy. Numerical simulations of the spherical blast initiation problem with a simple chemical reaction model are used to examine the various competing physical processes in the flow. Unsteadiness of the decaying blast wave is found to be the dominant mechanism that can cause the detonation to fail to initiate. On the basis of this detailed investigation, various simplifying assumptions are made in the governing equations and an analytical model developed for the critical energy that depends only on theoretically computed quantities such as the ZND induction time. The results of the model are compared with an earlier model and experimental data. This chapter is essentially identical to a paper published in the Journal of Fluid Mechanics (Eckett et al., 2000), of which the present author is the principal author.

In chapter 3, numerical simulations of cellular detonations are presented to demonstrate the viability of numerical simulations as a reliable tool for the prediction of cell size and cellular structure. The bulk of the section is concerned with improving the current state of the art in reaction modeling used for detonation simulations. A more accurate reaction model than those used previously is necessary for reliable quantitative predictions from numerical simulations. The method of detailed reaction mechanism reduction based on Intrinsic Low-Dimensional Manifolds (ILDM), originally developed for flame calculations (Maas and Pope, 1992b), is shown to be applicable to ignition type problems such as detonations when coupled with a separate technique for the induction zone. The reduced reaction mechanism is then used to simulate a cellular detonation in H_2–O_2–Ar. The results of the simulation are compared with a more expensive detailed chemistry simulation of the same problem and with experimental data.

Chapter 2 Direct Initiation and Critical Energy

2.1 Introduction

When a large amount of energy is released in a small region of an unconfined combustible gas mixture, a strong spherical blast wave ensues from the initial point. As the blast expands and decays, two possible outcomes have been observed experimentally. Firstly, the blast wave velocity may decay to an approximately constant value near the Chapman–Jouget (CJ) velocity of the mixture, in which case a self-supported spherical detonation has been successfully initiated in the gas. The other possibility is that the blast continues to decelerate below the CJ velocity and eventually decays away to an acoustic wave in the manner of a blast in a non-reacting gas. In this failed initiation event, the reaction zone decouples from the shock front and lags behind the shock, becoming a low speed flame.

This method of detonation initiation by an overdriven shock wave has been coined direct initiation, as opposed to the other main form of initiation known as deflagration to detonation transition (DDT). The main variable believed to determine the success or failure of direct initiation is the magnitude of the initial energy release, provided that the energy deposition is sufficiently fast and the igniter sufficiently small. Experiments suggest that for a given combustible gas mixture at given uniform premixed initial conditions, the energy release must be above a certain level, known as the critical energy, to successfully initiate a detonation.

The same arguments apply for direct initiation of cylindrical detonations with a line source and planar detonations with a plane source. The critical energy is an energy per unit length or per unit area respectively. Most previous work has focused on the spherically symmetric direct initiation as this is the most fundamental

geometry and the spherical critical energy is considered one of the best indicators of detonability or detonation sensitivity of combustible gas mixtures. This critical energy typically varies by several orders of magnitude between different mixtures allowing for simple ranking of mixture detonabilities without the need for highly accurate experiments.

Various attempts have been made to model the spherical critical energy in the past. An extensive review is given in Lee and Higgins (1999). Zel'dovich et al. (1956) were the first to present a theoretical discussion of the critical energy. They argued on the basis of the energy released inside a given spherical volume, the existence of a critical energy E_c, proportional to the cube of the reaction zone thickness. Although that paper did not give a satisfactory theory for the quantitative prediction of critical energies, it introduced the concept that the critical energy is a dynamic parameter of detonation and depends on the reaction kinetics of the combustible gas mixture.

Following Zel'dovich's findings, various workers produced phenomenological models that correlated the critical energy with other experimentally determined dynamic parameters of detonation, such as the cell width λ, the critical tube diameter d_c and the hydrodynamic thickness Δ_H. In all cases, the spherical critical energy was found to be proportional to the cube of the other dynamic parameter, consistent with Zel'dovich's theory. These models were reviewed by Lee (1977, 1984) and Benedick et al. (1986). This last work also compared the predictions of several models with experimental data for various fuel–air mixtures. These phenomenological models are based on experimental observations and the resulting equations merely correlate the critical energy to some other experimentally determined parameters. Admittedly, a parameter such as the cell width λ is considerably easier to measure experimentally than the critical energy, so there is merit to such theories. However, it would be desirable to have a model that gives more insight to the underlying physical processes governing direct initiation, and provides an expression for the critical energy that can be evaluated without the need for experimental data.

The first attempt at such a rigorous theoretical model was made by He and Clavin (1994). They assumed the point blast direct initiation problem could be adequately

described by a quasi-steady analysis. The nonlinear curvature effect of the detonation front then provides the mechanism of failure. Excessive curvature prevents a sonic point from appearing at the rear of the reaction zone, and the decaying blast wave fails to evolve into the quasi-steady velocity–curvature relationship. We will refer to this model as the critical curvature model.

The dominant balance in He and Clavin's model is competition between chemical heat release and front curvature. Such a quasi-steady model is popularly referred to as a D_n–κ model (Stewart and Bdzil, 1988), where D_n is the normal shock velocity and κ is the local front curvature. These models are typically only applicable in a regime near the CJ velocity. The D_n–κ concept was extended by Yao and Stewart (1996) to a $\dot{D}_n$–D_n–κ model as well as a $\ddot{D}_n$–$\dot{D}_n$–D_n–κ–$\dot{\kappa}$ model, where the dots refer to differentiation with respect to time. These time dependent models still assume that the dominant balance is between heat release and curvature, and that the detonation structure is characterized by a sonic point at the rear of the reaction zone. The unsteady terms are assumed to be small compared to the quasi-steady terms, restricting application of the models to slightly unsteady flow. There are a number of interesting consequences of these models, including the prediction of cellular detonations (Stewart et al., 1996).

In this work we present an alternative model for direct initiation that arises from a detailed analysis of the unsteady reaction zone structure. Our analytical approach is somewhat similar to Yao and Stewart's in writing the governing equations with the unsteady terms as a perturbation on the steady flow. However, we make no assumptions regarding the size of different terms in the equations until they have been examined via numerical simulation results. As we shall demonstrate later, direct initiation cannot be described as slightly unsteady, and a more general treatment of the unsteady terms must be made, where they are not assumed to be a small perturbation. The unsteadiness in the reaction zone arising from the deceleration of the blast wave is found to be the dominant mechanism causing failure in direct initiation.

The governing equations for flow along a particle path in the reaction zone are de-

veloped in §2.2. Numerical simulations of the spherical direct initiation problem with a one-step Arrhenius reaction rate law are outlined in §2.3, and used to examine the details of the flow in the reaction zone. Then in §2.4, analysis of the one-dimensional reaction zone structure leads to the development of a local initiation model. A quasi-unsteady computation of real gas reaction zones is used to validate the local model in §2.5. In §2.6, the local initiation model is applied to the global initiation event to produce an analytical equation for the critical energy. Finally, this equation is compared with the critical curvature model and experimental data in §2.7.

2.2 Governing Equations

2.2.1 Reactive Euler equations

Ignoring viscosity, heat transfer, diffusion and body forces, the governing equations for compressible reacting flow are the reactive Euler equations. If the multi-dimensional nature of detonations is also ignored then a one-dimensional description is valid. In a fixed reference frame, the reactive Euler equations for flows with planar, cylindrical or spherical symmetry are given by

$$\frac{\mathrm{D}\rho}{\mathrm{D}t} + \rho\frac{\partial u}{\partial r} + \frac{j}{r}\rho u = 0, \tag{2.1a}$$

$$\frac{\mathrm{D}u}{\mathrm{D}t} + \frac{1}{\rho}\frac{\partial P}{\partial r} = 0, \tag{2.1b}$$

$$\frac{\mathrm{D}e}{\mathrm{D}t} - \frac{P}{\rho^2}\frac{\mathrm{D}\rho}{\mathrm{D}t} = 0, \tag{2.1c}$$

$$\frac{\mathrm{D}y_k}{\mathrm{D}t} = \Omega_k, \tag{2.1d}$$

where u, ρ, P and e are the velocity, density, pressure and specific internal energy, r is the distance from the coordinate origin, t is the time, $j = 0$ for planar flow, 1 for cylindrically symmetric flow and 2 for spherically symmetric flow, y_k is the mass fraction of species k, and Ω_k is the production rate of species k, given by some kinetic rate law.

Using simple thermodynamic relations, the energy equation (2.1c) may be replaced by the adiabatic change equation from Fickett and Davis (1979),

$$\frac{\mathrm{D}P}{\mathrm{D}t} = c^2 \frac{\mathrm{D}\rho}{\mathrm{D}t} + \rho c^2 \dot{\sigma}, \tag{2.2}$$

where c is the frozen sound speed, $\dot{\sigma} = \sum \sigma_k \Omega_k$ is the total thermicity with the sum over all species, and σ_k is the thermicity coefficient of species k, given by

$$\sigma_k = \frac{1}{\rho c^2} \left.\frac{\partial P}{\partial y_k}\right|_{e,\rho,y_{j\neq k}} = -\frac{1}{\rho c^2} \frac{\left.\dfrac{\partial e}{\partial y_k}\right|_{P,\rho,y_{j\neq k}}}{\left.\dfrac{\partial e}{\partial P}\right|_{\rho,\boldsymbol{y}}}. \tag{2.3}$$

2.2.2 Reaction zone structure equations

The equations of motion can be rewritten in a reference frame attached to the shock using the following transformation:

$$x = R(t) - r,$$
$$w(x,t) = U(t) - u(r,t),$$

where R and U are the position and velocity of the shock in the fixed reference frame, and w is the flow velocity in the shock-attached reference frame. For the remainder of this section, partial derivatives with respect to t will indicate differentiation at constant x as opposed to constant r. Then (2.1a), (2.1b), (2.2) and (2.1d) become

$$\frac{\mathrm{D}\rho}{\mathrm{D}t} + \rho \frac{\partial w}{\partial x} + \frac{j}{R-x}\rho(U-w) = 0, \tag{2.4a}$$
$$\frac{\mathrm{D}w}{\mathrm{D}t} + \frac{1}{\rho}\frac{\partial P}{\partial x} = \frac{\mathrm{d}U}{\mathrm{d}t}, \tag{2.4b}$$
$$\frac{\mathrm{D}P}{\mathrm{D}t} = c^2 \frac{\mathrm{D}\rho}{\mathrm{D}t} + \rho c^2 \dot{\sigma}, \tag{2.4c}$$
$$\frac{\mathrm{D}y_k}{\mathrm{D}t} = \Omega_k. \tag{2.4d}$$

Equations (2.4a) and (2.4b) can be written as

$$\frac{\mathrm{D}\rho}{\mathrm{D}t} = -\frac{\rho}{w}\frac{\mathrm{D}w}{\mathrm{D}t} + \frac{\rho}{w}\frac{\partial w}{\partial t} - \frac{j}{R-x}\rho(U-w), \tag{2.5a}$$

$$\frac{\mathrm{D}P}{\mathrm{D}t} = -\rho w\frac{\mathrm{D}w}{\mathrm{D}t} + \frac{\partial P}{\partial t} + \rho w\frac{\mathrm{d}U}{\mathrm{d}t}. \tag{2.5b}$$

Substituting (2.5) into (2.4c) gives

$$\eta\frac{\mathrm{D}w}{\mathrm{D}t} = w\dot{\sigma} - \frac{j}{R-x}w(U-w) - M^2\frac{\mathrm{d}U}{\mathrm{d}t} + \frac{\partial w}{\partial t} - \frac{w}{\rho c^2}\frac{\partial P}{\partial t}. \tag{2.6a}$$

where the flow Mach number M and sonic parameter η are given by

$$M = \frac{w}{c}, \quad \eta = 1 - M^2.$$

Substituting (2.6a) into (2.5) gives

$$\eta\frac{\mathrm{D}\rho}{\mathrm{D}t} = -\rho\dot{\sigma} + \frac{j}{R-x}\rho M^2(U-w) + \frac{\rho w}{c^2}\frac{\mathrm{d}U}{\mathrm{d}t} - \frac{\rho w}{c^2}\frac{\partial w}{\partial t} + \frac{1}{c^2}\frac{\partial P}{\partial t}, \tag{2.6b}$$

$$\eta\frac{\mathrm{D}P}{\mathrm{D}t} = -\rho w^2\dot{\sigma} + \frac{j}{R-x}\rho w^2(U-w) + \rho w\frac{\mathrm{d}U}{\mathrm{d}t} - \rho w\frac{\partial w}{\partial t} + \frac{\partial P}{\partial t}. \tag{2.6c}$$

Equations (2.6) are the solutions for the velocity, density and pressure gradients along a Lagrangian particle path behind the shock. We will refer to them as the reaction zone structure equations. In each equation, the first term on the right-hand side is the contribution from the chemical heat release, the second is that due to wave curvature, and the remaining terms represent the purely unsteady contribution. Retaining only the heat release term, the equations reduce to the Zel'dovich–von Neumann–Doering (ZND) model of steady planar reacting flow (Fickett and Davis, 1979).

The simplest concept of detonation failure is a decoupling of the reaction zone from the shock front, or equivalently, the failure of particles to rapidly undergo reaction after they cross the shock. Since most reaction rate laws are strongly temperature dependent, the region of predominant reaction will be accompanied by a sharp temperature increase. Hence, the Lagrangian gradient of temperature will be

of most interest when considering possible failure of the detonation. To compute the temperature gradient we need to invoke an equation of state.

Consider a system of ideal gases. The thermal equation of state is

$$P = \rho R_g T, \tag{2.7}$$

where T is the temperature. R_g is the mixture gas constant, given by

$$R_g = \frac{\mathcal{R}}{W} = \mathcal{R} \sum \frac{y_k}{W_k}, \tag{2.8}$$

where $\mathcal{R}$ is the universal gas constant, W is the mean molar mass of the mixture, and W_k is the molar mass of species k. The frozen sound speed is

$$c = \left(\frac{\gamma P}{\rho} \right)^{1/2}, \tag{2.9}$$

where γ is the ratio of mixture specific heats. Equation (2.3) can be used to show that the thermicity coefficients are

$$\sigma_k = \frac{1}{\gamma} \left(\frac{W}{W_k} - \frac{e_k}{C_v T} \right), \tag{2.10}$$

where e_k is the specific internal energy of species k, and C_v is the mixture specific heat at constant volume. Taking the substantial derivative of (2.7) and using (2.6b), (2.6c), (2.8) – (2.10) gives

$$\begin{aligned} \eta C_P \frac{\mathrm{D}T}{\mathrm{D}t} = & -(1-\gamma M^2) \sum e_k \Omega_k - \frac{c^2}{\gamma} \sum \frac{W}{W_k} \Omega_k + \frac{j}{R-x} w^2 (U-w) \\ & + w \frac{\mathrm{d}U}{\mathrm{d}t} - w \frac{\partial w}{\partial t} + \frac{1}{\rho} \frac{\partial P}{\partial t}, \end{aligned} \tag{2.11}$$

where C_P is the mixture specific heat at constant pressure.

To enable analytical solution, we will now simplify the chemistry. Consider the one-step irreversible reaction, A $\rightarrow$ B, where the upstream fluid is totally species A, without dilution. The reactant and product are taken to be perfect gases (constant

specific heat) and to have the same specific heats. So the specific internal energies of species A and B are

$$e_{\mathrm{A}} = C_v T, \quad e_{\mathrm{B}} = C_v T - Q,$$

where Q is the heat of reaction. Define the progress variable Z as the mass fraction of product B, $Z = y_{\mathrm{B}} = 1 - y_{\mathrm{A}}$. Then, (2.11) becomes

$$\eta C_P \frac{\mathrm{D}T}{\mathrm{D}t} = (1 - \gamma M^2) Q \frac{\mathrm{D}Z}{\mathrm{D}t} + \frac{j}{R - x} w^2 (U - w) + w \frac{\mathrm{d}U}{\mathrm{d}t} - w \frac{\partial w}{\partial t} + \frac{1}{\rho} \frac{\partial P}{\partial t}. \tag{2.12}$$

The kinetics are assumed to be governed by a first-order Arrhenius rate law with linear depletion,

$$\frac{\mathrm{D}Z}{\mathrm{D}t} = k(1 - Z) \exp\left(-\frac{E_a}{R_g T}\right),$$

where E_a is the activation energy per unit mass and k is the pre-exponential rate multiplier. Then, (2.12) becomes

$$\begin{aligned}(1 - M^2) C_P \frac{\mathrm{D}T}{\mathrm{D}t} = (1 - \gamma M^2) Q k (1 - Z) \exp\left(-\frac{E_a}{R_g T}\right) + \frac{j}{R - x} w^2 (U - w) \\ + w \frac{\mathrm{d}U}{\mathrm{d}t} - w \frac{\partial w}{\partial t} + \frac{1}{\rho} \frac{\partial P}{\partial t}.\end{aligned} \tag{2.13}$$

Equation (2.13) is the temperature reaction zone structure equation for the one-step reaction model, and has the form of an energy equation. As before, the first term on the right-hand side is the contribution from heat release, the second term is that from wave curvature and the remaining terms are due to unsteadiness. We should emphasize that in this equation and the earlier reaction zone structure equations (2.6), the left-hand side contains a Lagrangian derivative. This could be divided into time and space partial derivatives, and one could argue that the term arising from the partial time derivative should be moved to the right-hand side and grouped with the other unsteady derivatives. This would ensure that all unsteadiness appears in the group of unsteady terms on the right-hand side and would permit direct comparison with the quasi-steady equations. In fact, such a comparison has been made and is discussed in the following section. However, for the purpose of analysis, we choose to

write the equations in the Lagrangian reference frame, where the unsteady terms on the right-hand side are only the unsteadiness that a particle sees, not the unsteadiness we traditionally think of in an Eulerian reference frame. The Lagrangian reference frame is a more natural choice when considering the reaction in a detonation as a convected adiabatic chain–thermal explosion. For the remainder of this work, we shall use the terminology "unsteady terms" or "unsteadiness" to denote only the unsteady terms on the right-hand side of the reaction zone structure equations (2.6) and (2.13). Note that the unsteady terms in (2.13) are proportional to the unsteady terms in the dilatational rate equation, (2.6b), so they may be interpreted as arising from the dilatational rate in the absence of heat release and curvature.

For a decelerating wave such as the blast wave in a direct initiation event, the unsteadiness expression in the energy equation (2.13) is of opposite sign to the heat release term. Thus the reaction may quench if the wave is decelerating too rapidly. For a convex-upstream wavefront such as the blast wave in a cylindrical or spherical direct initiation, the steady curvature term in (2.13) is of the same sign as the heat release term and so cannot possibly quench the reaction without the additional presence of unsteadiness. Note that a cylindrical or spherical blast wave will always be unsteady, even if propagating at constant velocity, since its curvature is changing with time. The time dependence of curvature can be an important effect, but it is important to realize that it appears in the unsteadiness expression in (2.13), not in the curvature term. For planar symmetry direct initiation, there is no curvature term at all, so again, curvature cannot quench the reaction. Note that the opposite trends occur in the velocity, density and pressure reaction zone structure equations (2.6), namely, for the direct initiation problem, the unsteadiness is of the same sign as the heat release while the curvature is of opposite sign. However, the strong nonlinear temperature dependence of the reaction rate makes temperature the critical variable. The relative sizes and behavior of the terms in (2.13) will be examined directly via numerical simulations in the next section. The goal is to identify the dominant balance in the direct initiation problem and any simplifying assumptions regarding the behavior of the terms in (2.13) that would permit further analytical work.

2.3 Numerical Simulations

2.3.1 Computational setup

Equations

Numerical simulations of the spherical blast wave initiation problem have been performed, using the one-step irreversible reaction described in §2.2.2. For this reaction model, the reactive Euler equations for flows with spherical symmetry, in a fixed reference frame and in non-dimensional conservative form, are

$$\frac{\partial \boldsymbol{W}}{\partial \tilde{t}} + \frac{\partial \boldsymbol{F}}{\partial \tilde{r}} = \boldsymbol{G} + \boldsymbol{S}, \tag{2.14a}$$

where

$$\begin{gathered}\boldsymbol{W} = \begin{pmatrix} \tilde{\rho} \\ \tilde{\rho}\tilde{u} \\ \tilde{E}_t \\ \tilde{\rho}Z \end{pmatrix}, \quad \boldsymbol{F} = \begin{pmatrix} \tilde{\rho}\tilde{u} \\ \tilde{\rho}\tilde{u}^2 + \tilde{P} \\ (\tilde{E}_t + \tilde{P})\tilde{u} \\ \tilde{\rho}\tilde{u}Z \end{pmatrix}, \quad \boldsymbol{G} = -\frac{2}{\tilde{r}} \begin{pmatrix} \tilde{\rho}\tilde{u} \\ \tilde{\rho}\tilde{u}^2 \\ (\tilde{E}_t + \tilde{P})\tilde{u} \\ \tilde{\rho}\tilde{u}Z \end{pmatrix}, \\ \boldsymbol{S} = \begin{pmatrix} 0 \\ 0 \\ 0 \\ \tilde{k}\tilde{\rho}(1-Z)\mathrm{e}^{-\tilde{E}_a/\tilde{T}} \end{pmatrix}.\end{gathered} \tag{2.14b}$$

$\boldsymbol{W}$ is the conservative solution vector, $\boldsymbol{F}$ is the convective flux, $\boldsymbol{G}$ and $\boldsymbol{S}$ are the geometry and reaction source terms respectively, and $E_t = \rho(e + u^2/2)$ is the total energy per unit volume. The dimensional flow variables have been made non-dimensional as follows:

$$\begin{gathered}u_{ref} \equiv (R_g T_0)^{1/2}, \quad \tilde{u} \equiv \frac{u}{u_{ref}}, \quad \tilde{\rho} \equiv \frac{\rho}{\rho_0}, \quad \tilde{P} \equiv \frac{P}{P_0}, \\ \tilde{T} \equiv \frac{T}{T_0}, \quad \tilde{e} \equiv \frac{e}{R_g T_0}, \quad \tilde{E}_t \equiv \frac{E_t}{P_0}, \quad \tilde{E}_a \equiv \frac{E_a}{R_g T_0},\end{gathered}$$

where subscript 0 denotes the uniform conditions upstream of the shock. In the numerical simulations, $\tilde{k}$ is an arbitrary parameter that merely defines the spatial and temporal scales. It has been chosen such that for a planar CJ wave, the half-reaction length $\Delta_{1/2}$ is scaled to unit length, that is,

$$\tilde{r} \equiv \frac{r}{\Delta_{1/2}}, \quad t_{ref} \equiv \frac{\Delta_{1/2}}{u_{ref}}, \quad \tilde{t} \equiv \frac{t}{t_{ref}}, \quad \tilde{k} \equiv k t_{ref}.$$

The non-dimensional equations of state are

$$\tilde{P} = \tilde{\rho}\tilde{T}, \tag{2.15a}$$

$$\tilde{e} = \frac{1}{\gamma - 1}\tilde{T} - Z\tilde{Q}, \tag{2.15b}$$

where $\tilde{Q} \equiv Q/R_g T_0$.

Numerical method

The numerical integration was performed using operator splitting, with the algorithm

$$\boldsymbol{W}^{n+1} = \mathcal{L}_S \mathcal{L}_{FG} \boldsymbol{W}^n,$$

where the superscript indicates the number of timesteps. When integrated in a uniform grid with a cell-centered, finite difference formulation, the convective and geometry source operator $\mathcal{L}_{FG}$ can be written as

$$\boldsymbol{W}_i^{n+1} = \boldsymbol{W}_i^n - \frac{\Delta\tilde{t}}{\Delta\tilde{r}} \left(\boldsymbol{F}_{i+1/2}^n - \boldsymbol{F}_{i-1/2}^n \right) + \Delta\tilde{t}\, \boldsymbol{G}_i^n,$$

where $\Delta\tilde{t}$ is the timestep and $\Delta\tilde{r}$ is the cell size. The subscript indicates the spatial cell number. $\boldsymbol{F}_{i+1/2}^n$ is the flux at the interface between cells i and $i+1$, and should be some conservative upwinding flux. In this work, we employed Roe's approximate Riemann solver (Roe, 1986) for the convective flux. Glaister's (1988) implementation for a general equation of state was used, with an extension for multi-species gases in chemical non-equilibrium (see Appendix B). Second-order temporal and spatial

accuracy was obtained via min–mod flux limiting, and the scheme was made entropy-satisfying with Harten's (1983) entropy fix. The time integration of the geometry term was performed with the forward Euler method, which is only first-order accurate. The benefit in making this integration second-order would be minimal given the small effect of these terms (see §2.3.2).

Finally, the reaction source operator $\mathcal{L}_S$ involves the integration of the equation,

$$\frac{\mathrm{d}\boldsymbol{W}}{\mathrm{d}\tilde{t}} = \boldsymbol{S},$$

which reduces to

$$\frac{\mathrm{d}Z}{\mathrm{d}\tilde{t}} = \tilde{k}(1-Z)\mathrm{e}^{-\tilde{E}_a/\tilde{T}}, \tag{2.16}$$

with $\tilde{\rho}$, $\tilde{u}$ and $\tilde{e}$ constant. If the temperature was constant for this step, (2.16) could be integrated exactly. In this work, we performed the integration using a nominally second-order time accurate predictor–corrector scheme. Equation (2.16) was first integrated for a half-timestep, with the temperature held constant. This gave an estimate for the average mass fraction in the timestep, $Z^{n+1/2}$. The temperature $\tilde{T}^{n+1/2}$ was then computed from the caloric equation of state (2.15b), noting that $\tilde{e}$ is fixed for this step. Finally, (2.16) was integrated for the whole timestep, using the average temperature $\tilde{T}^{n+1/2}$.

The flow solver was incorporated into the Amrita CFD programming system (Quirk, 1998), making use of Amrita's adaptive mesh refinement (AMR) algorithm. The simulations presented in this work used four levels of grid refinement, with refinement ratios of four in each case. Refinement was performed around the shock, where the pressure gradient exceeded a specified threshold, and in the reaction zone, where the species gradient exceeded another threshold. The refinement criteria were chosen to produce a finely resolved shock and a reaction zone with at least 50 mesh cells per half-reaction length.

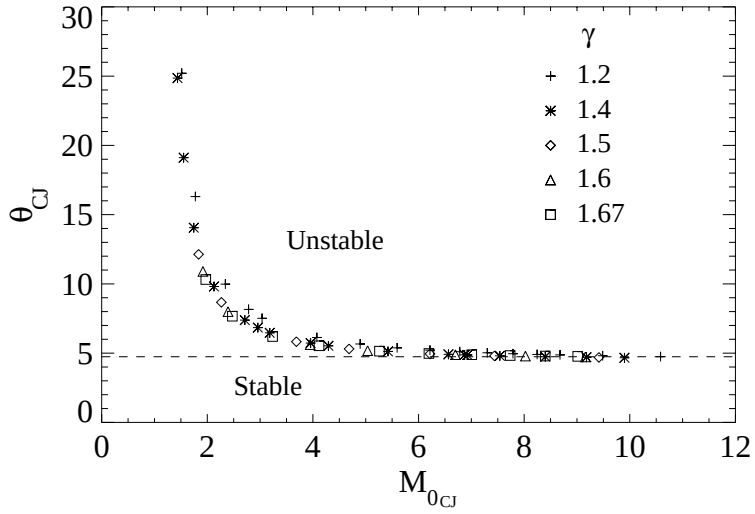

Figure 2.1: Neutral stability curve for planar CJ detonations with one-step Arrhenius rate law.

Computational cases

The choice of computational cases to study was made on the basis of the following argument. Throughout the analysis in this work, it is implicitly assumed that the detonation wave is hydrodynamically stable. Previous computations by He (1996) on spherical detonation initiation with Arrhenius reaction rate demonstrated that instability provides a secondary means of detonation quenching. To isolate the purely gasdynamic quenching mechanism, we chose to perform computations only with stable or slightly unstable mixtures. When slightly unstable, the instability growth rate is sufficiently slow that the gasdynamic quenching still dominates in the short times involved. Using the normal mode stability analysis method of Lee and Stewart (1990), the neutral stability curves for one-dimensional planar CJ detonations have been computed for various ratios of specific heat and are plotted in figure 2.1. Throughout this work, the subscript CJ will be used to denote flow variables for a detonation traveling at CJ velocity, so $M_{0_{CJ}}$ denotes the freestream Mach number M_0 for a CJ wave. θ is the activation energy normalized by the post-shock temperature T_s,

$$\theta \equiv \frac{E_a}{R_g T_s}, \tag{2.17}$$

so θ_{CJ} denotes the value of θ for a wave traveling at CJ velocity. When plotted in the $\tilde{Q}$–$\tilde{E}_a$ plane as originally done by Lee and Stewart (1990), the neutral stability curves for each value of γ are different, but when plotted in the θ_{CJ}–$M_{0_{CJ}}$ plane as in figure 2.1, they essentially collapse to a single curve. Furthermore, for strong detonations with large values of $M_{0_{CJ}}$, the neutral stability curve asymptotes to a constant value of $\theta_{CJ} \approx 4.74$. In this regime, the stability of the wave is then a function of θ_{CJ} only, an example of the dominant effect of θ for the Arrhenius reaction rate model. A further effect of θ is in the shape of the ZND reaction zone profile; the larger the value of θ, the more the ZND profile approaches that of a square-wave, with a near constant state induction zone followed by a rapid energy release. This type of reaction zone structure is typical of that observed in computations of real hydrocarbon mixtures. Hence it would be desirable to use a mixture with such a ZND profile in these computations. The need to maximize θ for a suitable ZND profile while remaining stable or near stable resulted in the choice of examining near-critically stable mixtures. With this restriction and figure 2.1 in mind, the range of behavior for the Arrhenius reaction rate model can be represented by just a single choice of $M_{0_{CJ}}$ and θ_{CJ}. However, ZND calculations also indicate that for the same value of $M_{0_{CJ}}$ and θ_{CJ}, lower values of γ produce reaction zone profiles slightly closer to a square-wave. The dependence upon γ is weak, but cannot be ignored given the desire to achieve a square-wave like profile.

Considering the arguments presented in the previous paragraph, two parameter sets were chosen for computational investigation. They are listed in table 2.1. The subscript vN denotes the post-shock state (von Neumann conditions) for a wave traveling at CJ velocity, while the subscript CJ on the state variables $\tilde{P}$ and $\tilde{T}$ denotes the equilibrium state at the rear of the reaction zone for a wave traveling at CJ velocity. The two cases have the same value of $M_{0_{CJ}}$ and close to the same value of θ, but have different values of γ. Both cases are marginally unstable.

	Case	A	B
Independent quantities	γ	1.2	1.4
	$\tilde{Q}$	22.5	12
	$\tilde{E}_a$	17	25
Dependent quantities	$\tilde{k}$	70.8	108.3
	$\tilde{U}_{CJ}$	4.70	5.08
	$M_{0_{CJ}}$	4.29	4.29
	θ_{CJ}	6.05	5.54
	$\tilde{P}_{vN}$	20.0	21.3
	$\tilde{P}_{CJ}$	10.5	11.2
	$\tilde{T}_{vN}$	2.81	4.52
	$\tilde{T}_{CJ}$	6.00	6.76

Table 2.1: Input fluid and chemical parameters for the numerical simulations.

Initial conditions

At early times in the flow, the blast wave will be a very strong shock, and the chemical energy released into the flow will be negligible compared to the blast source energy. Therefore, the flow will be closely approximated by the similarity solution for a non-reacting strong point blast with zero back-pressure (Taylor, 1950; Sedov, 1959). For a constant γ perfect gas, this point blast theory (PBT) similarity solution is given by

$$R = \left(\frac{E_{source}}{A_2\,\rho_0}\right)^{1/5} t^{2/5}, \quad U = \frac{\mathrm{d}R}{\mathrm{d}t} = \frac{2}{5}\left(\frac{E_{source}}{A_2\,\rho_0}\right)^{1/2} R^{-3/2},$$
$$u_s = \frac{2}{\gamma+1}U, \quad \rho_s = \frac{\gamma+1}{\gamma-1}\rho_0, \quad P_s = \frac{2}{\gamma+1}\rho_0 U^2,$$
$$\frac{u}{u_s} = f\left(\frac{r}{R}\right), \quad \frac{\rho}{\rho_s} = g\left(\frac{r}{R}\right), \quad \frac{P}{P_s} = h\left(\frac{r}{R}\right),$$

where subscript s denotes conditions immediately after the shock, E_{source} is the initial energy release, and A_2 is the energy integral constant, which is a function of γ. Korobeinikov (1991) lists the functions $f(r/R)$, $g(r/R)$ and $h(r/R)$, as well as an empirical curve fit for A_2, accurate to 0.31% in the range $1.2 \leqslant \gamma \leqslant 2.0$,

$$A_2 = 0.31246(\gamma-1)^{-1.1409-0.11735\log_{10}(\gamma-1)}. \tag{2.18}$$

The initial condition used in the numerical simulations was the PBT similarity solution, applied at an initial shock radius R_{source} much less than the shock radius of the critical flow regime later in the simulation. Numerical difficulties associated with the strong shock wave and the singularity at the origin in the PBT similarity solution placed a lower bound on the choice of the initial shock radius. However, in all computational cases presented here, the chemical energy inside the initial source region,

$$E_{chem} = \frac{4}{3}\pi R_{source}^3 \rho_0 Q,$$

was less than 3% of the source energy E_{source}, so the application of the non-reacting PBT was valid.

Consistent with the earlier normalizations, the non-dimensional source energy $\tilde{E}_{source}$ is defined by

$$\tilde{E}_{source} \equiv \frac{E_{source}}{P_0 \Delta_{1/2}^3}.$$

2.3.2 Computational results

Case A

Spatial pressure profiles are plotted in figure 2.2 for case A from table 2.1, with two different source energies. The first computation, with $\tilde{E}_{source} = 166 \times 10^6$, fails to initiate, so this represents a subcritical initiation energy. As the wave decays to the CJ state, where $P_s = P_{vN}$, the von Neumann spike immediately behind the shock decreases in size and the reaction zone lengthens. The post-shock pressure continues to decay to well below the von Neumann pressure, and the von Neumann spike disappears, signifying failure to initiate a detonation. In figure 2.2(b), where $\tilde{E}_{source} = 169 \times 10^6$, the early profiles closely match those in figure 2.2(a). But at around $\tilde{R} = 300$, the post-shock pressure begins to rise, overshooting P_{vN}, before settling back down to around P_{vN}. It then remains close to steady, indicating a spherical detonation has been successfully initiated. Hence this source energy is a supercritical initiation energy. The mechanism causing the re-initiation explosion in figure 2.2(b) appears to be the formation and amplification of a pressure pulse at

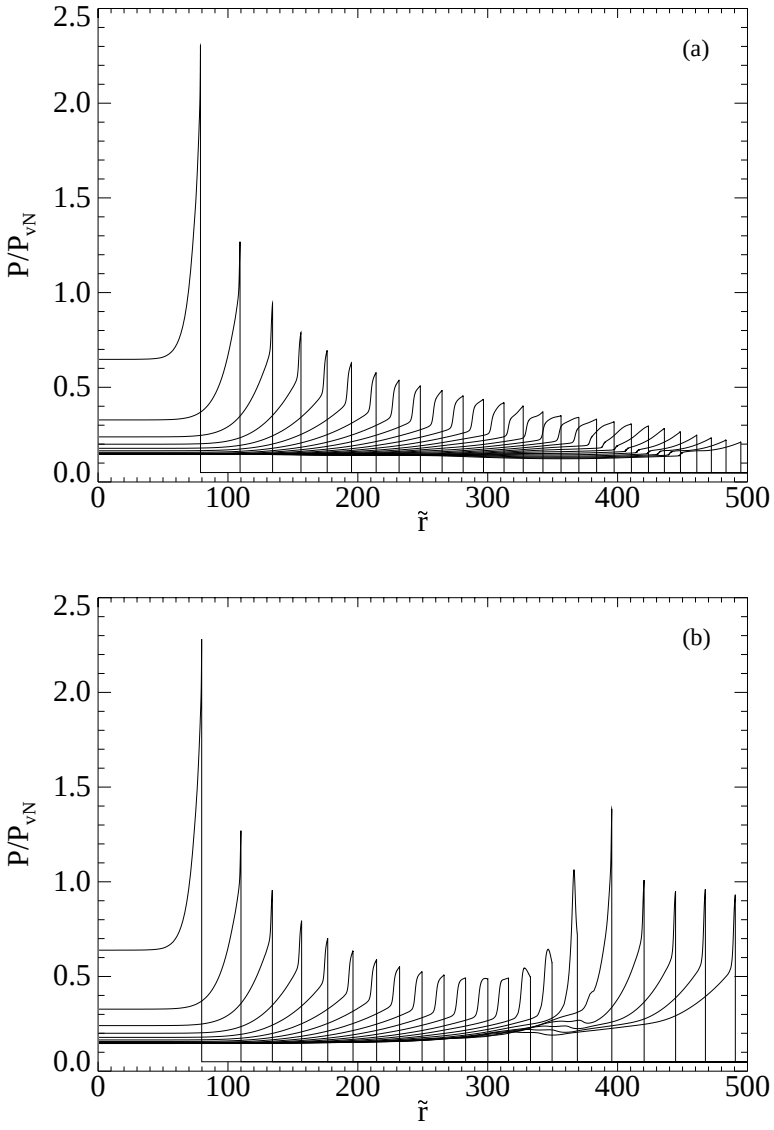

Figure 2.2: Spatial pressure profiles for case A, at roughly equal timesteps. (a) $\tilde{E}_{source} = 166 \times 10^6$; (b) $\tilde{E}_{source} = 169 \times 10^6$.

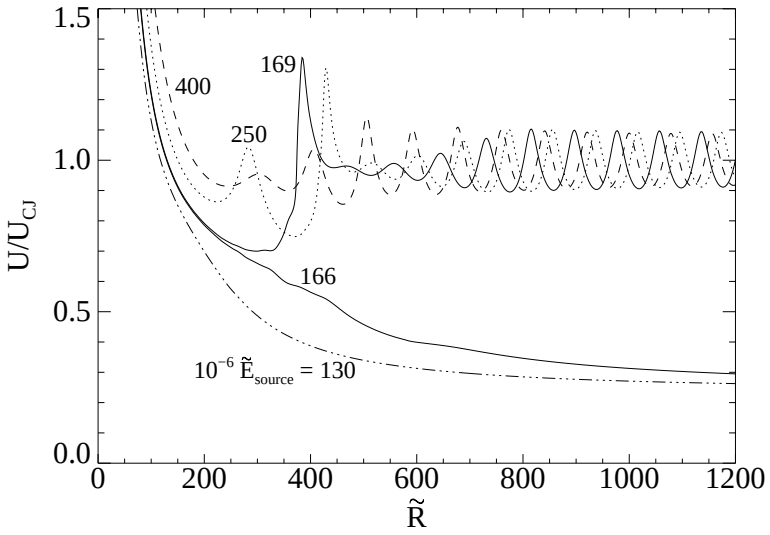

Figure 2.3: Leading shock velocity versus position for case A, with several different source energies. $\tilde{E}_{source} = 130 \times 10^6, 166 \times 10^6, 169 \times 10^6, 250 \times 10^6, 400 \times 10^6$.

the rear of the reaction zone. This mechanism has also been observed in previous numerical simulations (Clarke et al., 1986, 1990; Mazaheri, 1997).

The location and velocity of the leading shock were determined as follows. The shock pressure $\tilde{P}_s$ was first evaluated approximately as the instantaneous local maximum in the pressure profile just behind the shock. This local maximum exists because the pressure behind the shock decreases as a result of the exothermic reaction and/or geometric expansion. The shock location $\tilde{R}$ was then determined as the interpolated position in the spatial pressure profile for which the pressure was $(\tilde{P}_0 + \tilde{P}_s)/2$, roughly the midpoint of the numerically smeared shock. Having computed this at many timesteps in the computation, the shock velocity was finally determined in a postprocessing operation by a second-order differentiation of the data points $\tilde{R}(\tilde{t})$.

Figure 2.3 shows the velocity of the leading shock plotted against the shock radius, for case A with several different source energies. In the successfully initiated cases, the mild instability of the detonation wave is evident at late times. However, the instability develops only after the detonation initiation. Hence, the instability does not seem to influence the gasdynamic initiation process significantly. The two near-critical curves, $\tilde{E}_{source} = 166 \times 10^6$ and 169×10^6, begin to deviate significantly at

about $\tilde{R} = 225$, where $U/U_{CJ} = 0.75$. This point is the critical point of interest for these near-critical initiations, for it is here that failure or success is determined in the detonation initiation process. Everything after this, including the re-initiation mechanism for the super-critical case, is irrelevant if we are only concerned with the critical energy. This is in contrast to the proposition of Lee and Higgins (1999) that any model of initiation criteria must address the mechanism of re-acceleration of the decaying shock and transition to detonation. Our simulations indicate that it is possible to form an estimate of the critical initiation energy by examining the simpler problem of the failure mechanism involved in decoupling the reaction zone from the decaying blast wave. It is interesting to note that the critical point occurs well before the formation of the pressure pulse in figure 2.2(b). This suggests that the pressure pulse and the associated "quasi-steady" (Lee and Higgins, 1999) portion of the velocity profile are not the underlying factors controlling success or failure of initiation, but are merely the mechanisms by which successful initiation proceeds.

The position of the leading shock, the loci of 5% and 95% reaction, and the sonic surface are plotted against time in figure 2.4, for the two near-critical cases of the previous figure. In figure 2.4(a), the reaction zone is initially closely coupled to the shock wave when the shock is very strong, but it later detaches, indicating the detonation has failed and the reaction has quenched. By contrast, the reaction zone remains closely coupled to the shock wave in figure 2.4(b), indicating the successful initiation of a quasi-steady detonation.

The sonic surfaces in figures 2.4 have been defined as the loci of points for which the flow is sonic with respect to the shock front at a given instant in time. The physically significant sonic point occurs when the flow is sonic with respect to the rear end of the reaction zone, the limiting condition for which small disturbances can propagate into the reaction zone from the trailing expansion wave. However, there is no simple way to determine the location of the rear end of the reaction zone. In steady flow, the rear end of the reaction zone travels at the same velocity as the shock front, and these two sonic point definitions are equivalent, but they may differ in unsteady flow. For this reason, the sonic surface plotted in the r–t diagrams

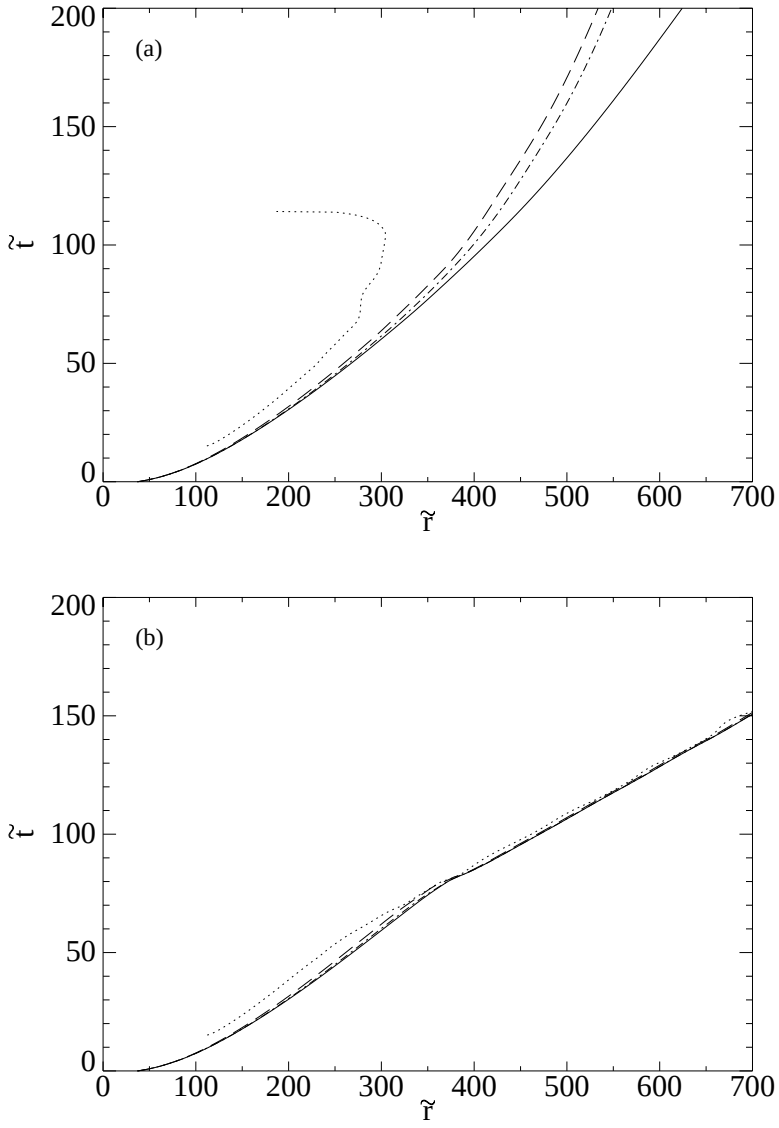

Figure 2.4: Leading shock position, reaction loci and sonic point location versus time, for case A. —— shock; $-\cdot-\cdot$ 5% reaction; $---$ 95% reaction; $\cdots\cdots$ sonic point. (a) $\tilde{E}_{source} = 166 \times 10^6$; (b) $\tilde{E}_{source} = 169 \times 10^6$.

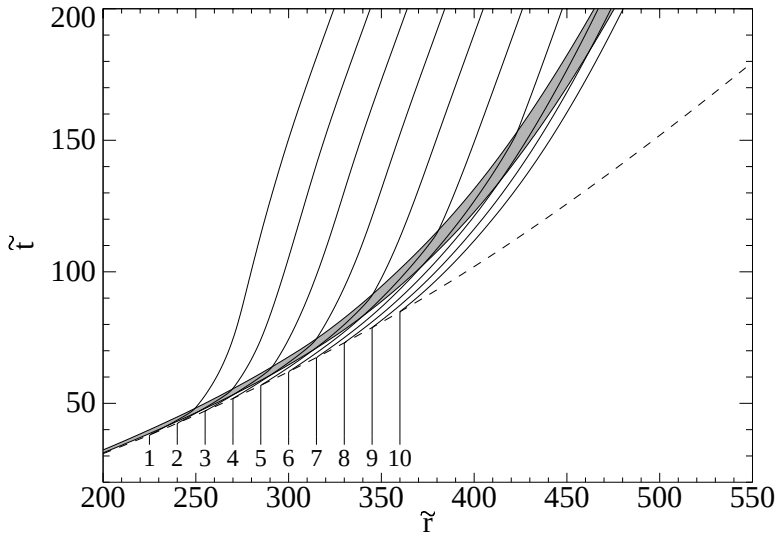

Figure 2.5: Particle paths for ten sample particles in case A, with $\tilde{E}_{source} = 160 \times 10^6$. Shock (dashed line); 5% to 95% reaction (shaded region); particle paths (solid lines).

cannot be regarded as the critical factor determining detonation initiation or failure. Its relevance is simply that it must eventually appear at the rear of the reaction zone if a quasi-steady, quasi-planar detonation is formed.

The reaction zone structure equations in §2.2.2 described the evolution of quantities along particle paths. To examine the behavior of these equations in the numerical simulations of the direct initiation problem, it was necessary to extract Lagrangian particle path data from the Eulerian flow solution. This was done by specifying some initial particle locations and then in a non-intrusive fractional step of the flow solver, integrating the particles' paths through the r–t solution field, using the local flow velocity. The flow velocity was determined spatially by linearly interpolating the velocity field at each CFD timestep, and then the time integration of the particle positions was performed with a nominally second order accurate predictor–corrector scheme. The particle positions and flow variables at those locations were then output as functions of time at each CFD timestep, where the flow variables were linearly interpolated from the spatial solution field.

For case A with $\tilde{E}_{source} = 160 \times 10^6$, a slightly subcritical energy, figure 2.5 shows the paths of ten sample particles that cross the leading shock around the time of

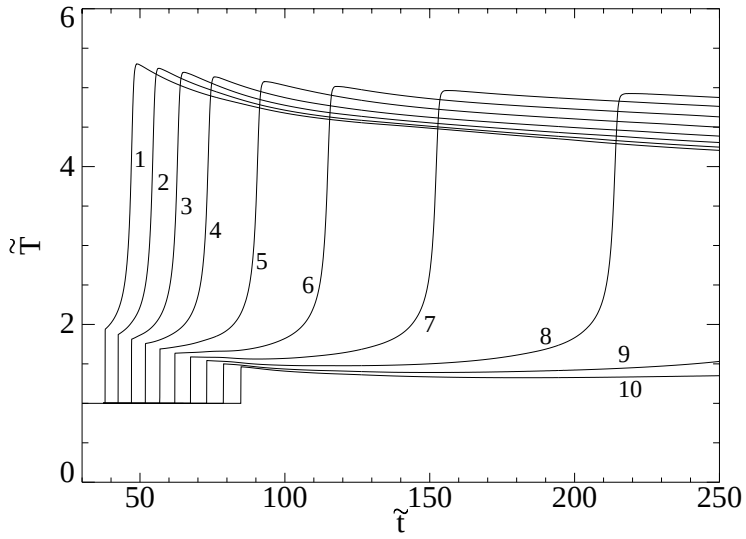

Figure 2.6: Temperature histories along the same ten particle paths as in figure 2.5, for case A with $\tilde{E}_{source} = 160 \times 10^6$.

detonation failure. The plot also shows the shock and partial reaction region, as in the previous r–t diagrams of figure 2.4. The earlier particles traverse the reaction zone rapidly, indicating that the flow is still detonating at this stage. By about particle 6, the reaction time has grown significantly, suggesting that the wave is failing here. The last particles never reach the reaction zone in the time plotted. Note that the partial reaction lines are essentially parallel to the streamlines at the late times, indicating that the reaction has completely quenched by then.

Figure 2.6 shows the temperature as a function of time along the same ten particle paths. The first few reach thermal runaway quickly, but by the sixth or seventh particle path, the explosion time has grown significantly. The last particles merely cool gradually and never react. The slight negative temperature gradient along the later particle paths immediately after the shock is the forcing of the unsteadiness, as discussed in §2.2.2. It is this gradient that prevents the particles from undergoing thermal runaway.

The magnitude of the various competing terms in the temperature reaction zone structure equation was next examined in the numerical simulations. In the non-dimensional notation of §2.3.1, the temperature equation (2.13) for spherical flow

$(j = 2)$ becomes

$$\underbrace{(1-M^2)\frac{\gamma}{\gamma-1}\frac{\mathrm{D}\tilde{T}}{\mathrm{D}\tilde{t}}}_{\text{total}} = \underbrace{(1-\gamma M^2)\tilde{Q}\tilde{k}(1-Z)\exp\left(-\frac{\tilde{E}_a}{\tilde{T}}\right)}_{\text{heat release}} + \underbrace{\frac{2}{\tilde{r}}\tilde{w}^2(\tilde{U}-\tilde{w})}_{\text{curvature}} + \underbrace{\tilde{w}\frac{\mathrm{d}\tilde{U}}{\mathrm{d}\tilde{t}} - \tilde{w}\frac{\partial\tilde{w}}{\partial\tilde{t}} + \frac{1}{\tilde{\rho}}\frac{\partial\tilde{P}}{\partial\tilde{t}}}_{\text{unsteadiness}}. \tag{2.19}$$

The unsteadiness terms were evaluated as the residual of this equation. As a consistency check, they were also evaluated with the aid of the mass and momentum conservation equations (2.5), in appropriate non-dimensional form, which gives

$$\tilde{w}\frac{\mathrm{d}\tilde{U}}{\mathrm{d}\tilde{t}} - \tilde{w}\frac{\partial\tilde{w}}{\partial\tilde{t}} + \frac{1}{\tilde{\rho}}\frac{\partial\tilde{P}}{\partial\tilde{t}} = \frac{1}{\tilde{\rho}}\left(\frac{\mathrm{D}\tilde{P}}{\mathrm{D}\tilde{t}} - \tilde{w}^2\frac{\mathrm{D}\tilde{\rho}}{\mathrm{D}\tilde{t}}\right) - \frac{2}{\tilde{r}}\tilde{w}^2(\tilde{U}-\tilde{w}). \tag{2.20}$$

The right-hand side of this equation was evaluated directly from the Lagrangian particle path data. The Lagrangian derivatives $\mathrm{D}\tilde{T}/\mathrm{D}\tilde{t}$, $\mathrm{D}\tilde{P}/\mathrm{D}\tilde{t}$ and $\mathrm{D}\tilde{\rho}/\mathrm{D}\tilde{t}$ in (2.19) and (2.20) were evaluated in a postprocessing operation by a second order differentiation of the particle path data points $\tilde{T}(\tilde{t})$, $\tilde{P}(\tilde{t})$ and $\tilde{\rho}(\tilde{t})$.

The terms in (2.19) have been computed along the same ten particle paths as in figure 2.5, and are plotted in figure 2.7 for a selection of the particles. The left border of each plot is the instant in time when the particle crosses the shock. For the particles prior to or at failure (particles 1, 5 and 6), it is clear that the curvature term makes a negligible contribution to the temperature gradient when compared with the magnitudes of the other terms on the right-hand side of (2.19). By contrast, the contribution from unsteadiness is significant. Along particle paths 1 and 5, the unsteadiness is a negative forcing on the temperature gradient that reduces the total temperature gradient below that due to heat release alone, although it is not strong enough to prevent reaction. For particle path 6, the unsteadiness is initially about equal to the heat release, causing the total gradient to be almost zero, and the reaction nearly quenches. By particle path 10, the unsteadiness dominates the

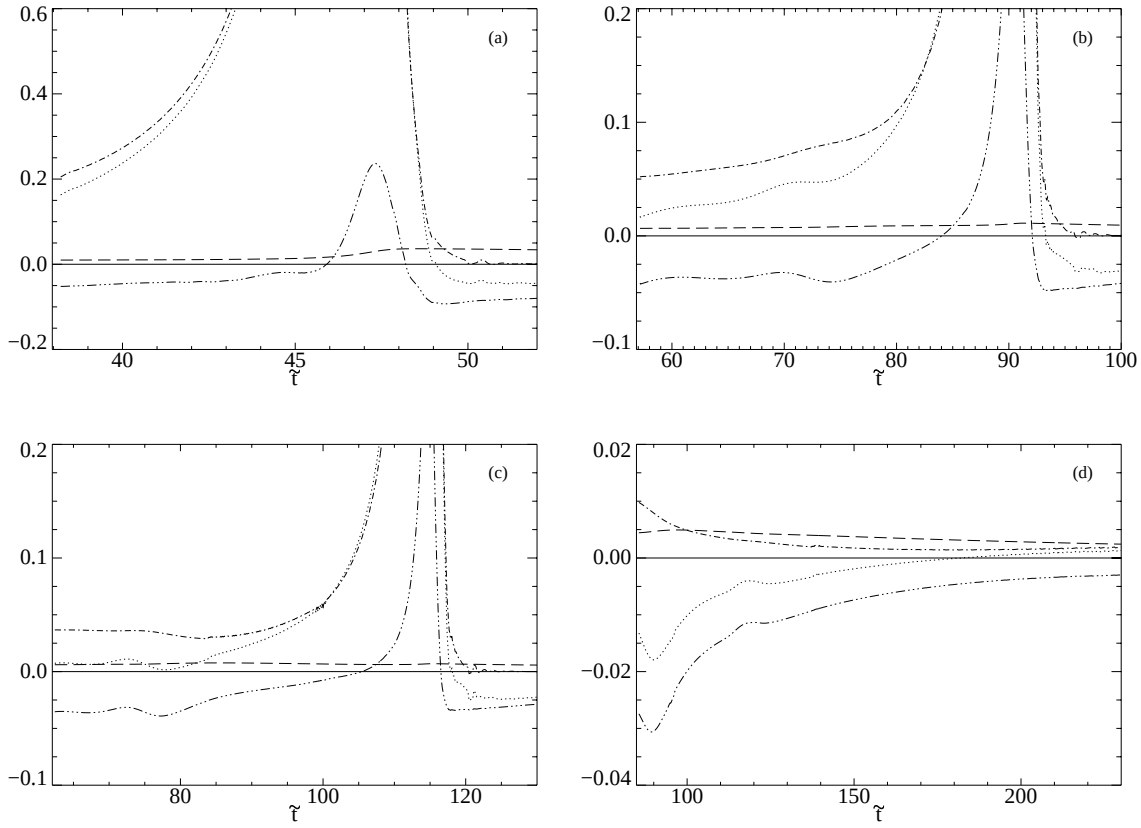

Figure 2.7: Terms in reaction zone temperature equation (2.19) along the same particle paths as in figure 2.5, for case A with $\tilde{E}_{source} = 160 \times 10^6$. $\cdots\cdots$ total temperature gradient; $-\cdot-\cdot$ heat release; $---$ curvature; $-\cdots-\cdots$ unsteadiness. (*a*) Particle 1; (*b*) Particle 5; (*c*) Particle 6; (*d*) Particle 10.

heat release, and the reaction is completely quenched. A final observation is that the unsteadiness expression is almost constant along each particle path within the induction zone. This is true for all particles that traverse the induction zone before detonation failure, that is, all the particles in figure 2.7 except particle path 10. These important observations regarding the contributions of curvature and unsteadiness to the Lagrangian temperature derivative will be used to develop a local initiation model in the following section.

In §2.2.2, it was noted that the temperature reaction zone structure equation could be written in a different form, with the partial time derivative from the temperature total derivative moved to the right hand side and grouped with the other unsteady terms. In that case, the non-dimensional equation equivalent to (2.19) would be

$$\underbrace{(1-M^2)\frac{\gamma}{\gamma-1}w\frac{\partial\tilde{T}}{\partial\tilde{x}}}_{\text{spatial}} = \underbrace{(1-\gamma M^2)\tilde{Q}\tilde{k}(1-Z)\exp\left(-\frac{\tilde{E}_a}{\tilde{T}}\right)}_{\text{heat release}} + \underbrace{\frac{2}{\tilde{r}}\tilde{w}^2(\tilde{U}-\tilde{w})}_{\text{curvature}} + \underbrace{\tilde{w}\frac{\mathrm{d}\tilde{U}}{\mathrm{d}\tilde{t}} - \tilde{w}\frac{\partial\tilde{w}}{\partial\tilde{t}} + \frac{1}{\tilde{\rho}}\frac{\partial\tilde{P}}{\partial\tilde{t}} - (1-M^2)\frac{\gamma}{\gamma-1}\frac{\partial\tilde{T}}{\partial\tilde{t}}}_{\text{unsteadiness}}. \tag{2.21}$$

The left-hand side is now related to the spatial temperature gradient, rather than the total temperature gradient. This form allows direct evaluation of the quasi-steady assumption since omitting the unsteadiness expression gives the standard quasi-steady equation for the spatial temperature distribution, such as equation (A 2a) in He and Clavin (1994).

In figure 2.8, the terms in (2.21) are plotted along the same four particle paths that were shown in figure 2.7. Several observations can be made. Firstly, the magnitude of the curvature term in the induction zone is still quite small compared to the unsteady terms. It is certainly not greater than the unsteady terms and hence a quasi-steady assumption is clearly erroneous for this flow. Secondly, all the terms on the right-hand side of the equation, including the unsteady terms, are actually of the same sign as the heat release in the induction zone. This makes a physical interpretation of

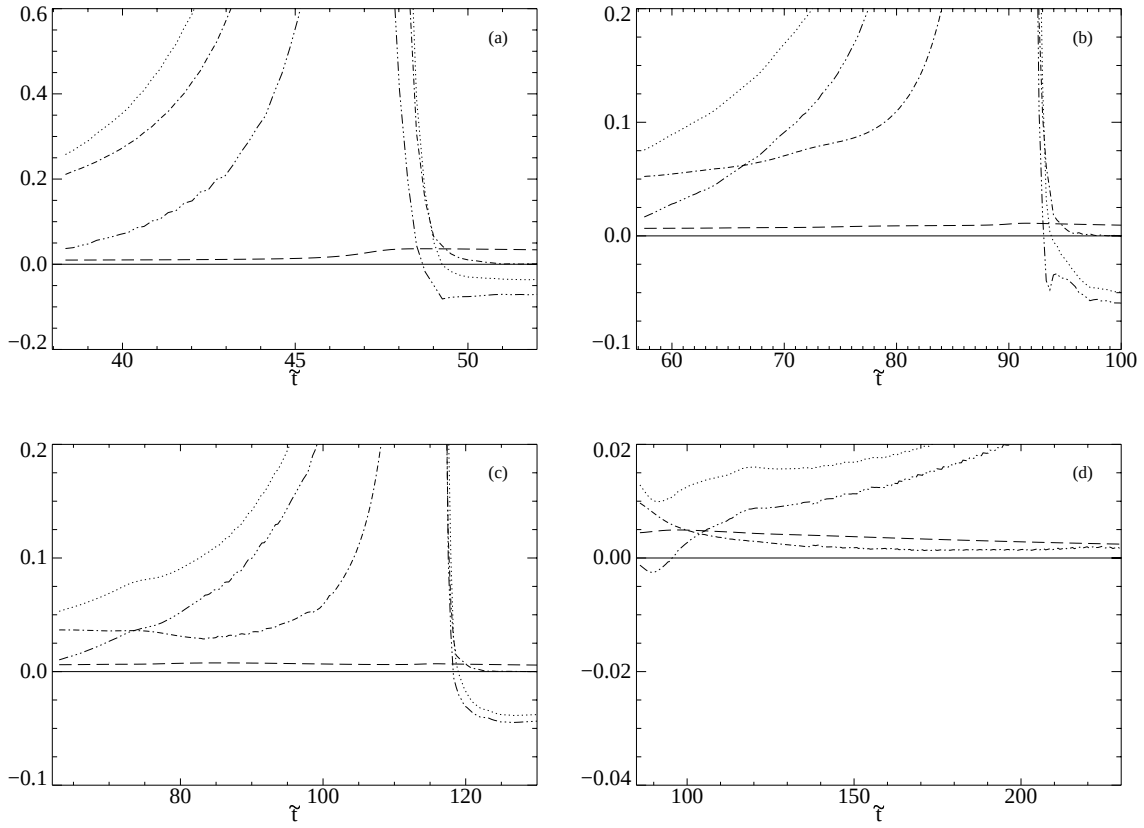

Figure 2.8: Terms in equation (2.21) along the same particle paths as in figure 2.5, for case A with $\tilde{E}_{source} = 160 \times 10^6$. $\cdots\cdots$ spatial temperature gradient; $-\cdot-\cdot$ heat release; $- - -$ curvature; $-\cdots-\cdots$ unsteadiness. (a) Particle 1; (b) Particle 5; (c) Particle 6; (d) Particle 10.

the failure mechanism more difficult than with the reaction zone structure equation (2.19). Finally, the unsteady terms show a steep variation through the induction zone, and no simplifying assumption regarding their behavior is apparent. Contrast this with figure 2.7 where prior to failure the unsteady terms were approximately constant in the induction zone. As will be seen in the next section, writing the equations in a form for which the unsteady terms are approximately constant is essential to our analysis as it reduces the governing PDE to an ODE. It is largely for this reason that we have chosen to use (2.19) in the analysis rather than (2.21).

It could also be argued that since equation (2.21) describes the spatial temperature gradient, the equation terms' spatial variation should be examined, rather than the variation along a particle path. That is, they should be plotted in an Eulerian reference frame rather than a Lagrangian frame. In figure 2.9, the terms in this equation are plotted against $\tilde{x}$, the distance behind the leading shock, at several instants in time around the time of detonation failure. The results are qualitatively similar to figure 2.8. The main differences are at the late times in figures 2.9(c) and (d), where the unsteady terms are negative in the early part of the induction zone, and are of comparable magnitude to the curvature term. They are still not small compared to the curvature term, so even at these late times, the quasi-steady assumption is invalid. Other than this, all the conclusions of the previous paragraph apply.

Case B

We now turn our attention to the other computational case listed in table 2.1, case B. Figure 2.10 shows the velocity of the leading shock plotted against the shock radius, with several different source energies. The behavior is more complex than in case A. For $\tilde{E}_{source} \leqslant 199 \times 10^6$, the detonation fails to initiate, with a monotonically decreasing shock strength. At $\tilde{E}_{source} = 200 \times 10^6$, the detonation initiates, with a re-initiation explosion similar to that observed for the marginally supercritical source energy in case A. However, for $206 \times 10^6 \leqslant \tilde{E}_{source} \leqslant 305 \times 10^6$, the detonation actually fails again, this time not with a monotonically decreasing shock strength, but with a single hump in the velocity profile. For $\tilde{E}_{source} \geqslant 306 \times 10^6$, the detonation initiates

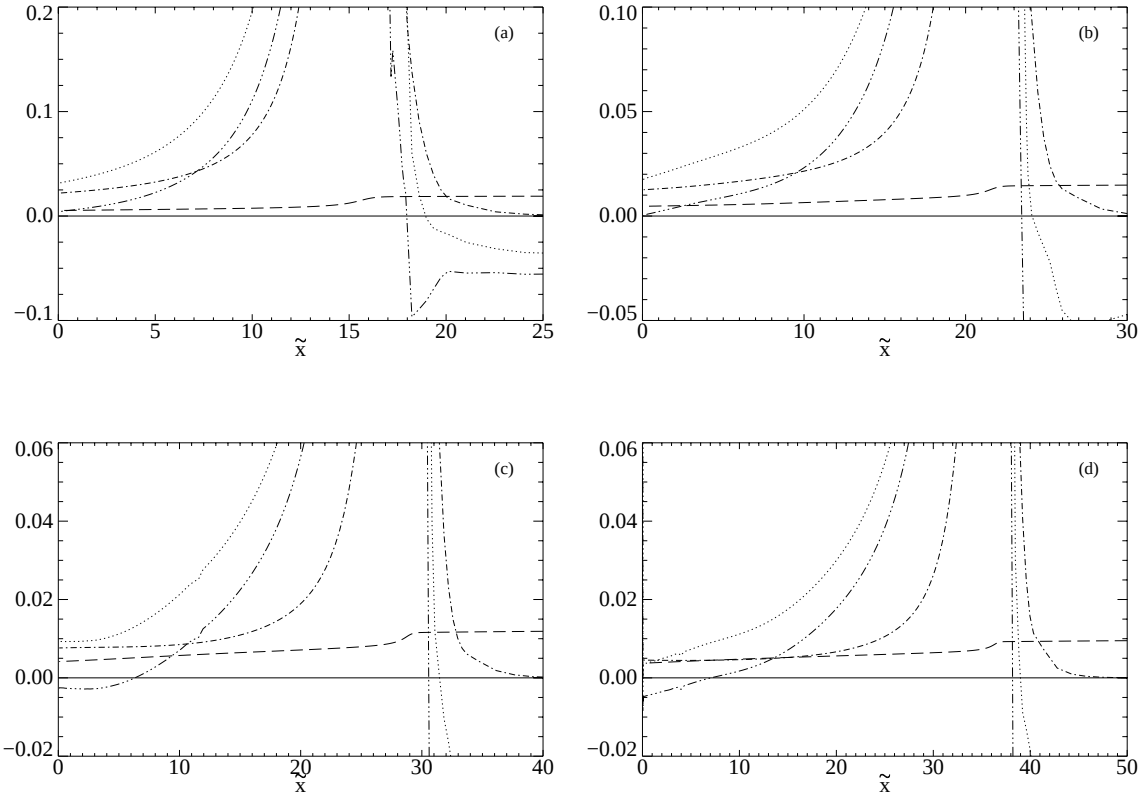

Figure 2.9: Spatial distribution of terms in equation (2.21), for case A with $\tilde{E}_{source} = 160 \times 10^6$. $\cdots\cdots$ spatial temperature gradient; $-\cdot-\cdot$ heat release; $---$ curvature; $-\cdots-\cdots$ unsteadiness. (a) $\tilde{t} = 70.5$; (b) $\tilde{t} = 80.3$; (c) $\tilde{t} = 90.2$; (d) $\tilde{t} = 100.2$.

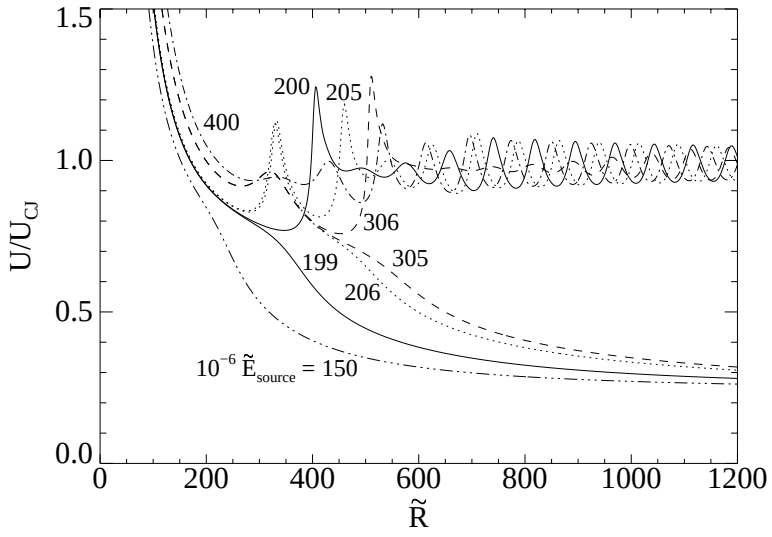

Figure 2.10: Leading shock velocity versus position for case B, with several different source energies. $\tilde{E}_{source} = 150 \times 10^6, 199 \times 10^6, 200 \times 10^6, 205 \times 10^6, 206 \times 10^6, 305 \times 10^6, 306 \times 10^6, 400 \times 10^6$.

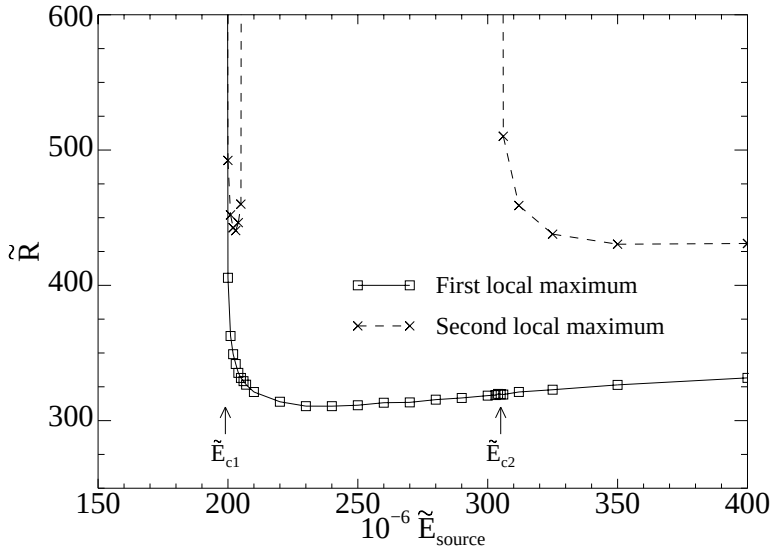

Figure 2.11: Location of first two local maxima in shock velocity profile for case B, as a function of source energy.

again, in a manner similar to that in case A. The complex behavior means we cannot identify a unique critical energy for this case. The behavior can be summarized by plotting the location of the first two local maxima in the velocity profiles for several different source energies, as shown in figure 2.11. There are thus two critical energies, which we designate as E_{c1} and E_{c2}, where $E_{c1} < E_{c2}$. An extensive scan of source energies in case A did not reveal the presence of a second critical energy, and we conclude that case A does have a unique critical energy.

A non-unique critical energy was also observed by Mazaheri (1997), although this study was only performed at $\gamma = 1.2$, where a second critical energy was found to exist for large activation energies. Our work shows that at larger γ, a second critical energy can exist even for lower activation energies near the neutral stability limit. This is an interesting result that challenges the very notion of critical energy, or at least, the ability of the one-step reaction model to capture a critical energy. However, it is the subject of a whole other research project in itself, and we will not pursue it further here. The velocity profiles around the first critical energy in case B appear to be very similar to those around the critical energy in case A. This suggests a universal behavior at the lowest critical energy. For the remainder of this work,

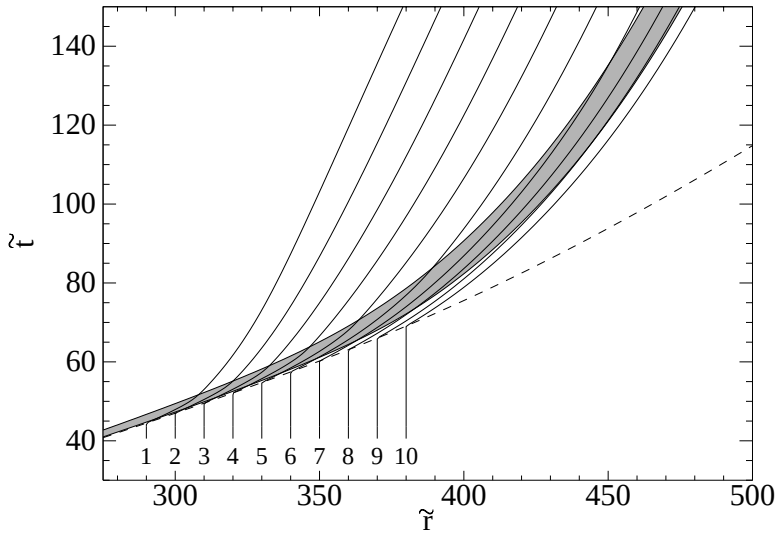

Figure 2.12: Particle paths for ten sample particles in case B, with $\tilde{E}_{source} = 199 \times 10^6$. Shock (dashed line); 5% to 95% reaction (shaded region); particle paths (solid lines).

including the development of a critical energy model equation, we will consider only this lower bound to the critical energy, where failure occurs with a monotonically decreasing shock strength. Hence, our model will at best give a lower bound estimate of the critical energy. In figure 2.10, the two curves near the first critical energy, $\tilde{E}_{source} = 199 \times 10^6$ and 200×10^6, begin to deviate significantly at about $\tilde{R} = 280$, where $U/U_{CJ} = 0.8$. This is the critical point for the first critical energy, and it occurs at a similar shock velocity to that in case A.

The Lagrangian particle path information from figures 2.5 to 2.7 has been repeated in figures 2.12 to 2.14 for case B, with $\tilde{E}_{source} = 199 \times 10^6$, a slightly subcritical source energy. Figure 2.12 shows the r–t diagram with the paths of ten sample particles that cross the shock around the time of failure. The first few react rapidly while the last couple do not reach the reaction zone at all. The plot is similar to the earlier r–t diagram for case A.

Figure 2.13 shows the evolution of the temperature along the same ten particle paths. Failure occurs more sharply than was observed in case A, with the reaction time growing rapidly around particle path 7, and the post-shock temperature gradient decreasing quickly. Along the last few particle paths, there is a strong negative tem-

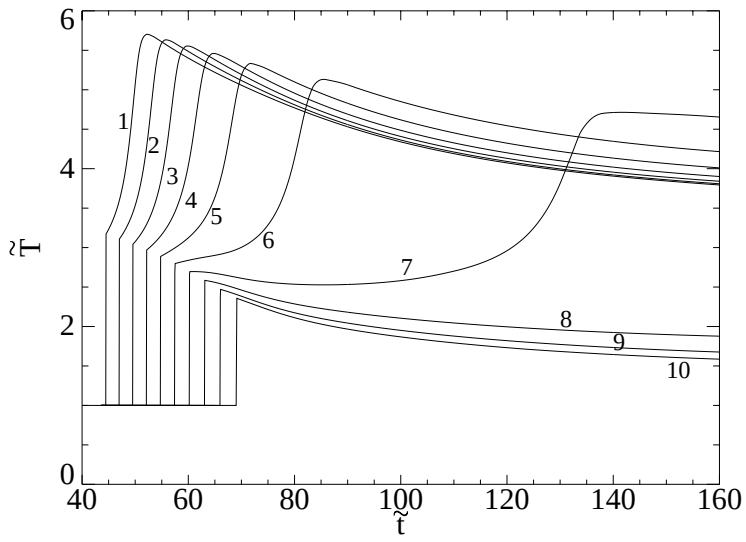

Figure 2.13: Temperature histories along the same ten particle paths as in figure 2.12, for case B with $\tilde{E}_{source} = 199 \times 10^6$.

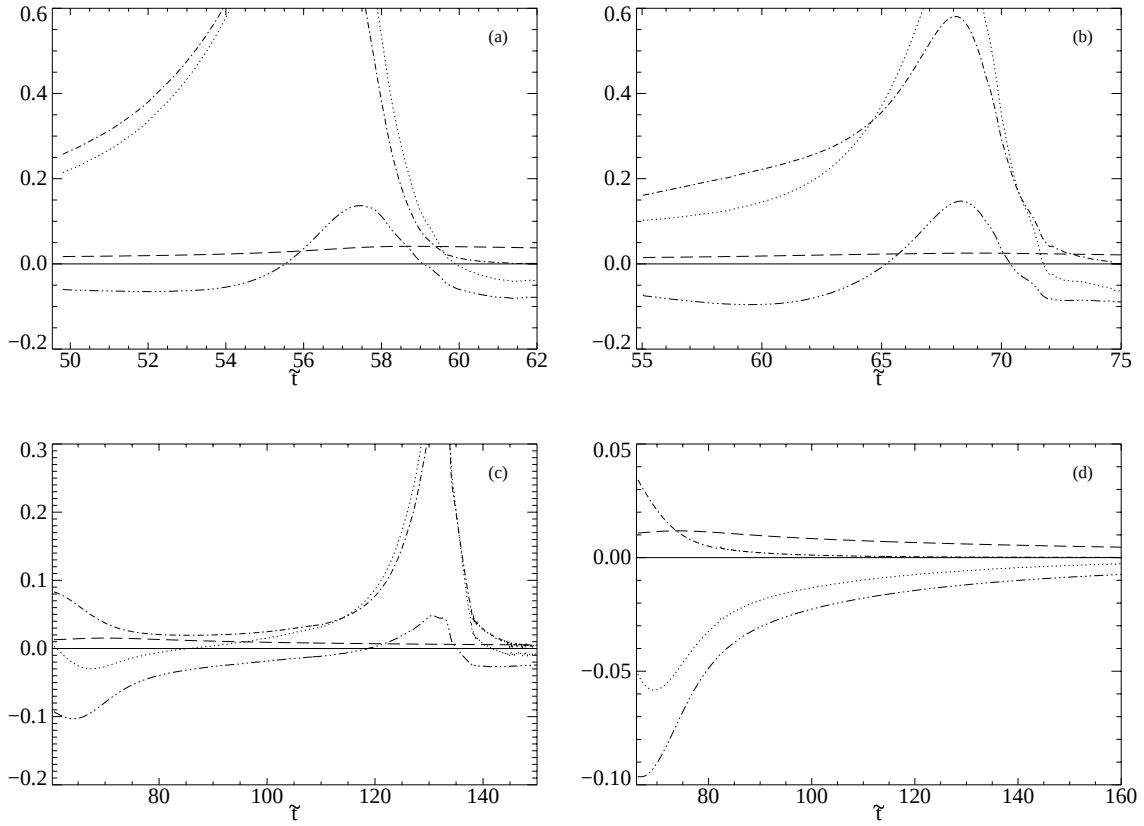

Figure 2.14: Terms in reaction zone temperature equation (2.19) along the same particle paths as in figure 2.12, for case B with $\tilde{E}_{source} = 199 \times 10^6$. $\cdots\cdots$ total temperature gradient; $-\cdot-\cdot$ heat release; $--$ curvature; $-\cdots-\cdots$ unsteadiness. (*a*) Particle 3; (*b*) Particle 5; (*c*) Particle 7; (*d*) Particle 9.

perature gradient behind the shock and the reaction quenches, indicating detonation failure.

The terms in the temperature reaction zone structure equation (2.19) are plotted along four of the particle paths in figure 2.14. As before, the curvature term is small compared to the contributions from heat release and unsteadiness, at least prior to failure. For particles 3 and 5, both before failure, the unsteadiness provides a negative forcing on the heat release term but is insufficient to prevent the reaction from proceeding. By particle path 7, the magnitude of the unsteadiness is as great as the heat release term, and it significantly delays the reaction. It completely quenches the reaction by particle 9. As in figure 2.7, the unsteadiness expression is almost constant in the induction zone, for the particles prior to failure (particles 3 and 5).

2.4 Local Initiation Model

In the previous section, the terms in the temperature reaction zone structure equation (2.13) were investigated along particle paths in the induction zones of near-critical blast initiations. It was found that the curvature term was negligible compared to the other terms. This same conclusion is obtained from an analytical consideration of the terms of the equation (see the Appendix). Additionally, the numerical simulations demonstrated that the unsteadiness expression was approximately constant. Thus, the unsteadiness expression can be approximated by its initial value on the particle path, that is, its value immediately after the shock at the time when the particle crosses the shock. Neglecting the curvature term, and setting the unsteadiness expression equal to its initial value immediately after the shock, (2.13) becomes

$$\begin{aligned}(1-M^2)C_P\frac{\mathrm{D}T}{\mathrm{D}t} = (1-\gamma M^2)Qk(1-Z)\exp\left(-\frac{E_a}{R_gT}\right)\\ +\left(w_s\frac{\mathrm{d}U}{\mathrm{d}t}-w_s\frac{\mathrm{d}w_s}{\mathrm{d}t}+\frac{1}{\rho_s}\frac{\mathrm{d}P_s}{\mathrm{d}t}\right)_i,\end{aligned} \tag{2.22}$$

where subscript s refers to conditions immediately after the shock, and subscript i refers to the time t_i when the particle under consideration initially crosses the shock.

Note the unsteadiness is now a constant forcing for a given particle, and we have reduced the equation from a PDE to an ODE.

Recall the definition of the non-dimensional activation energy θ from (2.17). In particular,

$$\theta_i = \frac{E_a}{R_g T_{s,i}},$$

where $T_{s,i}$ is the post-shock temperature at time t_i. Note that $T_{s,i}$ and θ_i are functions only of the time t_i. Since t_i is a constant for a given particle, then when applied along a particular particle path in (2.22), $T_{s,i}$ and θ_i will be constants. If the unsteadiness expression in (2.22) is of no greater magnitude than the heat release term, as was the case in the numerical simulations, then we can invoke standard large activation energy asymptotic expansions used to compute analytical induction times in the ZND model. Following this approach, we assume $\theta_i \gg 1$ and the temperature perturbation in the induction zone is small, $\delta T/T_{s,i} = O(1/\theta_i)$. Then the following asymptotic expansion applies in the induction zone:

$$\frac{T}{T_{s,i}} = 1 + \frac{1}{\theta_i}\hat{T}_1 + O\left(\frac{1}{\theta_i^2}\right),$$

where $\hat{T}_1$ is dimensionless and $O(1)$. Similarly, asymptotic expansions in Mach number and progress variable give

$$\frac{M}{M_{s,i}} = 1 + O\left(\frac{1}{\theta_i}\right),$$
$$Z = O\left(\frac{1}{\theta_i}\right).$$

Using the above asymptotic expansions in (2.22) and retaining only the leading order terms gives

$$(1-M_{s,i}^2)C_P T_{s,i}\frac{1}{\theta_i}\frac{\mathrm{D}\hat{T}_1}{\mathrm{D}t} = (1-\gamma M_{s,i}^2)Qk\mathrm{e}^{\hat{T}_1-\theta_i} + \left(w_s\frac{\mathrm{d}U}{\mathrm{d}t} - w_s\frac{\mathrm{d}w_s}{\mathrm{d}t} + \frac{1}{\rho_s}\frac{\mathrm{d}P_s}{\mathrm{d}t}\right)_i. \quad (2.23)$$

Define a non-dimensional time by

$$\zeta \equiv \frac{t - t_i}{\tau_i},$$

where

$$\tau = \frac{1}{k}\frac{1 - M_s^2}{1 - \gamma M_s^2}\frac{1}{\theta}\frac{C_P T_s}{Q}\mathrm{e}^{\theta}, \tag{2.24}$$

and τ_i is τ evaluated at time t_i. Then (2.23) reduces to

$$\frac{\mathrm{D}\hat{T}_1}{\mathrm{D}\zeta} = \mathrm{e}^{\hat{T}_1} - \alpha_i, \tag{2.25}$$

where

$$\alpha = -\frac{\theta\tau}{(1 - M_s^2)C_P T_s}\left(w_s\frac{\mathrm{d}U}{\mathrm{d}t} - w_s\frac{\mathrm{d}w_s}{\mathrm{d}t} + \frac{1}{\rho_s}\frac{\mathrm{d}P_s}{\mathrm{d}t}\right), \tag{2.26}$$

and α_i is α evaluated at time t_i.

If $\alpha_i = 0$, then (2.25) is identical to Frank-Kamenetskii's (1969) adiabatic homogeneous thermal explosion equation, under the approximation of large activation energy. With initial condition $\hat{T}_1 = 0$ when $\zeta = 0$, it has solution

$$\hat{T}_1 = \ln\left(\frac{1}{1 - \zeta}\right).$$

This "explodes" ($\hat{T}_1 \to \infty$) at $\zeta_{exp} = 1$, so τ is the asymptotic induction time for a ZND detonation. If instead we consider $\alpha_i > 0$, then (2.25) has solution

$$\hat{T}_1 = \ln\left\{\frac{\alpha_i}{1 - \mathrm{e}^{\alpha_i\zeta}(1 - \alpha_i)}\right\},$$

and now,

$$\zeta_{exp} = \frac{1}{\alpha_i}\ln\left(\frac{1}{1 - \alpha_i}\right).$$

Note that $\zeta_{exp} \to \infty$ as $\alpha_i \to 1$, so in this model, a particle will undergo reaction in finite time provided $\alpha_i < 1$ for that particle. We will refer to α as the initiation parameter, so the critical value of the initiation parameter is one.

The shock conditions are given by the perfect gas jump conditions. Using the

strong shock approximation for simplicity, these are

$$P_s = \frac{2}{\gamma+1}\rho_0 U^2, \tag{2.27a}$$

$$\rho_s = \frac{\gamma+1}{\gamma-1}\rho_0, \tag{2.27b}$$

$$w_s = \frac{\gamma-1}{\gamma+1}U, \tag{2.27c}$$

$$T_s = \frac{P_s}{\rho_s R_g} = \frac{2(\gamma-1)}{(\gamma+1)^2}\frac{U^2}{R_g}, \tag{2.27d}$$

$$M_s^2 = \frac{\gamma-1}{2\gamma}, \tag{2.27e}$$

where subscript 0 denotes the uniform conditions upstream of the shock. Substitution of (2.27) into (2.26) gives

$$\alpha = 6\frac{\gamma-1}{\gamma+1}\theta\frac{\tau}{t_d}, \tag{2.28}$$

where t_d is the characteristic shock decay time, defined by

$$\frac{1}{t_d} \equiv -\frac{1}{U}\frac{\mathrm{d}U}{\mathrm{d}t}. \tag{2.29}$$

Then setting $\alpha = 1$ in (2.28), the critical shock decay time is

$$t_{d,c} = 6\frac{\gamma-1}{\gamma+1}\theta\tau. \tag{2.30}$$

This equation is a local failure criterion as it predicts detonation success or failure based on a local analysis of the wave structure along a single particle path. In §2.6, the criterion will be utilized in a global analysis of the overall detonation initiation event in order to derive an equation for the critical energy. We refer to the model presented here as the critical decay rate (CDR) model.

Equation (2.30) indicates the critical shock decay time is proportional to the detonation induction time, as expected from dimensional analysis. Since $6(\gamma-1)/(\gamma+1) \sim O(1)$ for typical values of γ, and $\theta \gg 1$, the equation also demonstrates that $t_{d,c} \gg \tau$. Failure occurs for any $t_d \leqslant t_{d,c}$, so unsteadiness can be important even when $t_d \gg \tau$, that is, when the characteristic time of evolution is much greater than the

induction time. Contrast this with the statement of He and Clavin (1994): "When the characteristic time of evolution is much longer than the reaction time, unsteady terms may be neglected." The authors used this statement as the basis for eliminating the unsteady terms in the governing equations at the outset of their analysis. The results of our simulations and the argument presented above show that their assumption is incorrect. It is only when $t_d \gg \theta\tau$ that unsteadiness can be neglected and the flow considered quasi-steady.

2.5 Validation of Local Initiation Model with Detailed Kinetics

2.5.1 Quasi-unsteady reaction zone structure equations

Before considering the overall direct initiation event, an approximate numerical study of the local analysis can be made. Following a slightly different line of reasoning as in the previous section, imagine a hypothetical planar shock wave–reaction zone complex where the unsteady derivatives $\mathrm{d}U/\mathrm{d}t$, $\partial w/\partial t$ and $\partial P/\partial t$ can be approximated as constant along a particle path as the particle traverses the induction zone. The reaction zone structure equations (2.6) then become

$$\eta\frac{\mathrm{D}w}{\mathrm{D}t} = w\dot{\sigma} - M^2\left(\frac{\mathrm{d}U}{\mathrm{d}t}\right)_i + \left(\frac{\mathrm{d}w_s}{\mathrm{d}t}\right)_i - \frac{w}{\rho c^2}\left(\frac{\mathrm{d}P_s}{\mathrm{d}t}\right)_i, \tag{2.31a}$$

$$\eta\frac{\mathrm{D}\rho}{\mathrm{D}t} = -\rho\dot{\sigma} + \frac{\rho w}{c^2}\left(\frac{\mathrm{d}U}{\mathrm{d}t}\right)_i - \frac{\rho w}{c^2}\left(\frac{\mathrm{d}w_s}{\mathrm{d}t}\right)_i + \frac{1}{c^2}\left(\frac{\mathrm{d}P_s}{\mathrm{d}t}\right)_i, \tag{2.31b}$$

$$\eta\frac{\mathrm{D}P}{\mathrm{D}t} = -\rho w^2\dot{\sigma} + \rho w\left(\frac{\mathrm{d}U}{\mathrm{d}t}\right)_i - \rho w\left(\frac{\mathrm{d}w_s}{\mathrm{d}t}\right)_i + \left(\frac{\mathrm{d}P_s}{\mathrm{d}t}\right)_i. \tag{2.31c}$$

We refer to these equations as the quasi-unsteady planar reaction zone structure equations. The term quasi-unsteady indicates that the unsteadiness is dealt with in an approximate manner which reduces the equations to ODEs.

For a system of ideal gases the derivatives $\mathrm{d}w_s/\mathrm{d}t$ and $\mathrm{d}P_s/\mathrm{d}t$ can be expressed in

terms of $\mathrm{d}U/\mathrm{d}t$ as follows. The shock jump conditions are

$$\begin{aligned}\rho_0 U &= \rho_s w_s,\\ P_0 + \rho_0 U^2 &= P_s + \rho_s w_s^2,\\ h_0 + \tfrac{1}{2}U^2 &= h_s + \tfrac{1}{2}w_s^2,\end{aligned}$$

where h is the enthalpy. Differentiating these equations with respect to U and using the ideal gas caloric equation of state $\mathrm{d}h = C_P\,\mathrm{d}T$, the derivatives $\mathrm{d}\rho_s/\mathrm{d}U$, $\mathrm{d}w_s/\mathrm{d}U$ and $\mathrm{d}P_s/\mathrm{d}U$ can be solved. In particular,

$$\begin{aligned}\frac{\mathrm{d}w_s}{\mathrm{d}U} &= \frac{\rho_0}{\rho_s} + \frac{M_s^2}{1-M_s^2}\left\{(\gamma_s+1)\frac{\rho_0}{\rho_s} - 2\gamma_s + (\gamma_s-1)\frac{\rho_s}{\rho_0}\right\},\\ \frac{\mathrm{d}P_s}{\mathrm{d}U} &= \rho_0 U\left(2 - \frac{\rho_0}{\rho_s} - \frac{\mathrm{d}w_s}{\mathrm{d}U}\right).\end{aligned}$$

Then the unsteady derivatives in (2.31) can be determined by

$$\begin{aligned}\left(\frac{\mathrm{d}w_s}{\mathrm{d}t}\right)_i &= \left(\frac{\mathrm{d}w_s}{\mathrm{d}U}\right)_i \left(\frac{\mathrm{d}U}{\mathrm{d}t}\right)_i,\\ \left(\frac{\mathrm{d}P_s}{\mathrm{d}t}\right)_i &= \left(\frac{\mathrm{d}P_s}{\mathrm{d}U}\right)_i \left(\frac{\mathrm{d}U}{\mathrm{d}t}\right)_i.\end{aligned}$$

This reduces the unsteady derivatives in the reaction zone structure equations to a single parameter $(\mathrm{d}U/\mathrm{d}t)_i$, which can be specified in the form of a characteristic shock decay time t_d as in (2.29).

2.5.2 Numerical quenching experiment

Since the reaction zone structure equations have been reduced to simple ODEs, it is numerically inexpensive to integrate them for real gas systems. This has been done for H_2–air, H_2–O_2 and C_2H_4–air systems for various equivalence ratios, with detonation waves at CJ velocity. In this calculation and throughout the thesis, "air" is defined as $O_2 + 3.76N_2$. The detailed reaction mechanism used here was the hydrocarbon mechanism from Appendix A of Miller and Bowman (1989), with nitrogen chemistry

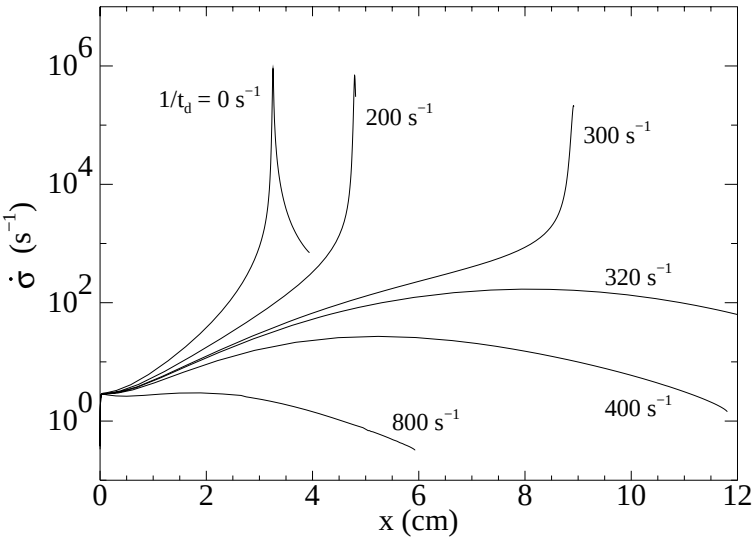

Figure 2.15: Total thermicity versus distance downstream of the shock, from quasi-unsteady calculations, for 15% H_2 in air and various shock decay times.

removed. For the H_2 systems, carbon chemistry was also removed. Realistic thermochemistry was obtained with use of the CHEMKIN package (Kee et al., 1989). The solution procedure first involved computing the CJ velocity using the chemical equilibrium code STANJAN (Reynolds, 1986). The root finder ZEROIN (Shampine and Watts, 1970) was then used to find the post-shock state, which provides the initial conditions for the reaction zone structure equations. For a given initial guess of the critical shock decay time, the equations were integrated forward in time using the backward differentiation stiff ODE solver DEBDF (Shampine and Watts, 1979). An indication of whether or not the reaction was quenched by the applied degree of unsteadiness t_d could be gauged from the total thermicity $\dot{\sigma}$. Figure 2.15 shows the variation of total thermicity through the reaction zone for 15% by volume H_2 in air, with various values of the shock decay time. It is clear from this plot that at quenching the thermicity fails to develop a sharp peak and the maximum greatly decreases. The variation of maximum thermicity $\dot{\sigma}_{max}$ with shock decay time is shown in figure 2.16. A somewhat arbitrary choice was made to define detonation failure as the point where the maximum thermicity dropped to 1% of its value at steady flow ($1/t_d = 0$). As demonstrated in figure 2.16, the determination of the critical shock

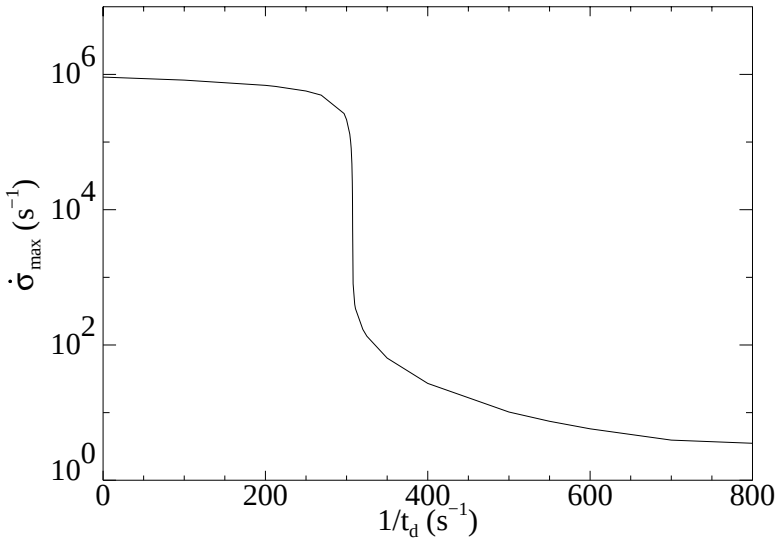

Figure 2.16: Maximum thermicity versus characteristic shock decay time, from quasi-unsteady calculations, for 15% H_2 in air.

decay time is not very sensitive to the cutoff value chosen.

2.5.3 Specification of model parameters

The numerically computed critical shock decay times were compared with the theoretical predictions from (2.30). The parameters used in (2.30) were determined as follows. The planar ZND induction time τ for the CJ wave was determined by integration of the planar steady form of the reaction zone structure equations (2.6a)–(2.6c), using the detailed reaction mechanism, behind a shock traveling at CJ velocity. The induction time was identified as the point of maximum temperature gradient dT/dt. The equivalent value of γ chosen for (2.30) was determined by matching the post-shock temperature in the detailed reaction system to that in the one-step model, as the temperature is the most important state quantity to represent correctly in the induction zone. For the constant γ model, the exact temperature ratio across the shock is given by

$$\frac{T_s}{T_0} = \frac{\{2\gamma M_0^2 - (\gamma - 1)\}\left(\gamma - 1 + \frac{2}{M_0^2}\right)}{(\gamma + 1)^2}.$$

This equation was solved to determine the equivalent constant value of γ for the detailed reaction system at a specified free stream Mach number and shock temperature ratio. The estimated value of θ for the detailed reaction system was determined by a method described in Shepherd (1986). This method proceeds by considering approximating a system of reactions by a single global rate. The conventional approximation to induction time corresponding to a global rate is

$$\tau = C \left[\text{fuel}\right]_i^a \left[\text{oxidizer}\right]_i^b \exp\left(\frac{E_a}{R_g T_i}\right),$$

where C is a pre-exponential constant, the square brackets indicate initial concentrations, a and b are empirical constants, and T_i is the initial temperature, in our case the post-shock temperature T_s. If we differentiate this expression with respect to T_i, holding the initial density and mass fractions constant, then the initial concentrations will remain constant, and θ will be given by

$$\theta = \frac{E_a}{R_g T_i} = -\frac{T_i}{\tau} \left.\frac{\partial \tau}{\partial T_i}\right|_{\rho_i,\, \boldsymbol{y}_i}.$$

This enables the determination of the global parameter θ by carrying out constant volume simulations to find τ, using a detailed reaction mechanism and realistic thermochemistry. The derivative was computed numerically by perturbing the initial temperature $T_i = T_s$ while holding the initial density $\rho_i = \rho_s$ and the initial mass fractions constant. The induction time τ was identified as the point of maximum temperature gradient dT/dt. The same reaction mechanism was used as in the quasi-unsteady and ZND simulations described previously.

2.5.4 Validation results

The numerically computed critical shock decay times are plotted with the CDR model predictions from (2.30) in figure 2.17. For each fuel–oxidizer mixture shown, the induction time varies by several orders of magnitude over the range of equivalence ratios. The critical shock decay time essentially follows the same trend, so to best

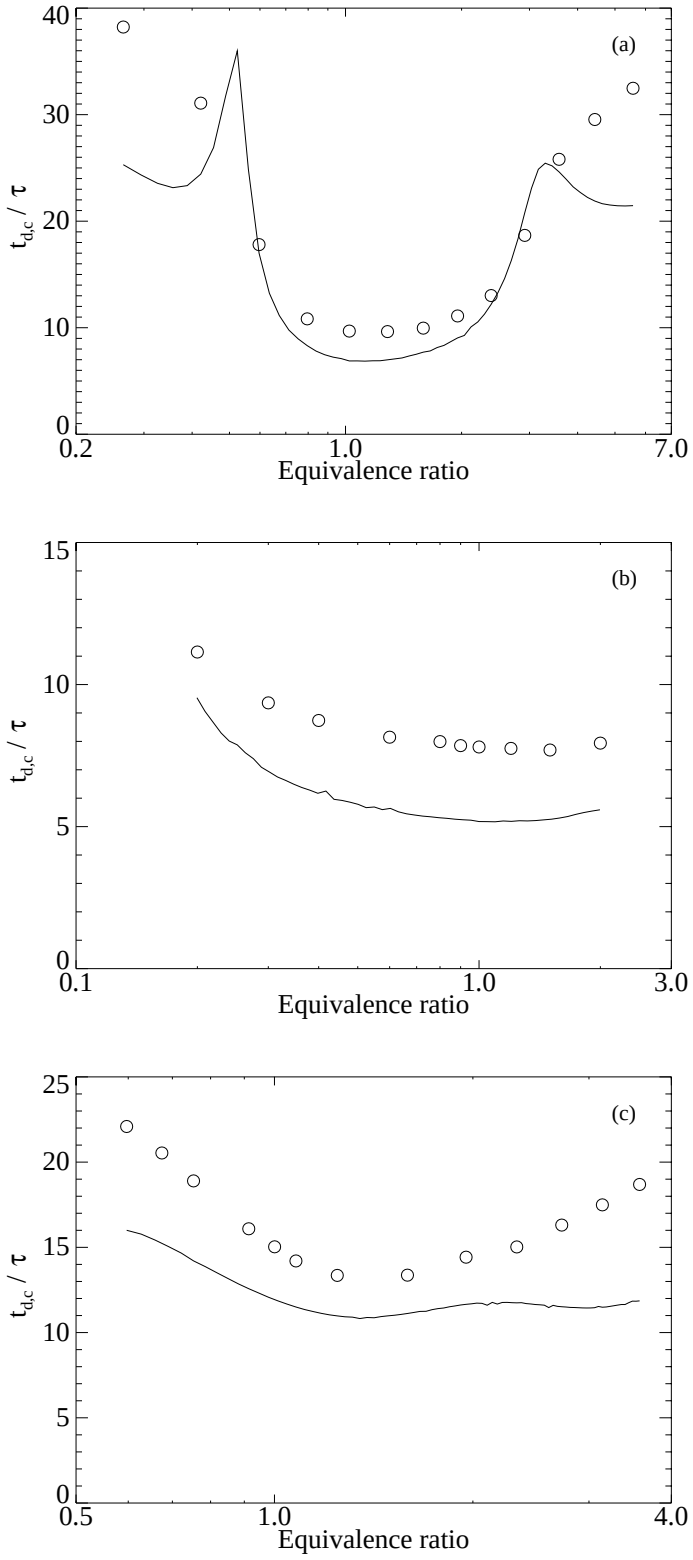

Figure 2.17: Critical shock decay time versus equivalence ratio. Lines: critical decay rate model, (2.30); symbols: numerical results from quasi-unsteady calculations with (2.31). (*a*) H_2–air; (*b*) H_2–O_2; (*c*) C_2H_4–air.

compare the numerical and theoretical values this dominant trend has been removed by normalizing the critical shock decay times by the induction times. The theoretical predictions agree reasonably well with the numerical data in all three cases, although in general the theory underpredicts the critical shock decay time by as much as 40%. We believe this is quite satisfactory considering the crude approximations made in using (a) the one-step mechanism to simulate the real chemical system, (b) the large activation energy asymptotics, and (c) the strong shock assumption. Note from (2.30) that the theoretical value of $t_{d,c}/\tau$ is proportional to θ. The unusual behavior of θ near the lean and rich ends of the H_2–air system has been previously documented (Shepherd, 1986), and is evident in the theoretical curve of figure 2.17(a). The same trend does not appear in the quasi-unsteady calculations.

2.6 Global Initiation Criterion

2.6.1 Critical energy equation

In §2.4, an initiation criterion was developed based on a local analysis of the reaction zone structure. To convert this criterion into a useful predictive formula for the critical energy, it must be applied to the global initiation event. *A priori* knowledge of the approximate blast wave velocity profile is required, so that the shock decay rate may be computed in terms of the controlling parameters of the problem.

The simplest choice, used by most previous workers on the blast initiation problem, is the Taylor–Sedov similarity solution for a non-reacting strong point blast (Taylor, 1950; Sedov, 1959). The equations for this point blast theory (PBT) were listed in §2.3.1 for the spherical case ($j = 2$). In more generality, the blast wave profile is given by

$$R = \left(\frac{E_{source}}{A_j\,\rho_0}\right)^{\frac{1}{j+1}} \left(\frac{2}{j+3}\frac{1}{U}\right)^{\frac{2}{j+1}} = \left(\frac{E_{source}}{A_j\,\rho_0}\right)^{\frac{1}{j+3}} t^{\frac{2}{j+3}},$$

$$t = \left(\frac{E_{source}}{A_j\,\rho_0}\right)^{\frac{1}{j+1}} \left(\frac{2}{j+3}\frac{1}{U}\right)^{\frac{j+3}{j+1}},$$

where E_{source} is the initial energy release for spherically symmetric flow, the energy release per unit length for cylindrically symmetric flow, or the energy release per unit area for planar flow. A_j is the energy integral constant, and is a function of j and γ. A correlation for the spherical case ($j = 2$) was given in (2.18).

However, the PBT does not account for the significant effect of chemical energy release, and to a lesser extent, finite back pressure. Korobeinikov (1968) proposed a method for including the effect of chemical energy release on the analytical blast wave profile, using a linearization of the reacting flow governing equations about the non-reacting PBT solution. This linearization results in the following solution,

$$R = \left(\frac{E_{source}}{A_j\,\rho_0}\right)^{\frac{1}{j+1}} \left(\frac{2}{j+3}\frac{1}{U}\right)^{\frac{2}{j+1}} \exp\left\{\frac{B_j Q}{(j+1)U^2}\right\}, \tag{2.32a}$$

$$t = \left(\frac{E_{source}}{A_j\,\rho_0}\right)^{\frac{1}{j+1}} \left(\frac{2}{j+3}\frac{1}{U}\right)^{\frac{j+3}{j+1}} \left\{1 + \frac{(j+2)(j+3)}{(j+1)(3j+5)}\frac{B_j Q}{U^2}\right\}, \tag{2.32b}$$

where the last factor in each equation is the reacting flow correction. B_j is another energy integral constant, and is again a function of j and γ. Korobeinikov (1991) lists values of B_j for $j = 0, 1, 2$ and various values of γ. A fit of this data in the spherical case ($j = 2$) gives

$$B_2 = 4.1263(\gamma - 1)^{1.2530 + 0.14936\log_{10}(\gamma - 1)},$$

accurate to 0.29% in the range $1.2 \leqslant \gamma \leqslant 2.0$.

The linearized solution given by (2.32) should strictly only be valid before the blast wave has decayed to the CJ velocity. However, in practice, it is a good approximation for a considerably longer time, at least in the case of initiation failure. This is evident in figure 2.18 where the numerical blast wave velocity profile of a near-critical initiation event, case A with $\tilde{E}_{source} = 166 \times 10^6$, is plotted with the corrected PBT profile. While there is some discrepancy between the curves, the discrepancy gets no worse at the lower shock velocities. Hence, the theoretical curve seems to be applicable down to at least $U = 0.7U_{CJ}$. For comparison, the standard non-reacting PBT profile is also plotted in this figure. Clearly, the corrected PBT curve is a much better approximation to the numerical curve. The corrected PBT curve could be

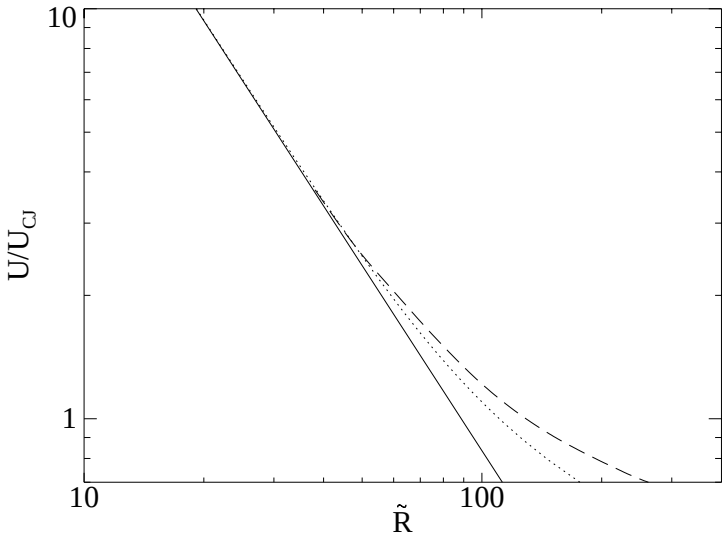

Figure 2.18: Shock velocity profiles for case A with $\tilde{E}_{source} = 166 \times 10^6$. —— Taylor–Sedov non-reacting point blast theory (PBT); $\cdots\cdots$ PBT with linearized reacting flow correction; – – – numerical simulation.

shifted even closer to the numerical curve by additionally considering the correction due to finite back pressure, but the correction is very small for the regime shown in figure 2.18, so the improvement would be negligible.

The characteristic shock decay time t_d for the corrected PBT can be found by differentiating (2.32b), giving

$$t_d = -\frac{U}{\mathrm{d}U/\mathrm{d}t} = \frac{j+3}{j+1}\left(\frac{2}{j+3}\right)^{\frac{j+3}{j+1}}\left(\frac{E_{source}}{A_j\,\rho_0}\right)^{\frac{1}{j+1}}\left(1+\frac{j+2}{j+1}\,\frac{B_j Q}{U^2}\right)U^{-\frac{j+3}{j+1}}. \quad (2.33)$$

It must now be decided at what point in the blast wave profile to evaluate t_d and check against the failure criterion (2.30). The simplest choice is to evaluate the model at $U = U_{CJ}$, since failure is likely to occur in that vicinity. However, closer examination of the numerical simulation results in figures 2.3 and 2.10 reveals that failure actually occurs somewhat below U_{CJ} in the critical initiations. Denote the velocity of the leading shock at failure as U_*. We will discuss the selection of U_* later in this section. Define θ_* and τ_* as the values of θ and τ when $U = U_*$. Then setting $E_{source} = E_c$ when $t_d = t_{d,c}$, and combining (2.33) with (2.30), gives the critical

energy:

$$E_c = A_j \left(6 \frac{j+1}{j+3} \frac{\gamma-1}{\gamma+1} \theta_* \right)^{j+1} \left(\frac{j+3}{2} \right)^{j+3} \left(1 + \frac{j+2}{j+1} \frac{B_j Q}{U_*^2} \right)^{-(j+1)} \rho_0 U_*^{j+3} \tau_*^{j+1}. \tag{2.34}$$

This is the final model equation for the critical energy, under the assumptions of the critical decay rate (CDR) model. For spherically symmetric flow ($j = 2$), (2.34) gives

$$E_c = 4.56 \times 10^3 A_2 \left(\frac{\gamma-1}{\gamma+1} \theta_* \right)^3 \left(1 + \frac{4}{3} \frac{B_2 Q}{U_*^2} \right)^{-3} \rho_0 U_*^5 \tau_*^3. \tag{2.35}$$

2.6.2 Comparison with numerical results

Using the non-dimensional notation of §2.3, (2.35) becomes

$$\tilde{E}_c = 4.56 \times 10^3 A_2 \left(\frac{\gamma-1}{\gamma+1} \theta_* \right)^3 \left(1 + \frac{4}{3} \frac{B_2 \tilde{Q}}{\tilde{U}_*^2} \right)^{-3} \tilde{U}_*^5 \tilde{\tau}_*^3. \tag{2.36}$$

This equation can be used to predict critical energies for the one-step model used in the numerical simulations. The selection of $\tilde{U}_*$ can be made empirically by examining shock velocity profiles from numerical simulations. The failure point is identified as the point where the profiles of the marginally subcritical and marginally supercritical initiation energies start to deviate significantly. This was done in §2.3.2, where it was determined that $U_* = 0.75 U_{CJ}$ in case A and $U_* = 0.8 U_{CJ}$ for the first critical energy in case B. Since $U_* < U_{CJ}$ there is no steady ZND solution, so the induction time τ_* must be computed by some method other than a ZND calculation. In this work, we have used a constant pressure reaction behind a shock traveling at velocity U_*, and identified the induction time as the point of maximum temperature gradient. A constant pressure assumption gives induction times in very close agreement with the ZND model. This can be verified by considering the one-step reaction model. Under the assumption of constant pressure, the asymptotic induction time is given by

$$\tau = \frac{1}{k} \frac{1}{\theta} \frac{C_P T_s}{Q} \mathrm{e}^{\theta}.$$

	Critical energy $\tilde{E}_c$	
Case	Model	Numerical
A	34.6×10^6	166×10^6
B	52.3×10^6	199×10^6

Table 2.2: Comparison between model predictions and numerical results for critical energy.

Comparing this with (2.24), the ratio of the asymptotic induction time in the constant pressure model to that in the ZND model is

$$\frac{1-\gamma M_s^2}{1-M_s^2}.$$

In the strong shock limit, this ratio is

$$\frac{\gamma(3-\gamma)}{\gamma+1},$$

and for γ not much larger than one, this ratio is very close to one.

The critical energy predictions of (2.36) are listed in table 2.2 for the two computational cases. They are compared with the values determined directly from the numerical simulations, where the first critical energy $\tilde{E}_{c1}$ is listed for case B. The model underpredicts the critical energy by a factor of 4 to 5. Some disagreement between the model and the numerics was expected, as the numerical simulations used a relatively low activation energy that produced a reaction zone with no clearly identifiable induction zone. The model assumes an ideal asymptotic induction zone, and this is closer to what is observed in real gas systems. Hence the numerical simulations were intended mainly for qualitative validation of the model, rather than quantitative comparison.

2.6.3 Specification of model parameters for real gas systems

For practical application of the critical energy equation (2.34) in real gas detonations, various parameters need to be determined. The value of θ_* can be determined by the

method described in §2.5.3, with a constant volume reaction behind a shock traveling at velocity U_*. Similarly, the value of γ is determined by matching the shock temperature ratio at the shock velocity U_*. The induction times τ_* are computed from a constant pressure calculation, as for the one-step model earlier in this section. The heat of reaction Q is defined as the difference between the heats of formation of the reactant and product. The heats of formation are the enthalpies of the reactant mixture and the equilibrium product mixture, with each at a standard reference temperature of 300 K. The equilibrium product composition is taken from the constant pressure reaction calculation behind a shock traveling at velocity U_*.

All that remains is the specification of the shock velocity U_* where the critical decay rate model will be applied. Without the benefit of numerical results for each real gas detonation, a theoretical prescription is necessary. For this work, we have assumed $U_* = U_c$, where U_c is the shock velocity corresponding to the critical radius R_c for a slightly curved, quasi-steady detonation. Although failure occurs at a shock radius smaller than the critical radius, as shown in the following section, this quasi-steady solution appears to be the attractor for successfully initiated detonations with a marginally supercritical energy (He and Clavin, 1994). So U_c will be a reasonable estimate to the shock velocity in the critical region of the flow. We have taken the following expression for the velocity U_c, derived from a square-wave detonation model (He and Clavin, 1994):

$$U_c = U_{CJ}\left(1 - \frac{1}{2\theta_{CJ}}\right). \tag{2.37}$$

Yao and Stewart (1995) give an almost identical expression for U_c, derived from large activation energy asymptotics. It is worth noting that the high sensitivity of the induction time τ to the post-shock temperature T_s and hence shock velocity U means the critical energy predictions of the CDR model will be very sensitive to the choice of U_*. Our choice here is by no means the definitive one, determination of which is an area for future study.

2.7 Comparison with Experiment

2.7.1 CDR model versus critical curvature model and experiment

The global initiation criterion for spherically symmetric detonations, (2.35), is compared with various sets of experimental data in figures 2.19 to 2.21. In all cases the initial conditions were approximately 1 bar and 300 K. The values of U_*, τ_*, γ, Q and θ_* were determined as outlined in §2.6. The hydrocarbon reaction mechanism of Miller and Bowman (1989) was used in the hydrogen and ethylene calculations for figures 2.19 and 2.20. A natural gas reaction mechanism from the Gas Research Institute (Bowman et al., 1995) was used in the calculations for figure 2.21, as this is a more recent mechanism which has been extensively tested for methane and ethane.

For comparison, the critical energy predictions of the critical curvature model (He and Clavin, 1994) are also shown in these figures. This model gives the critical energy as

$$E_c = A_j \left(\frac{j+3}{2}\right)^2 \rho_0 \, U_c^2 \, R_c^{j+1}, \tag{2.38}$$

where R_c is the critical radius and U_c is the corresponding shock velocity. Using the authors' asymptotic square-wave detonation model, the critical radius is given by

$$R_c = \frac{8\mathrm{e}j \, \theta_{CJ}}{1-\gamma^{-2}} \, \Delta_{CJ}, \tag{2.39}$$

where Δ_{CJ} is the induction length for a CJ detonation. U_c was given in (2.37). Then (2.38) becomes

$$E_c = A_j \left(\frac{j+3}{2}\right)^2 \left(\frac{8\mathrm{e}j \, \theta_{CJ}}{1-\gamma^{-2}}\right)^{j+1} \left(1 - \frac{1}{2\theta_{CJ}}\right)^2 \rho_0 \, U_{CJ}^2 \, \Delta_{CJ}^{j+1}.$$

For spherically symmetric flow ($j = 2$),

$$E_c = 5.14 \times 10^5 A_2 \left(\frac{\theta_{CJ}}{1-\gamma^{-2}}\right)^3 \left(1 - \frac{1}{2\theta_{CJ}}\right)^2 \rho_0 \, U_{CJ}^2 \, \Delta_{CJ}^3, \tag{2.40}$$

and this equation was used to generate the curves in figures 2.19 to 2.21.

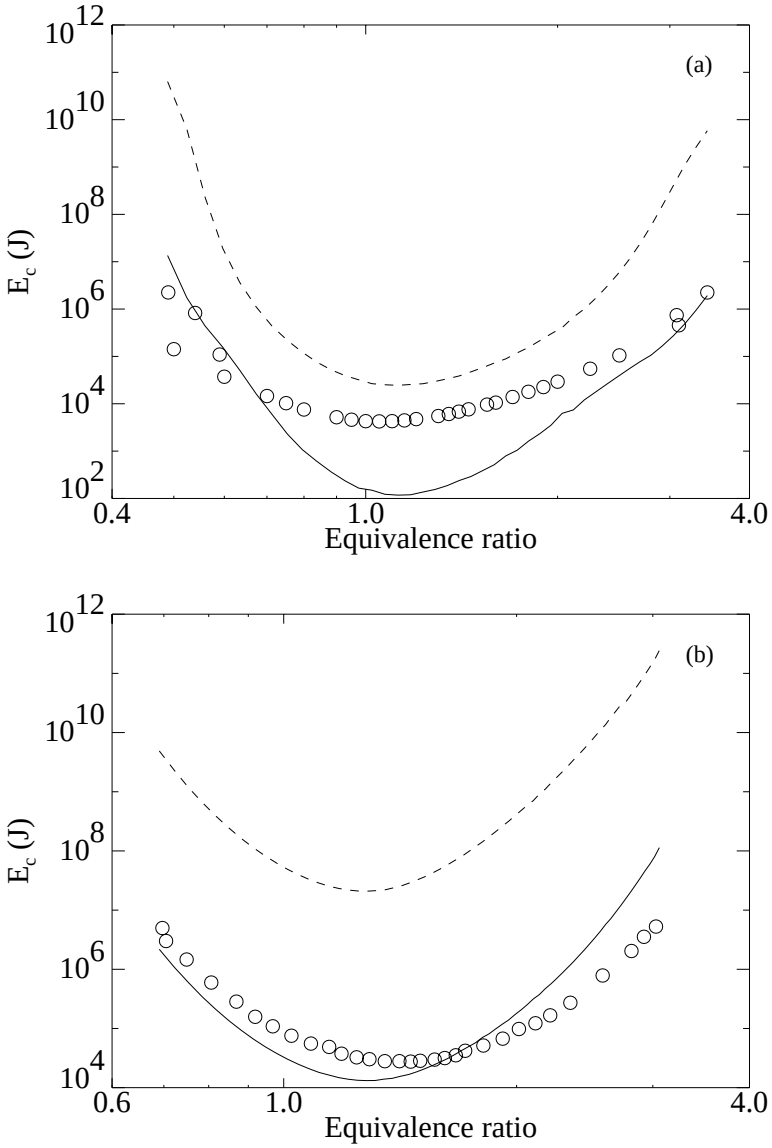

Figure 2.19: Comparison between theory and experiment for critical energy versus equivalence ratio. —— critical decay rate model, (2.35); – – – critical curvature model (He and Clavin, 1994), (2.40); ∘ experiment (Benedick et al., 1986). (*a*) H_2–air; (*b*) C_2H_4–air.

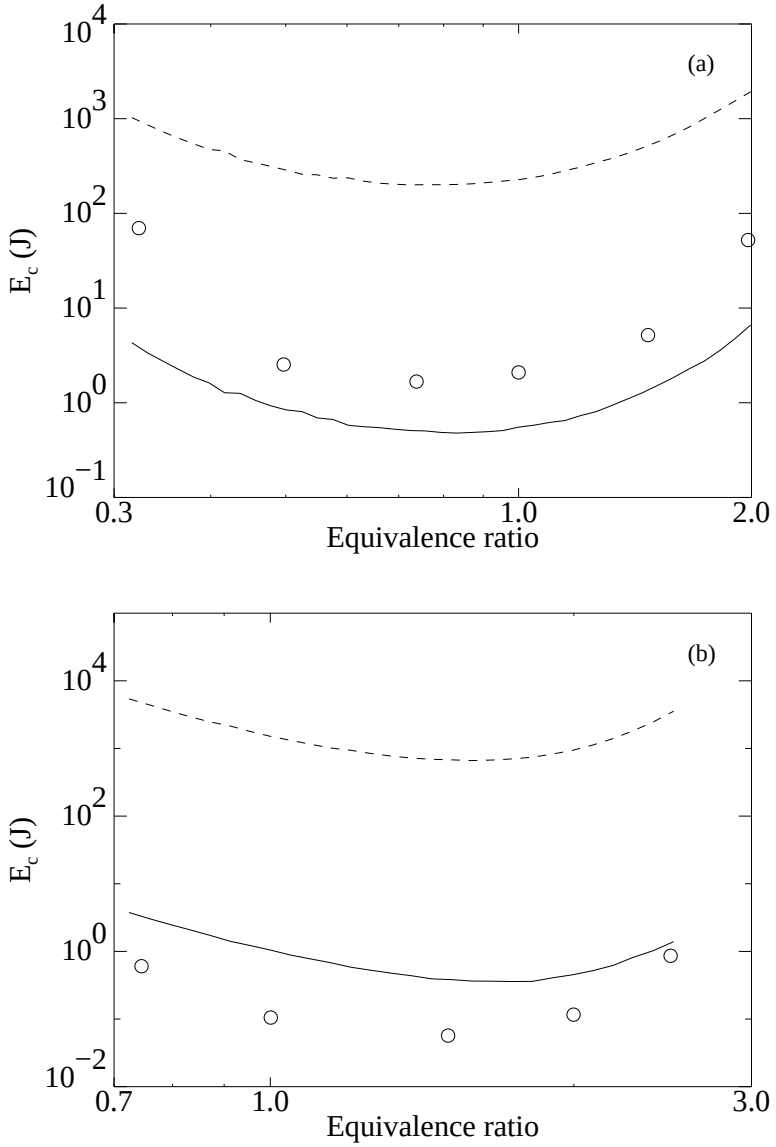

Figure 2.20: Comparison between theory and experiment for critical energy versus equivalence ratio. —— critical decay rate model, (2.35); – – – critical curvature model (He and Clavin, 1994), (2.40); ∘ experiment (Matsui and Lee, 1979). (*a*) H_2–O_2; (*b*) C_2H_4–O_2.

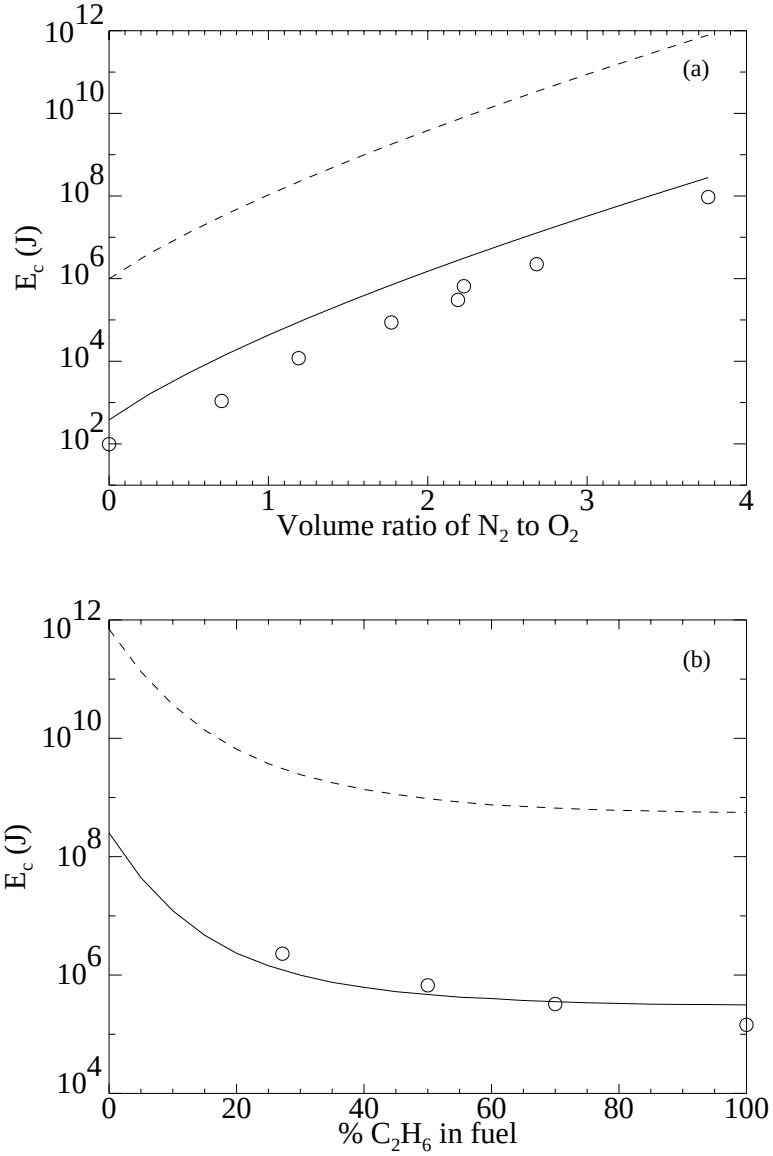

Figure 2.21: Comparison between theory and experiment for critical energy. —— critical decay rate model, (2.35); – – – critical curvature model (He and Clavin, 1994), (2.40); ∘ experiment. (*a*) Stoichiometric CH_4–O_2–N_2 (experimental data from Bull et al. (1976)); (*b*) Stoichiometric CH_4–C_2H_6–air (experimental data from Bull et al. (1979)).

The figures show that the critical decay rate (CDR) model generally gives critical energies about three orders of magnitude less than the critical curvature model. The CDR model also agrees with the experimental data to within an order of magnitude, except in the case of near-stoichiometric hydrogen–air. The agreement is particularly good in the hydrocarbon cases. The model slightly overpredicts the critical energy in most of these cases, but this is a substantial improvement on the large overprediction of the critical curvature model. Admittedly, the critical curvature model could be applied more accurately by computing the slightly curved quasi-steady U–R solution using a real reaction mechanism and locating the critical point U_c–R_c, as described in He (1996). This would then be substituted into (2.38) rather than the approximate results of the square-wave model. However, use of the square-wave model to find the critical point is only slightly different and the critical energy predictions would be similar. Comparison between the CDR and critical curvature models is less conclusive in the hydrogen figures where the experimental data generally lies between the two models.

While discussing the critical curvature model of He and Clavin (1994), it is instructive to calculate the critical radius R_c for the two computational cases presented here, and compare with the numerical results in figures 2.3 and 2.10. Assuming $\Delta_{CJ} \approx \Delta_{1/2}$, then $\tilde{R}_c \approx R_c/\Delta_{CJ}$, which can be calculated directly from (2.39). For case A, $\tilde{R}_c = 861$, which is much greater than the shock radius in the critical regime from the numerical simulations, $\tilde{R} \approx 225$. For case B, $\tilde{R}_c = 492$, which is also considerably greater than the shock radius in the critical regime for the first critical energy, $\tilde{R} \approx 285$. This supports our assertion that the critical radius is not the controlling variable for direct initiation.

The U-shaped curve for hydrogen–air experiments in figure 2.19(a) has a significantly different shape than that of the models. This indicates that hydrogen–air has a more complicated behavior than is accounted for in the models. Near-stoichiometric hydrogen–air mixtures have an unusually long recombination zone relative to the size of the induction zone (Shepherd, 1986), but this property does not exist away from stoichiometry. Models based purely on analysis of the induction zone will not in-

clude the effect of the recombination zone. This may explain the CDR model's large discrepancy with the experimental data for near-stoichiometric hydrogen–air.

The slight deviation of the experimental data from the CDR model for rich ethylene–air mixtures is due to the fact that the Miller–Bowman hydrocarbon mechanism does not include any large hydrocarbon molecules. Rich mixtures will involve the recombination of ethylene molecules early in the induction zone to form large hydrocarbons not included in the mechanism. Hence the mechanism is not expected to accurately compute the dynamic parameters in the rich regime.

2.7.2 Sources of error in model inputs

While the agreement between experiment and the CDR model appears approximate at best, it must be noted that the error bars on both the experimental data and model predictions are quite large. The model relies on an accurate reaction mechanism for the computation of the induction time τ_* and global activation energy θ_*. Despite extensive efforts in the development of these mechanisms in recent decades, there is still considerable uncertainty in their accuracy, particularly when applied to the high pressures associated with detonations in gases initially at standard pressure. Seemingly satisfactory mechanisms for a given mixture often give induction times that differ by a factor of two or more. Since the dynamic parameters τ_* and θ_* are each cubed in the spherically symmetric model equation (2.35), this could give an order of magnitude error in the predicted critical energy.

2.7.3 Sources of error in experimental data

There are also many sources of uncertainty in the experimental data:

1. The data sets presented in figures 2.19 to 2.21 consist mostly of averages of "Go" and "No Go" experiments which bracket the critical energy quite coarsely.

2. There are significant differences in experimental data obtained from various types of initiation sources. The most common sources are exploding wires,

electrical sparks and solid explosives. It is often unclear exactly how much of the nominal source energy actually goes into the gas, and also whether the energy is deposited sufficiently rapidly and compactly to act like an instantaneous point source. These uncertainties are particularly significant for exploding wires and electrical sparks. For this reason, we have chosen not to use any experimental data from these two initiation sources. The data in figures 2.19 and 2.21 used high explosives as the initiation source.

3. For very sensitive mixtures with E_c of the order of 1 J or less, typical of near stoichiometric fuel–O_2 mixtures, use of even high explosives for the initiation source becomes difficult. The electrical charge used to initiate the small piece of high explosive is no longer a negligible energy source. Furthermore, it is unlikely a clean spherical detonation can be formed in the high explosive before the blast wave travels into the gas. For this reason, no satisfactory experiments have been performed to date with fuel–O_2 mixtures using a high explosive initiation source. Hence, we have chosen not to consider any fuel–O_2 critical energy data determined from point initiation experiments. The data in figure 2.20 has been taken from Matsui and Lee (1979) who actually performed critical tube diameter experiments with planar detonations and converted the data to critical energies using a phenomenological model known as the work done model (Lee and Matsui, 1977). This data is thus subject to errors introduced by the use of the model, which is at best accurate to within an order of magnitude (Benedick et al., 1986).

4. It is difficult to perform direct initiation experiments with insensitive mixtures that have large critical energies. A very large experimental facility is required if a definite decision is to made between a "Go" and "No Go" outcome from velocity or pressure profiles, before wave reflection occurs. The initiator energy must be small compared to the total energy inside the experiment containment. In the past, several experiments with rich or lean fuel–air mixtures have suffered from considerable uncertainty due to this factor. The same can also be said of

near stoichiometric fuel–air mixtures with very insensitive fuels such as methane.

The above arguments demonstrate the large uncertainties in most experimental data on critical energies. This is particularly true of fuel–oxygen mixtures, for which various experimental results often differ by orders of magnitude. An example is hydrogen, where the experiments of Litchfield et al. (1963) with H_2–O_2 mixtures using exploding wire and electrical spark initiation sources gave critical energies respectively nearly one and two orders of magnitude higher than those of Matsui and Lee (1979) shown in figure 2.20.

2.8 Conclusions

The one-dimensional reaction zone structure in gaseous detonations is controlled by a competition between heat release, wave curvature and unsteadiness. In direct initiation by a blast wave, numerical simulations with a simple one-step reaction model and Arrhenius reaction rate demonstrated that the dominant balance is between heat release and unsteadiness. Hence the primary physical mechanism by which a detonation may fail to initiate is excessive unsteadiness in the reaction zone arising from the deceleration of the leading shock. The critical amount of unsteadiness was determined from a large activation energy asymptotic analysis of the reactive Euler equations with the one-step reaction model. The local initiation model was validated through quasi-unsteady calculations with real gas kinetics. It was found that the model agreed with the numerical calculations to within 40%, for a number of fuel–oxidizer mixtures over a wide range of stoichiometries.

An analytical equation for the critical energy was developed from the local initiation model by means of an assumed blast wave velocity profile. Closure can be obtained by applying the local initiation model at a prescribed critical point in the velocity profile. The optimal choice of this point remains an unresolved issue, and in this work we have made an ad-hoc assumption to use the shock velocity corresponding to the critical radius in the quasi-steady slightly-curved nonlinear detonation relationship. The analytical equation thus obtained was found to give order of magnitude

agreement with numerical and experimental data. The agreement with experiment is quite satisfactory at present. With the large uncertainties inherent in both experimental data and theoretical reaction mechanisms, we cannot hope to validate direct initiation models against experiment to more than an order of magnitude comparison. Greater accuracy of experiments and reaction mechanisms is required before more detailed validation will be possible.

We propose the CDR model as a model for spherical, cylindrical and planar direct initiation. However, we have only validated it with numerical and experimental data in the case of spherical detonations. The application to cylindrical and planar detonations is speculative and is a possible subject of further research. Validation of the planar case with numerical simulations using the one-step Arrhenius reaction model may be complicated by the difficulty of distinguishing between "Go" and "No Go" initiation events. This complication was observed by Mazaheri (1997). It is an effect of the slow rate of blast wave decay in the planar case, coupled with the one-step model's non-physical properties at low temperatures and the inevitable completion of reaction at long but finite times. However, this is a numerical artifact of the one-step model and not something observed in real detonations, so we do not believe it is a reason for discounting any direct initiation model in the planar case.

The numerical simulations presented here for case B also identified an interesting phenomenon, that of a non-unique critical energy. Whether this is a physical phenomenon or another artifact of the one-step model is a question for further study. Simulations with realistic thermochemistry would be very illuminating in this regard. With this non-uniqueness in mind, we chose to examine only the lower critical energy since there appeared to be some universality of behavior between cases A and B. For the lower critical energy, there was a clear and sudden distinction between marginally subcritical and supercritical initiation cases that occurred in the initial blast wave decay. Our model is an attempt to explain this behavior. Clearly, our global initiation model cannot hope to explain the more complicated dynamics associated with the higher critical energy, since it is based on an assumed monotonically decaying blast wave law. So at best, the model gives a lower bound estimate to the critical energy.

Chapter 3 Reduced Reaction Mechanisms and Cellular Detonations

3.1 Introduction

3.1.1 Reaction Models

In numerical simulations of gaseous detonations, the governing equations are the reactive Euler equations, assuming that transport effects are negligible. Closure of these equations is attained by prescription of (a) an equation of state, and (b) a reaction model. For gaseous mixtures, the equation of state is usually that of an ideal (thermally perfect) gas, that may or may not also be calorically perfect. Choices for the reaction model include the following, listed in increasing order of complexity:

1. One-step reaction model
2. Two-step induction parameter model
3. Reduced reaction mechanism
4. Detailed reaction mechanism

The simplest choice is the one-step reaction model, where a single irreversible reaction A $\rightarrow$ B occurs between two thermally and calorically perfect gases with the same constant specific heat, releasing heat of reaction Q. The reaction rate usually has an Arrhenius form,

$$\frac{\mathrm{D}Z}{\mathrm{D}t} = k(1-Z)\exp\left(-\frac{E_a}{R_g T}\right),$$

where Z is the mass fraction of product B, E_a is the activation energy per unit mass, k is the pre-exponential rate multiplier, R_g is the specific gas constant, T is

the temperature and t is the time. Such a model was used in the theoretical and numerical work of §2. The one-step reaction model has been used extensively for many years due to its simplicity and excellent computational efficiency. Its simplicity permits theoretical solution of certain classical problems, and comparison with theory has been its primary application in numerical simulations. The most notable example of this is the exact linear stability theory for one-dimensional pulsating detonations which was described by Erpenbeck (1964) and verified numerically by Fickett and Wood (1966). An alternative approach using normal modes was later presented by Lee and Stewart (1990) and verified numerically by Bourlioux et al. (1991). The one-step reaction model has also seen limited application in simulations of multi-dimensional detonations, where its computational efficiency makes highly resolved calculations possible (Bourlioux and Majda, 1992; Quirk, 1994b).

Although computationally efficient and able to capture many generic features of gaseous detonations, the one-step reaction model has several drawbacks when attempting to simulate detonations in realistic systems. Firstly, it has no induction zone, the energetically neutral region of radical accumulation that exists at the start of the reaction zone in real gas detonations. The length of the induction zone is known to be a very important parameter that controls much of the dynamic behavior of detonations. Secondly, when used with a large activation energy on a detonation that is not strongly overdriven, the one-step reaction model exhibits wildly chaotic instabilities that cause the detonation to fail, for example, in initiation simulations (He, 1996). Thirdly, it provides no mechanism for quenching of the reaction causing initiation simulations to always eventually produce a detonation (Mazaheri, 1997). Finally, it is almost impossible to choose the parameters γ, Q, E_a and k in such a way that the computed detonation gives close quantitative agreement with all properties of any real detonation.

The first attempt at improving this reaction model for detonation simulations was made by Korobeinikov et al. (1972) who proposed an empirical two-step induction parameter model. The first reaction step modeled an energetically neutral induction phase, and the second step, which commenced only when the first step was complete,

modeled the energy release. Each step had an Arrhenius type reaction rate expression although the second step was made reversible. The various parameters in these expressions were carefully chosen to model some highly diluted fuel–oxygen systems. The equation of state was a thermally and calorically perfect gas, as in the one-step reaction model. The induction parameter model was an extension of the one-step reaction model most notably by the addition of the induction process, in recognition of its fundamental importance in detonation simulations.

Taki and Fujiwara (1978) used Korobeinikov's induction parameter model to produce the first two-dimensional detonation simulation. In their calculation of a detonation traveling down a two-dimensional channel, they were able to capture the transverse wave structure giving rise to the characteristic cellular pattern of detonations.

Oran et al. (1981) later improved Korobeinikov's model by proposing a method for determining the induction time in the first step and the maximum energy release in the second step. The method involved fitting data obtained from many homogeneous reaction calculations with a detailed reaction mechanism. They were thus able to extend the range of application of a given model beyond the narrow range applicable in the Korobeinikov model. Oran et al. (1982) used their model to simulate two-dimensional cellular detonations and examine the unreacted pockets formed behind the detonation front.

Induction parameter models have been used in many numerical simulations of multi-dimensional detonations since. The only significant extension to the models was made by Lefebvre et al. (1992) who relaxed the restriction of a calorically perfect gas and determined empirical expressions for the ratio of specific heat and molecular weight as functions of temperature and the second reaction progress variable. They were then able to produce what at the time was believed to be a more realistic simulation of a H_2–O_2–Ar detonation (Lefebvre et al., 1993a).

Induction parameter models offer an advantage over one-step reaction models by directly considering the induction region. Although fewer theoretical studies have been made on these models, they permit more realistic simulations of unsteady multi-

dimensional detonations, and the increased number of empirical parameters gives a greater chance of quantitatively matching with a real system. All this is achieved at little extra computational cost. However, in some instances where accurate quantitative agreement with a real gas system is desired, induction parameter models may still be inadequate. The number of "tunable" parameters makes any such quantitative agreement dubious. Additionally, the range of application of any given model is quite narrow, typically only valid for a given fuel and oxidant, for certain stoichiometries, with a given diluent and certain dilution ratios, and within certain temperature and pressure ranges. Development of a new model for different mixtures or conditions is a tedious process that requires extensive parameter fitting and is nearly impossible to automate for all systems. For these reasons, a more sophisticated reaction model is often desired.

The ultimate choice for a thermochemical model that can produce accurate simulations of detonations with potentially excellent quantitative agreement with experimental results is the use of detailed reaction mechanisms. In this case, the chemical reaction is described by an extensive list of elementary reactions between different molecular species with rate expressions given for each reaction. The fluid composition is given by a set of species, which are typically assumed to be ideal (thermally perfect) but not calorically perfect gases. The caloric equation of state for each species is specified as a function $h(T)$ or $e(T)$ for the enthalpy h or internal energy e as a function of temperature T. The specific heats are determined by derivatives of these functions. Implementation of a detailed reaction mechanism in a numerical simulation is typically made via a chemical kinetics software package such as CHEMKIN (Kee et al., 1989) and a list of polynomial fits to the species equation of state data such as those given in the JANAF tables (Stull and Prophet, 1971).

However, a detailed reaction mechanism is very computationally expensive in a detonation simulation. The ordinary differential equations (ODEs) representing the chemical reactions are typically very stiff, requiring the use of an implicit ODE integrator designed for stiff equations. Such integration techniques involve the calculation of Jacobian matrices and hence their computational expense scales roughly as the square

of the number of equations. For a system with n_s molecular species and n_e atomic elements, the minimum number of ODEs required to describe the chemical reactions is $n_s - n_e$, which is approximately equal to n_s if n_s is large. For a typical C_1- or C_2-hydrocarbon, n_s may be of the order of 50. Then the chemical step of an operator-split numerical simulation with this detailed reaction mechanism would take at least 50^2 times as long as that with an equivalent one-step reaction model. In reality, the one-step reaction models and two-step induction parameter models can usually be integrated with a cheaper explicit ODE integrator, so the difference in computational times would be even greater. Admittedly, the chemical step in the one and two-step reaction model simulations is often computationally faster than the convective fluid dynamics step, but it will certainly be a lot slower in the detailed kinetics simulation and the end result is that the computation will be orders of magnitude slower. This all assumes that the same amount of numerical resolution is sufficient to attain a grid-resolved solution with each reaction model, when in actuality the fine temporal and length scales introduced by the detailed reaction mechanism means even more resolution is required, further heightening the problem.

For these reasons, detailed reaction mechanisms are not usually considered a viable option for numerical simulations of multi-dimensional detonations. To date, the only fully resolved computation of a multi-dimensional detonation using detailed chemistry was performed by Oran et al. (1998). Their computation was of a two-dimensional cellular detonation in stoichiometric H_2–O_2 with 70% Ar dilution. This mixture produces a very regular cellular pattern. Thus it is possible to compute the correct bulk features of the flow with only a small number of cells across the transverse dimension of the channel. Despite this being a very simple mixture to study, both in the small number of species and regularity of cells, the computational effort was extensive, requiring up to days of run time on massively parallel computers. Admittedly, this work used a uniform computational grid and significant improvements could be expected with adaptive mesh refinement (AMR), but the issue of successfully using AMR with parallel computing is still a topic of research.

When a more accurate description of the chemical kinetics is desired than can be provided by a one or two-step model, and when detailed kinetics is too expensive, there is one final option, reduced reaction mechanisms. These models are developed from parent detailed reaction mechanisms which are systematically reduced to much smaller mechanisms with fewer reactions and/or species. The same non-calorically-perfect equations of state are used for the individual species, but the ODEs governing the chemical reactions are greatly reduced in number and perhaps complexity. The goal is to retain the essential features of the chemistry in a computationally efficient implementation.

3.1.2 Methods of Mechanism Reduction

Several methods for reducing reaction mechanisms have been proposed in recent decades, most originating in the low-speed numerical combustion community. The methods are reviewed by Tomlin et al. (1997). Some reduction is often possible by simply eliminating unimportant reactions from the detailed reaction mechanism, but most reduction techniques are based on the more sophisticated concept of timescale separation. Detailed reaction mechanisms contain many different chemical processes occurring on timescales that range over many orders of magnitude, from seconds down to nanoseconds. It is this feature that gives rise to the stiffness of the governing equations for the chemical reactions. Yet the fluid mechanics in chemically reacting flows usually occurs at a narrower range on the order of milliseconds to microseconds. There are typically many chemical processes that are much faster than the fluid dynamic processes, so if we are only interested in computing behavior on the scale of the fluid mechanics, several chemical processes will have already self-equilibrated. The timescale-based reduction techniques are all based on decoupling the fast equilibrating chemical processes, either explicitly or implicitly.

The oldest such technique is the Quasi Steady State Approximation (QSSA), a mathematical technique that originated early in the twentieth century and was formalized for combustion systems by Peters (Peters, 1988, 1991; Peters and Rogg, 1992).

It involves setting certain species in steady–state and certain reactions in partial equilibrium. A reduced set of global reactions is thus obtained, where the rates of these reactions are given as functions of several rates in the original detailed mechanism. The ODEs for these reduced reaction rates can then be solved in conjunction with algebraic expressions for the concentrations of the steady–state species. Typically, partial equilibrium relations are used to simplify these algebraic relations to explicit expressions for efficient solution. QSSA is a relatively simple technique to apply, although it involves considerable "chemist's intuition" to know which species to set in steady–state and which reactions in partial equilibrium. Tools have been developed to aid this process (Turanyi et al., 1996), but they still require the prescription of a set of appropriate model problems in which to examine the rates. Hence, the method is certainly far from being fully automated and is essentially still a hand-powered analytical technique.

The modern techniques of Intrinsic Low-Dimensional Manifolds (ILDM) and Computational Singular Perturbations (CSP) are numerical methods that automate the process of mechanism reduction and also provide a better mechanism due to greater flexibility in the reduction constraints. They offer considerable advantages over QSSA but are significantly more complicated to implement. The ILDM method (Maas and Pope, 1992a,b) explicitly computes the low-dimensional manifolds on which the slow chemistry evolves in the reaction state space, then tabulates the computed results in a lookup table for later use in a computational fluid dynamics (CFD) code. The CSP method (Lam and Goussis, 1988; Lam, 1993) is similar, although it uses a transformation of the system basis vectors to automatically compute the optimum steady state and partial equilibrium relationships. Unlike ILDM, it gives rise to an explicit reduced mechanism, so is of more benefit to a chemist or someone attempting to gain an understanding of the rate-limiting chemistry. However, ILDM is more suitable for efficient numerical simulations in a hydrodynamics code.

To date, mechanism reduction has not been used extensively in detonation simulations. Paczko and Klein (1993) proposed a QSSA mechanism suitable for hydrogen detonations with limited success in steady one-dimensional calculations. They also

offered an improved model which was derived from the QSSA model using lumping techniques. Neither model was applied to unsteady simulations. The group of Powers and co-workers (Singh and Powers, 1999; Paolucci et al., 2000) have recently begun investigation into using ILDM for gaseous nitramine detonation simulations.

In this work, we consider both QSSA and ILDM as approaches to mechanism reduction for gaseous detonations. §3.2 firstly describes the one-dimensional unsteady H_2–O_2 detonation simulations performed with detailed chemistry to later be used as validation of the reduced mechanisms. In §3.3, the QSSA method is used to derive a reduced mechanism for hydrogen detonations and comparisons are made with detailed chemistry for one-dimensional steady and unsteady detonations. The deficiencies of the method are also highlighted. The ILDM method is described in §3.4, and is used to develop a reduced model for hydrogen detonation simulations. As for the QSSA model, the results are compared with detailed chemistry for one-dimensional steady and unsteady detonations. Finally, the ILDM mechanism is used to compute a two-dimensional cellular detonation in H_2–O_2-Ar in §3.5 and compared with the detailed chemistry results of Oran et al. (1998).

3.2 One-Dimensional Detonation Simulations with Detailed Chemistry

Although it is generally not feasible to use detailed reaction mechanisms in multi-dimensional detonation simulations, one-dimensional simulations can be performed in a reasonable amount of computational time on a single processor machine. The implementation of detailed chemistry into a one-dimensional unsteady flow solver provides a means of validating reduced mechanisms and a good template for the implementation of reduced mechanisms into an unsteady flow solver.

3.2.1 Computational setup

Equations

The governing equations are the one-dimensional multi-species reactive Euler equations,

$$\frac{\partial \boldsymbol{W}}{\partial t} + \frac{\partial \boldsymbol{F}}{\partial x} = \boldsymbol{S}, \tag{3.1a}$$

where

$$\boldsymbol{W} = \begin{pmatrix} \rho \\ \rho u \\ E_t \\ \rho y_1 \\ \vdots \\ \rho y_{n_s} \end{pmatrix}, \quad \boldsymbol{F} = \begin{pmatrix} \rho u \\ \rho u^2 + P \\ (E_t + P)u \\ \rho u y_1 \\ \vdots \\ \rho u y_{n_s} \end{pmatrix}, \quad \boldsymbol{S} = \begin{pmatrix} 0 \\ 0 \\ 0 \\ \rho \Omega_1 \\ \vdots \\ \rho \Omega_{n_s} \end{pmatrix}. \tag{3.1b}$$

u, ρ and P are the velocity, density and pressure, x is the distance, t is the time, and y_k is the mass fraction of species k. E_t is the total energy per unit volume,

$$E_t = \rho \left(e + \frac{u^2}{2} \right),$$

where e is the specific internal energy. Ω_k is the production rate of species k, given by some kinetic rate law,

$$\frac{\mathrm{d}y_k}{\mathrm{d}t} = \Omega_k, \qquad k = 1, \ldots, n_s. \tag{3.2}$$

It can also be expressed as

$$\Omega_k = \frac{W_k \, \dot{\omega}_k}{\rho}, \tag{3.3}$$

where $\dot{\omega}_k$ is the net molar production rate of species k.

For a system of reacting ideal gases, calculation of $\dot{\omega}_k$ requires a detailed mechanism of elementary reactions, having the form

$$\sum_{k=1}^{n_s} \nu'_{kl} X_k \rightleftharpoons \sum_{k=1}^{n_s} \nu''_{kl} X_k, \qquad l = 1, \ldots, n_q, \tag{3.4}$$

where ν'_{kl} and ν''_{kl} are the forward and backward stoichiometric coefficients respectively, X_k is the chemical symbol for the species k, and n_q is the total number of reactions in the mechanism. Then the net molar production rate of species k is given by

$$\dot{\omega}_k = \sum_{l=1}^{n_q} (\nu''_{kl} - \nu'_{kl}) q_l, \tag{3.5}$$

where q_l is the net rate of progress for reaction l. For example, in a reversible two-body reaction, the net rate of progress is

$$q_l = k_{f_l} \prod_{k=1}^{n_s} [X_k]^{\nu'_{kl}} - k_{b_l} \prod_{k=1}^{n_s} [X_k]^{\nu''_{kl}}, \tag{3.6}$$

where k_{f_l} and k_{b_l} are the forward and backward rate coefficients of reaction l, and $[X_k]$ is the concentration of species k. The forward rate coefficients are typically expressed in the form

$$k_{f_l} = A_l \, T^{\beta_l} \, \exp\left(-\frac{E_{a_l}}{\mathcal{R}T}\right), \tag{3.7}$$

where A_l is the pre-exponential factor, β_l is the temperature exponent, E_{a_l} is the activation energy per unit mole, T is the temperature, and $\mathcal{R}$ is the universal gas constant. The backward rate constants k_{b_l} are given in terms of k_{f_l} by chemical equilibrium considerations (Kee et al., 1989).

The equations are closed with the specification of an equation of state $P = P(\rho, e, \boldsymbol{y})$. For a system of ideal gases, this is

$$P = \rho R_g(\boldsymbol{y}) T(e, \boldsymbol{y}). \tag{3.8}$$

R_g is the mixture gas constant, given by

$$R_g(\boldsymbol{y}) = \frac{\mathcal{R}}{W(\boldsymbol{y})} = \mathcal{R} \sum_{k=1}^{n_s} \frac{y_k}{W_k},$$

where W is the mean molar mass of the mixture, and W_k is the molar mass of species k.

Numerical method

The simulations were performed with the Amrita CFD programming system (Quirk, 1998), making use of Amrita's adaptive mesh refinement (AMR) algorithm. The numerical integration in the flow solver was performed using timestep splitting, with the algorithm

$$\boldsymbol{W}^{n+1} = \mathcal{L}_S \mathcal{L}_F \boldsymbol{W}^n,$$

where the superscript indicates the number of timesteps.

The convective operator $\mathcal{L}_F$ is the integration of the equation

$$\frac{\partial \boldsymbol{W}}{\partial t} + \frac{\partial \boldsymbol{F}}{\partial x} = \boldsymbol{0}.$$

When integrated in a uniform grid with a cell-centered, finite difference formulation, it can be written as

$$\boldsymbol{W}_i^{n+1} = \boldsymbol{W}_i^n - \frac{\Delta t}{\Delta x}\left(\boldsymbol{F}_{i+1/2}^n - \boldsymbol{F}_{i-1/2}^n\right), \tag{3.9}$$

where Δt is the timestep, Δx is the cell size and $\boldsymbol{F}_{i+1/2}^n$ is the flux at the interface between cells i and $i+1$. The subscript i indicates the spatial cell number. As in the integration of the reactive Euler equations with the one-step reaction model in §2, we employed Roe's approximate Riemann solver (Roe, 1986) for the convective flux. Glaister's (1988) implementation for a general equation of state was used, with an extension for multi-species gases in chemical non-equilibrium (see Appendix B). Second-order temporal and spatial accuracy was obtained via min–mod flux limiting, and the scheme was made entropy-satisfying with Harten's entropy fix.

The temperature $T(e, \boldsymbol{y})$ was determined by implicit solution of the equation

$$e = \sum_{k=1}^{n_s} y_k e_k(T), \tag{3.10}$$

where e_k is the specific internal energy of species k and is a known function of temperature. Solution of (3.10) was obtained by a Newton-Raphson technique. The

functions $e_k(T)$ are nearly linear, so the solution always converges no matter how poor the initial guess, and convergence is very rapid. But for maximum efficiency, the initial guess for the temperature was taken to be the result of the previous call to the temperature solver. Calls are typically made for neighboring grid cells in succession, and the temperature in the neighboring cell is a good first estimate.

For evaluation of the sound speed and the eigenvectors of the system Jacobian, the flow solver also required specification of the partial derivatives of pressure with respect to density, internal energy and the species mass fractions. These are given by the derivatives of (3.8):

$$\left.\frac{\partial P}{\partial \rho}\right|_{e,\boldsymbol{y}} = R_g(\boldsymbol{y})T, \tag{3.11a}$$

$$\left.\frac{\partial P}{\partial e}\right|_{\rho,\boldsymbol{y}} = \frac{\rho R_g(\boldsymbol{y})}{C_v(T,\boldsymbol{y})}, \tag{3.11b}$$

$$\left.\frac{\partial P}{\partial y_k}\right|_{\rho,e,y_{j\neq k}} = \rho R_g(\boldsymbol{y}) \left\{ T\frac{W(\boldsymbol{y})}{W_k} - \frac{e_k(T)}{C_v(T,\boldsymbol{y})} \right\}, \tag{3.11c}$$

where $T = T(e, \boldsymbol{y})$. C_v is the mixture specific heat at constant volume, given by

$$C_v(T,\boldsymbol{y}) = \sum_{k=1}^{n_s} y_k C_{v_k}(T).$$

The species data W_k, $e_k(T)$ and $C_{v_k}(T)$ were obtained from CHEMKIN (Kee et al., 1989).

The reaction source operator $\mathcal{L}_S$ involves the integration of the equation,

$$\frac{\mathrm{d}\boldsymbol{W}}{\mathrm{d}t} = \boldsymbol{S},$$

which reduces to (3.2), with ρ, u and e constant. The net molar production rate of the k-th species, $\dot{\omega}_k(\rho, T, \boldsymbol{y})$ in (3.3), was computed with CHEMKIN and an appropriate reaction mechanism. The system of ODEs (3.2) is typically very stiff and must be integrated with an implicit integrator designed for use with stiff equations. In this work, the backward differentiation solver DEBDF (Shampine and Watts, 1979) was

used. This solver includes an adaptive time step and local error control. The timestep Δt used in the CFD code was taken to be that given by the Courant–Friedrichs–Lewy (CFL) condition for the convective step, and the ODE solver automatically subcycled as necessary in the reactive step.

Note that the system of equations (3.1) is actually over-specified. If there are n_e atomic elements, then there are an additional n_e element mass conservation constraints, which means n_e of the species conservation equations in (3.1) are superfluous. However, numerical integration of the ODEs (3.2) is typically more well-behaved when all equations are included. Any standard integrator such as DEBDF should maintain mass conservation within roundoff error, and if $n_s \gg n_e$ as is typical, there is little extra expense in integrating all of the equations.

3.2.2 Code verification

Various verifications of the reactive code were performed. To avoid the difficulty of hydrodynamic instability that occurs in one-dimensional detonation simulations, our initial verifications utilized an endothermic reaction to ensure a stable one-dimensional unsteady solution. The system chosen was dissociating oxygen, with a single reversible reaction describing the dissociation:

$$\mathrm{O_2} + \mathrm{M} \rightleftharpoons \mathrm{O} + \mathrm{O} + \mathrm{M}.$$

The reaction rate was extracted from the Maas and Warnatz (1988) hydrogen reaction mechanism.

Figure 3.1 shows the results of a one-dimensional dissociating shock which has propagated down a duct for a certain length of time t. The computation was initialized by interpolating the one-dimensional steady solution onto the computational grid with the shock front at location $x = 0$. The solid lines represent the exact theoretical solution, which is the initial condition propagated a distance Ut down the duct, where U is the steady shock velocity. The points represent the unsteady numerical solution, and the agreement with the theoretical solution is excellent. Hence the code is able

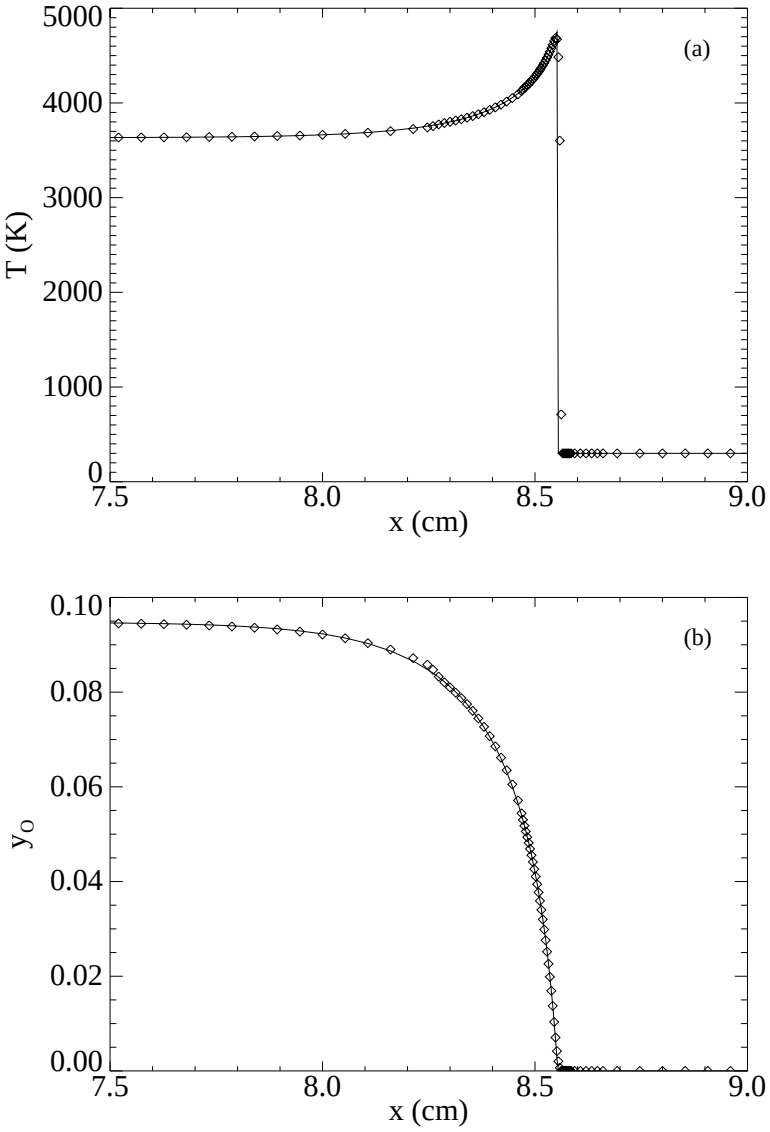

Figure 3.1: One-dimensional shock propagation in dissociating O_2, initially at 0.1 atm and 300 K. $U = 3300$ m/s, $t = 25.92$ μs. Points: numerical; Lines: theoretical. (a) Temperature; (b) Mass fraction of O.

Initial states:	P (atm)	ρ (kg/m^3)	composition
Left	60	5	equilibrium O_2–O
Right	0.1	0.05	equilibrium O_2–O

Table 3.1: Initial conditions for shock tube calculations shown in figs. 3.2 and 3.3.

to successfully propagate a steady one-dimensional profile. Mesh refinement was also incorporated into this simulation, with refinement on the gradients of density and oxygen atom mass fraction. The refinement in the reaction zone and leading shock wave is evident in the figure.

To test the code on a more dynamic flow, the next verification was the computation of a one-dimensional shock tube, with the same simple dissociating gas. In general, for a reactive flow, the solution of a shock tube Riemann problem is not a self-similar centered wave system since the reaction provides a length scale. Hence, an analytical solution does not exist. However, there is such a similarity solution in the limits of frozen and equilibrium flow, that is, when the reaction length approaches infinity and zero respectively, removing the associated length scale and making the flow self-similar.

Figures 3.2 and 3.3 show the results of a shock tube calculation in the frozen and equilibrium limits. In each case, the diaphragm was located at $x = 0$ and the initial conditions were those in table 3.1. The analytical solutions are described in Appendix C. For the numerical simulations, the frozen flow case was simulated by simply turning off the reactive step in the flow solver. The equilibrium case was approximated by turning the reactive step back on and thus computing the chemical non-equilibrium flow, but using a physical scale for the problem much greater than the reaction length such that the reaction proceeded almost immediately to equilibrium. Mesh refinement was used in the simulations, with refinement on the temperature gradient to finely resolve the shock wave, and on the gradient of oxygen atom mass fraction to finely resolve the contact surface as well as the post-shock reaction zone in the equilibrium case. In both cases, the agreement between the numerical and exact solutions are seen to be excellent. The only evidence of the actual non-equilibrium nature of the simulations in figure 3.3 is the von Neumann spike in temperature behind

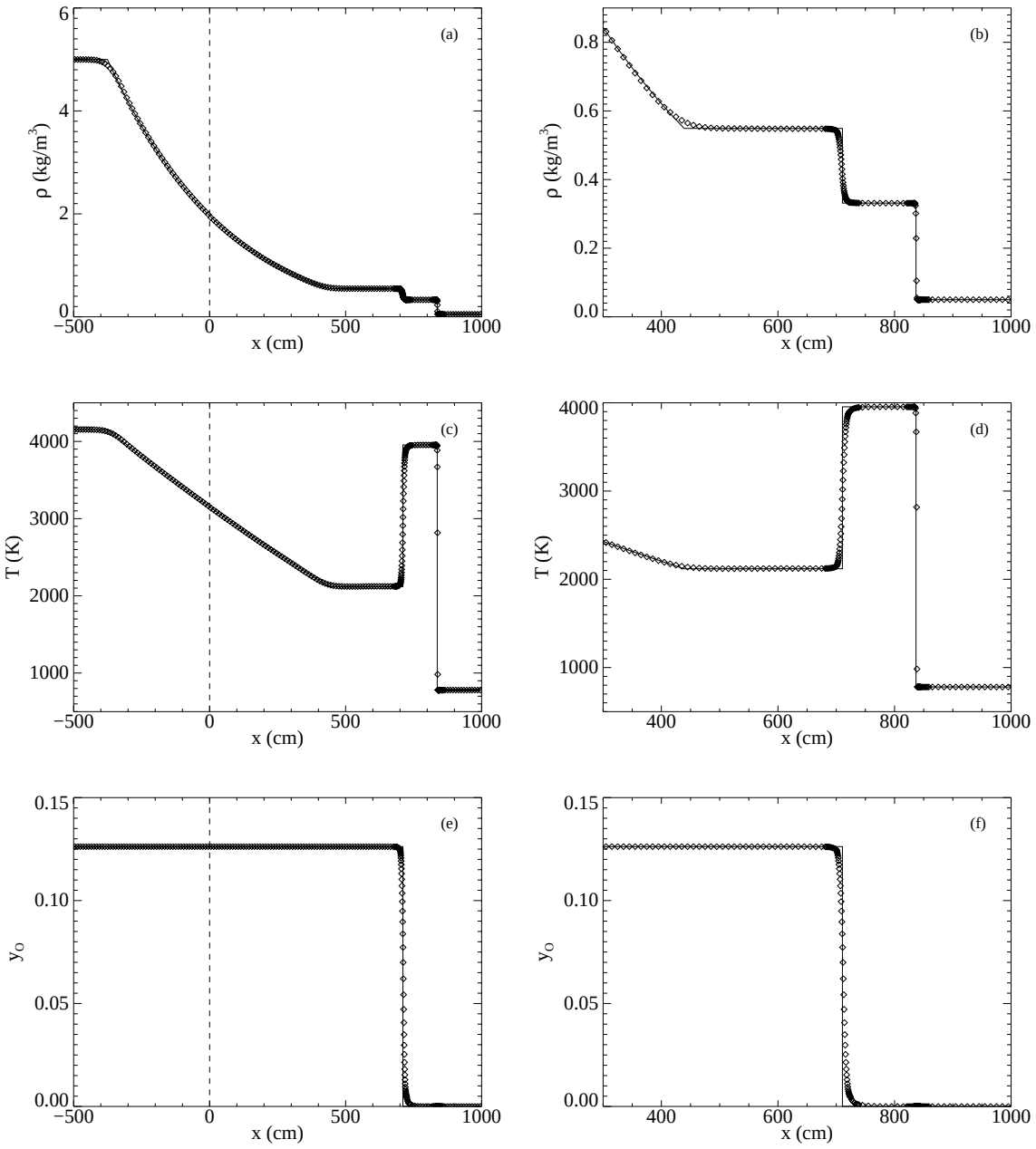

Figure 3.2: Shock tube with dissociating O_2 in frozen limit. Points: Numerical solution, computed with reactive step deactivated; Lines: Theoretical solution, determined analytically from Appendix C. $t = 3$ ms. (a,b) Density; (c,d) Temperature; (e,f) Mass fraction of O.

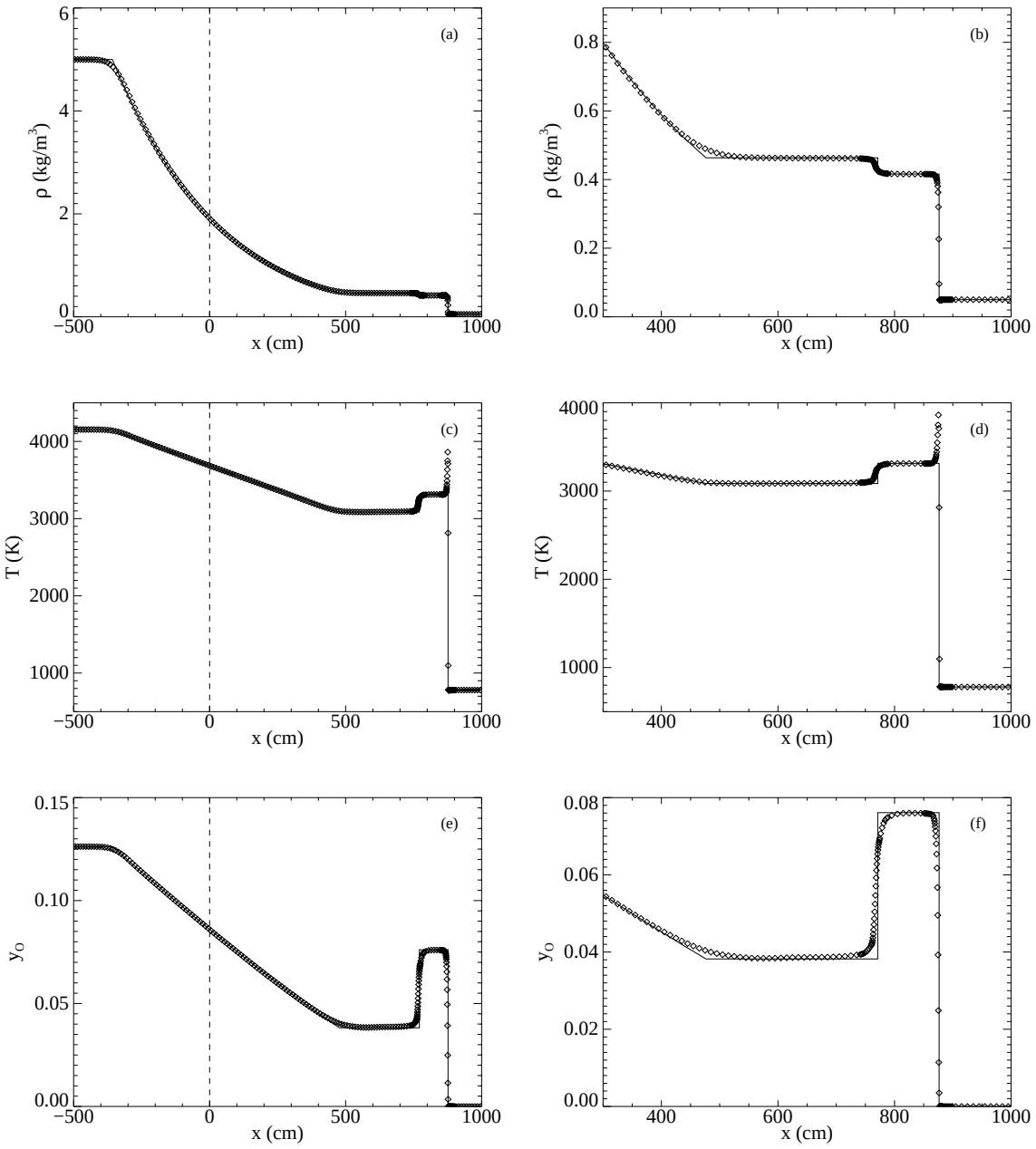

Figure 3.3: Shock tube with dissociating O_2 in near-equilibrium limit. Points: Numerical solution, computed with fast reaction which proceeds almost immediately to equilibrium; Lines: Theoretical solution, determined analytically from Appendix C. $t = 3$ ms. (a,b) Density; (c,d) Temperature; (e,f) Mass fraction of O.

the leading shock wave, where the flow rapidly changes from a frozen post-shock state to an equilibrium post-shock state.

3.2.3 Unsteady detonation simulations

The code was then applied to a one-dimensional detonation simulation. The system studied was stoichiometric H_2–O_2, initially at 1 atm and 300 K, and the reaction mechanism used was taken from Maas and Warnatz (1988). For reference, the reaction mechanism is listed in Appendix D. Various degrees of overdrive were considered, where the overdrive factor f is defined as

$$f = \left(\frac{U_{ZND}}{U_{CJ}} \right)^2 .$$

U_{ZND} is the detonation velocity of the equivalent steady ZND (Zel'dovich–von Neumann–Doering) detonation and U_{CJ} is the minimum velocity for which a ZND solution exists, the Chapman–Jouget velocity. At the CJ velocity and slightly above, the one-dimensional detonation in this system is unstable and the front velocity oscillates periodically. This is typically known as a "galloping detonation" (Fickett and Davis, 1979). Far enough above the CJ velocity, the detonation becomes stable and the resulting solution is the steady ZND wave propagating down the duct at constant velocity U_{ZND}.

The simulations were initialized by grafting the ZND solution onto the computational grid. At the freestream end of the computational domain, the boundary condition used was linear extrapolation. At the other end behind the detonation, the boundary conditions were the fixed overdriving piston conditions corresponding to the ZND farfield equilibrium state. Previous galloping detonation simulations with the one-step reaction model, such as those by Bourlioux et al. (1991), generally used an applied perturbation to the ZND initial conditions to trigger the instability. However, we found that if the simulation was sufficiently well resolved, the instability grew quite quickly from the numerical startup error, so no applied perturbation was necessary.

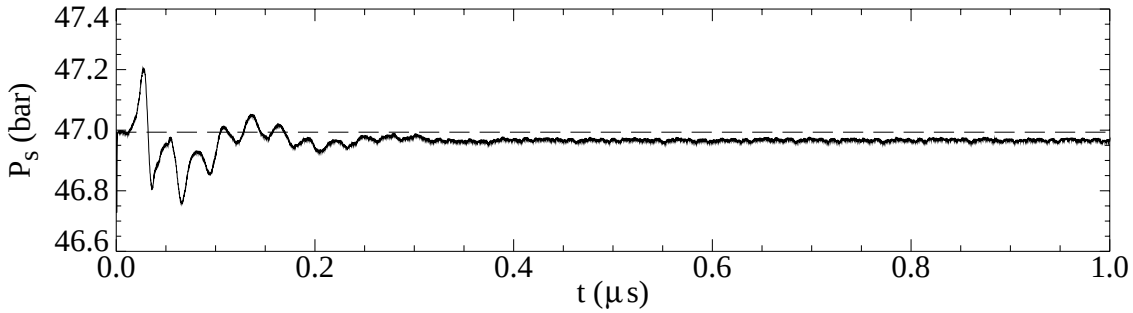

Figure 3.4: Shock pressure versus time, for a stable one-dimensional detonation in stoichiometric H_2–O_2, initially at 1 atm and 300 K, with $f = 1.4$. $P_{vN} = 46.99$ bar. Finest grid level contains 100 cells per ZND induction length.

Mesh refinement was performed around the shock, where the density gradient exceeded a specified threshold, and in the reaction zone, where the gradient of HO_2 mass fraction exceeded another threshold. HO_2 was chosen because the ZND profiles suggested this species had the most substantial gradients in the induction region, ensuring that the induction part of the reaction zone would not be missed by the mesh refinement. Four or five refinement levels were used, with refinement ratios of four between each level. The refinement criteria were chosen to produce a finely resolved shock and a reaction zone with a prescribed number of mesh cells per ZND induction length.

Figure 3.4 shows the pressure behind the leading shock, P_s, versus time, for an overdrive factor $f = 1.4$. The dashed line shows the value of the von Neumann (vN) pressure, P_{vN}, the post-shock pressure in the steady ZND solution. After the initial perturbation from the startup error, P_s soon settles to almost exactly P_{vN}. This indicates the detonation is sufficiently overdriven to be hydrodynamically stable and travels at the steady ZND velocity U_{ZND}. The startup error is caused by the prescribed sharp shock of the initial ZND profile numerically smearing itself across a few cells of the computational grid and flexing in velocity as it does so. Profiles of the temperature and mass fraction of H at a late time are shown in figure 3.5. The theoretical solution is also shown as a solid line, where this is the ZND solution propagated a distance $U_{ZND}\, t$ down the duct. The slight phase error between the numerical and theoretical solutions is mostly due to the residual effect of the startup error. If the simulation

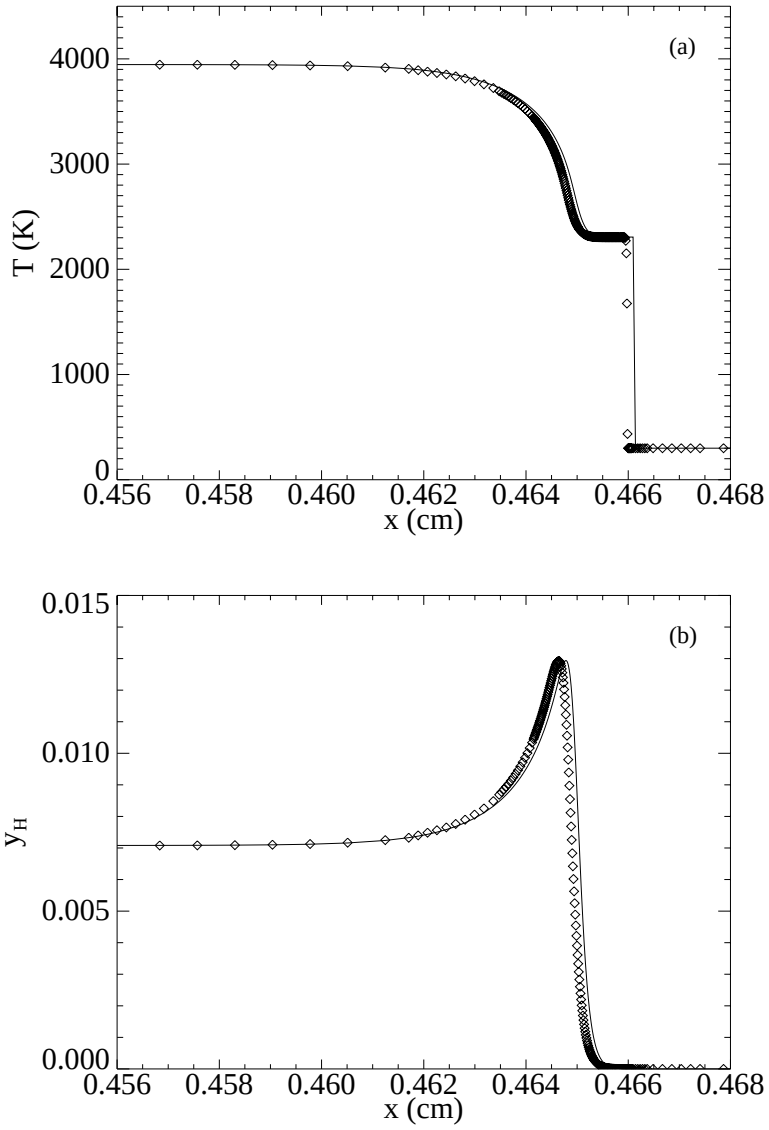

Figure 3.5: One-dimensional detonation in stoichiometric H_2–O_2, initially at 1 atm and 300 K, with $f = 1.4$. $t = 1.387$ μs. Points: numerical; Lines: ZND theory. (a) Temperature; (b) Mass fraction of H.

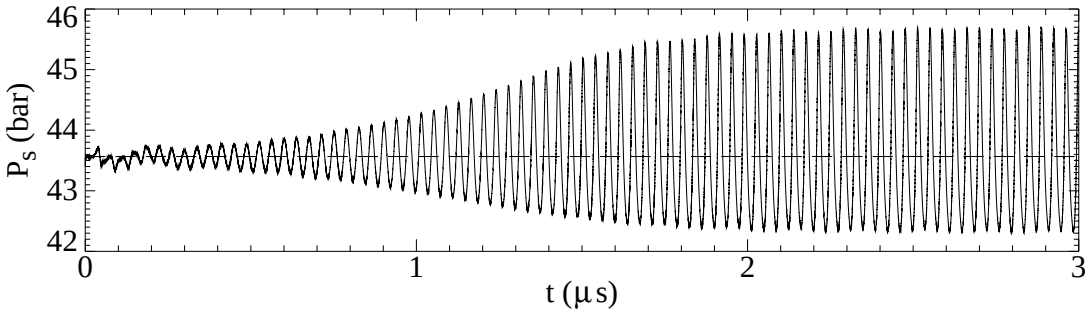

Figure 3.6: Shock pressure versus time, for a one-dimensional detonation in stoichiometric H_2–O_2, initially at 1 atm and 300 K, with $f = 1.3$. $P_{vN} = 43.57$ bar. Finest grid level contains 200 cells per ZND induction length.

was restarted with a numerically smeared shock as the initial condition, this phase error could essentially be eliminated. Other than this small difference, the numerical and theoretical solutions are practically identical. The computation of this overdriven stable detonation thus serves as a further verification of the unsteady reactive flow solver.

When the overdrive factor is reduced to 1.3, figure 3.6 shows that the detonation becomes hydrodynamically unstable. This is a physical instability rather than numerical, akin to the physical instability predicted by linear stability analysis of the one-step reaction model (Erpenbeck, 1964; Lee and Stewart, 1990). The computed detonation eventually reaches a periodic oscillating solution characteristic of a galloping detonation. When the overdrive factor is further reduced to 1.2, figure 3.7 shows that the detonation develops a second longitudinal instability of longer period and greater magnitude than the first.

To verify grid convergence, the most important numerical details were extracted from the computational pressure traces of one case repeated with various grid scales. The case chosen was an overdrive factor of 1.3, with one unstable mode (see figure 3.6). The growth of the initial perturbation is usually not of great interest and it depends upon a number of factors, some of which are numerical, so it is more pertinent to study the final periodic solution, which is a physical phenomenon. The quantities extracted from the simulations were the period and magnitude of the final periodic oscillations. The simulations were repeated with different sizes of the finest grid level

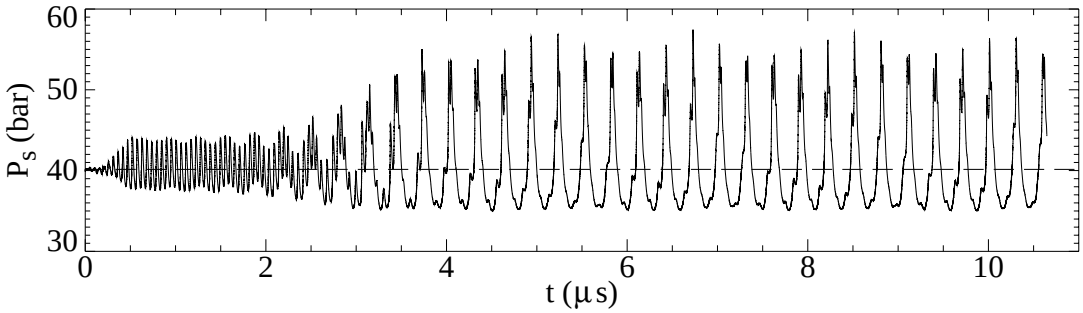

Figure 3.7: Shock pressure versus time, for a one-dimensional detonation in stoichiometric H_2–O_2, initially at 1 atm and 300 K, with $f = 1.2$. $P_{vN} = 40.14$ bar. Finest grid level contains 200 cells per ZND induction length.

corresponding to prescribed numbers of cells per ZND induction length. The period and average pressure peaks and troughs are plotted in figure 3.8. The data was taken for $t \geq 3\mu$s, where figure 3.6 shows the detonation has certainly reached its final periodic configuration.

Figure 3.8(a) shows the average oscillation period along with the spread between the maximum and minimum periods. Noting the small range on the period axis, all these simulations appear to be grid converged, with the possible exception of the simulation with 75 fine mesh cells per induction length. The ZND induction time τ for this case was 27.7 ns, based on the point of maximum temperature gradient, so the oscillation period is about 1.35τ. Alpert and Toong (1972) found that the shortest galloping detonation period observed in experiments with various H_2–O_2 mixtures was on average about 1.7τ. This compares quite well with our numerical result. The experiments reviewed by Alpert and Toong were all of the oscillations witnessed behind the bow shock of a blunt body moving through a detonable gas at near CJ velocity. Fickett and Davis (1979) note that this is the only experimental configuration where "fast–gallop" detonations have been observed. In all other detonation configurations, the multi-dimensional transverse instability dominates and the longitudinal instability is usually not evident.

Figure 3.8(b) shows the average pressure peak and trough observed in the final periodic oscillations of each simulation, along with the spread between the maximums and minimums. The spread of the data values was very small in all cases. As the num-

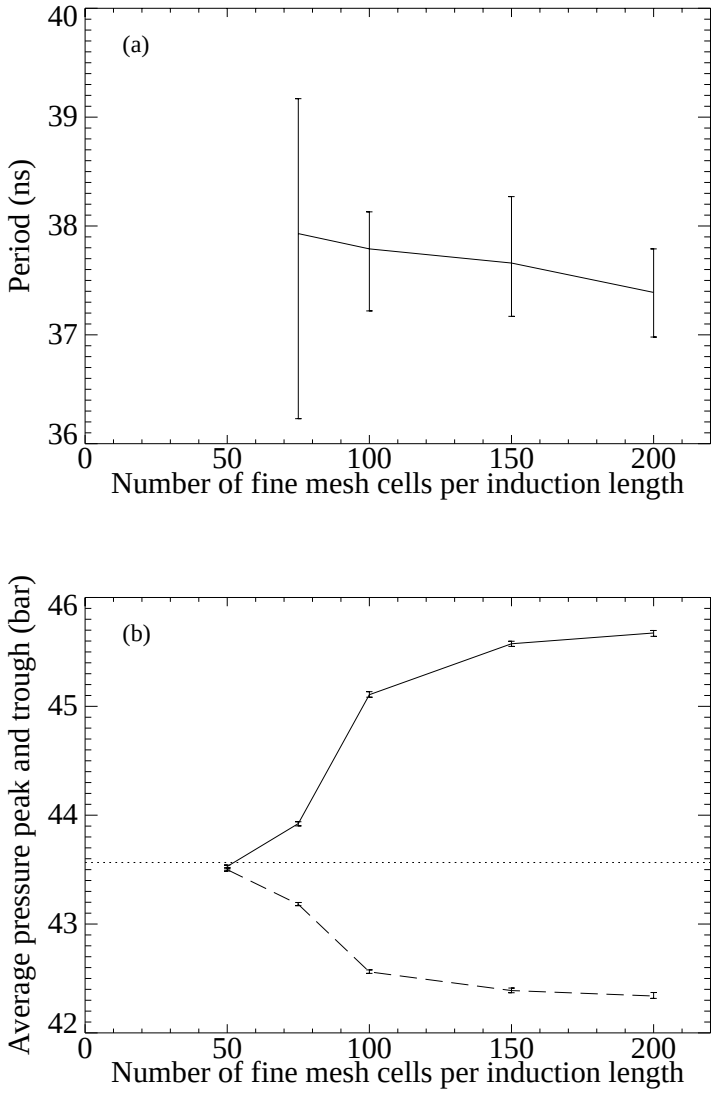

Figure 3.8: One-dimensional detonation in stoichiometric H_2–O_2, initially at 1 atm and 300 K, with $f = 1.3$. (a) Period of oscillation. (b) Pressure peak (solid line) and trough (dashed line).

ber of fine mesh cells per induction length was decreased, the oscillations decreased in magnitude. They actually disappeared completely when only 50 cells were used, giving the false result that this detonation is hydrodynamically stable. At least 150 cells per induction length are required for grid convergence. The simulation presented in figure 3.6 used 200 mesh cells per induction length and is thus a grid converged solution.

3.3 Quasi Steady State Approximation

3.3.1 Reduced mechanism for H_2–O_2

The first mechanism reduction technique examined was the Quasi Steady State Approximation (QSSA) method. The work loosely followed that of Paczko and Klein (1993) who developed a three-step reduced mechanism intended for H_2–O_2–H_2O detonations at all conditions and stoichiometries. The starting detailed mechanism adopted by these workers was that of Maas and Warnatz (1988), listed in Appendix D. In an effort to firstly reproduce the previous results, we used the same starting mechanism. It should be noted that a reduced mechanism is at best only as good as its parent detailed reaction mechanism. The Maas and Warnatz mechanism is by no means the ideal choice since this mechanism was not designed for use at the high pressures typically seen in detonations. If a reduced mechanism were to be used for useful predicative simulations, a better choice would need to be made on the basis of a mechanism validation study such as that performed by Schultz and Shepherd (1999). However, we are here only interested in the validation of a reduced mechanism against its parent detailed mechanism, so any detailed mechanism will suffice.

The most important and difficult step in the QSSA method is identifying the steady–state species. These are the species that have creation and destruction rates that are always much greater than their sum, the species net production rate. When this is the case, the balance equation for the species net molar production rate, (3.5), is the sum of large positive and negative numbers that nearly cancel, so $\dot{\omega}_k \approx 0$.

Alternatively, Peters (1988) suggests that since the net production rate is small, the steady–state species may be identified as those whose concentrations remain low throughout the reaction zone. Appropriate selection of the steady–state species requires experience with the reactive system under consideration, or considerable effort in examining species production rates under a variety of thermodynamic conditions.

Once the steady–state species are identified, the remainder of the reduction process essentially follows a predefined path. It consists of the following steps (Peters, 1988):

1. Write the steady–state relations from the balance equations for the steady–state species.

2. Use the steady–state relations to eliminate the fastest reaction rates from the balance equations of the remaining species.

3. Using the stoichiometry of the remaining balance equations, determine the global reactions in the reduced system and their rates in terms of reaction rates of the original system.

4. Introduce partial equilibrium or truncation relations to simplify the algebraic steady–state relations for numerical efficiency.

The coupled differential–algebraic equation system can then be implemented in a hydrodynamics code. For maximum efficiency, the reaction rates of the global reduced reactions are sometimes fit to explicit empirical expressions.

For the hydrogen reaction mechanism, we attempted to derive a reduced mechanism suitable for detonations in H_2–O_2–N_2 over a wide range of stoichiometries between very lean and very rich. Some past experience with these systems was beneficial (Shepherd, 1986). The ignition process in H_2–O_2 reactive systems follows the following main pathway. After an initiation step,

$$H_2 + O_2 \rightarrow HO_2 + H, \tag{R10r}$$

which creates a small amount of radicals, one of two ignition modes commences. The

first is a fast chain branching sub-mechanism,

$$O_2 + H \rightleftharpoons OH + O, \tag{R1}$$

$$H_2 + O \rightleftharpoons OH + H, \tag{R2}$$

$$H_2 + OH \rightleftharpoons H_2O + H, \tag{R3}$$

which dominates at high temperature. The second, which dominates at low temperature, is the much slower chain termination reaction,

$$H + O_2 + M \rightleftharpoons HO_2 + M. \tag{R8}$$

In deflagrations, HO_2 from (R8) diffuses to the vessel walls where it is lost in surface reactions. This is the first flammability limit. However, in detonations, diffusion is too slow to be significant, and the HO_2 is converted back to the chain branching radical pool via the following reactions:

$$HO_2 + H \rightleftharpoons OH + OH, \tag{R9}$$

or

$$HO_2 + HO_2 \rightarrow H_2O_2 + O_2, \tag{R14}$$

$$H_2O_2 + M \rightleftharpoons OH + OH + M. \tag{R15r}$$

After a sufficient quantity of chain branching radicals have been produced, the main energy release occurs in the thermal explosion recombination reaction,

$$H + OH + M \rightleftharpoons H_2O + M. \tag{R6}$$

So in a detonation, the energy release always occurs, whether after a short chain branching induction period or a long chain termination dominated induction period. The crossover temperature between these two modes occurs when the forward rates

of (R1) and (R8) compete equally for the H radicals. Due to the pressure dependence of the three-body reaction (R8), the crossover temperature is somewhat dependent on pressure, varying between about 1100 K at 1 atm and 1700 K at 40 atm. The von Neumann temperature in a CJ detonation in H_2–O_2 or H_2–air with ambient temperature near room temperature typically ranges from 900 to 1500 K. So both ignition modes are possible, and to cover a range of conditions and mixtures the reduced mechanism must be able to represent both modes. This means at least one of the chain branching radicals H, O or OH must be retained in the reactive system and not set to steady–state. In addition, HO_2 or H_2O_2 must be retained to represent the chain termination process.

A quantitative indication of which species are in steady–state can be gained by examining the ZND reaction zone profile in a model problem. The case presented here is a CJ detonation in stoichiometric H_2–air initially at 1 atm and 300 K. In this calculation and throughout the thesis, "air" is defined as $O_2 + 3.76N_2$. The case considered here is a chain branching type ignition. The following results were also verified to be true for a typical chain termination ignition. H_2O_2 was first deemed to be in steady–state by noting that its maximum concentration in the reaction zone was small, about an order of magnitude less than the next smallest species, HO_2. As explained above, HO_2 must then be retained to represent the chain termination ignition process. Figure 3.9 shows the creation and destruction rates for the radical species H, O, OH and HO_2 in the ZND calculation. In this figure and later ZND plots, x is the distance behind the shock front so the shock is at the left edge of the figures and is traveling to the left. Only quantities behind the shock are shown. The induction length in this reaction is 0.023 cm, based on the point of maximum temperature gradient. This corresponds roughly to the peak in the net production rate of each radical. For the three chain branching radicals, H, O and OH, the creation and destruction rates are almost the same and each significantly greater than their net sum in the induction region. As a result, all are nearly in steady–state. The greatest discrepancy between the creation and destruction rates for any of the chain branching radicals is for the hydrogen atom. Hence, we chose to retain H in the

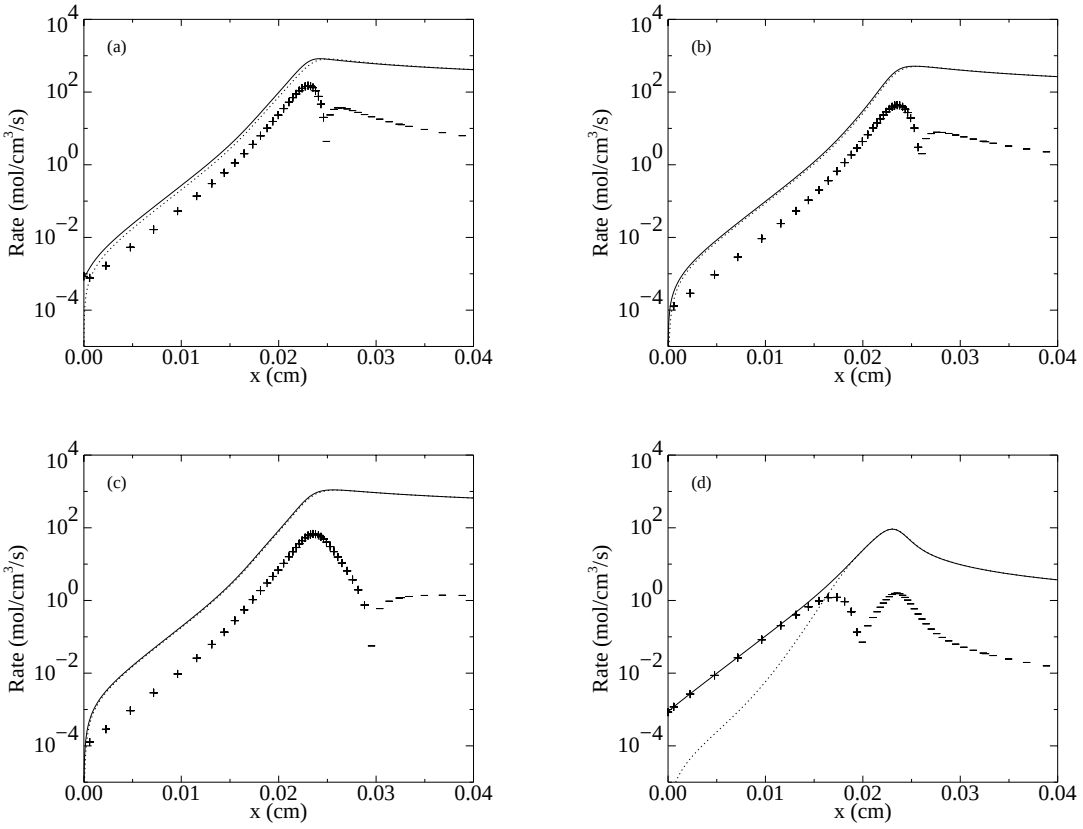

Figure 3.9: ZND calculation of a CJ detonation in stoichiometric H_2–air, initially at 1 atm and 300 K. Species creation rates (solid lines), destruction rates (dotted lines) and absolute value of the net production rates (+ symbol for positive, - symbol for negative). (a) H; (b) O; (c) OH; (d) HO_2.

system while setting O and OH in steady–state. Interestingly, even though this is a chain-branching type ignition, the species HO_2 is certainly not in steady–state in the induction zone, further justifying the choice to keep it in the system.

Setting the species O, OH and H_2O_2 to steady–state gives the following balance relations,

$$0 = \dot{\omega}_{\mathrm{O}} = q_1 - q_2 + q_4 - 2q_7 + q_{11} - q_{12} - q_{18}, \tag{3.12a}$$

$$0 = \dot{\omega}_{\mathrm{OH}} = q_1 + q_2 - q_3 - 2q_4 - q_6 + 2q_9 + q_{12} - q_{13} - 2q_{15} + q_{17} + q_{18} - q_{19}, \tag{3.12b}$$

$$0 = \dot{\omega}_{\mathrm{H_2O_2}} = q_{14} + q_{15} - q_{16} - q_{17} - q_{18} - q_{19}, \tag{3.12c}$$

where q_i is the net rate of progress for reaction (Ri) in the detailed mechanism. The fastest reactions that consume each of the steady–state species are (R2), (R3) and (R15) respectively. So elimination of those will remove some of the fastest timescales in the system. Using the above three algebraic steady–state relations to eliminate q_2, q_3 and q_{15} from the balance equations of the remaining species gives the required reduced system. By examining the stoichiometry of these reduced balance equations, a global reduced mechanism can be identified. With five remaining species and two element conservation constraints, there are three degrees of freedom left in the reduced system. Hence, the chemical system has been reduced from one with six degrees of freedom to one with three. While this reduction might appear modest, much greater reduction factors could be expected for larger detailed mechanisms such as hydrocarbons. The following three-step reduced mechanism for H_2–O_2 systems is obtained:

$$3\mathrm{H_2} + \mathrm{O_2} \rightleftharpoons 2\mathrm{H} + 2\mathrm{H_2O}, \tag{I}$$

$$2\mathrm{H} \rightleftharpoons \mathrm{H_2}, \tag{II}$$

$$\mathrm{HO_2} + \mathrm{H} \rightleftharpoons \mathrm{H_2} + \mathrm{O_2}. \tag{III}$$

Note that these reactions are symbolic only, and do not represent real elementary reactions or reaction pathways. The rates of progress for the reduced reactions are

also determined from the stoichiometry of the reduced balance equations:

$$q_I = q_1 - q_7 + q_9 + q_{11} + q_{14} - q_{16} - q_{18} - q_{19}, \tag{3.13a}$$

$$q_{II} = q_5 + q_6 + q_7 + q_8 - q_{14} + q_{16} + q_{17} + q_{18} + q_{19}, \tag{3.13b}$$

$$q_{III} = -q_8 + q_9 + q_{10} + q_{11} + q_{12} + q_{13} + 2q_{14} - q_{16} - q_{18} - q_{19}. \tag{3.13c}$$

The species net production rates in the reduced system are finally obtained from the stoichiometry of the reactions (I) to (III) and their corresponding rates of progress (3.13):

$$\dot{\omega}_{\mathrm{H_2}} = -3q_I + q_{II} + q_{III}, \tag{3.14a}$$

$$\dot{\omega}_{\mathrm{O_2}} = -q_I + q_{III}, \tag{3.14b}$$

$$\dot{\omega}_{\mathrm{H_2O}} = 2q_I, \tag{3.14c}$$

$$\dot{\omega}_{\mathrm{H}} = 2q_I - 2q_{II} - q_{III}, \tag{3.14d}$$

$$\dot{\omega}_{\mathrm{HO_2}} = -q_{III}. \tag{3.14e}$$

3.3.2 Implementation in a one-dimensional CFD code

The governing equations are simply a slight modification of those for detailed chemistry in (3.1):

$$\frac{\partial \boldsymbol{W}}{\partial t} + \frac{\partial \boldsymbol{F}}{\partial x} = \boldsymbol{S}, \tag{3.15a}$$

where

$$\boldsymbol{W} = \begin{pmatrix} \rho \\ \rho u \\ E_t \\ \rho y_1 \\ \vdots \\ \rho y_{n_{s,r}} \end{pmatrix}, \quad \boldsymbol{F} = \begin{pmatrix} \rho u \\ \rho u^2 + P \\ (E_t + P)u \\ \rho u y_1 \\ \vdots \\ \rho u y_{n_{s,r}} \end{pmatrix}, \quad \boldsymbol{S} = \begin{pmatrix} 0 \\ 0 \\ 0 \\ \rho \Omega_1 \\ \vdots \\ \rho \Omega_{n_{s,r}} \end{pmatrix}. \tag{3.15b}$$

$n_{s,r}$ is the number of species in the reduced mechanism, five in the case of the H_2–O_2 reduced mechanism from the previous section. The species production rates Ω_k can be expressed in terms of net molar production rates $\dot{\omega}_k$ as in (3.3). Rather than using CHEMKIN (Kee et al., 1989) to evaluate $\dot{\omega}_k$, they are evaluated from a set of reduced balance equations such as (3.14), where the reduced reaction rates $\{q_I, q_{II}, \dots\}$ are expressed in terms of several reaction rates q_i from the original detailed mechanism, as in (3.13). The rates q_i are evaluated with CHEMKIN. The equation of state is the same ideal gas equation used in the detailed mechanism, (3.8), except $\boldsymbol{y}$ here refers only to the mass fractions of the species retained in the reduced system.

Note that the expressions for the reduced rates in (3.13) contain some rates from the original detailed mechanism that are functions of the concentrations of the steady–state species. For example,

$$q_{18} = k_{18f}[H_2O_2][O] - k_{18r}[OH][HO_2]$$

contains all three steady–state species concentrations. Thus, to evaluate the reduced rates of progress, an approximation to the concentrations of the removed steady–state species is required. This is obtained by solving the coupled system of algebraic steady–state relations (3.12). However, these equations are nonlinear in the unknowns [O], [OH] and $[H_2O_2]$, so an explicit solution is not possible. They must be solved implicitly in conjunction with the integration of the ODEs for the remaining species. Hence, all that has been achieved is the conversion of a differential equation system to a differential–algebraic equation system with the same number of equations. Clearly, this is not likely to give significant computational cost savings, if any at all.

The standard solution to this dilemma is to truncate the algebraic equations, removing enough of the smaller terms to permit explicit solution (Peters, 1988). This is equivalent to making some partial equilibrium assumptions. For the previously considered model problem of stoichiometric H_2–air, a chain branching type ignition, examination of the individual reaction rates of progress in the reaction zone revealed

that the following truncations of (3.12) were the most valid:

$$0 = \dot{\omega}_{\mathrm{O}} = q_1 - q_2, \tag{3.16a}$$

$$0 = \dot{\omega}_{\mathrm{OH}} = q_1 + q_2 - q_3 - q_{6f} + 2q_{9f}. \tag{3.16b}$$

The full expression for $\dot{\omega}_{\mathrm{H_2O_2}}$ was retained. These truncated relations permitted explicit solution of the steady–state species concentrations.

3.3.3 Validation in ZND calculations

The first validation of the QSSA reduced mechanism was the comparison of ZND steady one-dimensional reaction zone profiles with detailed chemistry. Figure 3.10 shows the profiles for a typical chain branching ignition. The initial condition for each calculation was the von Neumann state behind a shock traveling at CJ velocity, where the CJ velocity was firstly computed by an equilibrium calculation with STANJAN (Reynolds, 1986). Since the reduced mechanism contains a reduced list of chemical species, the CJ equilibrium state and corresponding CJ detonation velocity was different from that for the detailed mechanism. This explains the difference in von Neumann pressure and temperature at $x = 0$ in the figure. The other major feature to note is that the reduced mechanism underpredicts the induction length by about 50%. Adjusting the von Neumann state to match that used in the detailed mechanism only moved the induction lengths slightly closer together. Hence, the error in induction length is caused mostly by the difference in chemical kinetics, not the difference in thermodynamic CJ conditions. The mass fractions of the two radical species retained in the reduced system are also shown in the figure. The peak fraction of HO_2 is very well predicted while the peak fraction of H is overpredicted by about 40%.

Figure 3.11 shows the same profiles for a typical chain termination dominated ignition. The reaction zone profiles are characterized by a much longer induction length, about 1000 times greater than the previous case. In this case, there is much less error in the von Neumann state. The induction length is again underpredicted,

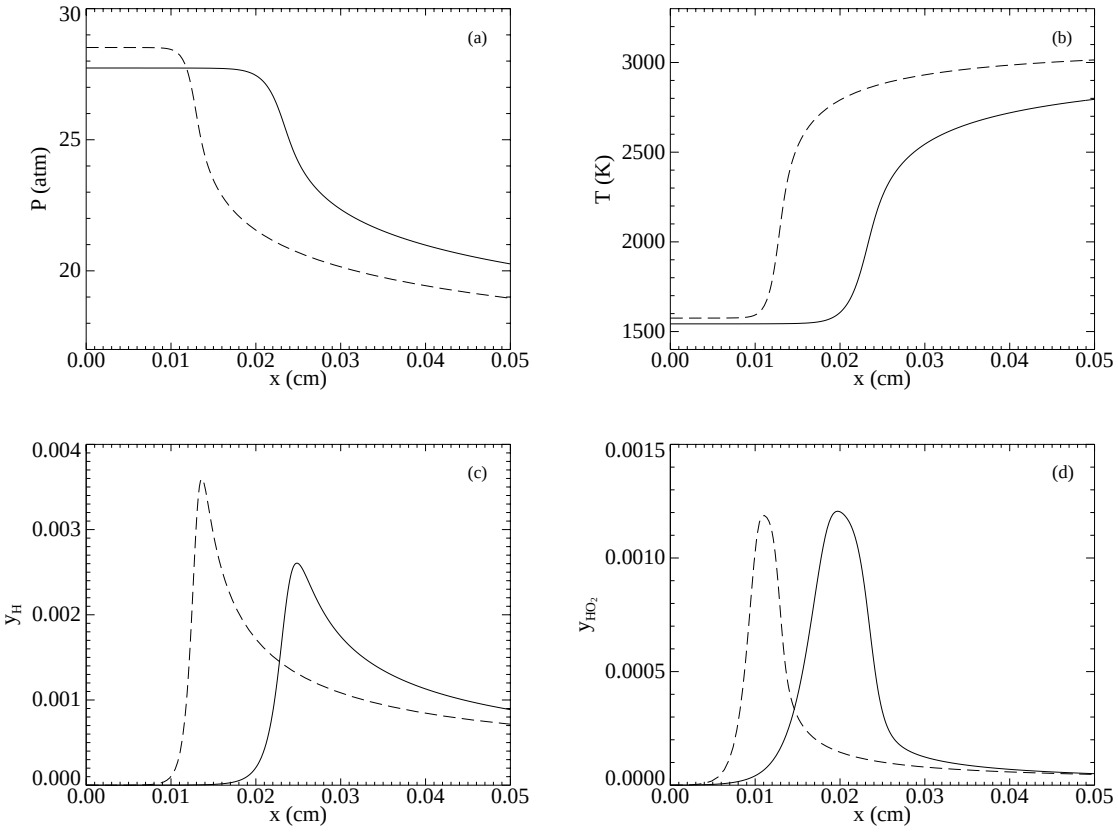

Figure 3.10: ZND calculation of a CJ detonation in stoichiometric H_2–air, initially at 1 atm and 300 K. Solid lines: detailed reaction mechanism; Dashed lines: three-step QSSA reduced mechanism. (a) Pressure; (b) Temperature; (c) Mass fraction of H; (d) Mass fraction of HO_2.

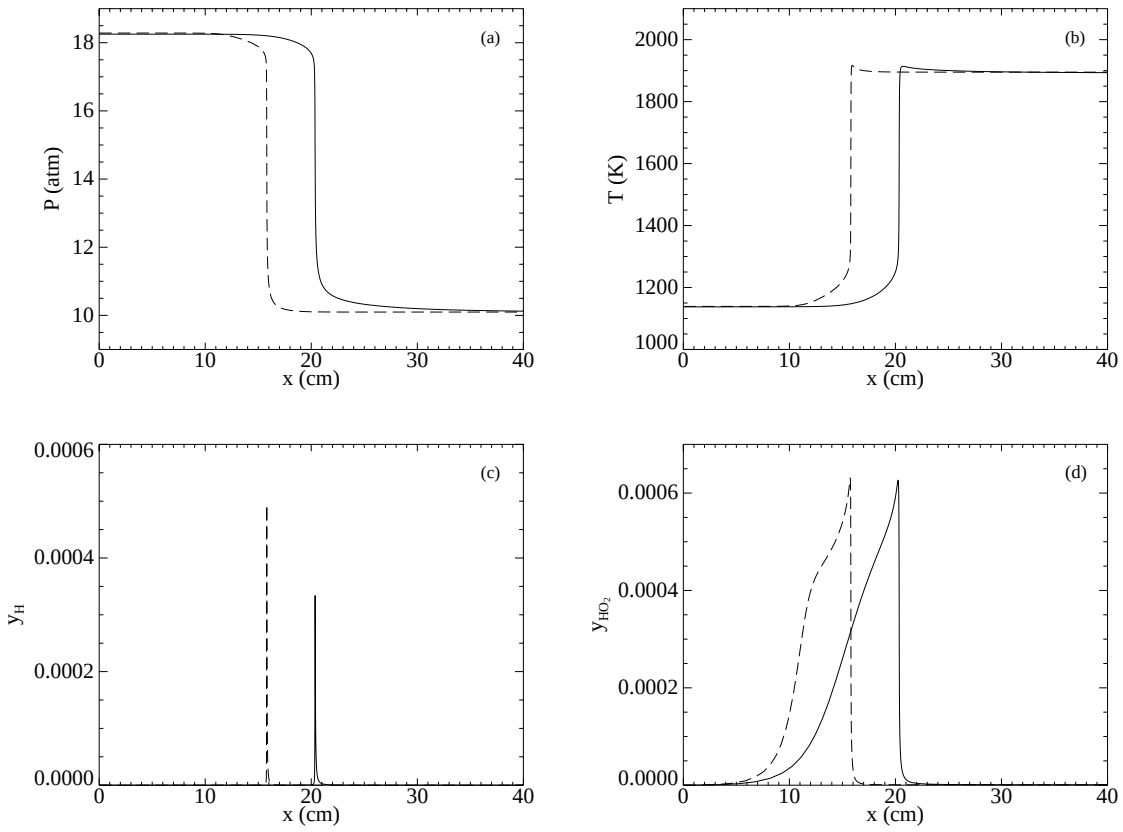

Figure 3.11: ZND calculation of a CJ detonation in lean (equivalence ratio = 0.6) H_2–O_2 with 75% N_2 dilution, initially at 1 atm and 300 K. Solid lines: detailed reaction mechanism; Dashed lines: three-step QSSA reduced mechanism. (a) Pressure; (b) Temperature; (c) Mass fraction of H; (d) Mass fraction of HO_2.

although only by about 25%. The species profiles show similar trends as the previous case.

The reduced mechanism ZND profiles in figures 3.10 and 3.11 are qualitatively very similar to those of Paczko and Klein (1993). They chose the same steady–state species, but their reduced reaction mechanism was slightly different since they removed several less important rates from the expressions for the reduced reaction rates and made different truncation approximations for the steady–state species concentrations.

The most important quantitative features of the ZND calculations are the CJ velocity and the induction length. They are plotted in figure 3.12 for H_2–air detonations over a range of stoichiometries. The induction length was defined as the location of maximum total thermicity, that is, the location of maximum energy release (see §2.2.1 for the definition of thermicity). It is almost identical to the location of maximum temperature gradient. Figure 3.12(a) demonstrates excellent agreement between the detailed and reduced mechanisms in the CJ detonation velocity, with the greatest error of about 1.5% occurring for near stoichiometric mixtures. Figure 3.12(b) shows that the error in induction length is more substantial. Again, the worst agreement is near stoichiometric, where the induction length is underpredicted by as much as a factor of two. However, given the many orders of magnitude variation with changing stoichiometry, this error might be considered acceptable.

The reduced mechanism ZND results presented until this point have not included any truncation of the algebraic steady–state relationships as described in §3.3.1. With a view towards computational efficiency in an unsteady CFD code, we next applied the aforementioned truncations to reduce the steady–state relations to explicit equations. This caused no change in the CJ velocity since the thermodynamics was unchanged, but the kinetic rate equations were modified. Figure 3.12(b) is repeated in figure 3.13 with the addition of the results for the reduced mechanism with truncation. Near stoichiometric and to the slightly rich side, there is little change, with the agreement between detailed and reduced mechanisms getting only slightly worse. But on the lean and very rich sides of stoichiometric, the induction length is much greater and the agreement is very poor. The assumptions made in the truncation were based on

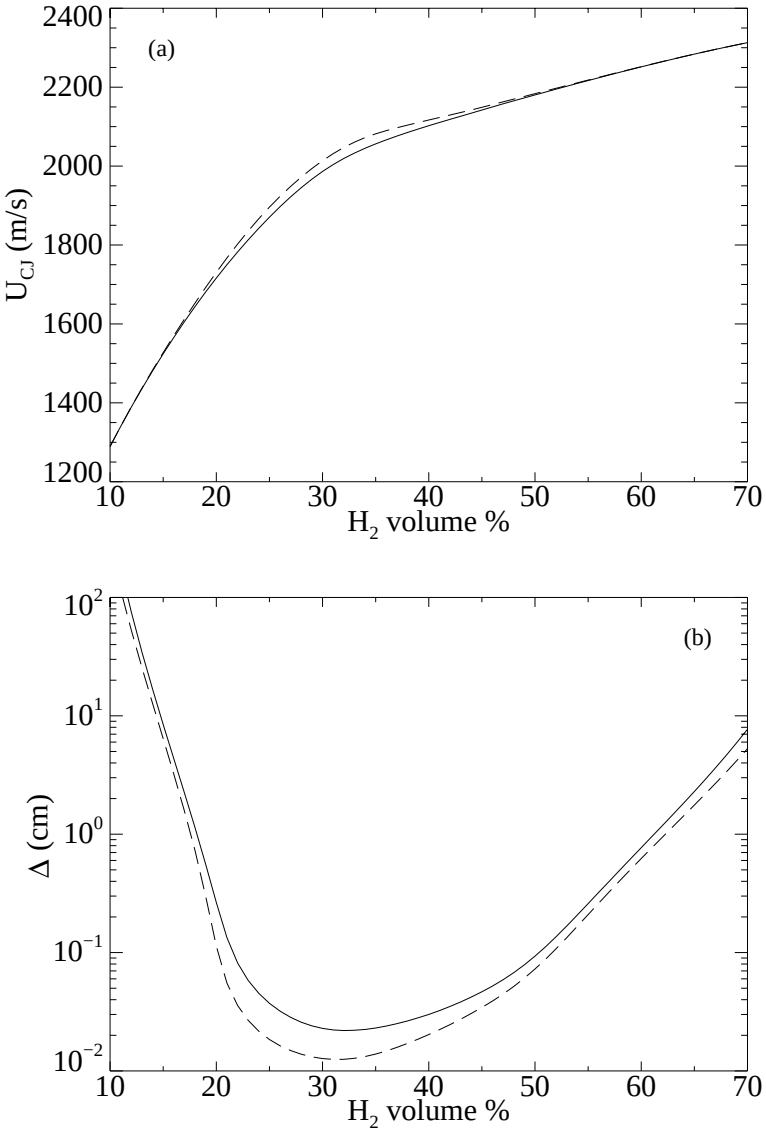

Figure 3.12: ZND calculations of CJ detonations in H_2–air, initially at 1 atm and 300 K. Solid lines: detailed reaction mechanism; Dashed lines: three-step QSSA reduced mechanism. (a) CJ detonation velocity; (b) Induction length.

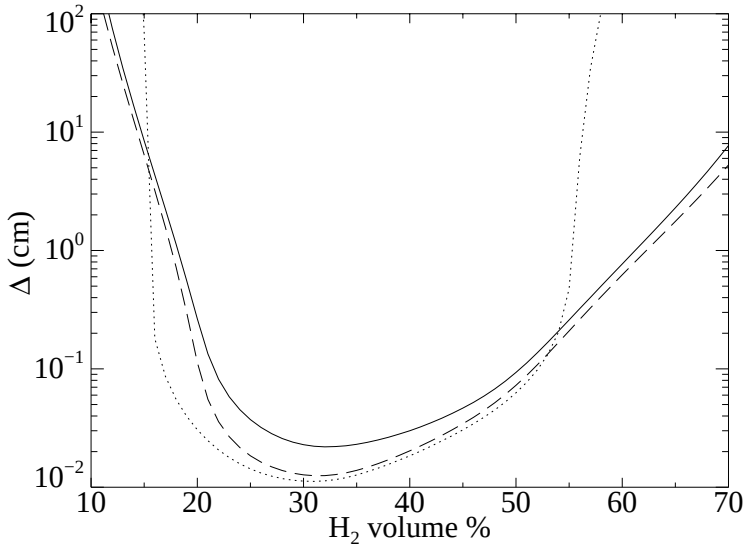

Figure 3.13: ZND induction lengths of CJ detonations in H_2–air, initially at 1 atm and 300 K. Solid line: detailed reaction mechanism; Dashed line: three-step QSSA reduced mechanism with no truncation of steady–state equations; Dotted line: three-step QSSA reduced mechanism with truncation of steady–state equations.

a near stoichiometric, chain branching ignition model problem. Figure 3.13 suggests that these assumptions are not correct for chain termination dominated ignitions. This demonstrates one of the weaknesses of this reduction technique. By simplifying the reduced mechanism for more efficient computation, we have reduced its range of applicability.

3.3.4 Validation in one-dimensional detonation simulations

The next validation of the QSSA reduced mechanism was comparison with detailed chemistry in unsteady one-dimensional detonation simulations. The model problem chosen was stoichiometric H_2–O_2 initially at 1 atm and 300 K. For computational efficiency, the algebraic steady–state relations were truncated as described in §3.3.1. This case is a chain branching ignition, so the truncation relations are valid, as described above.

Figure 3.14 shows the pressure behind the leading shock as a function of time, for a detonation with an overdrive factor of 1.4. This result can be directly compared to figure 3.4 for detailed chemistry. As in the detailed chemistry case, the reduced

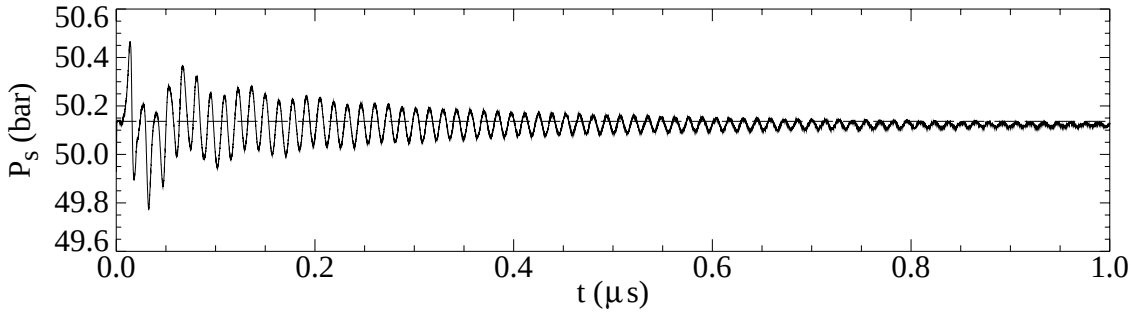

Figure 3.14: Shock pressure versus time, for a stable one-dimensional detonation in stoichiometric H_2–O_2, initially at 1 atm and 300 K, with $f = 1.4$, computed with the three-step QSSA reduced mechanism. $P_{vN} = 50.14$ bar. Finest grid level contains 100 cells per ZND induction length.

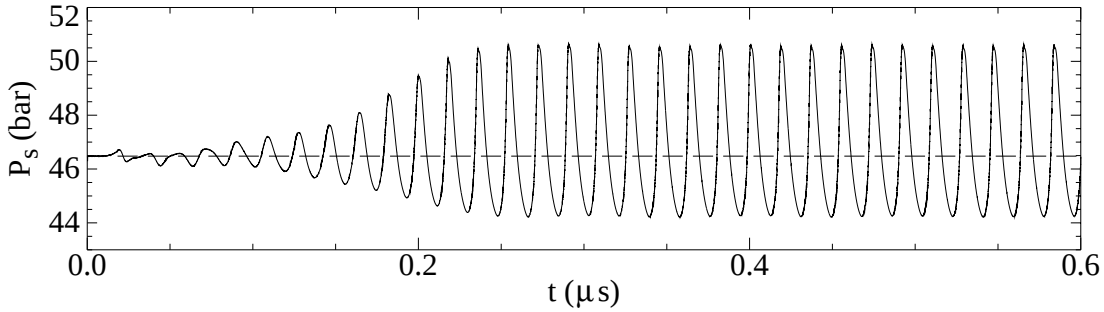

Figure 3.15: Shock pressure versus time, for a one-dimensional detonation in stoichiometric H_2–O_2, initially at 1 atm and 300 K, with $f = 1.3$, computed with the three-step QSSA reduced mechanism. $P_{vN} = 46.48$ bar. Finest grid level contains 200 cells per ZND induction length.

mechanism correctly predicts that this detonation is stable to small perturbations. However, the oscillations from the startup error disturbance take longer to die down, suggesting the reduced mechanism detonation is closer to the neutral stability limit and almost unstable.

When the overdrive factor is reduced to 1.3, the reduced mechanism detonation becomes unstable, as shown in figure 3.15. One unstable mode develops from the initial perturbation, as in figure 3.6 for detailed chemistry. However, the nonlinear oscillations grow more rapidly and the final periodic oscillations are greater in magnitude. This suggests that the reduced mechanism detonation is more unstable and thus further below the neutral stability limit, consistent with the previous observation regarding the $f = 1.4$ detonation.

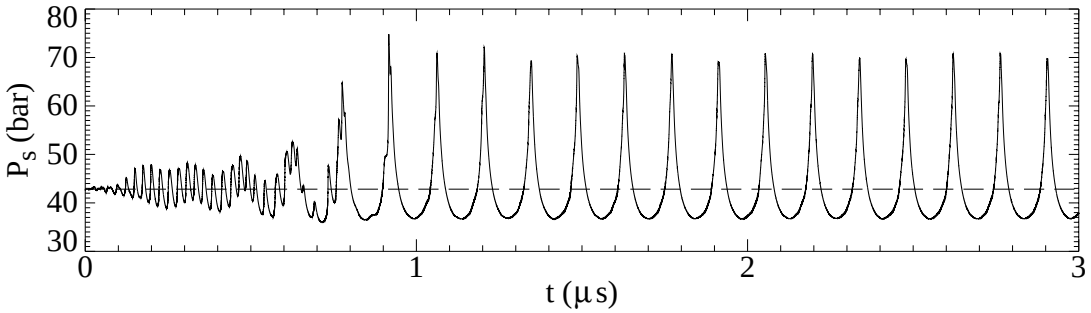

Figure 3.16: Shock pressure versus time, for a one-dimensional detonation in stoichiometric H_2–O_2, initially at 1 atm and 300 K, with $f = 1.2$, computed with the three-step QSSA reduced mechanism. $P_{vN} = 42.83$ bar. Finest grid level contains 200 cells per ZND induction length.

Finally, when the overdrive factor is reduced to 1.2, the reduced mechanism detonation develops two unstable modes, as shown in figure 3.16. This is consistent with the detailed chemistry simulation in figure 3.7. However, the final periodic oscillations are of greater magnitude. Additionally, the long period second mode appears to completely eliminate the first mode, unlike in the detailed chemistry simulation where the two modes co-exist in the final solution.

To check grid convergence and quantify the differences between the reduced and detailed mechanisms, the same numerical features of the $f = 1.3$ detonation were extracted as in the detailed chemistry case. Figure 3.17 shows this data for the reduced mechanism. It can be directly compared with figure 3.8 for the detailed mechanism. The data was taken for $t \geq 0.3\mu$s, where figure 3.15 shows the detonation has reached its final periodic configuration.

The plots of oscillation period and pressure turning points both suggest that the reduced mechanism simulation is grid converged for as few as 50 fine mesh cells per induction length. This represents a substantial improvement over the detailed mechanism where 150 cells were required. The improvement arises because the mechanism reduction removes some of the fastest chemical processes. Without these small temporal and spatial scales, the solution can be fully resolved on a coarser grid. This is one of the advantages of using reduced mechanisms.

The induction time τ for the reduced mechanism ZND solution with $f = 1.3$ was

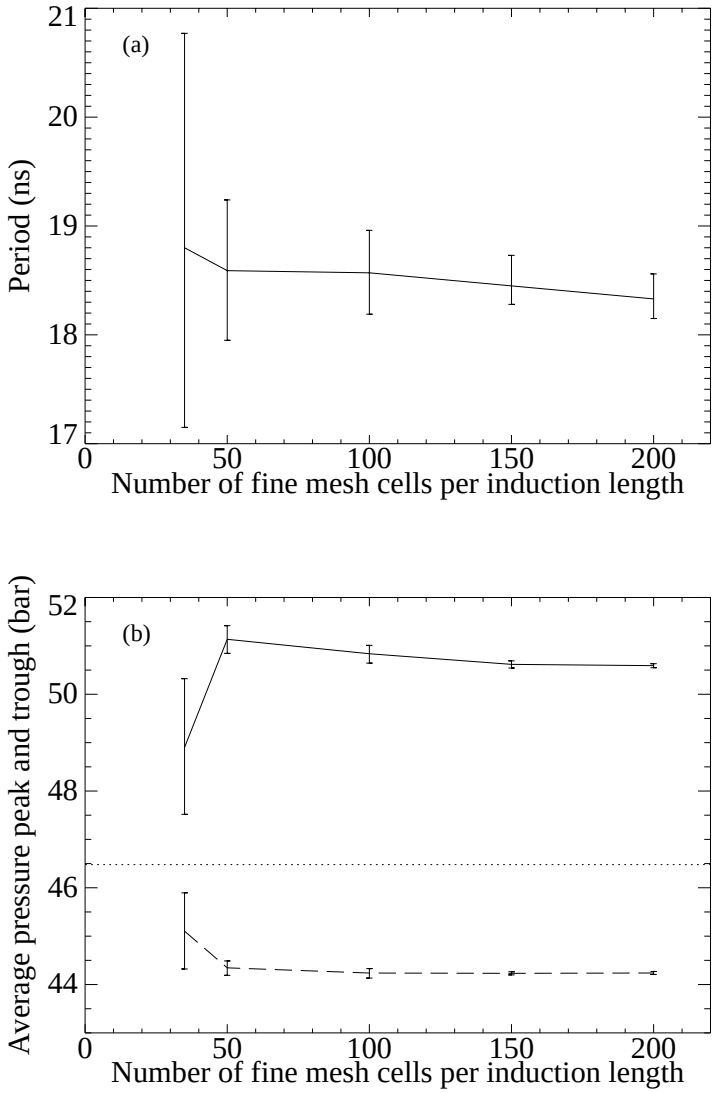

Figure 3.17: One-dimensional detonation in stoichiometric H_2–O_2, initially at 1 atm and 300 K, with $f = 1.3$, computed with the three-step QSSA reduced mechanism. (a) Period of oscillation. (b) Pressure peak (solid line) and trough (dashed line).

13.4 ns, so the oscillation period is about 1.37τ. This agrees extremely well with the value of 1.35τ found in the case of the detailed mechanism. So the difference between the oscillation periods in figures 3.17(a) and 3.8(a) can be attributed solely to the differences in the ZND induction time, which sets the scale for the unsteady solution. The magnitude of the oscillations can best be compared by computing the grid converged values of $\Delta P/P_{vN}$ where ΔP is the difference between the average pressure peak and trough. For the detailed mechanism in figure 3.8(b), this quantity is 0.076, while for the reduced mechanism in figure 3.17(b), it is 0.136. So the reduced mechanism overpredicts the oscillation magnitude by about 80%. This is consistent with the earlier observation that the reduced mechanism shifts the neutral stability limit to a greater overdrive factor for this mixture, so at a given overdrive less than the neutral stability limit, the detonation is more unstable.

3.3.5 Conclusions on the QSSA method

The QSSA reduced mechanism for H_2–O_2 developed in this section offers the following benefits over using detailed chemistry. It is significantly more computationally efficient, taking about 70% less Central Processing Unit (CPU) time to propagate a detonation a given number of induction lengths, with the same number of fine mesh cells per induction length. This speed-up could be further improved by fitting the reduced reaction rates (3.13) to simple empirical expressions, although this is a process difficult to generalize to all reactive systems. The relative improvement in CPU time is further enhanced by noting that a coarser grid in the reduced mechanism computation will give the same effective resolution as a fine grid in the detailed mechanism case. Compared with other options for mechanism reduction, the QSSA technique offers the advantage of simplicity, at least for small chemical systems such as hydrogen.

However, the QSSA method also suffers from a number of problems that have been identified in this work. The CJ detonation velocity was accurately predicted by the reduced system, but the induction length was in error by as much as a factor of two.

In an effort to improve this error, we also developed a four-step QSSA reduced mechanism by removing the steady–state assumption from the chain branching radical OH. This reduced the maximum error in induction length to 27% for the H_2–air mixtures considered in figure 3.12(b). While this is a significant improvement, a reduction from six degrees of freedom to four is not sufficient to give much computational savings, so this is not an acceptable approach. Paczko and Klein (1993) suggested improving the three-step mechanism by replacing the H radical with a lumped chain branching radical pool. The steady–state relations for the chain branching radicals were replaced by higher order asymptotic equations. While this approach also gave great improvement in the computed induction lengths, it is not a method easily extensible to more complex chemical systems. Hence, we do not consider this an acceptable alternative for developing a general mechanism reduction capability. A further error produced by the reduced mechanism was revealed by the unsteady detonation simulations. The neutral stability limit was shifted such that the magnitude of the nonlinear instability of a single unstable mode detonation was overpredicted by 80%.

The QSSA technique also suffers from a number of implementation difficulties. It requires considerable experience with a given chemical system to know *a priori* which species are likely to be in steady–state. In the absence of this knowledge, the determination of the steady–state species is a lengthy process which is not easily generalized, and is prohibitively difficult for large chemical systems. It involves the examination of results for a selection of model problems, and the derived reduced mechanism will thus be somewhat optimized to those model problems. Care must be taken to ensure the reduced mechanism is not applied at conditions far outside those considered in the model problems. To enhance computational efficiency, the algebraic steady–state relations typically have to be truncated, as was done here. This was found to further reduce the range of validity of the reduced mechanism. As a result of the problems with the QSSA method identified in this work, we decided not to pursue this technique further in gaseous detonation simulations.

3.4 Intrinsic Low-Dimensional Manifolds

The method of Intrinsic Low-Dimensional Manifolds (ILDM) is considerably more complicated than the QSSA method described in the previous section, but offers a number of advantages. It is intended to be an automated reduction technique that requires no user input other than a starting detailed reaction mechanism and the desired number of degrees of freedom in the reduced system. A locally optimized reduced system is computed at each thermodynamic state in a given domain, thus avoiding the problem of applying a single global reduced mechanism at states for which it was not designed. The parameterized reduced system is tabulated in a lookup table for later use in a CFD code. An explicit reduced mechanism is not produced, but the method is designed to permit efficient, accurate CFD computations.

The ILDM technique was developed by Maas and Pope (1992a,b). It was originally developed for use in low-speed flame calculations that couple fluid mechanics, chemistry, and transport processes such as diffusion and viscosity. Previous results have shown it to be highly successful in the simulation of adiabatic homogeneous systems (Maas and Pope, 1992b), perfectly stirred reactors (Maas and Pope, 1992a), laminar one-dimensional premixed flames (Maas and Pope, 1994; Eggels and DeGoey, 1995a,b; Eggels et al., 1997; Schmidt et al., 1996, 1998), laminar one-dimensional diffusion flames (Blasenbrey et al., 1998), turbulent premixed flames (Gicquel et al., 1999) and turbulent diffusion flames (Norris and Pope, 1995; Nau et al., 1996; Nooren et al., 1997; Xiao et al., 1998).

Until now, ILDMs have not been successfully applied to detonations. The potential application to detonations introduces a number of differences from flame calculations. On the one hand, they are somewhat simpler since transport processes are typically neglected in detonation simulations. This removes the difficulties of computing the projection of the diffusion terms onto the manifold (Maas and Pope, 1992a; Blasenbrey et al., 1998) and the extra lookup table dimensions arising from variation of the elemental composition. On the other hand, detonations have the complication of an additional timescale, the induction time, that must be resolved in the calcula-

tion. The induction time is typically shorter than the flow timescales, increasing the necessary size of the resolved slow subspace.

3.4.1 Theoretical method

The following description of the ILDM theory mostly follows that of Maas and Pope (1992b). It is included here for completeness, to highlight the differences in detonation applications, and to define our implementation of the method since several variants now exist in the literature.

The ILDM method is based on dynamical systems theory. From numerical simulations of chemically reacting systems with detailed chemistry, the empirical observation can be made that these systems are rapidly attracted to low-dimensional manifolds in the chemical state space. Fast chemical processes relax towards the manifold and slow processes represent movements tangential to the manifold. If the equilibration of the fast processes and subsequent collapse onto the low-dimensional manifold occurs faster than the shortest timescale of interest in the flow, then the chemical system can be approximated as lying only on the manifold. This greatly reduces the number of degrees of freedom of the reactive system. The location of the low-dimensional manifold is computed as follows.

The ODEs representing the thermochemistry in the reactive step of a compressible CFD code were described in §3.2.1. They are precisely the equations of a homogeneous, adiabatic, constant volume reaction, and can be written in the following form:

$$\frac{\mathrm{d}\boldsymbol{\psi}}{\mathrm{d}t} = \boldsymbol{f}(\boldsymbol{\psi}), \tag{3.17}$$

where

$$\boldsymbol{\psi} = (\rho, e, \phi_1, \phi_2, \ldots, \phi_{n_s})^T, \qquad \phi_k = \frac{y_k}{W_k},$$
$$\boldsymbol{f} = \left(0, 0, \frac{\dot{\omega}_1(\boldsymbol{\psi})}{\rho}, \frac{\dot{\omega}_2(\boldsymbol{\psi})}{\rho}, \ldots, \frac{\dot{\omega}_{n_s}(\boldsymbol{\psi})}{\rho}\right)^T.$$

ϕ_k is the specific mole number of species k. The form of $\boldsymbol{f}$ given above is that for a

system of ideal gases, although the technique described below is not constrained to a particular equation of state. The inclusion of the thermodynamic variables ρ and e in the state vector $\boldsymbol{\psi}$ appears trivial since they are conserved quantities in this case, but they are included here with a mind to the eventual CFD application where they will be variables and will be necessary to define the full thermochemical state of the fluid. Equation (3.17) differs from the original formulation of Maas and Pope (1992b) in that their homogeneous system was an adiabatic, constant pressure reaction, with the state vector containing pressure and enthalpy as the independent thermodynamic variables. This is the natural choice for low-speed combustion, but density and energy are the natural choice for high-speed compressible reacting flow.

In addition, there are n_e element conservation constraints,

$$\chi_j = \sum_{k=1}^{n_s} \mu_{kj}\phi_k, \qquad j = 1, \ldots, n_e,$$

where μ_{kj} is the number of atoms of element j in species k, and χ_j is the specific element mole number of element j. For a premixed diffusionless fluid, such as that in a detonation, the χ_j are constant and uniform throughout. With the additional two constraints of ρ and e constant, there are a total of $2 + n_e$ conserved variables, so the $2 + n_s$-dimensional state space in (3.17) has $n_s - n_e$ degrees of freedom.

The individual chemical processes inherent in this system can be extracted by an eigen-analysis of the Jacobian $\boldsymbol{f}_{\boldsymbol{\psi}}$. The inverse of the real parts of the eigenvalues are the $2 + n_s$ different timescales associated with movement in the state space. The eigenvectors are the corresponding directions of movement, and in general are composed of linear combinations of species. $2 + n_e$ of the eigenvalues are zero, having eigenvectors corresponding to the conserved variables.

The low-dimensional manifold is defined by the points in the state space for which the rate vector $\boldsymbol{f}$ is perpendicular to the $n_s - n_e - n_r$ eigenvectors associated with the fastest relaxing timescales (most negative eigenvalues). n_r is the user-prescribed dimension of the manifold, that is, the number of degrees of freedom desired in the reduced system. This is the one parameter that must be provided by the user. An

appropriate choice is not always simple, but can be made by comparing the eigenvalues of the Jacobian at various states in a model problem with the timescales of the flow in the final application.

In practice, the eigenvectors are often ill-conditioned, with several being almost degenerate. To avoid the numerical difficulties associated with near degenerate eigenvectors, we use an alternative basis given by the real Schur vectors of the Jacobian, as suggested by Maas and Pope (1992b). The real Schur decomposition is defined as

$$Q^T \boldsymbol{f}_{\boldsymbol{\psi}} Q = T.$$

T is quasi-upper triangular with eigenvalues of $\boldsymbol{f}_{\boldsymbol{\psi}}$ (or 2×2 complex eigenvalue blocks) on the diagonal, sorted in order of descending real part. The columns of Q are the real Schur vectors and have the advantage over the eigenvectors of being orthogonal. Then the manifold is defined by

$$\mathbf{0} = Q_L^T(\boldsymbol{\psi})\, \boldsymbol{f}(\boldsymbol{\psi}), \tag{3.18}$$

where Q_L^T is the $(n_s - n_e - n_r) \times (2 + n_s)$ lower sub-matrix of Q^T corresponding to the fast subspace of the system at the state $\boldsymbol{\psi}$.

3.4.2 Numerical solution of the manifold

While the theoretical definition of the manifold is elegantly simple, the numerical solution of manifold points in the state space is far more complicated. The equation system (3.18) contains $2 + n_s$ unknowns and only $n_s - n_e - n_r$ equations, so it is incomplete. The system must be closed by the addition of $2 + n_e + n_r$ auxiliary equations. $2 + n_e$ of these are readily available from the conservation of ρ, e and $\boldsymbol{\chi}$:

$$0 = \rho - \vartheta_\rho, \tag{3.19a}$$

$$0 = e - \vartheta_e, \tag{3.19b}$$

$$0 = \chi_j(\boldsymbol{\phi}) - \vartheta_{\chi_j}, \qquad j = 1, \ldots, n_e, \tag{3.19c}$$

where $\boldsymbol{\vartheta} = (\vartheta_\rho, \vartheta_e, \vartheta_{\chi_1}, \vartheta_{\chi_2}, \ldots, \vartheta_{\chi_{ne}})^T$ are the conserved parameters of the system. The remaining n_r equations represent a parameterization of the manifold, defined in terms of a set of n_r variable parameters, $\boldsymbol{\theta}$, that may be thought of as reaction progress variables. This parameterization is somewhat arbitrary but must ensure uniqueness of the mapping from reduced to detailed chemistry, $\boldsymbol{\psi}(\vartheta_\rho, \vartheta_e, \boldsymbol{\theta})$. Maas and Pope (1992b) suggest that uniqueness is best guaranteed by choosing the mole numbers of major product species as parameters. Then the parameterization could be expressed as

$$0 = \phi_{k_i} - \theta_i, \qquad i = 1, \ldots, n_r, \tag{3.20}$$

where k_i is the index of the corresponding species.

Overall, the $2 + n_e + n_r$ auxiliary equations given by (3.19) and (3.20) may be written as

$$\mathbf{0} = \boldsymbol{p}(\boldsymbol{\psi}; \boldsymbol{\theta}, \boldsymbol{\vartheta}), \tag{3.21}$$

and the complete equation system for the manifold is

$$\mathbf{0} = \boldsymbol{g}(\boldsymbol{\psi}; \boldsymbol{\theta}, \boldsymbol{\vartheta}) = \begin{pmatrix} Q_L^T(\boldsymbol{\psi})\, \boldsymbol{f}(\boldsymbol{\psi}) \\ \boldsymbol{p}(\boldsymbol{\psi}; \boldsymbol{\theta}, \boldsymbol{\vartheta}) \end{pmatrix}. \tag{3.22}$$

For example, in an H_2–O_2–N_2 system with $n_s = 9$ species, appropriate choices for the parameterizing species of a two-dimensional ILDM ($n_r = 2$) might be H_2O and H_2. The manifold equations would then be

$2 + n_s = 11$ equations

$$\left\{ \begin{array}{ll} \mathbf{0} = Q_L^T(\boldsymbol{\psi})\, \boldsymbol{f}(\boldsymbol{\psi}) & n_s - n_e - n_r = 4 \text{ equations} \\ \left.\begin{array}{l} 0 = \rho - \vartheta_\rho \\ 0 = e - \vartheta_e \end{array}\right\} & 2 \text{ equations} \\ \left.\begin{array}{l} 0 = \chi_{\mathrm{H}}(\boldsymbol{\phi}) - \vartheta_{\mathrm{H}} \\ 0 = \chi_{\mathrm{O}}(\boldsymbol{\phi}) - \vartheta_{\mathrm{O}} \\ 0 = \chi_{\mathrm{N}}(\boldsymbol{\phi}) - \vartheta_{\mathrm{N}} \end{array}\right\} & n_e = 3 \text{ equations} \\ \left.\begin{array}{l} 0 = \phi_{\mathrm{H_2O}} - \theta_1 \\ 0 = \phi_{\mathrm{H_2}} - \theta_2 \end{array}\right\} & n_r = 2 \text{ equations} \end{array} \right.$$

In this work, the Schur decomposition of the Jacobian was computed with LAPACK (Anderson et al., 1995) and a version of BLAS optimized for Pentium-class Linux systems (Henry et al., 1999). CHEMKIN (Kee et al., 1989) was used for evaluation of the thermochemistry.

The manifold equations (3.22) were solved using one of two methods. The first method utilized the code PITCON (Rheinboldt and Burkardt, 1983), a one-dimensional arc-length continuation code. Given a solution point on a one-dimensional manifold, PITCON predicts the location of a neighboring solution point by approximating the local slope of the manifold, then uses Newton's method to correct the point. The advantage of using an arc-length continuation method over a standard Newton technique is that solutions can still be found along the curve near turning points, where the user-prescribed parameterization becomes poor. One of the parameterizing equations in (3.20) was omitted in each call to PITCON, with the other parameters held fixed. PITCON used the remaining degree of freedom to control the continuation process and find the next target point. When a multi-dimensional ILDM was required, repeated calls were made with different parameterization equations successively omitted so that the continuation process advanced in different axis directions of the $\boldsymbol{\theta}$ phase space. In this way, a Cartesian grid of solution points in the $\boldsymbol{\theta}$ space was gradually mapped out.

For CFD applications, it was necessary to extend this arc-length continuation method to compute the manifold in a domain that also involved a range of thermodynamic states. To achieve this, PITCON was also called with the density constraint (3.19a) or energy constraint (3.19b) as the omitted equation, allowing variation of those variables in addition to the variation of $\boldsymbol{\theta}$ described above. In this case, we were actually solving for a manifold in $(\vartheta_\rho, \vartheta_e, \boldsymbol{\theta})$ space. Such a manifold has dimension $2 + n_r$, since n_r denotes only the number of reduced chemical degrees of freedom.

The code PITCON requires calculation of not only $\boldsymbol{g}$ in (3.22) but also the partial derivatives $\boldsymbol{g}_{\boldsymbol{\psi}}$. No analytical prescription exists for $\partial Q/\partial \boldsymbol{\psi}$, so it must be computed numerically using finite differences. For even just a first-order one-sided difference,

$2 + n_s$ evaluations of Q would be required, one for each k in $\partial Q/\partial \psi_k$. The Schur decomposition required to compute Q is a tedious calculation, so the multiple evaluations would be very time consuming. Maas (1998) suggested an approximation that could greatly reduce this time. Since Q is usually only a weak function of $\boldsymbol{\psi}$ while $\boldsymbol{f}$ varies strongly with $\boldsymbol{\psi}$, then

$$\frac{\partial}{\partial \boldsymbol{\psi}} \left(Q_L^T \boldsymbol{f} \right) \approx Q_L^T \boldsymbol{f}_{\boldsymbol{\psi}},$$

and hence,

$$\boldsymbol{g}_{\boldsymbol{\psi}} \approx \begin{pmatrix} Q_L^T \boldsymbol{f}_{\boldsymbol{\psi}} \\ \boldsymbol{p}_{\boldsymbol{\psi}} \end{pmatrix}.$$

This is extremely fast to evaluate since Q and $\boldsymbol{f}_{\boldsymbol{\psi}}$ are already available from the original Schur decomposition to compute $\boldsymbol{g}$. Although this method does not successfully compute the continuation target points as often as complete numerical differentiation of $\boldsymbol{g}$, it is so much more efficient that it was viewed as a preferable alternative.

On the rare occasions when the approximate arc-length continuation process failed, the following slower but more robust technique was used. It is based on a pseudo time-stepping method proposed by Maas (1998). Consider the following system of ODEs:

$$Q_L^T(\boldsymbol{\psi}) \frac{\mathrm{d}\boldsymbol{\psi}}{\mathrm{d}t} = Q_L^T(\boldsymbol{\psi})\, \boldsymbol{f}(\boldsymbol{\psi}), \tag{3.23a}$$

$$\boldsymbol{p}_{\boldsymbol{\psi}} \frac{\mathrm{d}\boldsymbol{\psi}}{\mathrm{d}t} = \boldsymbol{0}, \tag{3.23b}$$

where (3.23b) is obtained by differentiating (3.21) with respect to time at fixed parameters $\boldsymbol{\theta}$ and $\boldsymbol{\vartheta}$. Given a desired target point $(\vartheta_\rho, \vartheta_e, \boldsymbol{\theta})$ and a reasonable initial guess for $\boldsymbol{\psi}$ that satisfies (3.21), if (3.23) is integrated forward in time until reaching steady–state ($t \to \infty$), then (3.23a) will reduce to (3.18) and $\boldsymbol{\psi}$ will be a solution of the system (3.22). The system of ODEs (3.23) is in general stiff, so it was integrated with the implicit backward differentiation integrator DEBDF (Shampine and Watts, 1979). Evaluation of the derivatives $\mathrm{d}\boldsymbol{\psi}/\mathrm{d}t$ for the integrator was achieved as follows.

At a particular point $\boldsymbol{\psi}$, (3.23) is a system of linear equations in the variables $\mathrm{d}\boldsymbol{\psi}/\mathrm{d}t$. It can be written symbolically as

$$A\frac{\mathrm{d}\boldsymbol{\psi}}{\mathrm{d}t} = \boldsymbol{b},$$

where A and $\boldsymbol{b}$ are a matrix and vector of constant scalars, for a given point $\boldsymbol{\psi}$. The solution of this linear system can be written conceptually as

$$\frac{\mathrm{d}\boldsymbol{\psi}}{\mathrm{d}t} = A^{-1}\boldsymbol{b}.$$

In practice, it was solved by LU decomposition.

The solution of low-dimensional manifolds is also complicated by the fact that there are regions where (a) the solution is unphysical (such as negative quantities of some species), or (b) no manifold solution exists. In general, neither of these regions is known *a priori*. So the solution technique must identify the boundaries of these regions as it proceeds. In addition, there will be user-prescribed domain boundaries, given some knowledge of what parts of the state space are likely to be visited in a practical application. The final boundary of the computed manifold will be a combination of these physical, intrinsic and user-prescribed boundaries.

The solution algorithm adopted for a multi-dimensional ILDM was as follows:

1. Divide the parameter domain up into a multi-dimensional regular Cartesian grid, with some prescribed grid spacing and boundaries.

2. Find one point on the manifold, such as the equilibrium point at some value of density and energy in the domain. The equilibrium point is a zero-dimensional manifold (for fixed thermodynamic state), so it will always be part of an n_r-dimensional manifold for $n_r > 0$.

3. Use the arc-length continuation technique to move from this first point to a nearby grid point.

4. Loop over the following steps:

(a) Find a grid point in the domain which has already been solved, is not a boundary point and does not have all its neighbors also solved. Neighbors are defined as points with Cartesian grid co-ordinates differing by ± 1 in one parameter direction only, and lying within the user-prescribed domain.

(b) Use the arc-length continuation technique or pseudo time-stepping technique to find all unsolved neighbors of this point. Where a physical or intrinsic boundary is found between the point and its neighbor, use the neighbor's logical address to store this irregular (non-Cartesian) boundary point instead.

(c) When no more points of the type described in (a) exist, exit the loop.

5. Write each grid point to a file for later use in a table lookup. At each point, output the logical co-ordinates, physical parameters $(\vartheta_\rho, \vartheta_e, \boldsymbol{\theta})$, pressure, temperature, reaction rates of the parameterizing species $\mathrm{d}\boldsymbol{\theta}/\mathrm{d}t$, full composition $\boldsymbol{\phi}$, and partial derivatives of pressure $(\partial P/\partial\vartheta_\rho, \partial P/\partial\vartheta_e, \partial P/\partial\boldsymbol{\theta})$.

The reaction rates were simply the rates of the corresponding species in the detailed reaction:

$$\frac{\mathrm{d}\theta_i}{\mathrm{d}t} = \bar{f}_i(\vartheta_\rho, \vartheta_e, \boldsymbol{\theta}) = f_{2+k_i}\left(\boldsymbol{\psi}(\vartheta_\rho, \vartheta_e, \boldsymbol{\theta})\right). \tag{3.24}$$

The pressure partials were needed later in the convective step of the CFD code for the calculation of sound speed and the eigenvectors of the Euler equations' Jacobian. In this reduced chemistry system, no analytical prescription of the partial derivatives exists, akin to the equations (3.11) in the detailed chemistry system. Hence, they had to be determined by numerical finite differences of the pressure. This could have been done by simply differencing neighboring grid points, but this would be highly inaccurate if the grid was coarse. Thus we chose to use the arc-length continuation process to compute manifold points a small distance either side of the grid points, in each of the parameter directions, and use the computed pressures to calculate the pressure partial derivatives at the grid points. Second-order central differencing was

used, giving expressions such as

$$\frac{\partial P}{\partial \theta_1} = \frac{P(\vartheta_\rho, \vartheta_e, \theta_1 + \delta_{\theta_1}, \theta_2, \ldots, \theta_{n_r}) - P(\vartheta_\rho, \vartheta_e, \theta_1 - \delta_{\theta_1}, \theta_2, \ldots, \theta_{n_r})}{2\delta_{\theta_1}},$$

and similarly for the other partial derivatives. An appropriate choice for the small perturbations such as δ_{θ_1} was found to be 1% of the regular Cartesian grid spacing in that co-ordinate direction. At manifold boundaries, solutions could not always be found on both sides of the grid point. In these cases, first-order single-sided differencing was used. The use of small perturbations for the numerical differences, rather than just the neighboring grid points, increased the total CPU time of the ILDM code by a factor of two or three. However, the greatly increased accuracy of the pressure partials warranted the extra computational effort.

The original table storage algorithm proposed by Maas and Pope (1992a) utilized adaptive grid refinement to place more grid points in regions where the reaction rates varied sharply, and thus increase the accuracy of the table lookup interpolation. As will be discussed later in §3.4.4, this was not deemed to be very beneficial in this detonation work, and so was not implemented. The possibility of adaptive grid refinement being necessary for other detonation systems remains an area of future study.

3.4.3 Verification of the ILDM code

The ILDM code was first used to compute one and two-dimensional manifolds of a CO–H_2–air system studied by Maas and Pope (1992b) in their original work. This was a homogeneous adiabatic constant pressure system, so it was necessary to use pressure and enthalpy as the thermodynamic variables in the state variable $\boldsymbol{\psi}$, rather than density and energy as described above, but the necessary changes to the code were very minor. The detailed reaction mechanism used was that listed in Maas and Pope (1992b). It contained $n_s = 13$ species and 67 irreversible reactions. With $n_e = 4$ elements, the detailed chemistry system had nine degrees of freedom.

Figure 3.18 shows the computed one-dimensional manifold for this system, pro-

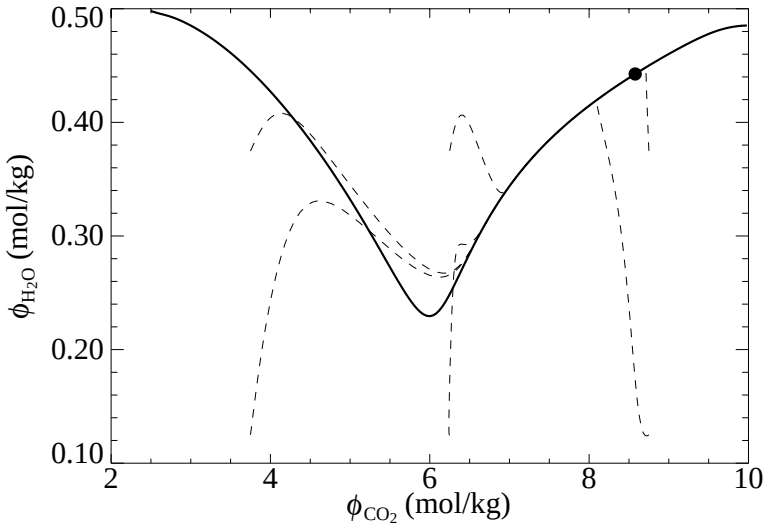

Figure 3.18: Adiabatic constant pressure reaction in mixtures with the same elemental composition as stoichiometric CO–H_2–air, and with $P = 1$ bar, $h = -1$ MJ/kg. —— One-dimensional ILDM; – – – sample reaction trajectories; • equilibrium point.

jected from the 13-dimensional composition space down onto a two-dimensional plane showing the mole numbers of CO_2 and H_2O. It is simply plotted in this reduced space for visualization purposes. The variable ϕ_{CO_2} was used as the single reaction progress parameter θ_1, although the computed manifold is independent of this choice. Also shown on this plot are some sample constant pressure reaction trajectories in mixtures all having the same pressure, enthalpy and elemental composition (and hence the same equilibrium point) but different initial molecular compositions. As expected, the reaction trajectories all collapse onto the one-dimensional manifold before slowly completing reaction to equilibrium. The plot agrees perfectly with that of Maas and Pope (1992b), after correction of an error in their originally published work (Maas, 1999).

The two-dimensional manifold for the same system is shown in figure 3.19. The parameterizing species were the major products CO_2 and H_2O, and an example third species, H, is shown in the figure. The relation $\phi_H(\phi_{CO_2}, \phi_{H_2O})$ is a unique mapping, as are the relations for the other ten dependent species, so this was a suitable choice for the parameterization. The earlier one-dimensional manifold is also shown in this figure. It lies on the two-dimensional manifold since it is a subspace of the two-

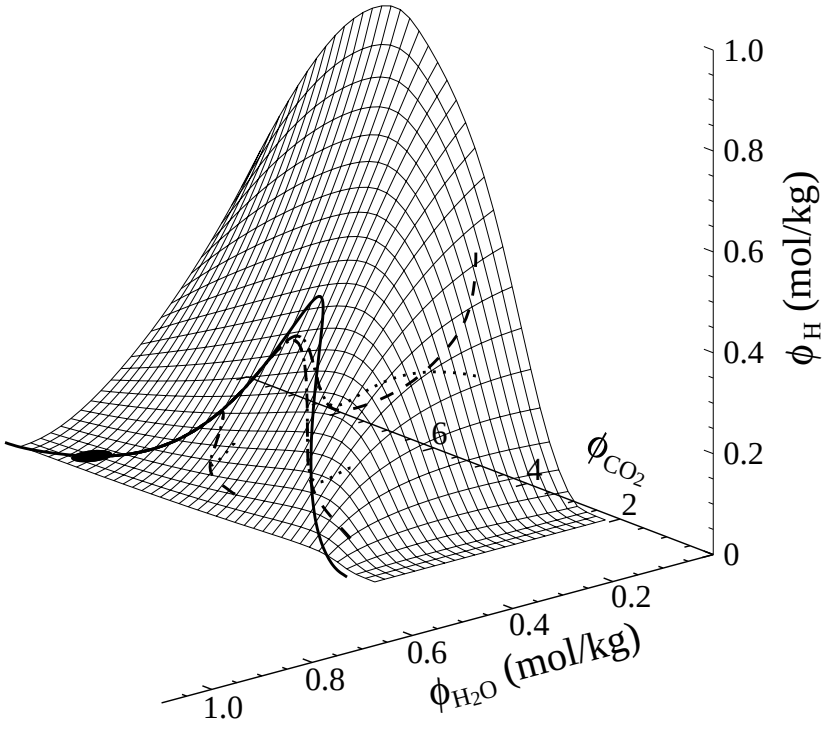

Figure 3.19: Adiabatic constant pressure reaction in mixtures with the same elemental composition as stoichiometric CO–H_2–air, and with $P = 1$ bar, $h = -1$ MJ/kg. Surface: two-dimensional ILDM; —— one-dimensional ILDM; – – – sample reaction trajectories; ····· vertical projection of reaction trajectories onto two-dimensional ILDM; • equilibrium point.

dimensional manifold. As before, some sample reaction trajectories are shown. To visualize the distance of the reaction trajectories away from the manifold, the vertical projections of the trajectories onto the two-dimensional manifold are also shown. Except for perhaps the far right trajectory, all the trajectories collapse onto the two-dimensional manifold very quickly, indicating that this is an appropriate choice of manifold dimension. At a later time, the trajectories then collapse onto the one-dimensional manifold, demonstrating a cascade of manifolds in time. For the far right trajectory, there is considerable discrepancy between the reaction trajectory and the manifold for a lengthy portion of the trajectory, suggesting a higher dimensional manifold may be necessary when the initial conditions are towards the right of the figure. The qualitative agreement with the two-dimensional manifolds published by Maas and Pope (1992b) is excellent, again verifying the correct manifold solution by the code.

3.4.4 Implementation and validation in constant volume combustion

The ILDM method presented in §3.4.1 is formulated for the ODEs governing constant volume or constant pressure reaction, rather than those governing ZND detonation. So the method was not implemented in a ZND code and a ZND validation study like that for the QSSA reduced mechanism in §3.3.3 was not performed for the ILDM method. Instead, initial validations of the ILDM technique were performed with adiabatic constant volume combustion calculations. Implementation in such a code is appropriate since the eventual implementation in the chemistry source term step of a CFD code is precisely an adiabatic constant volume process.

The example selected for the constant volume validation study was stoichiometric H_2–air, at a density $\rho = 4.58$ kg/m^3 and an internal energy $e = 1.28$ MJ/kg. These thermodynamic conditions approximately correspond to the von Neumann state of a CJ detonation in the mixture, so the induction region will be similar to that in the first ZND validation study of the earlier QSSA model (see figure 3.10). As for the QSSA model, the starting detailed reaction mechanism was from Maas and Warnatz

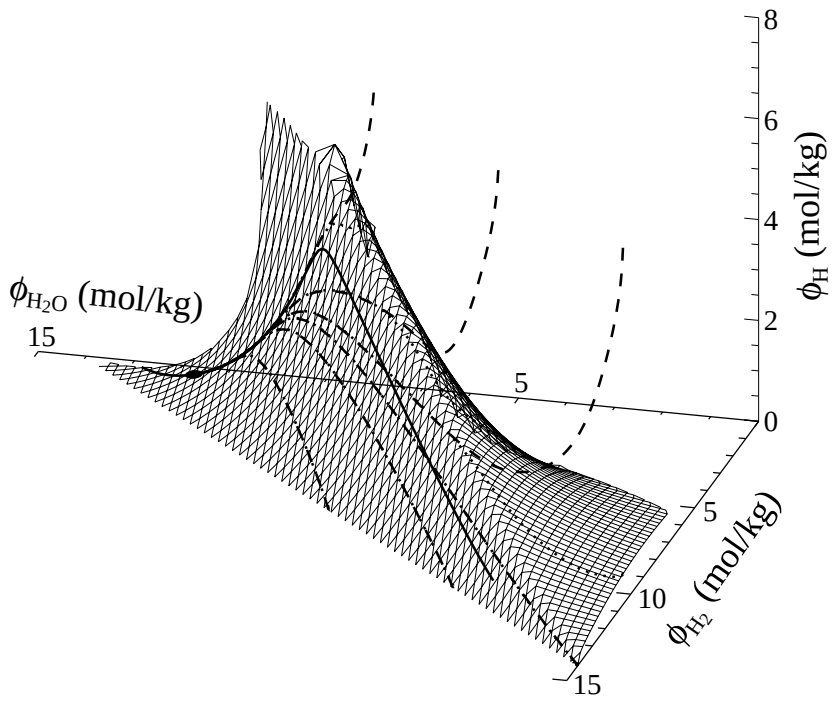

Figure 3.20: Adiabatic constant volume reaction in mixtures with the same elemental composition as stoichiometric H_2–air, and with $\rho = 4.58$ kg/m^3, $e = 1.28$ MJ/kg. Surface: two-dimensional ILDM; —— one-dimensional ILDM; – – – sample reaction trajectories; ····· vertical projection of reaction trajectories onto two-dimensional ILDM; • equilibrium point.

(1988).

The constant volume two-dimensional ILDM for this mixture, at the specified density and energy, is shown in figure 3.20. The parameterizing species were H_2O and H_2. The figure shows the projection of the manifold onto the three-dimensional space formed by the two parameterizing species and a third species, H. Also plotted is the one-dimensional ILDM and six sample reaction trajectories. None of the trajectories collapse onto the one-dimensional ILDM until very late times, near equilibrium. So clearly a one-dimensional ILDM is insufficient to describe the chemistry in this system. Three of the trajectories also take considerable time to collapse onto the two-dimensional ILDM and probably require a higher dimension. However, these three are all unusual contrived examples that start with a large amount of hydrogen radicals. Practical initial compositions are more likely to contain only major species. The

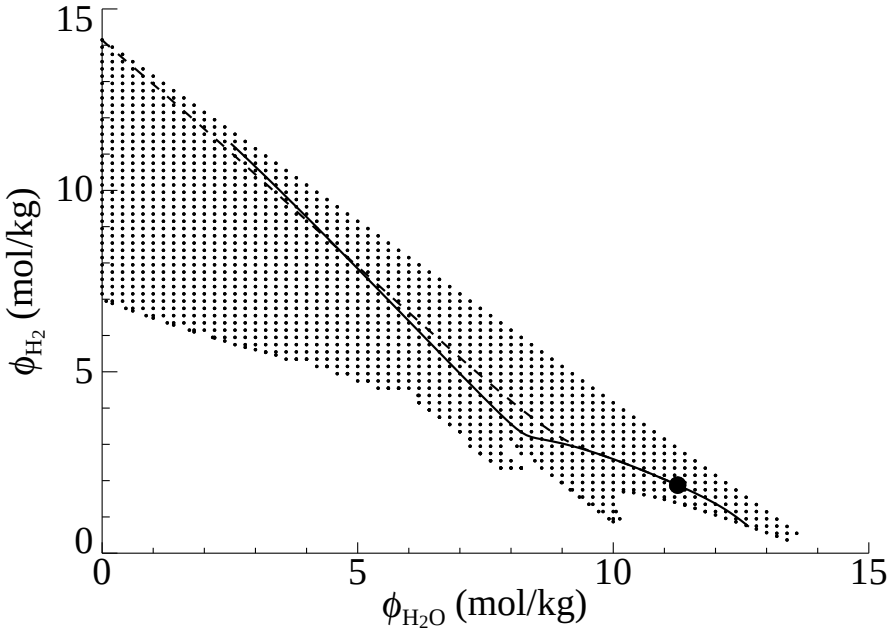

Figure 3.21: Adiabatic constant volume reaction in mixtures with the same elemental composition as stoichiometric H_2–air, and with $\rho = 4.58$ kg/m^3, $e = 1.28$ MJ/kg. Points: two-dimensional ILDM grid; —— one-dimensional ILDM; – – – sample reaction trajectory; • equilibrium point.

diagonal ILDM boundary to the lower left of the figure corresponds to the physical boundary of all hydrogen atoms being in the major species H_2 and H_2O, so practical initial compositions will all lie on this line. The three realistic trajectories that start from this line lie almost exactly on the manifold for all times, even at the start, so the two-dimensional ILDM appears to be sufficient to describe the entire reaction for these trajectories. The example selected for the constant volume validation study at the start of this section is one of these trajectories, the one starting from the lower right of the figure. Thus, we decided a two-dimensional ILDM would be sufficient in this validation study.

To show the domain of grid points found by the ILDM code, figure 3.20 is repeated in figure 3.21, this time viewed directly down on the two-dimensional plane formed by the parameterizing species. The grid spacing chosen in this case was 0.2 mol/kg in each parameter direction. Some of the intrinsic manifold boundaries are evident. As in the previous figure, the one-dimensional ILDM is also shown for comparison.

Only one of the sample reaction trajectories is shown, the one used in the constant volume validation study.

For the ILDM reduced system, the ODEs governing the constant volume reaction are

$$\frac{\mathrm{d}\theta_i}{\mathrm{d}t} = \bar{f}_i(\boldsymbol{\theta}; \rho, e), \qquad i = 1, \ldots, n_r. \tag{3.25}$$

The reduced reaction rates $\bar{\boldsymbol{f}}$ were interpolated from the ILDM lookup table, along with any other state variables desired for output, such as the temperature, pressure, or remaining species mole numbers.

One of the benefits of reducing reaction mechanisms by a technique such as ILDM is the removal of much of the system stiffness. Hence, the ODEs in (3.25) can often be integrated with a fast explicit integrator rather than the slow implicit integrators designed for stiff equations. For the hydrogen systems considered in this work, it was indeed found that an explicit integrator was viable and time steps could be taken by the integrator that were stable but not small compared with the induction time. However, the stability of explicit integrators degenerates as equilibrium is approached, and an implicit integrator was found to be more suitable there. As a result, we chose an adaptive ODE integrator, LSODA (Hindmarsh, 1983; Petzold, 1983), that automatically selects between an explicit Adams method for non-stiff equations and an implicit backward differentiation method for stiff equations. It switches between the two methods on successive integrator timesteps as the system evolves and the other method becomes more suitable.

The pre-computed ILDM lookup tables lay almost exactly on a regular Cartesian grid. They were irregular only at physical and intrinsic manifold boundaries found by the ILDM code, as evidenced in figure 3.21. A general implementation of the table interpolation in any number of dimensions on an irregular grid would be extremely difficult. However, multi-variate linear interpolation is straightforward on a regular Cartesian grid (see Appendix E). To enable use of this simpler interpolation, the irregular grid points were firstly extrapolated onto the regular Cartesian grid locations having the same logical co-ordinates. A similar extrapolation was used to fill in any

missing portions of the manifold within the requested domain, a rare occurrence, but one necessary for robustness of the interpolation scheme. An additional layer of ghost points was also extrapolated outside boundaries not aligned to the grid.

In general, the extrapolations were performed linearly, consistent with the interpolation scheme. The only instance when this caused problems was the extrapolation of the reaction rates $\mathrm{d}\boldsymbol{\theta}/\mathrm{d}t$. Near physical boundaries of the manifold, the reaction rates of the parameterizing species are very nonlinear, varying roughly exponentially. This is illustrated in figure 3.22 which is a schematic of the manifold domain near the initial trajectory point at the upper left of figure 3.21. The solid points and lines constitute the tabulated manifold grid, while the open points and dashed lines are the extrapolations onto a regular Cartesian grid. The initial part of the example reaction trajectory is also shown schematically. The grid was aligned such that points A′, C′ and F′ lie on the locus of points for which all hydrogen atoms are in H_2 and H_2O only, that is, the locus of typical detonation initial conditions. Points A, C and F, as solved by the ILDM code, don't quite coincide with points A′, C′ and F′ since the hydrogen-containing radicals didn't all proceed to zero at exactly the same rate, during the continuation along the paths BA, EC and IF. One of the radicals reached zero concentration on the manifold while the other radicals were still present in a small amount. Thus the physical domain boundary, as determined by the ILDM code, had slightly less than all of the hydrogen in H_2 and H_2O. Although not drawn to scale, the relevant dimensions are shown. Note that the irregular grid points A, C and F are actually very close to the regular grid points A′, C′ and F′. The numbers shown at each grid point are the values of $\mathrm{d}\theta_1/\mathrm{d}t$, the reduced reaction rate of the parameterizing species H_2O. Note the strongly nonlinear variation of the rate near the physical boundary.

When the reaction rates were extrapolated linearly, it was found that the extrapolated rates at initial condition points such as A′, C′ and F′ actually changed sign from that of the original extrapolating points. When the ILDM was then used to compute a constant volume reaction starting at one of these extrapolated boundary points, the reaction trajectory proceeded away from the manifold domain rather than into it.

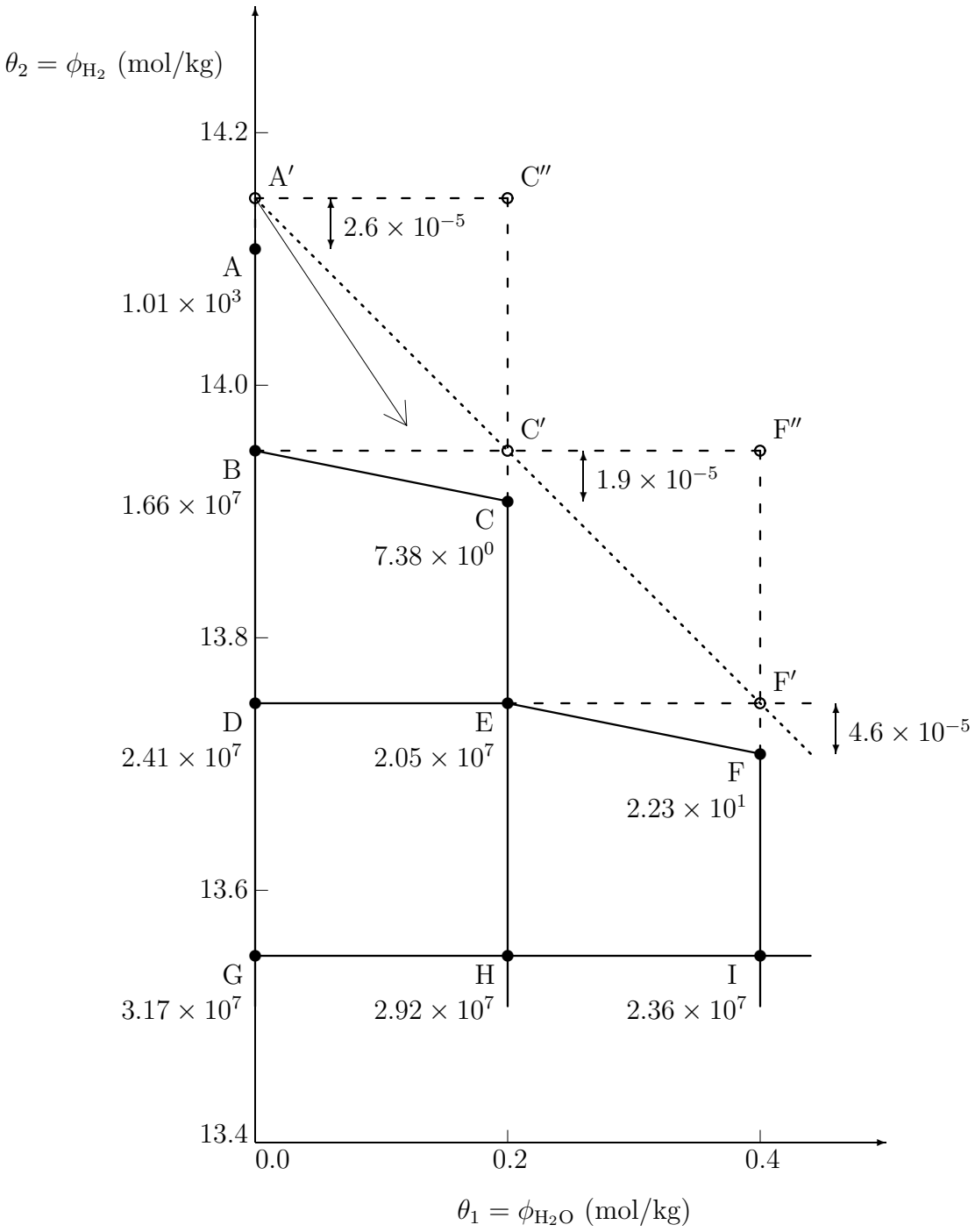

Figure 3.22: Schematic of two-dimensional ILDM grid near initial condition, for adiabatic constant volume reaction in mixtures with the same elemental composition as stoichiometric H_2–air, and with $\rho = 4.58$ kg/m^3, $e = 1.28$ MJ/kg. —●— computed ILDM grid; – –○– – extrapolated grid; ····· locus of typical initial conditions; ↘ initial reaction trajectory direction. Labeled lengths have units mol/kg. Labeled grid point values are $\mathrm{d}\theta_1/\mathrm{d}t$, with units mol/kg·s.

The example reaction trajectory starting at point A′ is one such case. Increasing the grid resolution in that region by a factor of 16 did not correct this failure, since the linearly extrapolated rates were still of the opposite sign. So the problem was not simply one of insufficient resolution, reparable by adaptive grid refinement. To avoid this non-physical and catastrophic behavior, all extrapolations of the reaction rates were performed logarithmically. In regions of the domain where the variation was close to linear, this was almost identical to linear extrapolation, while near the nonlinear boundaries it closely modeled the physically correct exponential variation. In the few instances where the two points used for the extrapolation had reaction rates of opposite sign, prohibiting logarithmic extrapolation, the extrapolated rate was set to zero, a slightly inaccurate approximation, but one that would ensure sensible interpolated rates in the eventual CFD application.

Logarithmic extrapolation of the reaction rates corrected the non-physical behavior of the reaction initially proceeding in the wrong direction. However, the computed constant volume reactions still had too short an induction time. This could be attributed in part to errors in linearly interpolating highly nonlinear data, but increasing the grid resolution by a factor of 16 in this region improved the results only slightly. The major source of error was instead a fundamental invalidity of the ILDM in the early part of the reaction trajectory. This can be explained as follows.

The basic assumption in applying ILDMs to reacting CFD problems is that the fluid state collapses onto the manifold much faster than the smallest timescale of interest. For low-speed flame calculations, this timescale is usually just the smallest convective flow timescale. However, for detonations and ignition problems we also have to resolve the induction time, and this is often considerably smaller. In figure 3.22, the induction region of the example reaction trajectory is contained completely within the first ILDM grid triangle A′BC′. Even though the initial part of the reaction trajectory appeared to lie close to the manifold in figure 3.20, it is possible that small differences between the trajectory and manifold will amount to large relative errors, given the very small radical concentrations and reaction rates. In this case, the ILDM would actually be a poor representation of the chemistry in the

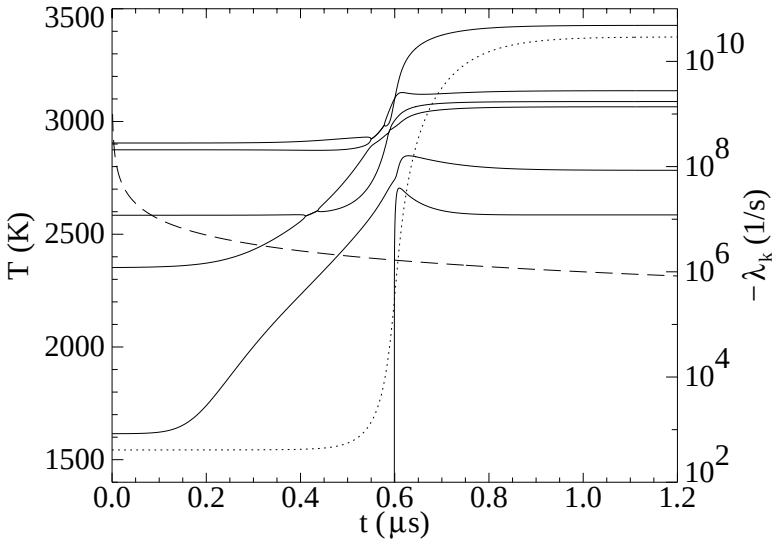

Figure 3.23: Adiabatic constant volume reaction in stoichiometric H_2–air, with $\rho = 4.58$ kg/m^3 and $e = 1.28$ MJ/kg. Solid lines: eigenvalues of system Jacobian $\boldsymbol{f}_{\boldsymbol{\psi}}$; Dotted line: temperature; Dashed line: locus of points for which $t\lambda_k = -1$.

induction region.

To verify this supposition, the eigenvalues of the system Jacobian $\boldsymbol{f}_{\boldsymbol{\psi}}$ can be examined at various stages of a constant volume reaction calculated with detailed chemistry. As discussed in the theoretical development of the ILDM method in §3.4.1, the inverses of the eigenvalues are the timescales of the respective chemical processes and they give an indication of the time required for each process to equilibrate. For the example constant volume reaction considered in this section, the eigenvalues λ_k are plotted in figure 3.23 as a function of the reaction time. The system has $n_s+2 = 11$ eigenvalues, but $n_e+2 = 5$ of these are zero, corresponding to the conserved variables. Only the remaining 6 eigenvalues are visible in the figure. The temperature profile is also shown to indicate the location of the energy release around $t = 0.6$ μs. In the equilibrium region, all of the eigenvalues are large negative numbers, representing a 0-dimensional manifold with relaxing processes that all equilibrate very quickly. On the other hand, in the induction region, one of the eigenvalues is positive (the one that disappears off the plot at $t = 0.6$ μs), indicating a non-relaxing chemical process, so there is at least one degree of freedom in the chemistry. Whether or not the other processes have relaxed onto the manifold at various times in the induction

zone can be estimated as follows. If a negative eigenvalue λ_k is constant from the start of the reaction for a period of time, then the associated chemical process will relax to equilibrium in a time on the order of the timescale $t = -1/\lambda_k$. The locus of points for which $t\lambda_k = -1$ is shown on the figure. At any given time in the reaction, all eigenvalues below this line have a characteristic timescale longer than the reaction time to that point, so will not have relaxed to equilibrium. The point at which a constant eigenvalue crosses this line is roughly the time that the associated chemical process approaches self-equilibrium. For this example, two of the processes equilibrate almost immediately, and a third at about 0.1 μs. The next eigenvalue crosses the line at about 0.3 μs, although it is not quite constant prior to this, so the equilibration time will be a little different. Since the eigenvalue is smaller in magnitude at earlier times, it has a larger characteristic timescale, so will take a little longer to equilibrate. But to first order, the number of eigenvalues below the $t\lambda_k = -1$ line is a good estimate of the number of non-equilibrated processes and hence the number of progress variables required to describe the reaction. Using this idea, we can deduce that the system can be represented by a two-dimensional manifold from about 0.3 μs, and a three-dimensional manifold from 0.1 μs. For an ILDM to accurately capture the full induction process, we would have to go to a four-dimensional manifold, although if a 0.1 μs error in induction time (17%) was considered acceptable, then a three-dimensional manifold might suffice. The fact that a lower dimensional manifold is not valid in the induction region is hardly surprising because induction zones typically involve many competing chemical processes. We would expect these observations to be true of any exothermic chemical system.

It would be desirable to find an alternative method for handling the chemistry in the induction region, in which case we would only need the ILDM to be valid from the start of the heat release. As shown in the figure, a two-dimensional manifold would then certainly be applicable in the H_2–O_2 example considered here. It might appear from this figure that even a one-dimensional manifold would be sufficient, but the second smallest magnitude eigenvalue is much smaller early in the induction zone, so it is not likely to actually equilibrate until some time in the heat release region. As

shown in figure 3.20, this is indeed what happens.

One possible method for handling the induction zone chemistry would be to use the full detailed reaction mechanism in the induction region, until the system has collapsed onto the low-dimensional manifold. However, this would greatly add to the computational expense and defeat the purpose of using reduced reaction mechanisms. Instead, we propose a different solution based on the use of an approximate "induction manifold." It will be outlined in detail in the following section on one-dimensional unsteady detonation simulations. Suffice to say for the constant volume calculation considered here, the proposed approximation reduces to simply using the exact detailed chemistry solution in the induction zone. The cutoff for switching to the ILDM method occurs when the specific mole number of some tracer species reaches a cutoff value ϕ_{cutoff}. For the example considered here, we chose one of the parameterizing species, H_2O, as the tracer species. Since the "approximation" is exact in the constant volume calculations, these calculations were used to determine an appropriate value for ϕ_{cutoff} to be used in the CFD simulations. The smallest value of ϕ_{cutoff} that gave satisfactory reaction profiles identified the point where the reaction had collapsed onto the low-dimensional manifold.

The results of the constant volume validation study are shown in figure 3.24, which compares the reaction zone profiles computed with detailed chemistry, the two-dimensional ILDM reduced mechanism, and the three-step QSSA reduced mechanism of §3.3. The agreement between the detailed mechanism and ILDM reduced mechanism is excellent, with only a very slight discrepancy between the profiles at the start of the energy release. The value of ϕ_{cutoff} chosen for switching from the detailed to reduced chemistry was 0.05 mol/kg, on the species H_2O. This is only about one quarter of the way through the first ILDM grid triangle in figure 3.22, demonstrating the very small region encompassed by the induction region in that figure. The value of ϕ_{cutoff} corresponds to $y_{H_2O} = 9 \times 10^{-4}$, and for this example the switching point occurred at 0.435 μs. Figure 3.24(b) shows that this is indeed a point in the induction zone where there has been no appreciable temperature rise. As demonstrated in figure 3.23, we would have expected a two-dimensional ILDM to

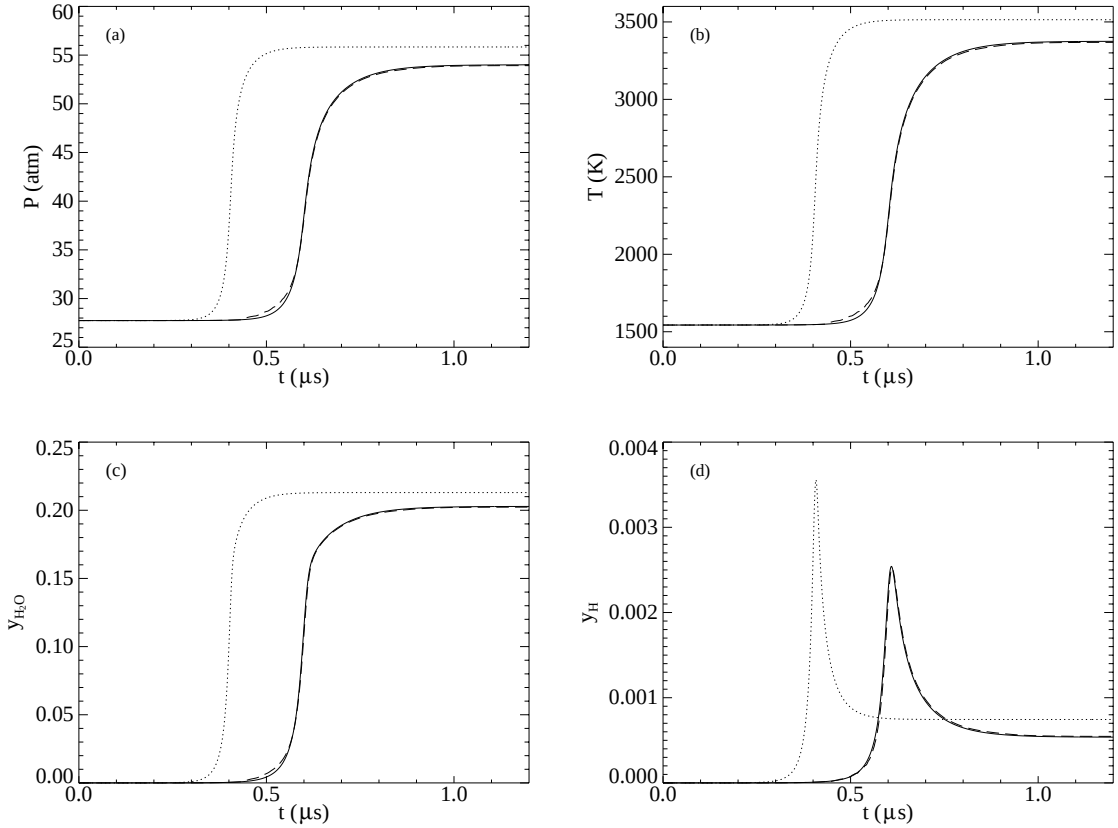

Figure 3.24: Adiabatic constant volume reaction in stoichiometric H_2–air, with $\rho = 4.58$ kg/m^3 and $e = 1.28$ MJ/kg. Solid lines: detailed reaction mechanism; Dashed lines: two-dimensional ILDM reduced mechanism, with $\phi_{cutoff} = 0.05$ mol/kg on H_2O; Dotted lines: three-step QSSA reduced mechanism. (a) Pressure; (b) Temperature; (c) Mass fraction of H_2O; (d) Mass fraction of H.

be a good approximation at this time.

Since exact detailed chemistry was used in the ILDM profiles for most of the induction region, this study is not a stern test of the ILDM reduced mechanism's ability to reproduce the correct induction time. However, figure 3.24 does show that the ILDM very accurately reproduces the heat release region and approach to equilibrium. Contrast this with the QSSA reduced mechanism results where there is considerable discrepancy in these regions. Admittedly, the QSSA induction time could be greatly improved when combined with an induction manifold approach as in the ILDM application, but the shape of the reaction zone profiles in the heat release region and beyond would be essentially unchanged. Figure 3.24 shows that the gradients in the heat release region are too steep and the equilibrium state is incorrect. Furthermore, the peak hydrogen atom mass fraction is overpredicted by about 40%, just as it was in the ZND validation study of figure 3.10. Clearly, the ILDM is a significant improvement over the QSSA technique, especially when considering that the ILDM reduced mechanism employed here was in effect only a two-step mechanism, one step less than the QSSA mechanism.

3.4.5 Implementation in a one-dimensional CFD code

Under the assumption that the thermochemical state of the system lies on the low-dimensional manifold at all times, only the components of the governing equations giving movement in the direction of the manifold need to be considered. Hence, the governing equations used for the one-dimensional detonation simulations with ILDM reduced chemistry were those used in the detailed chemistry simulations, (3.1), projected down onto the manifold. As described by Maas and Pope (1994), convective terms (the only transport terms in the Euler equations) are unchanged by this projection. Thus, the mass, momentum and energy equations were exactly the same as in the detailed chemical system. The only change was that the n_s conservation equations for species mass fractions $\boldsymbol{y}$ were replaced by n_r conservation equations for

the reduced progress variables $\boldsymbol{\theta}$. The set of governing equations is given by:

$$\frac{\partial \boldsymbol{W}}{\partial t} + \frac{\partial \boldsymbol{F}}{\partial x} = \boldsymbol{S}, \tag{3.26a}$$

where

$$\boldsymbol{W} = \begin{pmatrix} \rho \\ \rho u \\ E_t \\ \rho\theta_1 \\ \vdots \\ \rho\theta_{n_r} \end{pmatrix}, \quad \boldsymbol{F} = \begin{pmatrix} \rho u \\ \rho u^2 + P \\ (E_t + P)u \\ \rho u\theta_1 \\ \vdots \\ \rho u\theta_{n_r} \end{pmatrix}, \quad \boldsymbol{S} = \begin{pmatrix} 0 \\ 0 \\ 0 \\ \rho\bar{f}_1 \\ \vdots \\ \rho\bar{f}_{n_r} \end{pmatrix}. \tag{3.26b}$$

$\bar{\boldsymbol{f}}$ is the vector of reduced system reaction rates appearing in the constant volume ODEs that govern the chemical source term step, (3.25). These rates were determined by multi-variate linear interpolation of the ILDM lookup table, as described in the previous section. The only difference here is that data was required over a range of densities and energies, so the table had two additional degrees of freedom and $2 + n_r$ dimensions. The manifold solution algorithm described in the previous section simply used density and energy as two additional continuation parameters to solve this enlarged table. All the ILDMs used in this work for hydrogen systems had a reduced chemical dimension $n_r = 2$, with $\theta_1 = \phi_{\mathrm{H_2O}}$ and $\theta_2 = \phi_{\mathrm{H_2}}$. Adding density and energy as parameters, the lookup tables were four-dimensional.

To prevent the tables from becoming too large, constraints were applied to the manifold domain, based on phase space scatter plots of the accessed states in the equivalent detailed chemistry calculations. Examples of these scatter plots are shown in figure 3.25, for the detailed chemistry simulation of a stoichiometric H_2–O_2 detonation with overdrive factor $f = 1.2$ considered earlier in §3.2.3 and figure 3.7. The plotted points represent the spatial distribution of states for 50 evenly spaced times between $t = 0$ and 6.7 μs. The grids show the chosen ILDM grid spacing, and the thick lines are the chosen ILDM domain boundaries. The points to the lower left

(a)

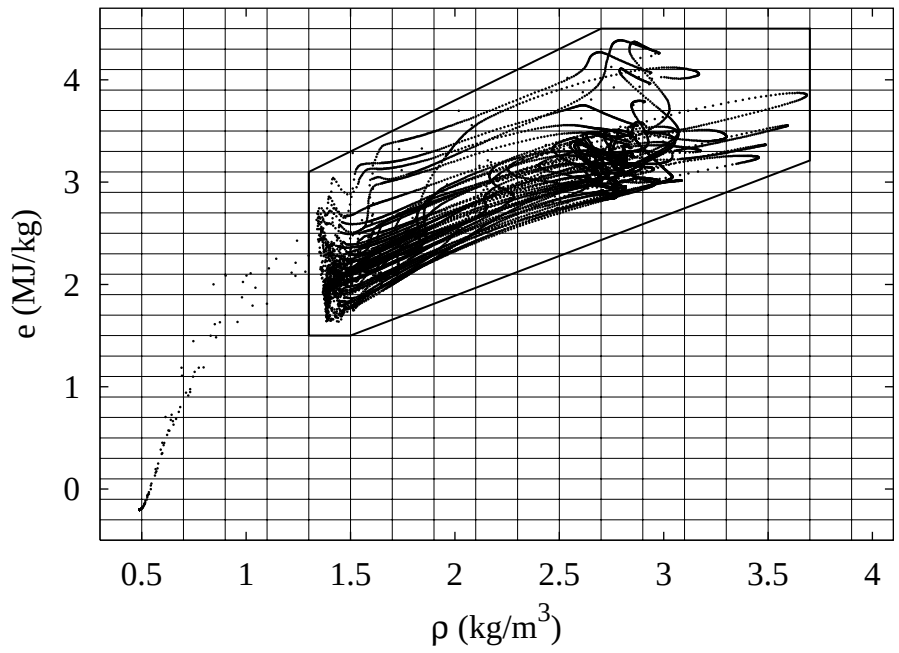

(b)

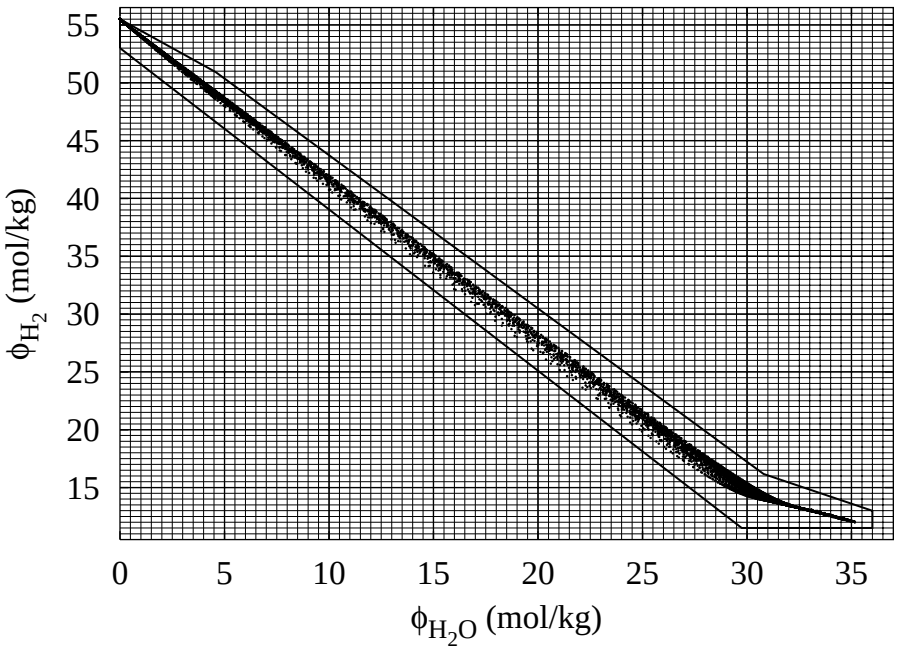

Figure 3.25: Phase space scatter plots of accessed states for a one-dimensional detonation in stoichiometric H_2–O_2, initially at 1 atm and 300 K, with $f = 1.2$, computed with detailed chemistry. (a) Density versus internal energy. (b) Specific mole numbers of H_2O versus H_2.

of the density–energy plot, outside the ILDM domain, are all points inside the numerically smeared leading shock wave. One interesting observation is that despite the large variations in the thermodynamic conditions during the galloping detonation oscillations, all the accessed states in the composition space tend to lie quite close to a single line, the steady ZND reaction trajectory. Hence, even in the absence of detailed chemistry results to guide the choice of restricted manifold domain, a good estimate of the necessary domain could be made by choosing only compositions close to the ZND reaction trajectory. With this approach, higher dimensional manifolds would even be feasible. The four-dimensional ILDM table represented in figure 3.25 contained about 10^6 grid points and required about 50 MB storage in a file of formatted double precision data. It was generated in about 18 hours on a single processor 750 MHz Linux workstation. This CPU time may seem large for a pre-processing step, but when considering that the generated table can be re-used on several different CFD simulations and each of those simulations could be extremely expensive two or three-dimensional flows, perhaps requiring parallel computing, the table generation is only a small fraction of the total computational effort. As an example of the multiple use of a single ILDM table, the table represented in figure 3.25 was also used for simulations of detonations in the same mixture with overdrive factors of 1.3 and 1.4. The large oscillations of the $f = 1.2$ detonation in figure 3.25 completely encompassed all of the accessed states in the more stable higher overdrive cases, even in the tightly constrained composition space.

Induction manifold

As discussed in §3.4.4, the ILDM is not expected to be a good representation of the chemical reactions in the induction zone since there are typically many chemical degrees of freedom there. Hence, an alternative method is required for the constant volume chemical source step in the induction zone. Rather than the expensive option of explicitly integrating the detailed chemistry reactions in each mesh cell at each timestep, a fast approximate technique is proposed. It is based on observations of the accessed states in the induction zone, for one-dimensional simulations with de-

tailed chemistry. Scatter plots of the induction zone composition space are shown in figure 3.26, for the same simulation considered earlier in figure 3.25. The plots show the specific mole numbers of several species plotted against the specific mole number of H_2O. The plotted range is up to $\phi_{H_2O} = 0.1$ mol/kg, only one-fifth of the way through the first ILDM grid cell at the upper left of figure 3.25(b). At this point, the temperature in the steady ZND profile is only 1.7 K greater than the von Neumann temperature, so this is certainly in the range of the energetically neutral induction zone. The figure shows a strong correlation between all of the chemical species, suggesting the chemical composition lies roughly on a one-dimensional manifold. We refer to this as the induction manifold, as distinguished from the intrinsic low-dimensional manifold which is prevalent at later times. Hence, a single reaction progress variable can be used to describe the chemical state in the induction zone. For convenience, this reaction progress variable was chosen to be θ_1, the specific mole number of H_2O. So the reaction rates and composition in the induction zone are approximately a function of only three variables, namely ρ, e and θ_1.

A further approximation is made by assuming the flow in the induction zone is quasi-steady. As shown in §2.4, a criterion for quasi-steadiness in one-dimensional exothermic reacting flow behind a decelerating shock is $t_d \gg \theta\tau$, where t_d is the characteristic shock decay time, θ is the global activation energy normalized by the von Neumann temperature, and τ is the ZND induction time. The characteristic shock decay time was defined in (2.29). Using the strong shock approximation (2.27a), it can also be expressed as

$$\frac{1}{t_d} = -\frac{1}{2P_s}\frac{\mathrm{d}P_s}{\mathrm{d}t}. \tag{3.27}$$

To check the quasi-steady criterion in the case of one-dimensional galloping detonations, consider the earlier example of the $f = 1.2$ detonation in stoichiometric H_2–O_2. Figure 3.7 shows that the average pressure peak and trough of the final large amplitude oscillations were 55.5 and 35.5 bar respectively. The time between a peak and a trough, half the oscillation period, was 0.15 μs. Taking the shock pressure decay rate $\mathrm{d}P_s/\mathrm{d}t$ as the average decay rate between a peak and a trough, and using

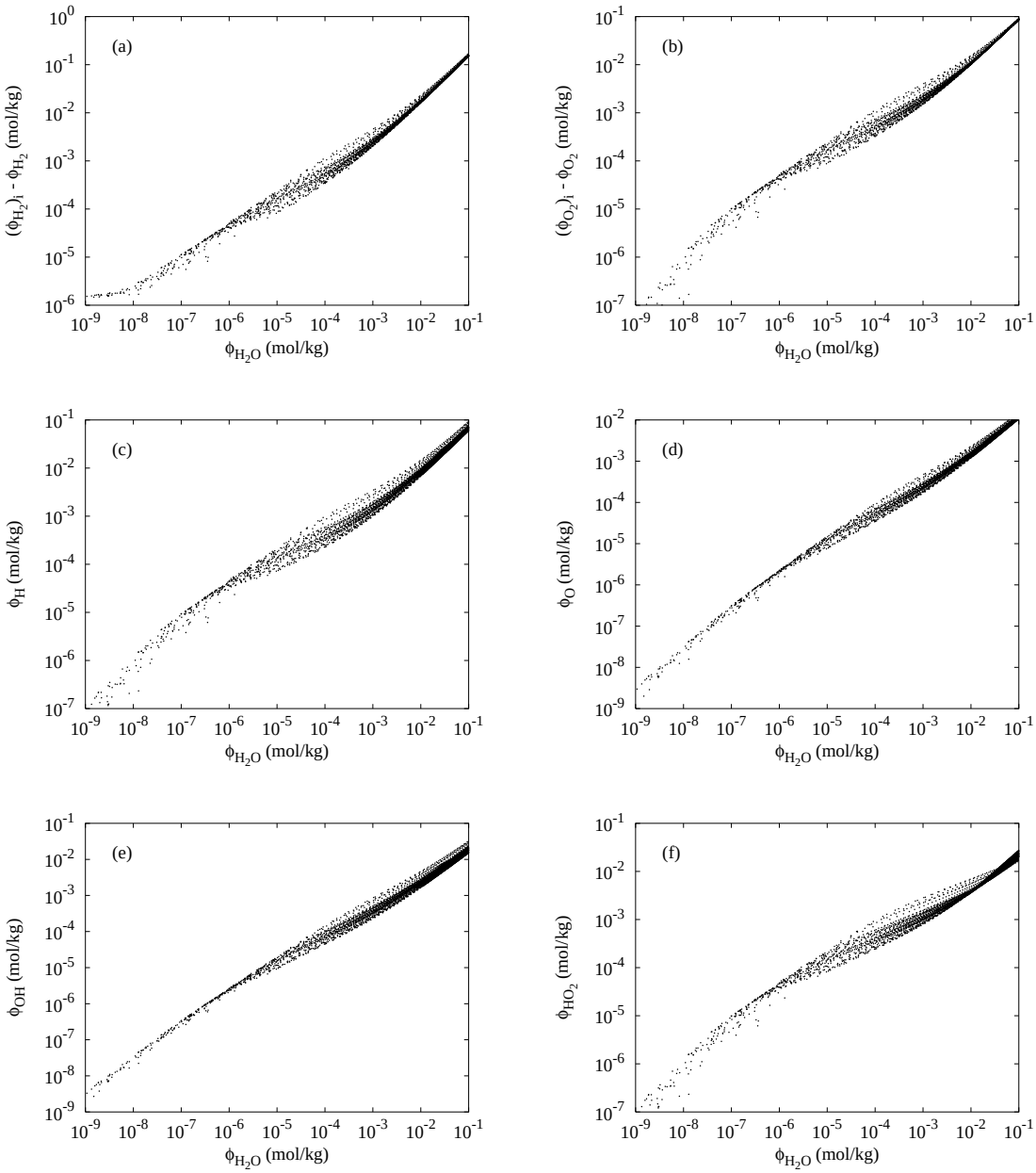

Figure 3.26: Composition space scatter plots of accessed states in the induction zone for a one-dimensional detonation in stoichiometric H_2–O_2, initially at 1 atm and 300 K, with $f = 1.2$, computed with detailed chemistry. Specific mole numbers of H_2O versus (a) H_2; (b) O_2; (c) H; (d) O; (e) OH; (f) HO_2.

$P_{vN} = 40.14$ bar as the average pressure P_s in (3.27), gives a characteristic shock decay time of $t_d = 0.60$ μs. The ZND induction time for this case was $\tau = 0.038$ μs, and the normalized activation energy, as determined by the method outlined in §2.5.3, was $\theta = 5.15$. Hence, $t_d/\theta\tau = 3.1$, which is somewhat greater than one. The same calculation for the single oscillatory mode of the $f = 1.3$ detonation in figure 3.6 gives $t_d/\theta\tau = 3.8$, a similar result. So the quasi-steady assumption is approximately valid for galloping detonations. Since direct initiation was shown to not be quasi-steady in chapter 2, the induction manifold approximation described below would not be valid for direct initiation computations. In that case, explicit detailed chemistry would have to be used in the induction zone.

As discussed above, the induction zone in galloping detonations is nearly energetically neutral and quasi-steady. Hence, it can be approximately represented as a constant volume reaction. In addition, it can be described by an induction manifold with only three independent variables, ρ, e and θ_1. For a detonation traveling into a premixed fluid, the initial composition for the constant volume reaction is fixed as the freestream composition. With the small number of degrees of freedom and fixed initial composition, it is inexpensive to pre-compute a table of constant volume reactions spanning the entire range of interest of the three variables. We refer to this as the induction manifold lookup table. For each density and energy in a two-dimensional grid, constant volume reactions were computed, using an initial composition corresponding to the freestream composition in the CFD application. The stiff ODE integrator DEBDF (Shampine and Watts, 1979) was used, and the full chemical composition $\boldsymbol{\phi}$ was output to the table at every timestep of the integrator, from $t = 0$ (the shock) until the reaction progress variable θ_1 was greater than ϕ_{cutoff}, the point at which a switch to the ILDM would be made in the CFD application. An appropriate choice for ϕ_{cutoff} was made in a constant volume validation study, as described in §3.4.4.

The package DEBDF includes error control by adaptive time-stepping, so in general, the timesteps output to the table were not evenly spaced. This could have been avoided by requesting output from the integrator at equal time intervals, but given the highly nonlinear variation of species populations in the induction zone, the

variable timesteps selected by the integrator are preferable for minimizing the subsequent interpolation errors. The following interpolation algorithm was only slightly more complicated with the unevenly spaced temporal data.

In the table lookup procedure for the chemical source step in the induction zone, the input ρ and e were firstly used to determine the bounding table grid rectangle $\{(\rho_0, e_0), (\rho_1, e_0), (\rho_0, e_1), (\rho_1, e_1)\}$. For each of these density–energy pairs, an effective reaction time, t_{eff}, was interpolated as the point in that constant volume reaction data for which the specific mole number of the induction manifold parameterizing species (in this case, H_2O) was equal to the input reaction progress variable (in this case, θ_1). Given the required CFD timestep Δt, the new composition at the end of the timestep was interpolated at $t = t_{\mathit{eff}} + \Delta t$. Finally, the new composition at the required density and energy was reconstructed from the compositions at the bounding grid rectangle points using bivariate linear interpolation (see Appendix E). Included in this new composition was the induction manifold reaction progress variable (in this case, θ_1), and the other elements of the ILDM chemical parameters $\boldsymbol{\theta}$. The other elements play only a passive role in the induction manifold but are necessary to track because they become important when the fluid progresses onto the ILDM. Note that the use of an induction manifold lookup table as described above completely eliminates any reaction rate integration in the induction zone, so this is a very fast computational step.

When the induction manifold reaction progress variable (in this case, θ_1) becomes greater than ϕ_{cutoff} in the CFD code, and evaluation of the chemical source step is switched from the induction manifold to the ILDM, the full chemical composition in the induction manifold description has to be projected onto the ILDM. Assuming the ILDM is approximately valid at that time, then the induction manifold state must lie close to the ILDM. Hence, any projection method would be valid. In this work, vertical projection was chosen, that is, the values of $\boldsymbol{\theta}$ from the induction manifold state were retained in the ILDM state, with all other species simply vertically projected onto the ILDM.

In the freestream ahead of the leading shock wave, the reaction rates are negligible.

To prevent the unnecessary evaluation of the chemical source step there, a threshold value of internal energy e_{cutoff}, or density ρ_{cutoff}, was used. It was chosen as some value that would always lie between the freestream value and post-shock value. For example, for the system considered in figure 3.25, $\rho_{cutoff} = 1.3$ kg/m^3 was used. Thus, the induction manifold was actually used to evaluate the chemical source term for some computational mesh cells in the latter part of the numerically smeared leading shock. However, with sufficient mesh refinement, the shock was made thin enough that negligible reaction occurred in these cells.

Equation of state

The evaluation of the convective operator requires a caloric equation of state to determine pressure and the partial derivatives of pressure with respect to ρ, e and $\boldsymbol{\theta}$ (see Appendix B). This can be achieved in the different regions of the detonation as follows.

Upstream of the leading shock wave and within the numerically smeared shock structure, the chemical reactions are essentially frozen and the composition is constant at $\boldsymbol{\phi}_0 = \boldsymbol{\phi}(\rho_0, e_0, \boldsymbol{\theta}_0)$, where the subscript 0 denotes the freestream state. Hence, the pressure can be evaluated from the constrained ideal gas relation,

$$P(\rho, e) = \rho R_g(\boldsymbol{\phi}_0)\, T(e, \boldsymbol{\phi}_0). \tag{3.28}$$

The partial derivatives of pressure with respect to density and internal energy are

$$\left.\frac{\partial P}{\partial \rho}\right|_e = R_g(\boldsymbol{\phi}_0)\, T(e, \boldsymbol{\phi}_0), \tag{3.29a}$$

$$\left.\frac{\partial P}{\partial e}\right|_\rho = \frac{\rho R_g(\boldsymbol{\phi}_0)}{C_v(T, \boldsymbol{\phi}_0)}. \tag{3.29b}$$

The partial derivatives of pressure with respect to θ_i are ill-defined, because pressure is not a function of θ_i in this case. However, the derivatives have no physical relevance since the only place they are used in the flow solver is as pre-multipliers to terms involving $\Delta\theta_i$ (see Appendix B), which are always zero here. Hence, a dummy

placeholder was assigned to these derivatives.

In the induction zone, the pressure could be determined from the induction manifold composition, but $\boldsymbol{\phi}$ is in general an unknown function of $(\rho, e, \boldsymbol{\theta})$, so the partial derivatives cannot be evaluated analytically. They could be evaluated with a complicated numerical differencing of the induction manifold lookup table. However, the composition of the major species is almost identical to that in the freestream, so the pressure partial derivatives can be reasonably well approximated by again assuming a frozen chemical state and using the expressions (3.29).

In the ILDM region, the pressure and pressure partial derivatives were computed in the ILDM table generation, as discussed in §3.4.2. So they can be evaluated from the ILDM lookup table using the same multi-variate linear interpolation scheme as for the reaction rates in the chemical source step (see Appendix E).

One difficulty with patching together independent methods for the evaluation of the reaction rates and pressure is that there will be a slight discontinuity in these evaluations at the switching point. When applied in an unsteady one-dimensional detonation simulation, it was found that the discontinuity in reaction rates had no effect on the simulations, but the discontinuity in pressure could have a disastrous effect. If this discontinuity occurred in a relatively smooth part of the pressure distribution such as the induction zone, then however small the initial discontinuity, it would rapidly amplify and eventually cause a non-physical local explosion. This occurs because a discontinuity in pressure is coupled to a discontinuity in temperature. The only time the failure didn't occur was when the discontinuous switch happened in the numerically smeared shock structure, since the gradients there were already sufficiently large that a slight extra discontinuity was easily absorbed.

As a result, the only place where a switch in the equation of state evaluation method can safely occur is in the leading shock. This prohibits use of both the induction manifold and ILDM for the equation of state, since the switching point between these occurs late in the induction zone. Hence, unlike in the reaction rate evaluation, the ILDM lookup table must be used throughout the entire reaction zone, right up to a point inside the leading shock. There, a switch is made to the freestream

equation of state evaluation. Evaluation of the equation of state in the induction zone using the ILDM is valid since the thermodynamics is essentially constant throughout the induction zone. That is, if the ILDM adequately describes the thermodynamics of the system at the end of the induction zone, then it will adequately describe the thermodynamics anywhere in the induction zone too. The full chemical composition of the freestream was projected onto the ILDM using a vertical projection, as described earlier for the chemical source step.

The numerical method can be summarized as follows:

1. Convective step

   - $e < e_{cutoff}$ (or $\rho < \rho_{cutoff}$): Evaluate the pressure and pressure partial derivatives from the frozen freestream expressions (3.28) and (3.29).
   - $e \geq e_{cutoff}$ (or $\rho \geq \rho_{cutoff}$): Interpolate the pressure and pressure partial derivatives from the ILDM lookup table.

2. Chemical source step

   - $e < e_{cutoff}$ (or $\rho < \rho_{cutoff}$): Inert, so no effect.
   - $e \geq e_{cutoff}$ (or $\rho \geq \rho_{cutoff}$) and $\theta_1 < \phi_{cutoff}$: Interpolate the new chemical state $\boldsymbol{\theta}$ from the induction manifold lookup table.
   - $e \geq e_{cutoff}$ (or $\rho \geq \rho_{cutoff}$) and $\theta_1 \geq \phi_{cutoff}$: Interpolate the reaction rates $\mathrm{d}\boldsymbol{\theta}/\mathrm{d}t$ from the ILDM lookup table and integrate to get the new chemical state $\boldsymbol{\theta}$.

3.4.6 Validation in one-dimensional detonation simulations

The same one-dimensional detonation model problem considered earlier for the detailed mechanism and QSSA reduced mechanism was used to study the ILDM reduced mechanism. As above, the computed ILDM had dimension $n_r = 2$, with H_2O and H_2 as the parameterizing species. Since ZND profiles were not computed with the ILDM reduced mechanism, an alternative was required for the initial conditions in the

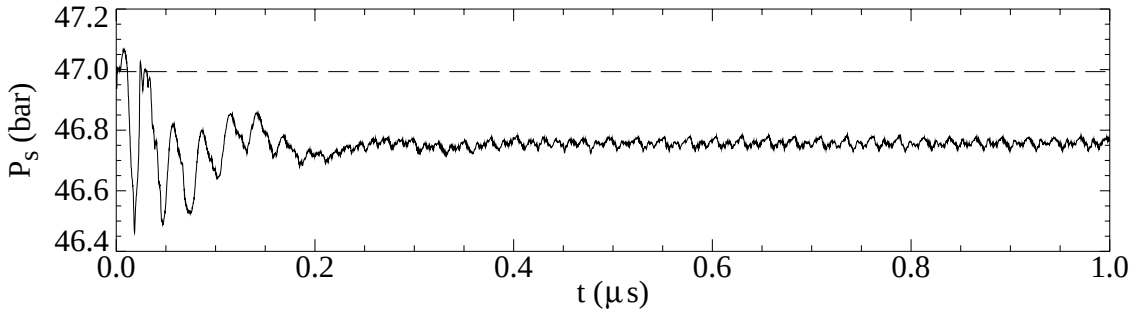

Figure 3.27: Shock pressure versus time, for a stable one-dimensional detonation in stoichiometric H_2–O_2, initially at 1 atm and 300 K, with $f = 1.4$, computed with a two-dimensional ILDM reduced mechanism. $\phi_{cutoff} = 0.1$ mol/kg on H_2O. $P_{vN} = 46.99$ bar. Finest grid level contains 100 cells per ZND induction length.

simulations. The ZND profiles with detailed chemistry were used, since the constant volume combustion validation study in §3.4.4 suggested the ILDM reduced mechanism was almost exactly the same in steady flow problems. Certainly, if this proved not to be true in the case of ZND profiles, then the error in the initial condition would simply provide an additional perturbation to trigger longitudinal instabilities in the detonation. Unlike the QSSA mechanism where species were physically removed from the system, the ILDM reduced mechanism gives precisely the same equilibrium solution as detailed chemistry. Two consequences of this are that the theoretical CJ detonation velocity is identical, and the rear boundary conditions provided by the detailed chemistry equilibrium solution are correct.

Figure 3.27 shows the pressure behind the leading shock as a function of time, for a stoichiometric H_2–O_2 detonation with an overdrive factor of 1.4. This result can be directly compared to figure 3.4 for the computation with detailed chemistry. As in the detailed chemistry case, the ILDM reduced mechanism correctly predicts that this detonation is stable to small perturbations. The only difference is that the final steady value for the post-shock pressure is slightly below the theoretical von Neumann pressure, more so than in the case of detailed chemistry. This suggests the detonation computed with the ILDM has a velocity deficit, which is not something we would expect. The main source of this error is the lookup table interpolation error of the numerical equilibrium state. It could be corrected by using some adaptive grid

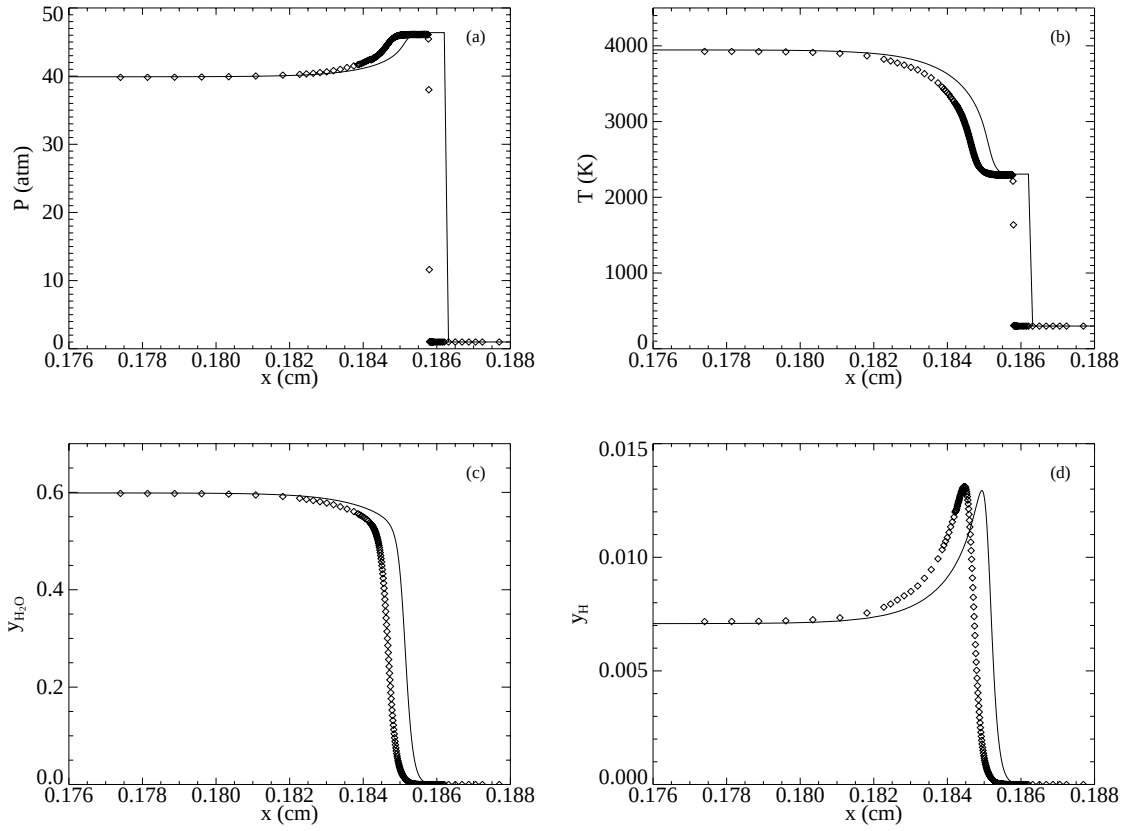

Figure 3.28: One-dimensional detonation in stoichiometric H_2–O_2, initially at 1 atm and 300 K, with $f = 1.4$. $\phi_{cutoff} = 0.1$ mol/kg on H_2O. $t = 0.554$ μs. Finest grid level contains 100 mesh cells per ZND induction length. Points: numerical results, with a two-dimensional ILDM reduced mechanism; Lines: ZND theory with detailed mechanism. (a) Pressure; (b) Temperature; (c) Mass fraction of H_2O; (d) Mass fraction of H.

refinement near the equilibrium states. Spatial profiles of pressure, temperature and some mass fractions at a late time are shown in figure 3.28. The plots of temperature and mass fraction of H can be directly compared to figure 3.5 for detailed chemistry. The theoretical solution shown as a solid line is the detailed chemistry ZND solution propagated a distance $U_{ZND}\,t$ down the duct. Other than the phase error due to the velocity deficit, the ILDM reduced mechanism agrees very well with the detailed chemistry ZND profiles. The numerical induction length in the figure, based on the maximum temperature gradient, is 11.5 ± 0.2 μm, where the uncertainty is due to the finite mesh size. This compares very well with detailed chemistry, where the ZND induction length was 11.8 μm and the numerical induction length in figure 3.5 was

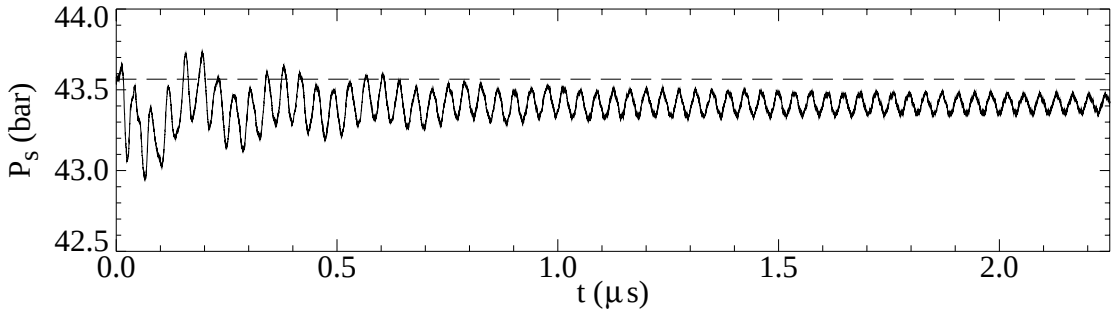

Figure 3.29: Shock pressure versus time, for a one-dimensional detonation in stoichiometric H_2–O_2, initially at 1 atm and 300 K, with $f = 1.3$, computed with a two-dimensional ILDM reduced mechanism. $\phi_{cutoff} = 0.1$ mol/kg on H_2O. $P_{vN} = 43.57$ bar. Finest grid level contains 200 cells per ZND induction length.

11.7 ± 0.2 μm. The computation of a stable one-dimensional detonation is a validation of the steady ZND profiles for the ILDM reduced mechanism. As for the constant volume combustion calculations in §3.4.4, the agreement with detailed chemistry is excellent, with negligible error in the reaction zone shape and induction length or time. This comparison of ZND profiles also validates the induction manifold approximation which was not critically tested by the constant volume combustion calculations.

Figure 3.29 shows the shock pressure versus time when the overdrive factor is decreased to 1.3. Unlike the detailed chemistry simulation in figure 3.6 which was slightly unstable, the ILDM reduced mechanism detonation is marginally stable. This suggests the neutral stability limit has been shifted by the mechanism reduction, from slightly above $f = 1.3$ to slightly below. Thus, the ILDM reduced mechanism appears to be slightly more stable than detailed chemistry, in contrast to the QSSA reduced mechanism which appeared to be slightly less stable.

When the overdrive factor is reduced to 1.2, figure 3.30 shows that the detonation develops two unstable modes, just as in the case of detailed chemistry (see figure 3.7). The final periodic oscillation is of slightly smaller magnitude, further supporting the notion that this detonation is slightly more hydrodynamically stable than its detailed chemistry counterpart. However, the agreement in the final periodic solutions is reasonably good. Most notably, there is evidence of both unstable modes in the final solution, an improvement on the QSSA reduced mechanism where the faster mode

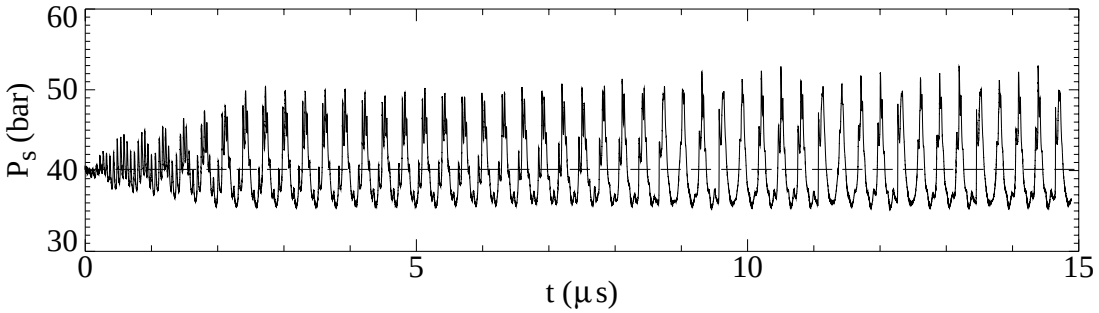

Figure 3.30: Shock pressure versus time, for a one-dimensional detonation in stoichiometric H_2–O_2, initially at 1 atm and 300 K, with $f = 1.2$, computed with a two-dimensional ILDM reduced mechanism. $\phi_{cutoff} = 0.1$ mol/kg on H_2O. $P_{vN} = 40.14$ bar. Finest grid level contains 200 cells per ZND induction length.

was damped out.

For a grid convergence study of the nonlinear instability, the $f = 1.3$ detonation is not suitable in this case since it was stable. Instead, we decreased the overdrive factor to $f = 1.27$, and the detonation developed one unstable mode similar to the $f = 1.3$ detailed chemistry detonation. This also gives some idea as to how much the neutral stability limit has been shifted. Unfortunately, some of the expected unstable simulations at $f = 1.27$ with the ILDM reduced mechanism were actually stable. This indicates that the numerical roundoff error is not always sufficient to trigger the instability. To ensure the instability developed when it was intrinsically present in the system, we applied a perturbation to the ZND initial conditions, consisting of a 10% increase in density between three and five induction lengths upstream of the initial shock front. The instability was triggered when the detonation ingested this dense pocket in the first few timesteps. Figure 3.31 shows the shock pressure versus time for one of these simulations.

The average pressure peaks and troughs as well as the average oscillation periods are shown in figure 3.32 for a range of resolutions. An approximate comparison can be made with figure 3.8 for the detailed mechanism, although that figure was for a different overdrive factor. The data was taken for $t \geq 1\mu$s, where figure 3.31 shows the detonation has reached its final configuration. This configuration shows some evidence of a second beating mode, causing the averages in figure 3.32 to not converge to single

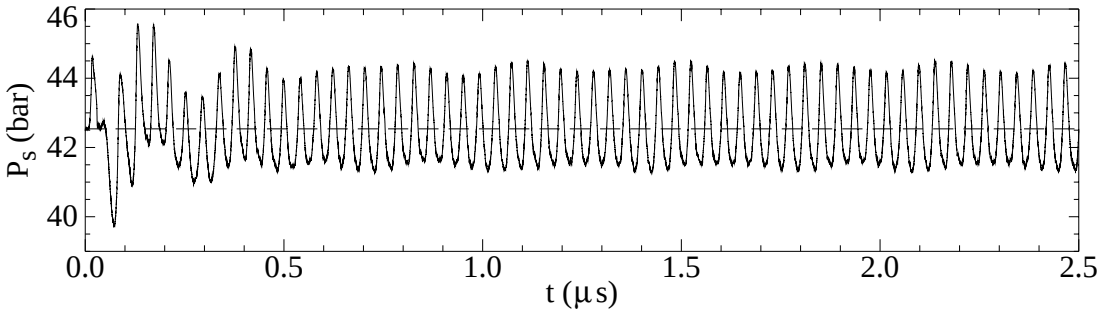

Figure 3.31: Shock pressure versus time, for a one-dimensional detonation in stoichiometric H_2–O_2, initially at 1 atm and 300 K, with $f = 1.27$, computed with a two-dimensional ILDM reduced mechanism. $\phi_{cutoff} = 0.1$ mol/kg on H_2O. $P_{vN} = 42.54$ bar. Finest grid level contains 200 cells per ZND induction length.

values. Despite this, the plots of oscillation period and pressure turning points both suggest that the ILDM reduced mechanism simulation is grid converged for as few as 75 fine mesh cells per induction length. Just as for the QSSA reduced mechanism, this represents a substantial improvement over the detailed mechanism where 150 cells were required.

The induction time τ for the detailed mechanism ZND solution was 30.4 ns, and as shown earlier in this section, the ILDM reduced mechanism ZND solution could be expected to have the same induction time. So the oscillation period is about 1.34τ. This agrees extremely well with the value of 1.35τ found in the case of the detailed mechanism.

3.4.7 Computational efficiency

Having successfully validated the ILDM method as a means for accurately reducing detailed reaction mechanisms, it is worth considering the increase in computational efficiency afforded by the reduction. Table 3.2 shows a comparison of the relative CPU times for a one-dimensional detonation simulation with various different thermochemical models. To avoid the difficulty of trying to match the amount of automatic mesh refinement between simulations, the computation did not use adaptive mesh refinement (AMR). The fixed grid had 20 mesh cells per reaction length. Despite this simplification, these relative scalings are indicative of all the AMR simulations

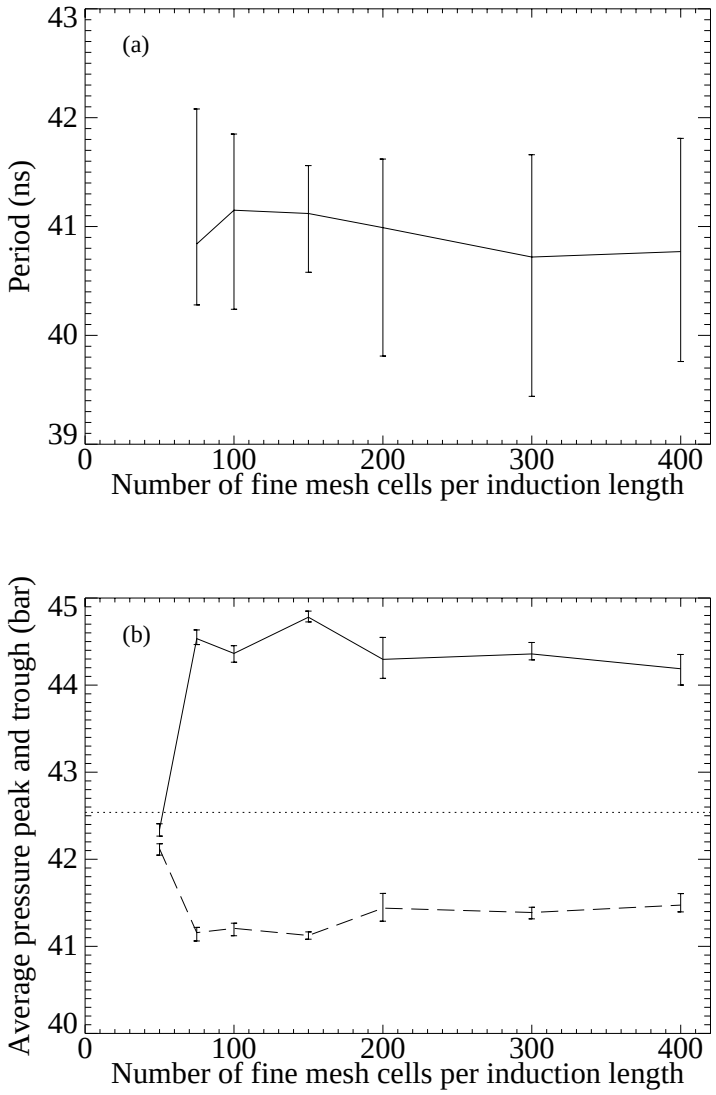

Figure 3.32: One-dimensional detonation in stoichiometric H_2–O_2, initially at 1 atm and 300 K, with $f = 1.27$, computed with a two-dimensional ILDM reduced mechanism. (a) Period of oscillation. (b) Pressure peak (solid line) and trough (dashed line).

Thermochemical model	Convective step	Chemistry step	Total
One-step Arrhenius	0.83	0.17	1
Two-dimensional ILDM reduced	5.8	5.6	11
Three-step QSSA reduced	9.1	36.	45
Detailed	18.	150.	170

Table 3.2: Relative CPU times to advance one reaction time for a one-dimensional detonation in stoichiometric H_2–O_2, initially at 1 atm and 300 K, with $f = 1.4$.

presented in this work, including the two-dimensional simulations in the next section.

Times for a roughly equivalent one-step Arrhenius model are also shown for comparison. Matching parameters between this model and a real system is difficult, but the CPU times are not too sensitive to the values of these parameters. Using the techniques described in §2.5.3 and §2.6.3, the parameters chosen were $\gamma = 1.3154$, $Q/R_gT_0 = 23.21$ and $E_a/R_gT_0 = 36.57$. The reaction time in this case is the half-reaction time, as opposed to the induction time in the other models. The CPU times are divided between the two steps of the timestep splitting, and are scaled such that the total time for the one-step Arrhenius model is one.

The advantages of the ILDM method are clearly evident. For the detailed mechanism, the great majority of CPU time is spent integrating the chemical reaction ODEs. The ILDM method reduces the chemistry time by about a factor of 27, and the total time by about a factor of 15. As a result, the computation is only about one order of magnitude slower than the one-step Arrhenius model, and many detonation simulations previously run with only a one-step model or two-step induction parameter model will now be viable with ILDM reduced mechanisms. This is encouraging, given the ILDM's vast improvement in the thermochemical description of the fluid. The slight improvement in CPU times of the convective step when going from detailed to reduced mechanisms is due to the reduced number of variables in the solution vector. Even though no reaction occurs in this step, the species information must still be advected. The ILDM method improves this even further since the equation of state for pressure is evaluated by simple table lookup rather than an iterative temperature solution.

It should also be noted that the CPU time using detailed chemistry will increase dramatically if we move to a larger chemical system. The chemistry step involves the finite difference calculation of Jacobian matrices, so the integration time will scale roughly with n_s^2. This makes multi-dimensional detonation simulations with detailed chemistry of large chemical systems completely infeasible, even on today's fastest parallel supercomputers. However, if these systems can be described by ILDMs of fairly low dimension, the CPU times using ILDM reduced mechanisms will not

be much greater than the hydrogen cases presented here. Thus, multi-dimensional simulations of more complex chemical systems such as hydrocarbons and nitramines should be possible.

3.5 Cellular Detonation Simulations

The ILDM method developed and validated in the previous section was applied to a simulation of a two-dimensional cellular detonation in a channel.

3.5.1 Computational setup

The governing equations were the two-dimensional reactive Euler equations. In the ILDM formulation they read:

$$\frac{\partial \boldsymbol{W}}{\partial t} + \frac{\partial \boldsymbol{F}_x}{\partial x} + \frac{\partial \boldsymbol{F}_y}{\partial y} = \boldsymbol{S}, \tag{3.30a}$$

where

$$\boldsymbol{W} = \begin{pmatrix} \rho \\ \rho u \\ \rho v \\ E_t \\ \rho\theta_1 \\ \vdots \\ \rho\theta_{n_r} \end{pmatrix}, \quad \boldsymbol{F}_x = \begin{pmatrix} \rho u \\ \rho u^2 + P \\ \rho uv \\ (E_t + P)u \\ \rho u\theta_1 \\ \vdots \\ \rho u\theta_{n_r} \end{pmatrix}, \quad \boldsymbol{F}_y = \begin{pmatrix} \rho v \\ \rho uv \\ \rho v^2 + P \\ (E_t + P)v \\ \rho v\theta_1 \\ \vdots \\ \rho v\theta_{n_r} \end{pmatrix}, \quad \boldsymbol{S} = \begin{pmatrix} 0 \\ 0 \\ 0 \\ 0 \\ \rho\bar{f}_1 \\ \vdots \\ \rho\bar{f}_{n_r} \end{pmatrix}. \tag{3.30b}$$

u is the fluid velocity in the x-direction, the direction of the channel axis, while v is the fluid velocity in the y-direction. E_t is the total energy per unit volume,

$$E_t = \rho\left(e + \frac{u^2 + v^2}{2}\right),$$

and $\bar{\boldsymbol{f}}$ is the reaction rate of the reaction progress variables $\boldsymbol{\theta}$, given in (3.25).

The numerical integration in the flow solver was performed using timestep splitting, with the algorithm

$$\boldsymbol{W}^{n+1} = \frac{1}{2}\mathcal{L}_{F_x}\,\frac{1}{2}\mathcal{L}_{F_y}\,\mathcal{L}_S\,\frac{1}{2}\mathcal{L}_{F_y}\,\frac{1}{2}\mathcal{L}_{F_x}\,\boldsymbol{W}^n,$$

where the 1/2 denotes integration for a half-timestep. This splitting maintains second-order time accuracy of the coupled scheme (Strang, 1968). The convective operators $\mathcal{L}_{F_x}$ and $\mathcal{L}_{F_y}$ were of the same form as the one-dimensional convective operator $\mathcal{L}_F$ in (3.9), and integrated with the same one-dimensional flow solver.

The problem chosen was that studied by Oran et al. (1998). Using detailed chemistry, they simulated an unsupported (not overdriven) cellular detonation in a mixture of stoichiometric H_2–O_2 with 70% Ar dilution, initially at 6.67 kPa and 298 K. Their computation equivalent to that presented here was performed on a fixed, uniform grid and required about one day of CPU time on a 256-node CM-5 parallel Connection Machine (Weber et al., 1997). The large amount of work was justified in providing a benchmark for validation of detonation simulations with simpler thermochemical models. By contrast, the computation presented here with an ILDM reduced mechanism ran in five days on a single processor 750MHz Linux workstation. The decrease in computational effort was a result of using adaptive mesh refinement and reduced chemistry. A CFL number of 0.3 was used in both Oran et al.'s simulation and our work here. The detailed reaction mechanism used to generate the ILDM reduced mechanism was the same 8–species, 24–reversible reaction mechanism for H_2–O_2 combustion (Burks and Oran, 1992) used by Oran et al.

As in the original detailed mechanism study, our computational domain was a channel of width 6.016 cm. The finest grid size was 0.015 cm in the x-direction and 0.0235 cm in the y-direction, matching the resolution of Oran et al.'s benchmark calculation. This grid size corresponded to 256 mesh cells in the transverse direction across the channel, and, with a ZND induction length of about 0.15 cm, 10 mesh cells per ZND induction length in the streamwise direction. By repeating the simulation at finer resolution, Oran et al. (1998) showed the benchmark resolution to be sufficient

for a grid converged solution in this mixture. Two levels of mesh refinement were used in the present work, each with a refinement ratio of four, so there were 16 mesh cells across the channel in the coarsest grid. Refinement was performed on the gradient of density to finely capture the leading and transverse shock waves as well as the triple point slip lines. In addition, refinement was performed on the gradient of H_2O mole number to resolve the reaction zone. The gradients were examined in both the x and y-axis directions. To avoid the large amount of work required to resolve the trailing vortices behind the detonation, which do not affect the detonation front, refinement was not performed more than 10 cm behind the front.

The top and bottom boundary conditions were reflecting walls with inviscid slip conditions. The upstream and downstream boundary conditions were linearly extrapolated inflow and outflow respectively. By not overdriving the detonation with a rear piston condition, we simulate a self-propagating detonation that would theoretically travel at the CJ velocity if it were hydrodynamically stable.

The initial condition for the simulation was the detailed chemistry ZND profile for a CJ detonation interpolated onto the computational grid. Although the transverse instability would eventually grow from numerical roundoff error, this growth may require computation for a long propagation distance. To accelerate the growth, the transverse instability was triggered by an applied perturbation behind the initial detonation front. This perturbation consisted of a stationary pocket of fluid with the same composition as the unreacted freestream mixture, and with temperature and pressure equal to seven times that of the freestream. The pocket had an axial dimension of 1.05 cm and a transverse dimension of 1.41 cm, starting 0.3 cm behind the initial shock location and centered in the channel. The chosen perturbation was identical to that used by Oran et al. (1998).

3.5.2 Computational results

Figures 3.33 and 3.34 show a sequence of numerical schlieren–type images for the detonation front. They were produced in a manner similar to that described by Quirk

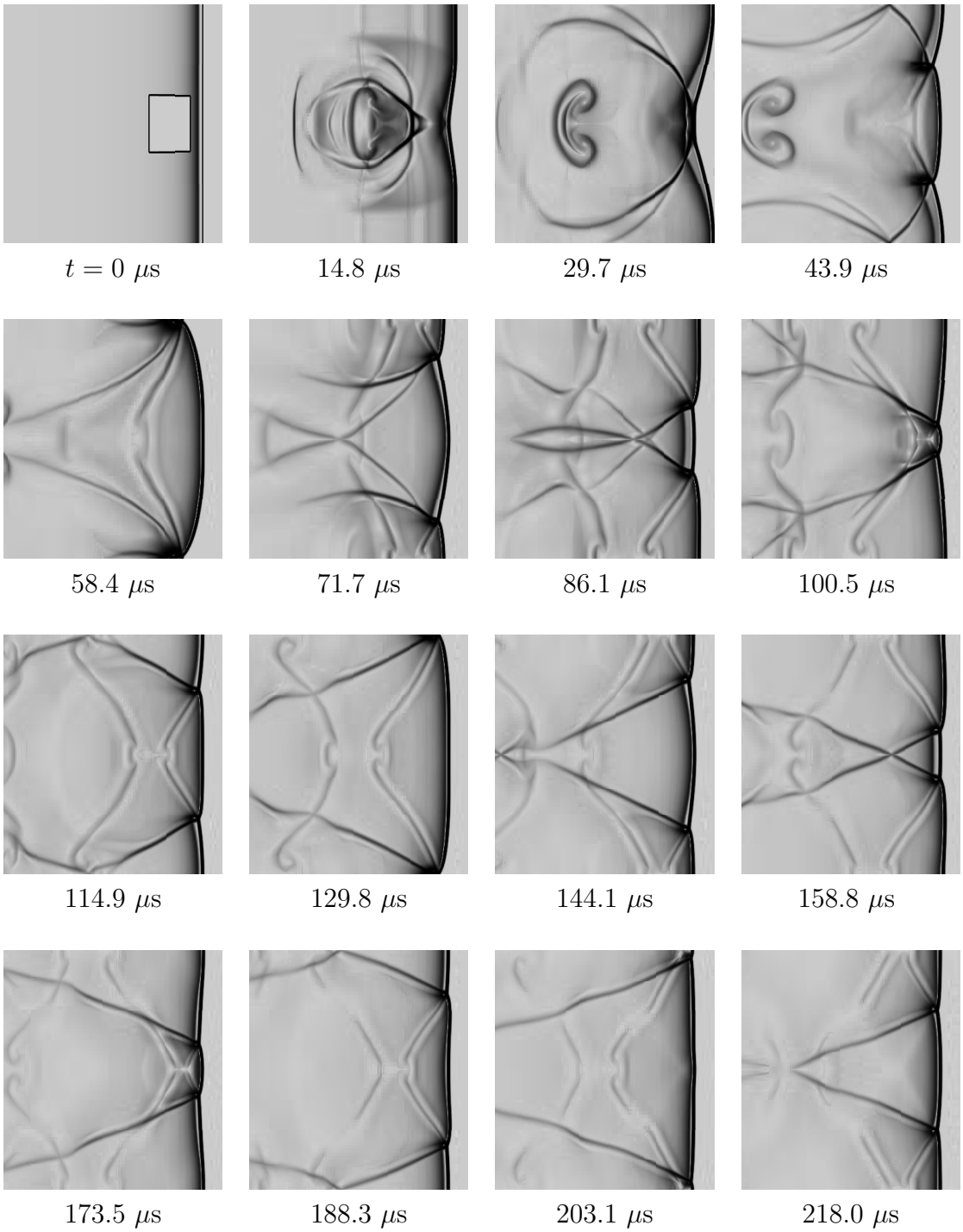

Figure 3.33: Numerical schlieren–type images for a two-dimensional CJ detonation in $2H_2 + O_2 + 7Ar$, initially at 6.67 kPa and 298 K.

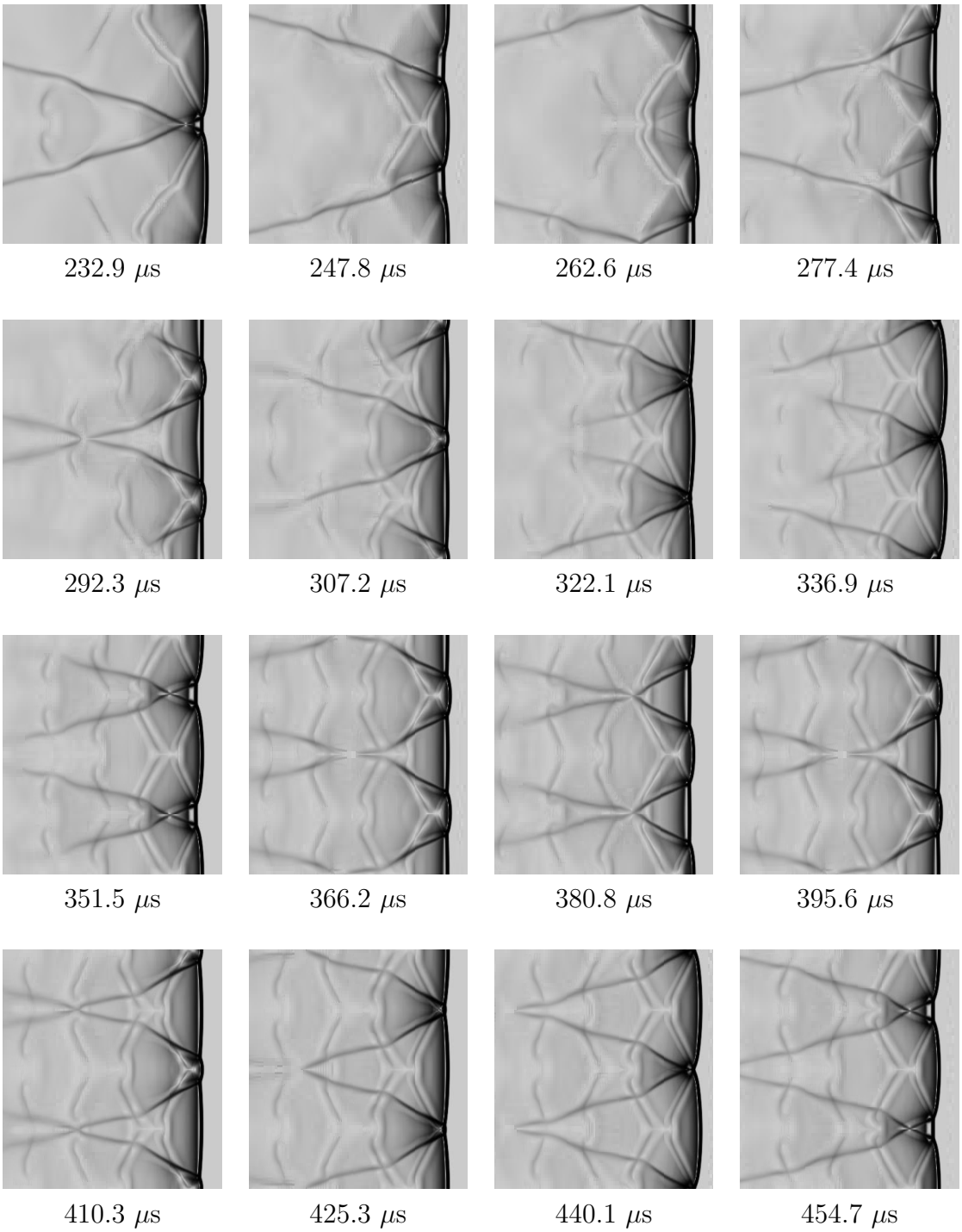

Figure 3.34: Numerical schlieren–type images (cont.).

(1994a), where the plotted variable is the magnitude of the local density gradient $|\boldsymbol{\nabla}\rho|$, with a nonlinear shading function to accentuate weak features of the flow. In this work, the greyscale shading function ν was

$$\nu = 0.8 \exp\left(-30 \frac{|\boldsymbol{\nabla}\rho|}{|\boldsymbol{\nabla}\rho|_{max}}\right).$$

The greyscale in the figures ranges from black for $\nu = 0$ to white for $\nu = 1$.

The initial perturbed region is visible in the first snapshot at $t = 0$. After the perturbation interacts with the detonation front, two transverse waves are generated. The intersection of each of these waves with the leading shock is similar to a Mach reflection. The leading shock forms the incident shock and Mach stem, while the transverse wave is the reflected shock. The intersection points are the triple points, and there is an associated slip line that separates fluid processed by the leading and reflected shock from that processed by the Mach stem. The incident shock is weaker than the Mach stem, evidenced by the long induction zone that appears behind the incident shock shortly before triple point collisions. Transverse instability of gaseous detonations has been observed experimentally for many years and the mechanism has been described in greater detail than that given here (Fickett and Davis, 1979). The configuration with two transverse waves that first forms is referred to as a mode two detonation. At about 200 μs, inflection points appear in the leading shock and two more transverse waves start to form. The final configuration has four transverse waves and is a mode four detonation. It appears to remain in the same periodic configuration from about 320 μs. Note the similarity of the three snapshots starting at 322.1 μs with the final three snapshots.

An example of the computational grid near the detonation front is shown in figure 3.35. Mesh refinement is evident around the various shock waves and slip lines, and throughout the reaction zone near the front.

Figure 3.36 shows various flowfield properties at a late time, $t = 422.3$ μs. The pressure and streamwise velocity plots are greyscale contour plots, with a nonlinear shading function to highlight particular features of the flow. The following greyscale

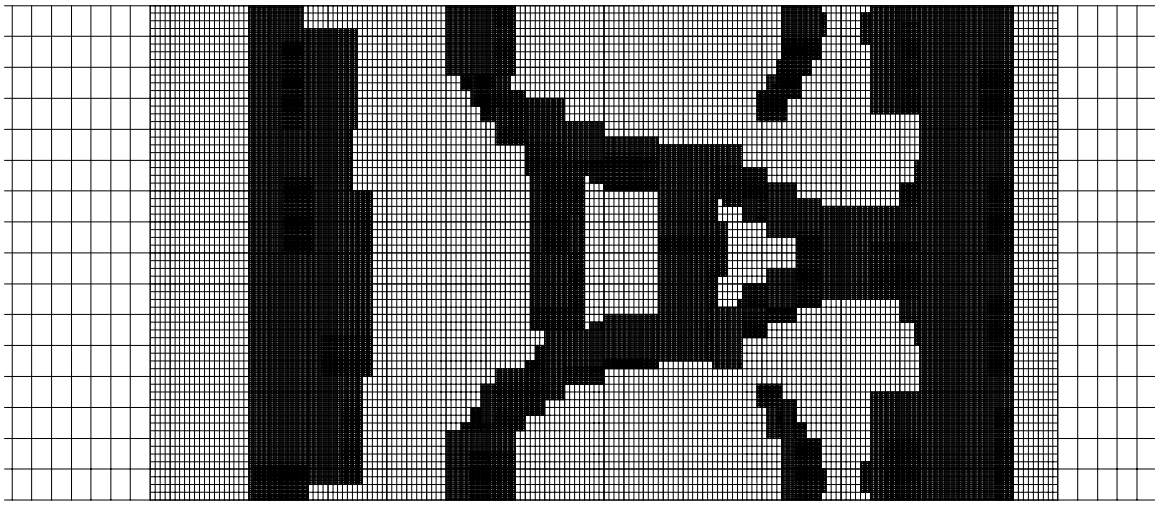

(a) Computational grid

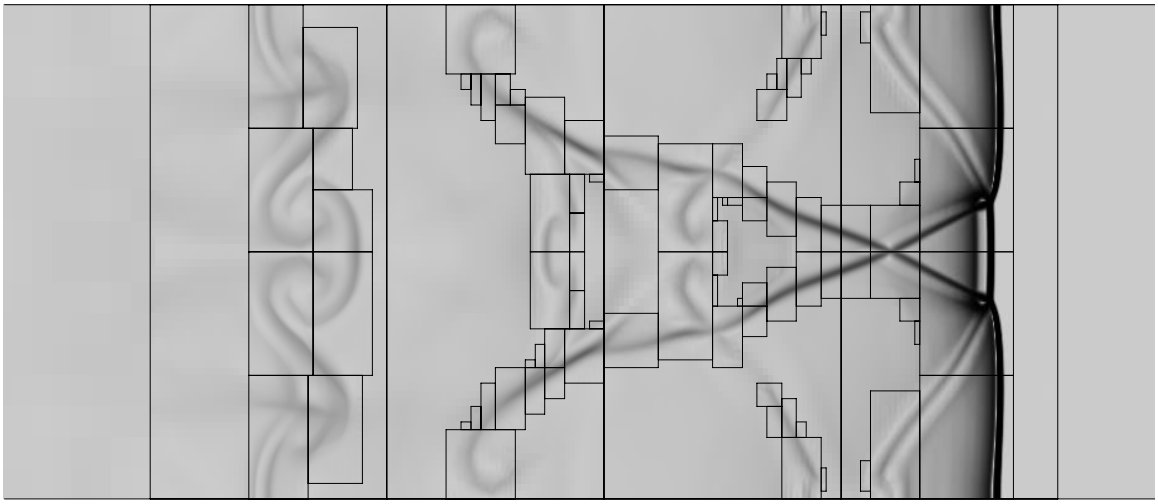

(b) Grid patch outlines and numerical schlieren–type image

Figure 3.35: Computational grid at $t = 158.8$ μs, for a two-dimensional CJ detonation in $2H_2 + O_2 + 7Ar$, initially at 6.67 kPa and 298 K.

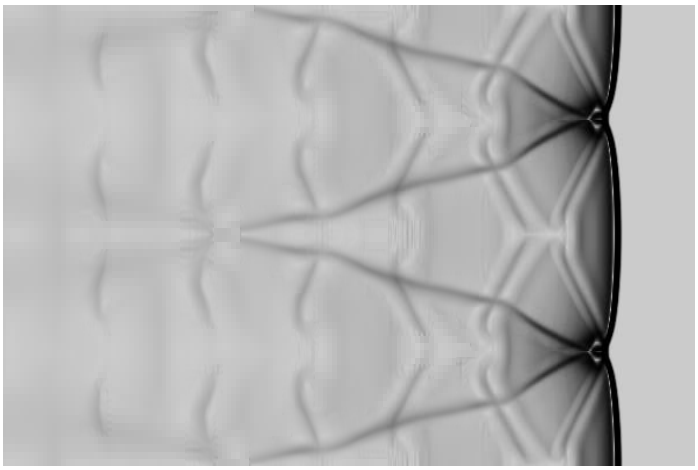

(a) Numerical schlieren–type image

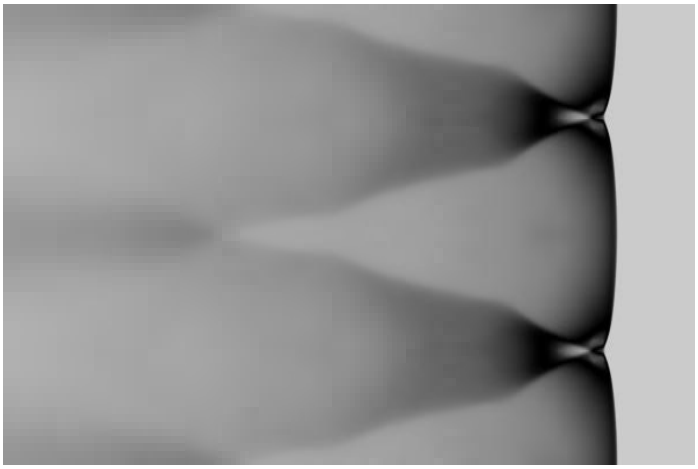

(b) Pressure

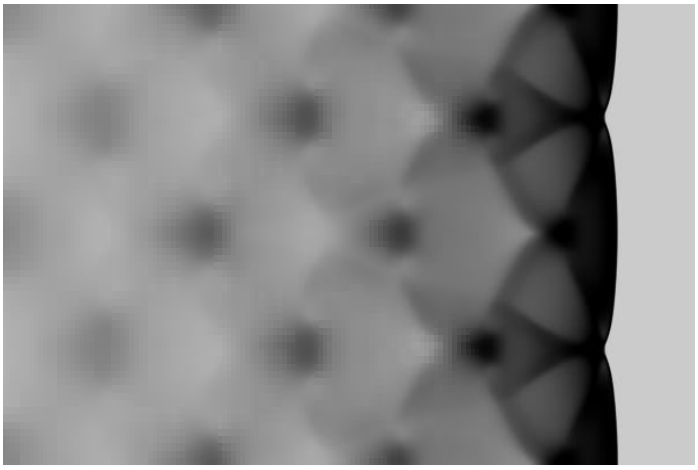

(c) Streamwise velocity

Figure 3.36: Flowfield at $t = 422.3$ μs, for a two-dimensional CJ detonation in $2H_2 + O_2 + 7Ar$, initially at 6.67 kPa and 298 K.

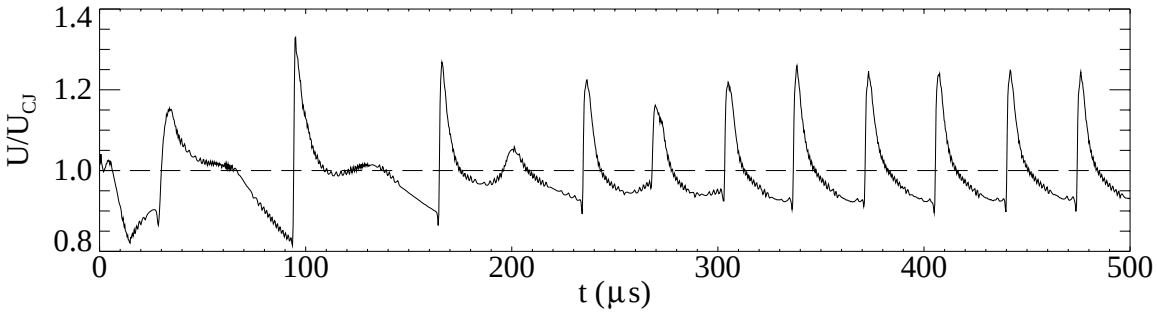

Figure 3.37: Centerline velocity of the leading shock, for a two-dimensional CJ detonation in $2H_2 + O_2 + 7Ar$, initially at 6.67 kPa and 298 K.

shading function was used for pressure,

$$\nu = 0.8 \left[1 - \exp \left\{ -25 \left(\frac{P - P_{feature}}{P_{max} - P_{min}} \right)^2 \right\} \right],$$

and similarly for the streamwise velocity u. The highlighted features were $P_{feature} =$ 180 kPa and $u_{feature} = 1150$ m/s. In the state shown, pairs of triple points are colliding. The localized dark regions in the streamwise velocity plots are embedded jets, which have been well documented. Their existence was first suggested by Subbotin (1975) on the basis of several experimental observations, and later observed in numerical simulations by Bourlioux and Majda (1992) and Quirk (1994b). The jets form at triple point collisions and give rise to the vortical structures barely evident in the schlieren image. The vortices produce the double–bow pattern slip lines (Fickett and Davis, 1979) visible in the schlieren image.

The locations of the leading shock wave on the channel centerline were tracked during the computation. They were then differentiated to give the centerline shock velocity shown in figure 3.37. It is normalized by the theoretical CJ velocity which was 1618 m/s for this mixture, as computed by STANJAN (Reynolds, 1986). The velocity appears to reach its final periodic configuration by about 350 μs. The sharp increases in velocity occur just after the triple point collisions and are associated with the embedded jets impinging on the shock front, causing it to suddenly bulge forward and the detonation to re-ignite.

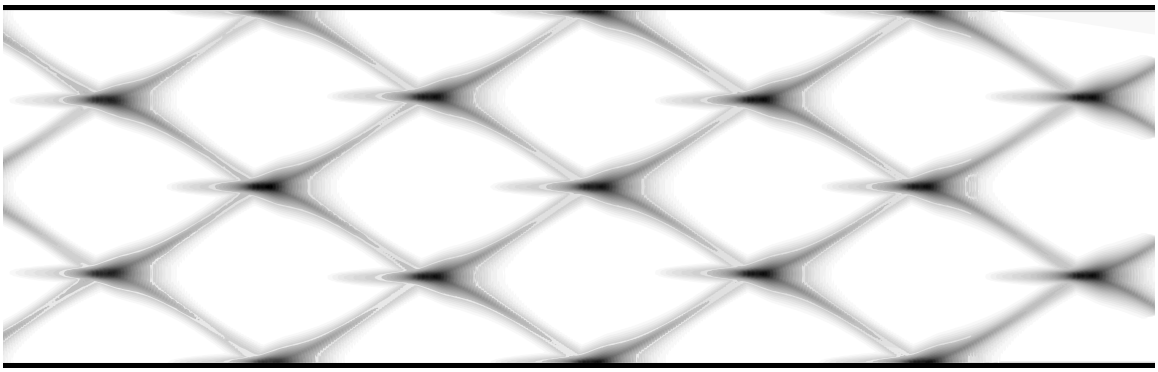

Figure 3.38: Cellular structure for a two-dimensional CJ detonation in $2H_2+O_2+7Ar$, initially at 6.67 kPa and 298 K.

The average detonation velocity in the final periodic regime after 350 μs was 1627 m/s, measuring times between velocity peaks. This is only about 0.06% greater than the theoretical CJ velocity, which supports the notion that in the absence of sidewall losses, a self-propagating cellular detonation travels with an average velocity approximately equal to the CJ velocity. It should also be noted that by measuring the average velocity between successive pairs of velocity peaks, we got speeds ranging from 1618 m/s to 1636 m/s, so the tolerance on the measured average velocity is quite large, about ± 9 m/s.

The characteristic cellular pattern traced out by the triple points is shown in figure 3.38. The plot is a linear greyscale record of the maximum pressure experienced at each point in the channel, so it is roughly equivalent to an experimental soot foil. The lines represent the triple point tracks. Only the later section of the channel is shown, where the detonation has reached its final configuration of a mode four detonation. The left edge of the plot is 50 cm downstream of the detonation front's initial location, and the detonation front reached this point at about $t = 309$ μs. The cellular structure is very regular, as expected for a heavily Ar diluted mixture (Fickett and Davis, 1979). The measured cell size is 3.0 cm width and 5.5 cm length, with variations of only ± 0.1 cm for different cells.

Cross-sectional cuts of various flowfield properties were taken at several locations and times within a half cell cycle. They are shown in Appendix F. One feature to note is the pressure amplification at the intersection points of transverse waves as

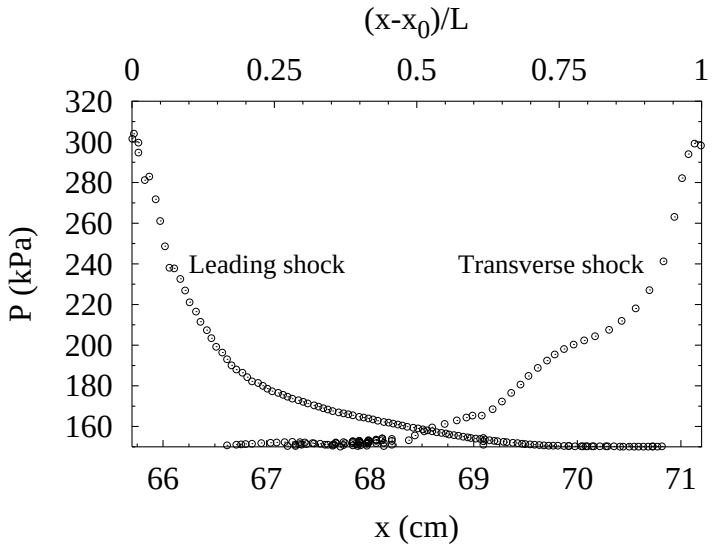

Figure 3.39: Local pressure maxima on the channel centerline within one cell of a two-dimensional CJ detonation in $2H_2 + O_2 + 7Ar$, initially at 6.67 kPa and 298 K.

these points approach the triple point collisions at the leading shock. This looks remarkably similar to the pressure pulse amplification seen in one-dimensional galloping detonation simulations. Another feature evident in the figures is the lengthening of the induction zone behind the incident leading shock just in front of a triple point collision. Finally, note the lack of variation in the H_2O mass fraction profiles between different locations and times. There is no evidence of any unreacted pockets left in the flow, suggesting that all of the fluid reacts to completion and hence all of the chemical energy is released. For this reason, we would not expect any average velocity deficit below CJ, and indeed none was observed.

The variation of shock pressure through a cell is shown in figure 3.39. The plot shows the local pressure maxima along the channel centerline, which is also the centerline of the cell. Data is plotted for all timesteps while the leading shock is passing through the region. The x-axis is non-dimensionalized by the cell length L, and the reference point x_0 is the left edge of this cell. The decay of the leading shock through the cell is evident, as is the amplification of the transverse shock intersection towards the end of the cell.

3.5.3 Discussion of results

The computational results of the two-dimensional cellular detonation with an ILDM reduced mechanism can be compared directly with the previous results of Oran et al. (1998) using detailed chemistry. In their work, the final configuration reached was also a mode four detonation, although it briefly transitioned to a mode six detonation before settling into the mode four configuration about 280 μs into the computation. The cell size was 3.0 cm in width and 5.5 cm in length which agrees perfectly with the present result.

One minor difference was that Oran et al. observed weak vertical striations in the flow that they attributed to longitudinal instability. However, our one-dimensional detonation simulations with this chemical system were hydrodynamically stable, even when computed with full detailed chemistry. This suggests a slight difference in the respective flow solvers and is not related to the used of reduced chemistry.

A more significant difference was the angle each transverse wave makes with the channel centerline. In Oran et al.'s calculation, the angle was considerably smaller. The intersection point of two transverse waves at the instant that they extended from adjacent triple point collisions was 5.2 cm behind the leading shock in figure 3.36(b), while it was 11.4 cm in the equivalent pressure contour plot of Oran et al.

A quantitative comparison can be made between the centerline velocities of the leading shock (see figure 3.37). The period and shape of the final periodic profiles agree very well, but the range between the maximum and minimum velocities was slightly greater in Oran et al.'s detailed chemistry calculation. Their velocity plot contained considerable noise, but the range in U/U_{CJ} was about 0.88 to 1.36, compared with 0.93 to 1.26 in our calculation. This difference is consistent with the observation made in the one-dimensional validation studies of §3.4.6 that the ILDM reduced mechanism detonation is slightly more stable than a detonation computed with the parent detailed mechanism.

The excellent agreement between computed cell sizes should be interpreted with caution. It is well known that propagating detonations confined in a channel usually

mode–lock, adjusting their natural cell size slightly to fit an integer number of cells across the width of the confinement (Fickett and Davis, 1979). The cells often become more regular than they would be without confinement. Thus, the only way to accurately compute the natural cell size or distribution of cell sizes in a given mixture with given initial conditions is to use a channel sufficiently wide that many cells fit across its width. Clearly, two cells across the channel is inadequate in this respect. Hence, the simulation presented here gives only a rough estimate of the cell size. The result of a mode four detonation indicates a natural spacing between about 3.5 and 4.5 transverse waves across the width of the duct, giving a cell width between 2.7 and 3.4 cm. The agreement between the detailed and reduced chemistry simulations is no better than this uncertainty.

That said, it is worth comparing the present results with previous simulations of the same detonation with other simplified reaction models. Table 3.3 lists the cell sizes from various numerical simulations and experiments, along with the average detonation velocities U_{ave} in those studies. Both of the numerical simulations by Lefebvre et al. used a two-step induction parameter model. The only difference was in the equation of state. Lefebvre et al. (1993b) used a perfect gas with model constants taken from the freestream mixture, and an empirical energy release step with a constant energy release rate tuned to give the correct CJ equilibrium state with an incorrect total energy release. Lefebvre et al. (1993a) used a more realistic equation of state with a specific heat ratio dependent on temperature and reaction progress, as well as an energy release rate based on detailed kinetics and giving the correct total energy release. The two experimental data points were obtained in channels of the same width, with one having a square cross-section (Lefebvre, 1992), and the other having a thin rectangular cross-section (Dormal et al., 1983) that reduces the effect of the third dimension and more closely models a two-dimensional flow.

Comparing the different results is difficult because the detonations traveled at markedly different average velocities. The different strengths of the leading shock waves alters the chemical induction time behind them and hence affects all chemical length scales in the flow, including the cell width. In particular, the two experiments

Study	λ (cm)	Cell aspect ratio	U_{ave} (m/s)
present work (2000)	3.0	0.55	1627
– two-dimensional simulation			
– 6.0 cm channel			
– ILDM reduced mechanism			
Oran et al. (1998)	3.0	0.55	1625
– two-dimensional simulation			
– 6.0 cm channel			
– detailed mechanism			
Lefebvre et al. (1993a)	6.0	0.57	1372
– two-dimensional simulation			
– 6.0 cm channel			
– induction parameter model			
– non-calorically-perfect gas			
Lefebvre et al. (1993b)	4.7	0.61	1623
– two-dimensional simulation			
– 4.7 cm channel			
– induction parameter model			
– perfect gas			
Lefebvre (1992)	6.1	0.53	1550
– experiment			
– 9.2×9.2 cm channel			
Dormal et al. (1983)	9.2	0.54	1475
– experiment			
– 9.2×3.2 cm channel			

Table 3.3: Summary of numerical and experimental results for unsupported detonations in $2H_2 + O_2 + 7Ar$, initially at 6.67 kPa and 298 K.

Shot number	Driver pressure (kPa)	λ (cm) Min.	Max.	Average	Cell aspect ratio	U_{ave} (m/s)
1332	1.0	3.2	4.3	3.8	0.65	1570
1333	1.4	3.0	4.1	3.7	0.66	1592

Table 3.4: Experimental results from the GALCIT detonation tube for unsupported detonations in $2H_2 + O_2 + 7Ar$, initially at 6.67 kPa and 298 K.

listed in table 3.3 were each in channels having a transverse dimension not much larger than the cell size, resulting in detonations with considerable wall losses and substantial velocity deficits below $U_{CJ} = 1618$ m/s.

To find the natural cell size that would be expected at CJ velocity with no confinement effects, an experiment was performed in a larger facility, the detonation tube at the Graduate Aeronautical Laboratories, California Institute of Technology (GALCIT). The apparatus and typical experimental procedure are described in detail by Akbar (1997) and Akbar et al. (1997). In brief, the facility is a 7.3 m long round tube with an inner diameter of 28.0 cm. Detonations are initiated at one end of the tube with an exploding wire and a small injection of sensitive acetylene–oxygen driver gas. The ensuing blast or detonation runs down the tube, soon forming an equilibrium detonation in the test gas. The detonation speed is measured with three piezoelectric pressure gauges and the cell size is measured on a cylindrical soot foil placed inside the tube at the far end. Some difficulties were encountered due to the very low pressure of the test gas, of which the driver gas pressure was a significant fraction. The total pressure in the tube, including the driver gas, was set to 6.67 kPa, so the partial pressure of the test gas was actually slightly less. Two shots were performed, one with a driver pressure of 1.0 kPa and the other with a driver pressure of 1.4 kPa. The results of the shots are summarized in table 3.4 and a soot foil from one of the shots is shown in figure 3.40. The cells are fairly regular, although not as regular as in the numerical simulation. This is to be expected since the experiment was not as confined. The spread of the measured cell widths is shown in table 3.4. The average detonation velocity was closer to the CJ velocity of 1618 m/s than the earlier experiments, although the deficit of 2 to 3% is a little larger than normally seen in

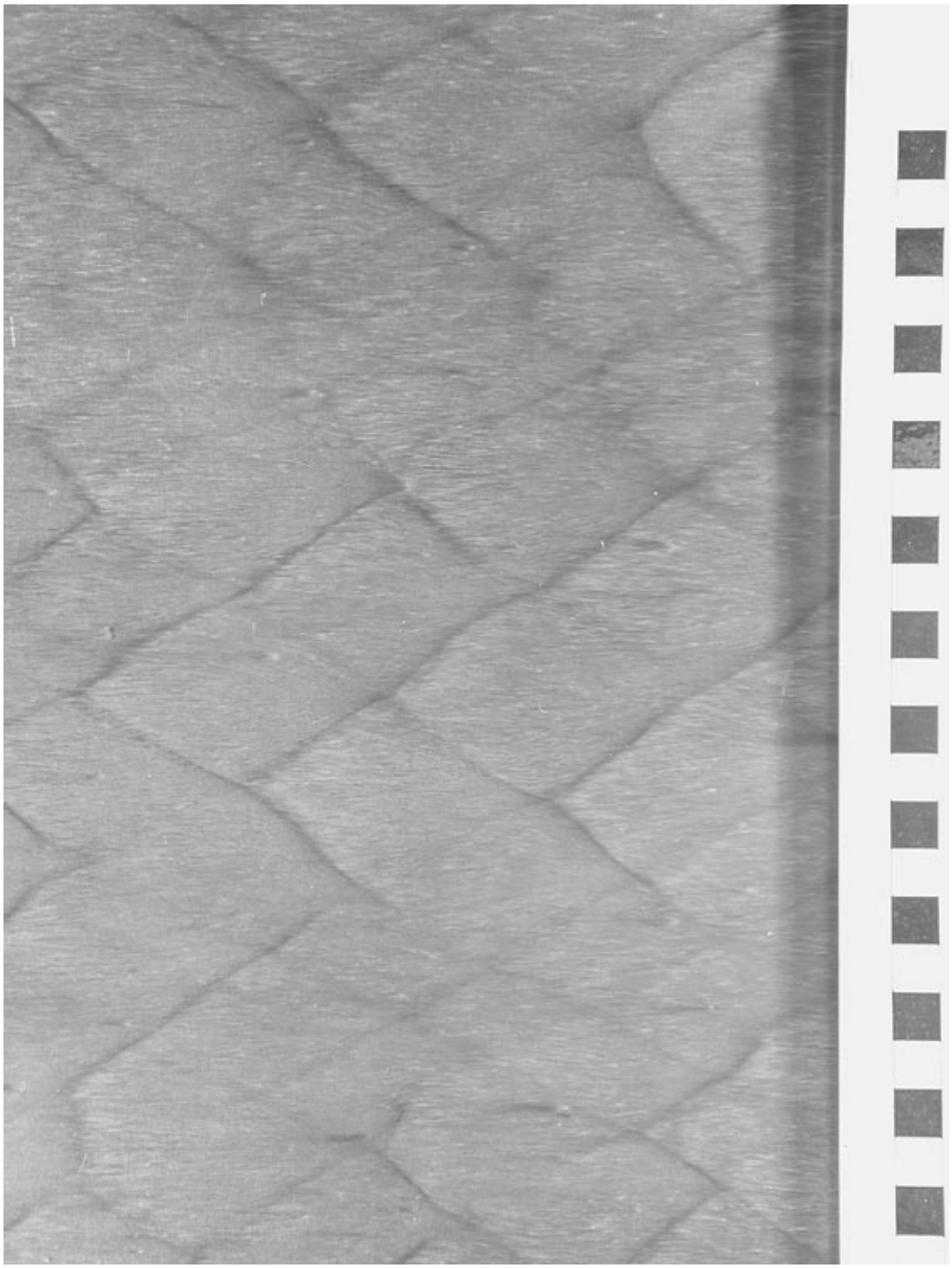

Figure 3.40: Experimental soot foil of an unsupported detonation in $2H_2 + O_2 + 7Ar$, initially at 6.67 kPa and 298 K, from shot 1332 in the GALCIT detonation tube. The scale is 1 cm per division. The detonation propagation direction is left to right.

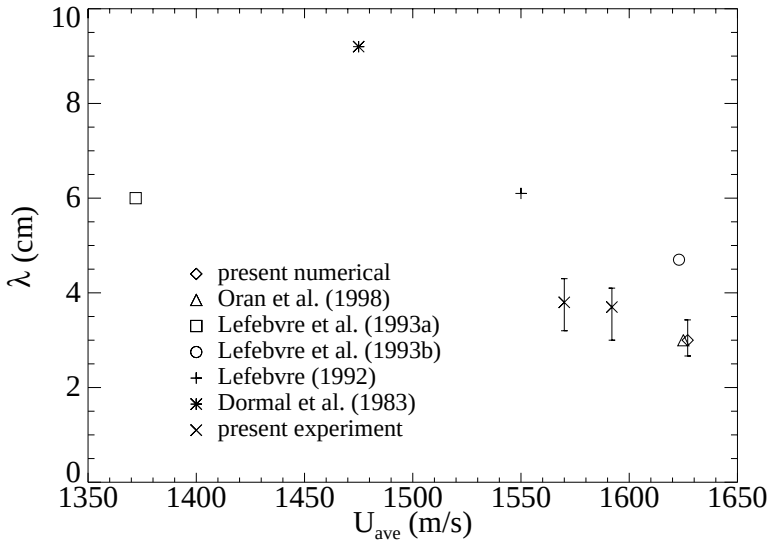

Figure 3.41: Cell width versus average detonation velocity for unsupported detonations in $2H_2 + O_2 + 7Ar$, initially at 6.67 kPa and 298 K.

this facility. The cell aspect ratio is considerably greater than all the numerical and experimental results in table 3.3. An aspect ratio of 0.65 to 0.66 gives an angle of the transverse wave tracks to the propagation direction of 33°, which is typical of unconfined detonations. A reduced aspect ratio is to be expected when there are strong confinement effects, as there was in all of the numerical and experimental studies of table 3.3.

Figure 3.41 shows the numerical and experimental data points from tables 3.3 and 3.4. The error bars on the present experiment points are the spread in measured cell widths listed in table 3.4, while the error bar on the present numerical point is the uncertainty in the numerically determined cell size due to mode–locking, as discussed earlier. The other experimental and numerical points would all have similar error bars, but since the uncertainties were not explicitly stated by the authors, they have not been shown. The experimental data points all follow a consistent trend of increasing cell width with decreasing detonation velocity. This is to be expected because decreasing the detonation velocity reduces the post-shock temperature and pressure, thereby increasing the reaction length and other related chemical length scales. The numerical data point from the realistic induction parameter model (Lefebvre et al.,

1993a) is clearly in error. The other data point from an induction parameter model (Lefebvre et al., 1993b) appears to be reasonable, although not as good as the detailed chemistry and ILDM reduced chemistry results. Furthermore, given the large errors in other computed flow quantities with the simple induction parameter model (Lefebvre et al., 1993b), as well as the contrived assumptions used to get the correct CJ state, this model is certainly seen as inferior to the detailed and ILDM reduced mechanisms.

The variation of shock pressures through a cell, shown earlier in figure 3.39, can be compared with an equivalent plot in Dormal et al. (1983) where the local pressure maxima were recorded from several piezoelectric gauges along a cell centerline. The plots are qualitatively very similar. There is some quantitative discrepancy between the actual pressure values but this is to be expected since the detonation in the experiment propagated at an average velocity about 10% less than in the numerical simulation.

The detailed chemistry and ILDM reduced chemistry computed cell sizes appear to be consistent with the experimental data, especially when allowing for the large uncertainty in both experimental and numerical cell size determination in channels of small width. However, we believe the validation of the ILDM reduced chemistry simulation with the detailed chemistry simulation is sufficient validation, since there are several reasons one would not expect perfect agreement between an experiment and a two-dimensional simulation. These include:

1. In an experiment, there are viscous boundary layer losses and heat losses at the walls of the channel. These are most pronounced when there are few cells across the width of the channel, that is, close to the detonation limit. The losses cause such detonations to propagate at average velocities below CJ, and the cell size to be greater than the unconfined natural cell size, as seen in figure 3.41. However, inviscid numerical simulations would be expected to propagate at the CJ velocity, and have close to the natural cell size if the channel is wide enough.

2. Experimental cell sizes are usually measured from soot foil traces which show a

lot of variability, especially in fuel–O_2 and fuel–air mixtures. Different observers can measure markedly different average cell sizes from the same foil. Unfortunately, the variability is rarely quoted with the published average measurements. Thus, the cell width is an ill-defined quantity for many mixtures.

3. In an experiment in a square or rectangular channel, there will be "slapping" transverse waves in the third dimension. Besides complicating the interpretation of flow visualization, it is not known how this changes the cell size or structure from a purely two-dimensional flow. This is a still a topic of research. The three-dimensional effect can be reduced by using a channel with a thin third dimension, but not eliminated.

4. The majority of published cell size data is for round tubes, which have a completely different instability structure than rectangular channels. Two-dimensional simulations are expected to more closely model thin channel experiments.

3.6 Conclusions

Reduced reaction mechanisms have been demonstrated as a viable option for gaseous detonation simulations when more accuracy is desired than an empirical one or two-step reaction model. The simple technique of Quasi Steady State Approximation was used to develop a three-step reduced mechanism for H_2–O_2–diluent systems suitable for detonation simulations across a wide range of conditions and mixtures. The mechanism was found to predict ZND induction lengths to within a factor of two, and give reasonable agreement with detailed chemistry in one-dimensional unsteady detonation simulations. However, due to the significant quantitative errors as well as a number of implementation difficulties when trying to improve the computational efficiency of the model or apply it to a large chemical system, we decided to pursue a more advanced reduction technique.

The method of Intrinsic Low-Dimensional Manifolds was discussed and a code for computing manifolds of arbitrary dimension was developed. The code was verified

against published homogeneous combustion results and then used to compute two-dimensional manifolds for H_2–O_2–diluent detonation systems. Implementation of the method into ignition-type applications was demonstrated to be feasible with the use of a separate induction manifold to represent the chemical reactions in the induction zone where the system had not yet collapsed onto the low-dimensional manifold. This method permitted accurate reproduction of the induction time while still maintaining the excellent computational efficiency of the scheme. Without the use of an induction manifold, a three or four-dimensional ILDM would have been necessary to capture the induction region in the H_2–O_2–diluent examples. The ILDM reduced mechanism coupled with the induction manifold was found to reproduce detailed chemistry constant volume combustion and steady ZND detonation almost exactly, a major improvement on the three-step QSSA mechanism. It was also found to give reasonably good agreement with detailed chemistry in unsteady one-dimensional detonation simulations, although, as for the QSSA method, the neutral stability limit was slightly shifted.

Finally, the ILDM reduced mechanism was used to simulate a two-dimensional cellular detonation in 70% Ar diluted stoichiometric H_2–O_2. The agreement with previously published detailed chemistry results for this mixture was excellent, showing significant improvements on earlier induction parameter models. The predicted mode number of the detonation was the same as in the detailed chemistry simulation. The detailed chemistry and ILDM reduced chemistry results were consistent with experimental data, verifying the ability to accurately simulate gaseous detonations with an inviscid Euler code and a sufficiently advanced chemical model, at least in the case of regular detonations and the absence of significant wall losses.

Numerical simulations of a one-dimensional unsteady H_2–O_2 detonation on a fixed mesh took about four times less CPU time with ILDM reduced chemistry than with the QSSA reduced mechanism, and 15 times less than with detailed chemistry. The improvement over detailed chemistry would be even greater when noting that a coarser mesh could be used for a grid converged solution with the reduced mechanism. The ILDM simulations were about an order of magnitude more expensive than a simple one-step Arrhenius model and presumably a few times slower than a two-step perfect

gas induction parameter model, but the greatly improved accuracy warrants this extra expense in many situations. The true value of ILDM reduced mechanisms will come in simulations of larger chemical systems such as hydrocarbons or nitramines. For these systems, detailed chemistry simulations of multi-dimensional detonations are completely infeasible, but with only a few extra manifold dimensions, ILDM reduced chemistry could be applied to these systems, at an expense not too much greater than the hydrogen simulations presented here.

Bibliography

Akbar, R. (1997). *Mach Reflection of Gaseous Detonations*. Ph.D. thesis, Rensselaer Polytechnic Institute.

Akbar, R., M. Kaneshige, E. Schultz, and J. E. Shepherd (1997). Detonations in H_2–N_2O–CH_4–NH_3–O_2–N_2 mixtures. Technical Report FM97-3, Graduate Aeronautical Laboratories at California Institute of Technology.

Alpert, R. L. and T. Y. Toong (1972). Periodicity in exothermic hypersonic flows about blunt projectiles. *Astronautica Acta 17*, 539–560.

Anderson, E., Z. Bai, C. Bischof, J. Demmel, J. Dongarra, J. Du Croz, A. Greenbaum, S. Hammarling, A. McKenney, S. Ostrouchov, and D. Sorensen (1995). *LAPACK Users' Guide* (2nd ed.). SIAM.

Benedick, W. B., C. M. Guirao, R. Knystautas, and J. H. S. Lee (1986). Critical charge for the direct initiation of detonation in gaseous fuel–air mixtures. *Prog. Astronaut. Aeronaut. 106*, 181–202.

Blasenbrey, T., D. Schmidt, and U. Maas (1998). Automatically simplified chemical kinetics and molecular transport and its applications in premixed and non-premixed laminar flame calculations. In *27th Symp. (Intl) on Combustion*, pp. 505–511. The Combustion Institute.

Bourlioux, A. and A. J. Majda (1992). Theoretical and numerical structure for unstable two-dimensional detonations. *Combust. Flame 90*, 211–229.

Bourlioux, A., A. J. Majda, and V. Roytburd (1991). Theoretical and numerical structure for unstable one-dimensional detonations. *SIAM J. Appl. Math. 51*, 303–343.

Bowman, C. T., R. K. Hanson, D. F. Davidson, W. C. Gardiner, Jr., V. Lissianski, G. P. Smith, D. M. Golden, M. Frenklach, and M. Goldenberg (1995). *GRI-Mech 2.11*. `http://www.me.berkeley.edu/gri_mech/`.

Bull, D. C., J. E. Elsworth, and G. Hooper (1979). Susceptibility of methane-ethane mixtures to gaseous detonation in air. *Combust. Flame 34*, 327–330.

Bull, D. C., J. E. Elsworth, G. Hooper, and C. P. Quinn (1976). A study of spherical detonation in mixtures of methane and oxygen diluted by nitrogen. *J. Phys.* D *Appl. Phys. 9*, 1991–2000.

Burks, T. L. and E. S. Oran (1992). A computational study of the chemical kinetics of hydrogen combustion. NRL Memorandum Report 4446, Naval Research Laboratory.

Clarke, J. F., D. R. Kassoy, N. E. Meharzi, N. E. Riley, and R. Vasantha (1990). On the evolution of plane detonations. *Proc. R. Soc. Lond.* A *429*, 259–283.

Clarke, J. F., D. R. Kassoy, and N. Riley (1986). On the direct initiation of a plane detonation wave. *Proc. R. Soc. Lond.* A *408*, 129–148.

Dormal, M., J. C. Liboutin, and P. J. Van Tiggelen (1983). Etude experimentale des parametres a l'interieur d'une maille de detonation. *Explosifs 36*, 76–94.

Eckett, C. A., J. J. Quirk, and J. E. Shepherd (2000). The role of unsteadiness in direct initiation of gaseous detonations. *J. Fluid Mech. 421*, 147–183.

Eggels, R. L. G. M. and L. P. H. DeGoey (1995a). Mathematically reduced reaction-mechanisms applied to adiabatic flat hydrogen–air flames. *Combust. Flame 100*, 559–570.

Eggels, R. L. G. M. and L. P. H. DeGoey (1995b). Modeling of burner-stabilized hydrogen/air flames using mathematically reduced reaction schemes. *Combust. Sci. Technol. 107*, 165–180.

Eggels, R. L. G. M., J. J. J. Louis, J. B. W. Kok, and L. P. H. DeGoey (1997). Comparison of conventional and low-dimensional manifold methods to reduce reaction mechanisms. *Combust. Sci. Technol. 123*, 347–362.

Erpenbeck, J. J. (1964). Stability of idealized one-reaction detonations. *Phys. Fluids 7*, 684–696.

Fickett, W. and W. C. Davis (1979). *Detonation*. University of California Press.

Fickett, W. and W. W. Wood (1966). Flow calculations for pulsating one-dimensional detonations. *Phys. Fluids 9*, 903–916.

Frank-Kamenetskii, D. A. (1969). *Diffusion and Heat Transfer in Chemical Kinetics*. Plenum.

Gavrikov, A. I., A. A. Efimenko, and S. B. Dorofeev (2000). A model for detonation cell size prediction from chemical kinetics. *Combust. Flame 120*, 19–33.

Gicquel, O., D. Thevenin, M. Hilka, and N. Darabiha (1999). Direct numerical simulation of turbulent premixed flames using intrinsic low-dimensional manifolds. *Combust. Theor. Model. 3*, 479–502.

Glaister, P. (1988). An approximate linearised Riemann solver for the Euler equations for real gases. *J. Comput. Phys. 74*, 382–408.

Harten, A. (1983). High resolution schemes for hyperbolic conservation–laws. *J. Comput. Phys. 49*, 357–393.

He, L. (1996). Theoretical determination of the critical conditions for the direct initiation of detonations in hydrogen–oxygen mixtures. *Combust. Flame 104*, 401–418.

He, L. and P. Clavin (1994). On the direct initiation of gaseous detonations by an energy source. *J. Fluid Mech. 277*, 227–248.

Henry, G., B. Cole, and P. Fay (1999). *ASCI Red Pentium II BLAS 1.2D*. `http://www.cs.utk.edu/~ghenry/distrib/`.

Hindmarsh, A. C. (1983). ODEPACK: A systematized collection of ODE solvers. In R. S. Stepleman et al. (Eds.), *Scientific Computing*, pp. 55–64. Amsterdam: North-Holland.

Kee, R. J., F. M. Rupley, and J. A. Miller (1989). CHEMKIN-II: A Fortran chemical kinetics package for the analysis of gas-phase chemical kinetics. Technical Report SAND89-8009, Sandia National Laboratories.

Korobeinikov, V. P. (1968). Point explosion in a detonating gas. *Soviet Physics – Doklady 12*, 1003–1005.

Korobeinikov, V. P. (1991). *Problems of Point-Blast Theory*. American Institute of Physics.

Korobeinikov, V. P., V. A. Levin, V. V. Markov, and G. G. Chernyi (1972). Propagation of blast wave in a combustible gas. *Astronautica Acta 17*, 529–537.

Lam, S. H. (1993). Using CSP to understand complex chemical kinetics. *Combust. Sci. Technol. 89*, 375–404.

Lam, S. H. and D. A. Goussis (1988). Understanding complex chemical kinetics with computational singular perturbations. In *22nd Symp. (Intl) on Combustion*, pp. 931–941. The Combustion Institute.

Lee, H. I. and D. S. Stewart (1990). Calculation of linear detonation instability: One-dimensional instability of plane detonation. *J. Fluid Mech. 216*, 103–132.

Lee, J. H. S. (1977). Initiation of gaseous detonation. *Ann. Rev. Phys. Chem. 28*, 75–104.

Lee, J. H. S. (1984). Dynamic parameters of gaseous detonations. *Ann. Rev. Fluid Mech. 16*, 311–336.

Lee, J. H. S. (1996). On the critical diameter problem. In J. R. Bowen (Ed.), *Dynamics of Exothermicity*, pp. 321–336. Netherlands: Gordon and Breech Science Publishers.

Lee, J. H. S. and A. J. Higgins (1999). Comments on criteria for direct initiation of detonation. *Phil. Trans. R. Soc. Lond.* A *357*, 3503–3521.

Lee, J. H. S. and H. Matsui (1977). A comparison of the critical energies for direct initiation of spherical detonations in acetylene-oxygen mixtures. *Combust. Flame 28*, 61–66.

Lefebvre, M. H. (1992). *Contribution a L'etude Numerique des Detonations, Modelisation de la Structure Cellulaire et Role de la Cinetique Chimique*. Ph.D. thesis, Universite Catholique de Louvain, Belgium.

Lefebvre, M. H., E. S. Oran, and K. Kailasanath (1992). Computations of detonation structure: The influence of model parameters. NRL Memorandum Report NRL/MR/4404-92-6961, Naval Research Laboratory.

Lefebvre, M. H., E. S. Oran, K. Kailasanath, and P. J. Van Tiggelen (1993a). The influence of the heat capacity and diluent on detonation structure. *Combust. Flame 95*, 206–218.

Lefebvre, M. H., E. S. Oran, K. Kailasanath, and P. J. Van Tiggelen (1993b). Simulation of cellular structure in a detonation wave. *Prog. Astronaut. Aeronaut. 153*, 64–77.

Litchfield, E. L., M. H. Hay, and D. R. Forshey (1963). Direct electrical initiation of freely expanding gaseous detonation waves. In *9th Symp. (Intl) on Combustion*, pp. 282–286. Academic.

Maas, U. (1998). Efficient calculation of intrinsic low-dimensional manifolds for the simplification of chemical kinetics. *Comput. Visual. Sci. 1*, 69–81.

Maas, U. (1999). Personal communication.

Maas, U. and S. B. Pope (1992a). Implementation of simplified chemical kinetics based on intrinsic low–dimensional manifolds. In *24th Symp. (Intl) on Combustion*, pp. 103–112. The Combustion Institute.

Maas, U. and S. B. Pope (1992b). Simplifying chemical kinetics: Intrinsic low–dimensional manifolds in composition space. *Combust. Flame 88*, 239–264.

Maas, U. and S. B. Pope (1994). Laminar flame calculations using simplified chemical kinetics based on intrinsic low–dimensional manifolds. In *25th Symp. (Intl) on Combustion*, pp. 1349–1356. The Combustion Institute.

Maas, U. and J. Warnatz (1988). Ignition proceses in hydrogen–oxygen mixtures. *Combust. Flame 74*, 53–69.

Matsui, H. and J. H. S. Lee (1979). On the measure of the relative detonation hazards of gaseous fuel-oxygen and air mixtures. In *17th Symp. (Intl) on Combustion*, pp. 1269–1280. The Combustion Institute.

Mazaheri, K. (1997). *Mechanism of the Onset of Detonation in Blast Initiation*. Ph.D. thesis, Department of Mechanical Engineering, McGill University.

Miller, J. A. and C. T. Bowman (1989). Mechanism and modeling of nitrogen chemistry in combustion. *Prog. Energy Combust. Sci. 15*, 287–338.

Nau, M., W. Neef, U. Maas, J. Segatz, U. Riedel, and J. Warnatz (1996). Computational and experimental investigation of a turbulent non-premixed methane flame. In *26th Symp. (Intl) on Combustion*, pp. 83–89. The Combustion Institute.

Nooren, P. A., H. A. Wouters, T. W. J. Peeters, D. Roekaerts, U. Maas, and D. Schmidt (1997). Monte Carlo PDF modelling of a turbulent natural-gas diffusion flame. *Combust. Theor. Model. 1*, 79–96.

Norris, A. T. and S. B. Pope (1995). Modeling of extinction in turbulent–diffusion flames by the velocity–dissipation–composition PDF method. *Combust. Flame 100*, 211–220.

Oran, E. S., J. P. Boris, T. Young, M. Flanigan, T. Burks, and M. Picone (1981). Numerical simulations of detonations in hydrogen–air and methane–air mixtures. In *18th Symp. (Intl) on Combustion*, pp. 1641–1649. The Combustion Institute.

Oran, E. S., J. W. Weber, Jr., E. I. Stefaniw, M. H. Lefebvre, and J. D. Anderson, Jr. (1998). A numerical study of a two-dimensional H_2–O_2–Ar detonation using a detailed chemical reaction model. *Combust. Flame 113*, 147–163.

Oran, E. S., T. R. Young, J. P. Boris, J. M. Picone, and D. H. Edwards (1982). A study of detonation structure: The formation of unreacted gas pockets. In *19th Symp. (Intl) on Combustion*, pp. 573–582. The Combustion Institute.

Paczko, G. and R. Klein (1993). Reduced chemical kinetic schemes for hydrogen–air–steam detonation simulations. Unpublished. Presented at *14th ICDERS*, Coimbra, Portugal.

Paolucci, S., J. M. Powers, and S. Singh (2000). Application of intrinsic low dimensional manifolds to nitramine combustion. Unpublished. Presented at *8th Int. Conf. Numer. Combust.*, Amelia Island, Florida.

Peters, N. (1988). Systematic reduction of flame kinetics: Principles and details. *Prog. Astronaut. Aeronaut. 113*, 67–86.

Peters, N. (1991). Reducing mechanisms. In M. D. Smooke (Ed.), *Reduced Kinetic Mechanisms and Asymptotic Approximations for Methane–Air Flames*, Lecture Notes in Physics 384, pp. 48–67. Springer–Verlag.

Peters, N. and B. Rogg (Eds.) (1992). *Reduced Kinetic Mechanisms for Applications in Combustion Systems*. Lecture Notes in Physics m15. Springer–Verlag.

Petzold, L. (1983). Automatic selection of methods for solving stiff and nonstiff systems of ordinary differential-equations. *SIAM J. Sci. Stat. Comp. 4*, 136–148.

Quirk, J. J. (1994a). A contribution to the great Riemann solver debate. *Int. J. Numer. Meth. Fluids 18*, 555–574.

Quirk, J. J. (1994b). Godunov-type schemes applied to detonation flows. In J. Buckmaster et al. (Eds.), *Combustion in High-Speed Flows*, pp. 575–596. Kluwer Academic Publishers.

Quirk, J. J. (1998). (i) Amrita: A computational facility (for CFD modelling), (ii) Amr_sol: Design principles and practice. In H. Deconinck (Ed.), 29$^{\text{th}}$ *Computational Fluid Dynamics lecture series*. von Karman Institute. `http://www.amrita-cfd.org/doc`.

Reynolds, W. C. (1986). The element potential method for chemical equilibrium analysis: Implementation in the interactive program STANJAN. Technical report, Stanford University, Dept of Mech. Engng.

Rheinboldt, W. C. and J. Burkardt (1983). Algorithm 596: A program for a locally parameterized continuation process. *ACM Trans. Math. Soft. 9*, 236–241.

Roe, P. L. (1986). Characteristic-based schemes for the Euler equations. *Ann. Rev. Fluid Mech. 18*, 337–365.

Schmidt, D., T. Blasenbrey, and U. Maas (1998). Intrinsic low-dimensional manifolds of strained and unstrained flames. *Combust. Theor. Model. 2*, 135–152.

Schmidt, D., J. Segatz, U. Riedel, and J. Warnatz (1996). Simulation of laminar methane–air flames using automatically simplified chemical kinetics. *Combust. Sci. Technol. 113*, 3–16.

Schultz, E. and J. E. Shepherd (1999). Validation of detailed reaction mechanisms for detonation simulation. Technical Report FM99-5, Graduate Aeronautical Laboratories at California Institute of Technology.

Sedov, L. I. (1959). *Similarity and Dimensional Methods in Mechanics* (4th ed.). Academic.

Shampine, L. F. and H. A. Watts (1970). ZEROIN, a root-solving code. Technical Report SAND SC-TM-70-631, Sandia National Laboratories.

Shampine, L. F. and H. A. Watts (1979). DEPAC – Design of a user oriented package of ODE solvers. Technical Report SAND79-2374, Sandia National Laboratories.

Shepherd, J. E. (1986). Chemical kinetics of hydrogen–air–diluent detonations. *Prog. Astronaut. Aeronaut. 106*, 263–293.

Shuen, J.-S., M.-S. Liou, and B. van Leer (1990). Inviscid flux-splitting algorithms for real gases with non-equilibrium chemistry. *J. Comput. Phys. 90*, 371–395.

Singh, S. and J. M. Powers (1999). Modeling gas phase RDX combustion with intrinsic low dimensional manifolds. Unpublished. Paper no. 82 presented at *17th ICDERS*, Heidelberg, Germany.

Stewart, D. S., T. D. Aslam, and J. Yao (1996). On the evolution of cellular detonation. In *26th Symp. (Intl) on Combustion*, pp. 2981–2989. The Combustion Institute.

Stewart, D. S. and J. B. Bdzil (1988). The shock dynamics of stable multi-dimensional detonation. *Combust. Flame 72*, 311–323.

Strang, G. (1968). On the construction and comparison of difference schemes. *SIAM J. Numer. Anal. 5*, 506–517.

Stull, D. and H. Prophet (1971). *JANAF Thermochemical Tables*. U.S. National Bureau of Standards. NSRDS-NBS 37.

Subbotin, V. A. (1975). Collisions of transverse waves in gas detonations. *Fiz. Goreniya Vzryva 11*, 486–491.

Taki, S. and T. Fujiwara (1978). Numerical analysis of two-dimensional nonsteady detonations. *AIAA Journal 16*, 73–77.

Taylor, G. I. (1950). The formation of a blast wave by a very intense explosion. I. Theoretical discussion. *Proc. R. Soc. Lond.* A *201*, 159–174.

Thompson, P. A. (1988). *Compressible–Fluid Dynamics*. Rensselaer Polytechnic Institute.

Tomlin, A. S., T. Turanyi, and M. J. Pilling (1997). Mathematical tools for the construction, investigation and reduction of combustion mechanisms. In M. J. Pilling (Ed.), *Low–Temperature Combustion and Autoignition*, pp. 293–437. Elsevier.

Turanyi, T., K. J. Hughes, M. J. Pilling, and A. S. Tomlin (1996). KINALC: Program for the analysis of reaction mechanisms. *Combustion Simulations at The University of Leeds*. `http://chem.leeds.ac.uk/Combustion/Combustion.html`.

Weber, Jr., J. W., E. S. Oran, G. Patnaik, and J. D. Anderson, Jr. (1997). Load balancing and performance issues for data parallel simulation of stiff chemical nonequilibrium flows. *AIAA Journal 35*, 486–493.

Westbrook, C. (1982). Chemical kinetics of hydrocarbon oxidation in gaseous detonations. *Combust. Flame 46*, 191–210.

Xiao, K., D. Schmidt, and U. Maas (1998). PDF simulation of turbulent non-premixed CH_4/H_2–air flames using automatically reduced chemical kinetics. In *27th Symp. (Intl) on Combustion*, pp. 1073–1080. The Combustion Institute.

Yao, J. and D. S. Stewart (1995). On the normal shock velocity–curvature relationship for materials with large activation energy. *Combust. Flame 100*, 519–528.

Yao, J. and D. S. Stewart (1996). On the dynamics of multi-dimensional detonation. *J. Fluid Mech. 309*, 225–275.

Zel'dovich, I. B., S. M. Kogarko, and N. N. Simonov (1956). An experimental investigation of spherical detonation of gases. *Sov. Phys. Tech. Phys. 1*(8), 1689–1713.

Appendix A Analytical Ratio of Curvature to Unsteadiness

In section 2.3.2, the curvature term in the temperature reaction zone structure equation (2.13) was seen to be much smaller than the unsteadiness term, numerically. Here we examine the ratio of these terms analytically. Since the numerics suggested each of these terms were constant in the induction zone, prior to failure, we can approximate their ratio by their initial ratio just behind the leading shock. Using (2.13), and the strong shock perfect gas jump conditions (2.27), the ratio of curvature to unsteadiness is

$$\frac{j}{3}\frac{\gamma-1}{\gamma+1}\frac{U^2}{R}\frac{1}{\mathrm{d}U/\mathrm{d}t}.$$

To compute this ratio, a shock velocity profile is required. As detailed in §2.6, we adopt the modified Taylor–Sedov solution for a strong point blast with chemical energy release. Using (2.32a) and (2.33), the absolute value of the above ratio reduces to

$$\frac{2}{3}\,\frac{j}{j+1}\frac{\gamma-1}{\gamma+1}\left(1+\frac{j+2}{j+1}\,\frac{B_jQ}{U^2}\right)\exp\left\{-\frac{B_jQ}{(j+1)U^2}\right\}.$$

This expression appears quite complicated, but if we evaluate it in the spherical case ($j=2$) at the failure point $U=U_*$ for the real gas mixtures studied in figures 2.19 to 2.21, we find it is almost constant at 0.1, with the maximum value for any of the mixtures or stoichiometries being only 0.12. In the cylindrical case ($j=1$), the ratio will be even less. Hence, from an analytical consideration of the terms in the temperature reaction zone structure equation, we conclude that the curvature term is at least one order of magnitude smaller than the unsteadiness term in the critical region of the flow. Thus it is justifiably omitted from the analysis.

Appendix B Roe Solver for General Equation of State and Non-equilibrium Chemistry

For the numerical simulations in this work, the flow solver used for the convective step in the operator-split integration of the reactive Euler equations was an approximate Riemann solver based on Roe's method (Roe, 1986). Roe originally presented the scheme only for equilibrium perfect gases. Glaister (1988) later extended it to equilibrium fluids with arbitrary equation of state, $P = P(\rho, e)$. The method used here is based on Glaister's implementation, but extended to fluids in chemical non-equilibrium. The chemical reactions do not enter directly in the convective step, but the equation of state must be expressed as a function of the chemical composition, and the composition must be advected through the computational mesh in the convective step.

The formulation presented here is for two-dimensional flow but is also applicable to one-dimensional flow by simply omitting the y-directional dependencies. For generality, the chemical composition of the fluid will be described by a vector $\boldsymbol{Z} = (Z_1, Z_2, \ldots, Z_N)^T$. This could denote the single reaction progress variable Z in the one-step reaction model of chapter 2, the n_r reaction progress variables $\boldsymbol{\theta}$ in the ILDM reduced mechanism of §3.4, or the n_s species mass fractions $\boldsymbol{y}$ in the detailed reaction mechanism of §3.2.

The two-dimensional reactive Euler equations in conservative form are

$$\frac{\partial \boldsymbol{W}}{\partial t} + \frac{\partial \boldsymbol{F}_x}{\partial x} + \frac{\partial \boldsymbol{F}_y}{\partial y} = \boldsymbol{S},$$

where

$$\boldsymbol{W} = \begin{pmatrix} \rho \\ \rho u \\ \rho v \\ E_t \\ \rho Z_1 \\ \vdots \\ \rho Z_N \end{pmatrix}, \quad \boldsymbol{F}_x = \begin{pmatrix} \rho u \\ \rho u^2 + P \\ \rho uv \\ (E_t + P)u \\ \rho u Z_1 \\ \vdots \\ \rho u Z_N \end{pmatrix}, \quad \boldsymbol{F}_y = \begin{pmatrix} \rho v \\ \rho uv \\ \rho v^2 + P \\ (E_t + P)v \\ \rho v Z_1 \\ \vdots \\ \rho v Z_N \end{pmatrix}, \quad \boldsymbol{S} = \begin{pmatrix} 0 \\ 0 \\ 0 \\ 0 \\ \rho \Omega_1 \\ \vdots \\ \rho \Omega_N \end{pmatrix}.$$

E_t is the total energy per unit volume, given by

$$E_t = \rho \left(e + \frac{|\boldsymbol{u}|^2}{2} \right),$$

where $|\boldsymbol{u}|^2 = u^2 + v^2$. The caloric equation of state is expressed in the form,

$$P = P(\rho, e, Z_1, \ldots, Z_N).$$

The partial derivatives of pressure will be required, and for convenience, they are denoted by the shorthand notation,

$$P_\rho = \left.\frac{\partial P}{\partial \rho}\right|_{e,\boldsymbol{Z}}, \qquad P_e = \left.\frac{\partial P}{\partial e}\right|_{\rho,\boldsymbol{Z}},$$
$$P_{Z_k} = \left.\frac{\partial P}{\partial Z_k}\right|_{\rho,e,Z_{j\neq k}}, \qquad k = 1, \ldots, N.$$

The frozen sound speed $c = (\partial P/\partial \rho)_{s,\boldsymbol{Z}}$ can be shown to satisfy

$$c^2 = P_\rho + \frac{P P_e}{\rho^2}.$$

Finally, the specific total enthalpy is

$$H = \frac{E_t + P}{\rho} = e + \frac{P}{\rho} + \frac{|\boldsymbol{u}|^2}{2}.$$

In an operator-split solution, the x-direction convective step is the integration of

$$\frac{\partial \boldsymbol{W}}{\partial t} + \frac{\partial \boldsymbol{F}}{\partial x} = \boldsymbol{0}, \tag{B.1}$$

where $\boldsymbol{F} = \boldsymbol{F}_x$. The y-direction convective step is defined similarly, and is integrated with the same algorithm described henceforth for the x-direction. The Jacobian $\partial \boldsymbol{F}/\partial \boldsymbol{W}$ can be shown to be

$$\begin{pmatrix}
0 & 1 & 0 & 0 & 0 & \cdots\cdots & 0 \\
\left\{c^2 - u^2 - \frac{P_e}{\rho}\left(H - |\boldsymbol{u}|^2\right) - \sum_{k=1}^{N} \frac{Z_k P_{Z_k}}{\rho}\right\} & u\left(2 - \frac{P_e}{\rho}\right) & -\frac{vP_e}{\rho} & \frac{P_e}{\rho} & \frac{P_{Z_1}}{\rho} & \cdots\cdots & \frac{P_{Z_N}}{\rho} \\
-uv & v & u & 0 & 0 & \cdots\cdots & 0 \\
u\left\{c^2 - H - \frac{P_e}{\rho}\left(H - |\boldsymbol{u}|^2\right) - \sum_{k=1}^{N} \frac{Z_k P_{Z_k}}{\rho}\right\} & H - \frac{u^2 P_e}{\rho} & -\frac{uvP_e}{\rho} & u\left(1 + \frac{P_e}{\rho}\right) & \frac{uP_{Z_1}}{\rho} & \cdots\cdots & \frac{uP_{Z_N}}{\rho} \\
-uZ_1 & Z_1 & 0 & 0 & u & 0 \ \cdots & 0 \\
\vdots & \vdots & \vdots & \vdots & 0 & u \ \ddots & \vdots \\
\vdots & \vdots & \vdots & \vdots & \vdots & \ddots\ u & 0 \\
-uZ_N & Z_N & 0 & 0 & 0 & \cdots\ 0 & u
\end{pmatrix}.$$

The eigenvalues and right eigenvectors of the Jacobian are

$$\begin{aligned}
\lambda_1 &= u - c, & \boldsymbol{e}_1 &= \Big(1,\ u - c,\ v,\ H - uc,\ Z_1,\ \ldots,\ Z_N\Big)^T, \\
\lambda_2 &= u, & \boldsymbol{e}_2 &= \Big(1,\ u,\ v,\ H - \tfrac{\rho c^2}{P_e},\ Z_1,\ \ldots,\ Z_N\Big)^T, \\
\lambda_3 &= u, & \boldsymbol{e}_3 &= \Big(0,\ 0,\ 1,\ v,\ 0,\ \ldots,\ 0\Big)^T, \\
\lambda_4 &= u + c, & \boldsymbol{e}_4 &= \Big(1,\ u + c,\ v,\ H + uc,\ Z_1,\ \ldots,\ Z_N\Big)^T, \\
\lambda_{4+k} &= u, & \boldsymbol{e}_{4+k} &= \Big(0,\ 0,\ 0,\ -\tfrac{P_{Z_k}}{P_e},\ \underbrace{0,\ldots,0}_{k-1},\ 1,\ 0,\ldots,0\Big)^T.
\end{aligned}$$

Following Glaister (1988), the derivation of Roe's scheme now proceeds by the following steps:

1. Given two states $\boldsymbol{W}_L$ and $\boldsymbol{W}_R$ (left and right) close to an average state $\boldsymbol{W}$, seek coefficients $\{\alpha_k\ ;\ k = 1, 2, \ldots, 4+N\}$ such that

$$\Delta \boldsymbol{W} = \sum_{k=1}^{4+N} \alpha_i \boldsymbol{e}_i, \tag{B.2}$$

   to within $O(\Delta^2)$, where $\Delta(\cdot) = (\cdot)_R - (\cdot)_L$. It can be shown that the same $\{\alpha_i\}$ also satisfy

$$\Delta \boldsymbol{F} = \sum_{k=1}^{4+N} \lambda_i \alpha_i \boldsymbol{e}_i,$$

   to within $O(\Delta^2)$.

2. Then seek expressions for the Roe–averages $\widehat{\rho}$, $\widehat{u}$, $\widehat{v}$, $\widehat{e}$, $\widehat{Z_k}$, $\widehat{P}$, $\widehat{P_\rho}$, $\widehat{P_e}$ and $\widehat{P_{Z_k}}$ at the interface between the left and right cells. The averages must satisfy

$$\Delta \boldsymbol{W} = \sum_{k=1}^{4+N} \widehat{\alpha_i} \widehat{\boldsymbol{e}_i}, \tag{B.3a}$$

$$\Delta \boldsymbol{F} = \sum_{k=1}^{4+N} \widehat{\lambda_i} \widehat{\alpha_i} \widehat{\boldsymbol{e}_i}, \tag{B.3b}$$

   exactly, for $\boldsymbol{W}_L$ and $\boldsymbol{W}_R$ not necessarily close together.

In the final implementation of Roe's scheme, (B.1) is integrated in a cell-centered uniform grid as

$$\boldsymbol{W}_i^{n+1} = \boldsymbol{W}_i^n - \frac{\Delta t}{\Delta x} \left(\boldsymbol{F}_{i+1/2}^n - \boldsymbol{F}_{i-1/2}^n \right),$$

where the subscript is the spatial cell number, and the superscript is the timestep. The flux function $\boldsymbol{F}_{i+1/2}$ at the interface between cells i and $i+1$ is given by

$$\boldsymbol{F}_{i+1/2}(\boldsymbol{W}_L, \boldsymbol{W}_R) = \frac{1}{2}(\boldsymbol{F}_L + \boldsymbol{F}_R) - \frac{1}{2} \sum_{k=1}^{4+N} \widehat{\alpha_k} \left| \widehat{\lambda_k} \right| \widehat{\boldsymbol{e}_k},$$

in the first order accurate Roe scheme (Roe, 1986). For second order spatial and temporal accuracy, the approach adopted in this work is the use of a flux limiter. Roe (1986) suggested the flux function should then take the form

$$\boldsymbol{F}_{i+1/2}(\boldsymbol{W}_L, \boldsymbol{W}_R) = \frac{1}{2}(\boldsymbol{F}_L + \boldsymbol{F}_R) - \frac{1}{2}\sum_{k=1}^{4+N} \widehat{\alpha_k}\Big\{1 - \varphi(r_k)(1 - |\nu_k|)\Big\}\left|\widehat{\lambda_k}\right| \widehat{\boldsymbol{e}_k},$$

where $\nu_k = \widehat{\lambda_k}\Delta t/\Delta x$ is the CFL number of the k-th wave, $\varphi(r_k)$ is a nonlinear limiter function, and the parameter r_k is the ratio of the upwind to local wave strengths,

$$r_k = \begin{cases} \dfrac{(\widehat{\alpha_k})_{i-1/2}}{(\widehat{\alpha_k})_{i+1/2}}, & \widehat{\lambda_k} < 0, \\ \dfrac{(\widehat{\alpha_k})_{i+3/2}}{(\widehat{\alpha_k})_{i+1/2}}, & \widehat{\lambda_k} \geq 0. \end{cases}$$

Throughout this work, the limiter function adopted was the min–mod limiter,

$$\varphi(r_k) = \begin{cases} 0, & r_k < 0, \\ \min(1, r_k), & r_k \geq 0. \end{cases}$$

Finally, the scheme can be made entropy-satisfying with Harten's (1983) entropy fix. In regions where the wave CFL number ν_k is smaller than some tolerance δ, it is replaced by a larger value ν'_k:

$$\nu'_k = \frac{\mathrm{sgn}(\nu_k)}{2}\left(\frac{\nu_k^2}{\delta} + \delta\right), \qquad |\nu_k| < \delta.$$

The fix is only necessary on the contact, shear and reaction waves, that is, those with wave speed u for which entropy violation may occur. The value of δ used in this work was 0.1.

Solution of (B.2) is straightforward and yields the following coefficients:

$$\begin{aligned}
\alpha_1 &= \frac{1}{2c^2}(\Delta P - \rho c \Delta u), \\
\alpha_2 &= \Delta\rho - \frac{\Delta P}{c^2}, \\
\alpha_3 &= \rho \Delta v, \\
\alpha_4 &= \frac{1}{2c^2}(\Delta P + \rho c \Delta u), \\
\alpha_{4+k} &= \rho \Delta Z_k, \qquad k = 1, \ldots, N.
\end{aligned}$$

Solution of (B.3) is much more complicated. Unlike the equilibrium perfect gas case, the equations are incomplete. There are $7 + 2N$ unknowns to be solved and $8 + 2N$ equations in (B.3), but only $5+N$ of the equations are independent. After considerable algebra, basically proceeding along the lines of Glaister (1988), the following Roe–averages are obtained:

$$\begin{aligned}
\widehat{\rho} &= \sqrt{\rho_L \rho_R}, \\
\widehat{u} &= \frac{\sqrt{\rho_L}\, u_L + \sqrt{\rho_R}\, u_R}{\sqrt{\rho_L} + \sqrt{\rho_R}}, \\
\widehat{v} &= \frac{\sqrt{\rho_L}\, v_L + \sqrt{\rho_R}\, v_R}{\sqrt{\rho_L} + \sqrt{\rho_R}}, \\
\widehat{Z_k} &= \frac{\sqrt{\rho_L}\, (Z_k)_L + \sqrt{\rho_R}\, (Z_k)_R}{\sqrt{\rho_L} + \sqrt{\rho_R}}, \qquad k = 1, \ldots, N \\
\widehat{H} &= \frac{\sqrt{\rho_L}\, H_L + \sqrt{\rho_R}\, H_R}{\sqrt{\rho_L} + \sqrt{\rho_R}},
\end{aligned}$$

where

$$\widehat{H} \equiv \widehat{e} + \frac{\widehat{u}^2 + \widehat{v}^2}{2} + \frac{\widehat{P}}{\widehat{\rho}}. \tag{B.4}$$

The only remaining unused equation from (B.3) is

$$\Delta(\rho e) - \widehat{e}\Delta\rho - \widehat{\rho}\Delta e + \frac{\widehat{\rho}}{\widehat{P_e}} \left(\widehat{P_\rho}\Delta\rho + \widehat{P_e}\Delta e + \sum_{k=1}^{N} \widehat{P_{Z_k}} \Delta Z_k - \Delta P \right) = 0, \tag{B.5}$$

while we still have to determine expressions for $\widehat{e}$, $\widehat{P_\rho}$, $\widehat{P_e}$ and $\widehat{P_{Z_k}}$. The choices are

arbitrary, but a natural first choice from (B.5) is

$$\Delta(\rho e) - \widehat{e}\Delta\rho - \widehat{\rho}\Delta e = 0, \tag{B.6}$$

which yields

$$\widehat{e} = \frac{\sqrt{\rho_L}\, e_L + \sqrt{\rho_R}\, e_R}{\sqrt{\rho_L} + \sqrt{\rho_R}}.$$

$\widehat{P}$ is then determined from (B.4). Subtracting (B.6) from (B.5), we are left with

$$\Delta P = \widehat{P_\rho}\Delta\rho + \widehat{P_e}\Delta e + \sum_{k=1}^{N} \widehat{P_{Z_k}}\Delta Z_k. \tag{B.7}$$

Once again, the choice for the Roe–averages $\widehat{P_\rho}$, $\widehat{P_e}$ and $\widehat{P_{Z_k}}$ is somewhat arbitrary. As it turns out, finding any averages that satisfy (B.7) exactly for a general value of N is very difficult.

One method for finding such Roe–averages is to assume the following functional form:

$$\widehat{P_\rho} = \frac{\bar{P}^{(\rho)}(\rho_R) - \bar{P}^{(\rho)}(\rho_L)}{\Delta\rho}, \tag{B.8}$$

where $\bar{P}^{(\rho)}(\rho) = \bar{P}(\rho, e_L, e_R, (Z_1)_L, (Z_1)_R, \ldots, (Z_N)_L, (Z_N)_R)$ is a function that remains to be determined. Similar functional forms are assumed for $\widehat{P_e}$ and $\widehat{P_{Z_k}}$. If we assume $\bar{P}^{(\rho)}(\rho)$ is some linear combination of terms of the form $P(\rho, e_{i_0}, (Z_1)_{i_1}, \ldots, (Z_N)_{i_N})$, where $i_k = L$ or R, and similarly for $\bar{P}^{(e)}$, $\bar{P}^{(Z_k)}$, then it can be shown there is a unique solution that satisfies (B.7). Solutions for $\bar{P}^{(\rho)}$ with the first few values of N are as follows:

$N = 0$:

$$\bar{P}^{(\rho)}(\rho) = \frac{1}{2}\Big\{P\big(\rho, e_L\big) + P\big(\rho, e_R\big)\Big\}, \tag{B.9a}$$

$N = 1$:

$$\begin{aligned}\bar{P}^{(\rho)}(\rho) = \frac{1}{3}\Big\{P\big(\rho, e_L, (Z_1)_L\big) + P\big(\rho, e_R, (Z_1)_R\big)\Big\} \\ +\frac{1}{6}\Big\{P\big(\rho, e_L, (Z_1)_R\big) + P\big(\rho, e_R, (Z_1)_L\big)\Big\},\end{aligned} \tag{B.9b}$$

$N = 2$:

$$\bar{P}^{(\rho)}(\rho) = \frac{1}{4}\Big\{P\big(\rho, e_L, (Z_1)_L, (Z_2)_L\big) + P\big(\rho, e_R, (Z_1)_R, (Z_2)_R\big)\Big\} \tag{B.9c}$$
$$+\frac{1}{12}\Big\{P\big(\rho, e_L, (Z_1)_L, (Z_2)_R\big) + P\big(\rho, e_L, (Z_1)_R, (Z_2)_L\big) + P\big(\rho, e_R, (Z_1)_L, (Z_2)_L\big)$$
$$+P\big(\rho, e_R, (Z_1)_R, (Z_2)_L\big) + P\big(\rho, e_R, (Z_1)_L, (Z_2)_R\big) + P\big(\rho, e_L, (Z_1)_R, (Z_2)_R\big)\Big\},$$

and similarly for $\bar{P}^{(e)}, \bar{P}^{(Z_k)}$. The expressions (B.9) can be substituted into (B.8) to obtain the Roe–averages for the partial derivatives of pressure. For example, for $N = 0$, the expression for $\widehat{P_\rho}$ is

$$\widehat{P_\rho} = \frac{\frac{1}{2}\Big\{P\big(\rho_R, e_L\big) + P\big(\rho_R, e_R\big)\Big\} - \frac{1}{2}\Big\{P\big(\rho_L, e_L\big) + P\big(\rho_L, e_R\big)\Big\}}{\Delta\rho}. \tag{B.10}$$

The form (B.8) applies when $\Delta\rho \neq 0$. When $\Delta\rho = 0$, for consistency, we take the limit of (B.8) as $\Delta\rho \to 0$. For example, for $N = 0$,

$$\widehat{P_\rho} = \frac{1}{2}\Big\{P_\rho\big(\rho, e_L\big) + P_\rho\big(\rho, e_R\big)\Big\}, \qquad \rho = \rho_L = \rho_R. \tag{B.11}$$

Note that the $N = 0$ expressions for $\widehat{P_\rho}$ in (B.10) and (B.11) are identical to those given by Glaister (1988) for an equilibrium fluid.

The difficulty with this formulation is that the number of pressure terms in each of the expressions in (B.9) is 2^{N+1}. Since each expression must be evaluated for the left and right states in (B.8), and there are $2 + N$ different partial derivatives, then the number of functional evaluations of the equation of state required at each cell interface and each timestep is $(2 + N)\, 2^{2+N}$. For large N, this is prohibitively expensive, especially when considering that for systems such as non-calorically-perfect gases, the equation of state evaluation involves a costly iterative solution. Therefore, this formulation, while mathematically correct, is not a viable computational option.

We are thus forced to relax the restriction of (B.7). The resultant scheme will no longer be formally conservative, but it can be made very close to conservative. Shuen et al. (1990) proposed approximations $\widehat{P_\rho}$, $\widehat{P_e}$ and $\widehat{P_{Z_k}}$ that minimized

the errors with respect to the values $P_\rho(\widehat{\rho},\widehat{e},\widehat{Z_1},\ldots,\widehat{Z_N})$, $P_e(\widehat{\rho},\widehat{e},\widehat{Z_1},\ldots,\widehat{Z_N})$ and $P_{Z_k}(\widehat{\rho},\widehat{e},\widehat{Z_1},\ldots,\widehat{Z_N})$ respectively. However, past experience with reactive Roe schemes (J. J. Quirk and R. P. Fedkiw, private communication) suggests there is no detectable difference in the solution obtained by using almost any consistent approximation to the partial derivatives. As a result, the computationally efficient choice of simple arithmetic averaging is proposed, giving the following approximations:

$$\widehat{P}_\rho = \frac{1}{2}\Big\{P_\rho\big(\rho_L,e_L,(Z_1)_L,\ldots,(Z_N)_L\big)+P_\rho\big(\rho_R,e_R,(Z_1)_R,\ldots,(Z_N)_R\big)\Big\}, \qquad \text{(B.12a)}$$

$$\widehat{P}_e = \frac{1}{2}\Big\{P_e\big(\rho_L,e_L,(Z_1)_L,\ldots,(Z_N)_L\big)+P_e\big(\rho_R,e_R,(Z_1)_R,\ldots,(Z_N)_R\big)\Big\}, \qquad \text{(B.12b)}$$

$$\widehat{P}_{Z_k} = \frac{1}{2}\Big\{P_{Z_k}\big(\rho_L,e_L,(Z_1)_L,\ldots,(Z_N)_L\big)+P_{Z_k}\big(\rho_R,e_R,(Z_1)_R,\ldots,(Z_N)_R\big)\Big\}, \quad \text{(B.12c)}$$
$$k=1,\ldots,N.$$

It can be shown that these expressions actually satisfy (B.7) exactly in the case of the perfect gas one-step reaction model used in chapter 2. For the non-calorically-perfect, multi-species equation of state used in the detailed chemistry model (see §3.2.1), the verification studies of §3.2.2 showed that the flow solver gives acceptable results with this formulation, so the approximations of (B.12) are deemed to be adequate.

Appendix C Riemann Problem for a Mixture of Ideal Gases

The exact solution of the classical shock tube problem is referred to as the first Riemann problem. For a thermally and calorically perfect gas, it has an explicit analytical solution that is widely available in fluid mechanics texts. However, when the gas is a mixture of ideal gases that are not calorically perfect, an explicit solution does not exist. As described in §3.2.2, an exact similarity solution still exists provided the gases are chemically frozen or in chemical equilibrium. Among the many possible means to find this similarity solution, the following method was adopted in this work.

The basic wave structure that develops in the first Riemann problem is illustrated in the x–t diagram of figure C.1. A shock wave travels into the driven gas at speed

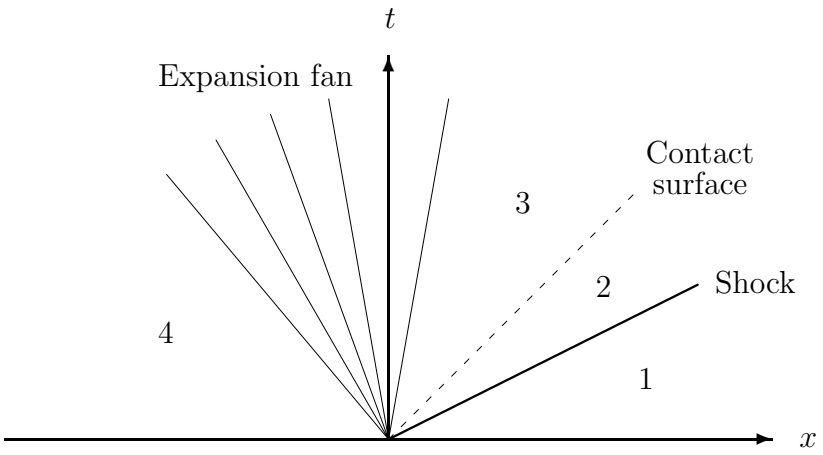

Figure C.1: x–t diagram of Riemann problem wave structure, initially with high pressure driver gas at $x < 0$ and low pressure driven gas at $x > 0$.

U and an expansion fan travels into the driver gas. The initial driver and driven gases remain separated by a contact surface. The states 1 to 4 are as labeled in the diagram.

The shock jump conditions between states 1 and 2 are as follows:

$$\rho_1 U = \rho_2 (U - u_2), \tag{C.1}$$

$$P_1 + \rho_1 U^2 = P_2 + \rho_2 (U - u_2)^2, \tag{C.2}$$

$$h_1 + \frac{1}{2} U^2 = h_2 + \frac{1}{2} (U - u_2)^2, \tag{C.3}$$

where h is the enthalpy. Equation (C.1) can be rearranged to give

$$u_2 = U \left(1 - \frac{\rho_1}{\rho_2} \right). \tag{C.4}$$

Substituting (C.4) into (C.2) and (C.3) gives

$$P_2 = P_1 + \rho_1 U^2 \left(1 - \frac{\rho_1}{\rho_2} \right). \tag{C.5}$$

$$h_2 = h_1 + \frac{1}{2} U^2 \left\{ 1 - \left(\frac{\rho_1}{\rho_2} \right)^2 \right\}. \tag{C.6}$$

In addition, specification of the caloric equation of state gives

$$h_2 = h(P_2, \rho_2, \boldsymbol{y}_2). \tag{C.7}$$

For frozen flow, $\boldsymbol{y}_2 = \boldsymbol{y}_1$ and (C.7) was evaluated for the system of ideal gases using CHEMKIN (Kee et al., 1989). For equilibrium flow, $\boldsymbol{y}_2 = \boldsymbol{y}_e(P_2, \rho_2)$ where $\boldsymbol{y}_e$ denotes the equilibrium composition at that thermodynamic condition. This equilibrium state was evaluated using EQUIL, the driver to STANJAN (Reynolds, 1986) included in CHEMKIN.

The expansion fan is a simple wave region where the left-facing C^- characteristics are straight lines and the J^+ Riemann invariant of the other family of characteristics, C^+, is constant everywhere (Thompson, 1988, chap. 8). That is,

$$\text{constant} = J^+ = u + \int_{P_{ref}}^{P} \frac{\mathrm{d}P}{\rho c},$$

where P_{ref} is some reference pressure. Equating J^+ at state 4 with that at some state inside the expansion fan, and noting that $u_4 = 0$, we get,

$$u = \int_P^{P_4} \frac{\mathrm{d}P'}{\rho c}. \tag{C.8}$$

In particular,

$$u_3 = \int_{P_3}^{P_4} \frac{\mathrm{d}P}{\rho c}. \tag{C.9}$$

Additionally, the expansion fan is homentropic, so $s = s_3 = s_4$ where s is the entropy. The position in the expansion fan is determined from the fact that the C^- characteristics are straight lines, that is,

$$\frac{\mathrm{d}x}{\mathrm{d}t} = u - c = \text{constant, along each } C^-,$$

and thus,

$$\frac{x}{t} = u - c. \tag{C.10}$$

The shock and expansion fan solutions are coupled at the contact surface, across which the pressure and velocity must match, that is, $P_2 = P_3$ and $u_2 = u_3$. The velocity of the contact surface is the flow velocity u_2 or u_3.

Given states 1 and 4, the Riemann problem was then solved using the following iterative algorithm:

1. Guess the shock speed U.
2. Solve the shock jump conditions to get state 2:
   (a) Guess ρ_1/ρ_2 between 0 and 1 $\Rightarrow \rho_2$.
   (b) Equation (C.5) $\Rightarrow P_2$.
   (c) Find the error between equations (C.6) and (C.7).
   (d) Iterate steps (a)–(c) until the error in (c) converges to zero.
   (e) Equation (C.4) $\Rightarrow u_2$.

3. With $P_3 = P_2$, integrate equation (C.9) to get u_3. The integration must be performed numerically, and in this work we employed Simpson's 1/3 rule. To evaluate the integrand, do the following:

   Frozen flow For each value of the integration variable P, iteratively solve

   $$s_4 = s(P, T, \boldsymbol{y}_4),$$

   to get T. The function $s(P, T, \boldsymbol{y}_4)$ was evaluated with CHEMKIN. Then,

   $$\rho = \frac{P}{R_g(\boldsymbol{y}_4)\, T}, \quad \text{and}$$
   $$c = \sqrt{\gamma(T, \boldsymbol{y}_4)\, R_g(\boldsymbol{y}_4)\, T}.$$

   Equilibrium flow Solve the equilibrium state at pressure P and entropy $s = s_4$, using EQUIL. This gives ρ and c, where here c is the equilibrium sound speed.

4. If $u_3 \neq u_2$, go back to step 1 and iterate.

5. Once steps 1–4 have converged, obtain all necessary intermediate states in the expansion fan. For each required pressure between P_4 and P_3, evaluate the other state variables T, ρ and c, and the composition $\boldsymbol{y}$, in the same manner the integrand was evaluated in step 3. In addition, get the corresponding velocities u by integrating equation (C.8) the same way (C.9) was integrated in step 3. Finally, equation (C.10) gives x/t for these expansion fan states.

Appendix D Maas and Warnatz H_2–O_2 Reaction Mechanism

Reaction mechanism for H_2–O_2–N_2 systems, from Maas and Warnatz (1988):

	Reactions	A_l (cm-s-mol)	β_l	E_{a_l} (J/mol)
1.	$O_2 + H \rightleftharpoons OH + O$	2.00e+14	0.00	70300
2.	$H_2 + O \rightleftharpoons OH + H$	5.06e+04	2.67	26300
3.	$H_2 + OH \rightleftharpoons H_2O + H$	1.00e+08	1.60	13800
4.	$OH + OH \rightleftharpoons H_2O + O$	1.50e+09	1.14	420
5.	$H + H + M \rightleftharpoons H_2 + M$	1.80e+18	-1.00	0
6.	$H + OH + M \rightleftharpoons H_2O + M$	2.20e+22	-2.00	0
7.	$O + O + M \rightleftharpoons O_2 + M$	2.90e+17	-1.00	0
8.	$H + O_2 + M \rightleftharpoons HO_2 + M$	2.30e+18	-0.80	0
9.	$HO_2 + H \rightleftharpoons OH + OH$	1.50e+14	0.00	4200
10.	$HO_2 + H \rightleftharpoons H_2 + O_2$	2.50e+13	0.00	2900
11.	$HO_2 + H \rightleftharpoons H_2O + O$	3.00e+13	0.00	7200
12.	$HO_2 + O \rightleftharpoons OH + O_2$	1.80e+13	0.00	-1700
13.	$HO_2 + OH \rightleftharpoons H_2O + O_2$	6.00e+13	0.00	0
14.	$HO_2 + HO_2 \rightarrow H_2O_2 + O_2$	2.50e+11	0.00	-5200
15.	$OH + OH + M \rightleftharpoons H_2O_2 + M$	3.25e+22	-2.00	0
16.	$H_2O_2 + H \rightleftharpoons H_2 + HO_2$	1.70e+12	0.00	15700
17.	$H_2O_2 + H \rightleftharpoons H_2O + OH$	1.00e+13	0.00	15000
18.	$H_2O_2 + O \rightleftharpoons OH + HO_2$	2.80e+13	0.00	26800
19.	$H_2O_2 + OH \rightleftharpoons H_2O + HO_2$	5.40e+12	0.00	4200

Enhanced third-body efficiencies for three-body reactions: O_2 0.35; H_2O 6.5; N_2 0.5

Appendix E Multi-Variate Linear Interpolation on a Regular Cartesian Grid

The first step in applying multi-variate linear interpolation on a regular Cartesian grid is locating the grid hyper-rectangle that bounds the desired interpolant point. In the ILDM table of this work, the logical co-ordinates corresponded to known physical co-ordinates, so this step was trivial. One method for then performing the multi-variate linear interpolation in the hyper-rectangle would be successive application of 1-dimensional linear interpolation in each of the co-ordinate directions. In this work, we adopted an alternative approach that computed the interpolation in a single step.

In two dimensions, the interpolation problem is illustrated in figure E.1, which shows an example interpolant point (x_1^*, x_2^*) and its bounding grid rectangle. Define weighting functions $\boldsymbol{\pi}$ for each co-ordinate direction as

$$\pi_1 = \frac{x_1^* - x_{1,0}}{x_{1,1} - x_{1,0}},$$
$$\pi_2 = \frac{x_2^* - x_{2,0}}{x_{2,1} - x_{2,0}}.$$

Then the interpolated value of some scalar ϱ at the interpolant point, ϱ^*, is given in terms of the function at the grid points by the following expression:

$$\varrho^* = \varrho^{(0)}(1-\pi_1)(1-\pi_2) + \varrho^{(1)}\pi_1(1-\pi_2) + \varrho^{(2)}(1-\pi_1)\pi_2 + \varrho^{(3)}\pi_1\pi_2.$$

This algorithm can be generalized to interpolation in N dimensions as follows. The co-ordinates of the bounding hyper-rectangle grid points are denoted by $(l_1^{(i)}, l_2^{(i)}, \ldots, l_N^{(i)})$, where $l_n^{(i)} = 0$ or 1 for each co-ordinate direction $n = 1, 2, \ldots, N$ and each grid point $i = 0, 1, \ldots, 2^N - 1$. The physical location of grid point i is $(x_{1,l_1^{(i)}}, x_{2,l_2^{(i)}}, \ldots, x_{N,l_N^{(i)}})$.

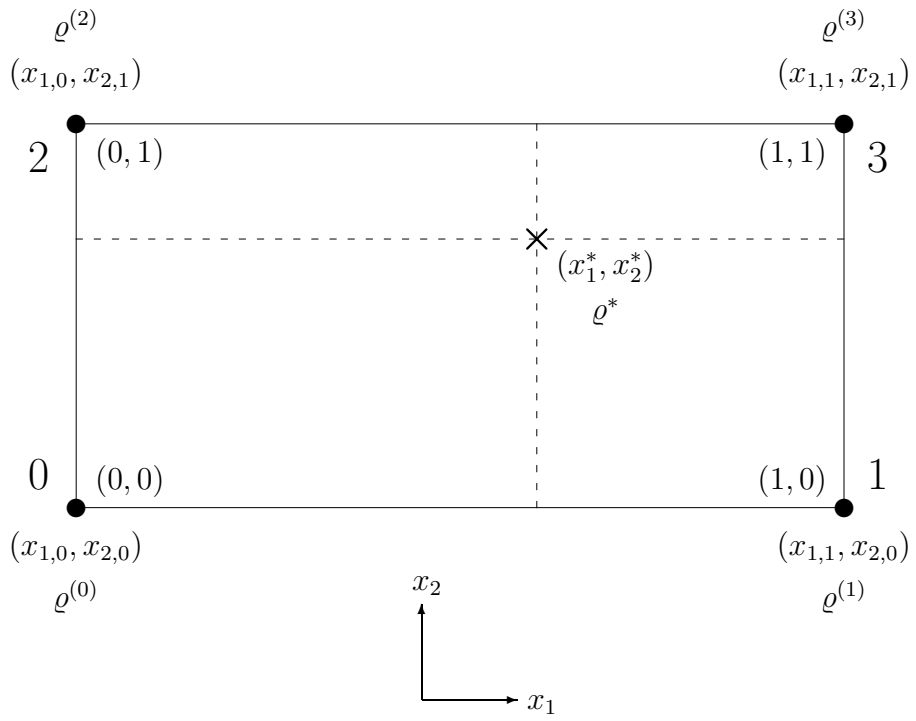

Figure E.1: Bivariate linear interpolation on a regular Cartesian grid.

As in the two-dimensional example, $x_{n,0} \leq x_n^*$ and $x_{n,1} > x_n^*$. In the numbering scheme adopted here, the grid point number i is the base 10 representation of the base 2 number $l_N^{(i)} l_{N-1}^{(i)} \ldots l_1^{(i)}$. The co-ordinates can be computed from the grid point number as follows:

$$l_n^{(i)} = \text{int}\left(\frac{i}{2^{n-1}}\right) \mod 2,$$

where "int" denotes the integer part and "mod" denotes the modulo operator. Then the weighting functions for each co-ordinate direction are given by

$$\pi_n = \frac{x_n^* - x_{n,0}}{x_{n,1} - x_{n,0}},$$

and the interpolated value is

$$\varrho^* = \sum_{i=0}^{2^N-1} \left[\varrho^{(i)} \prod_{n=1}^{N} \left\{ l_n^{(i)} \pi_n + (1 - l_n^{(i)})(1 - \pi_n) \right\} \right].$$

Appendix F Cross-Sectional Profiles in Two-Dimensional Detonation Simulations

(a) Numerical schlieren–type images

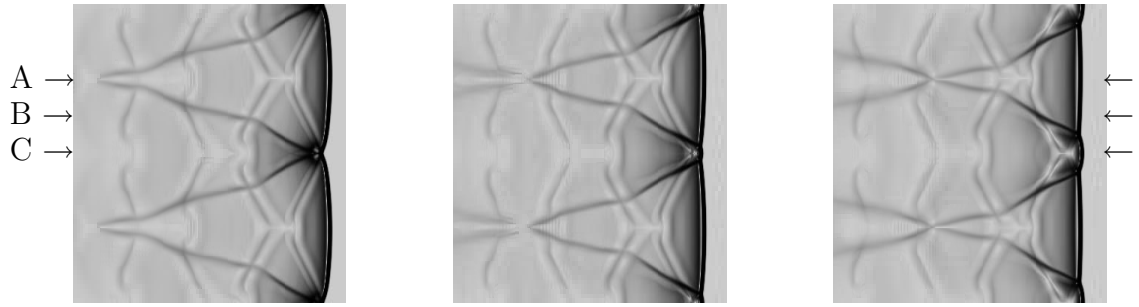

(b) Cross-section A

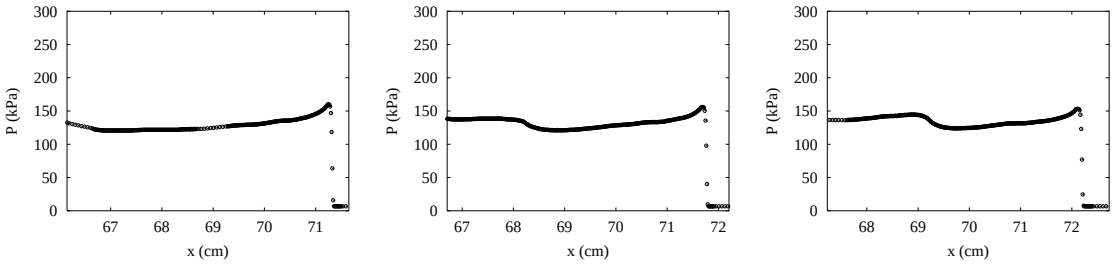

(c) Cross-section B

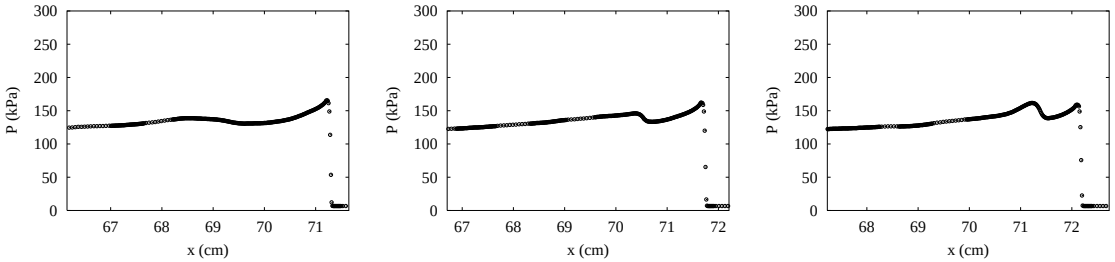

(d) Cross-section C

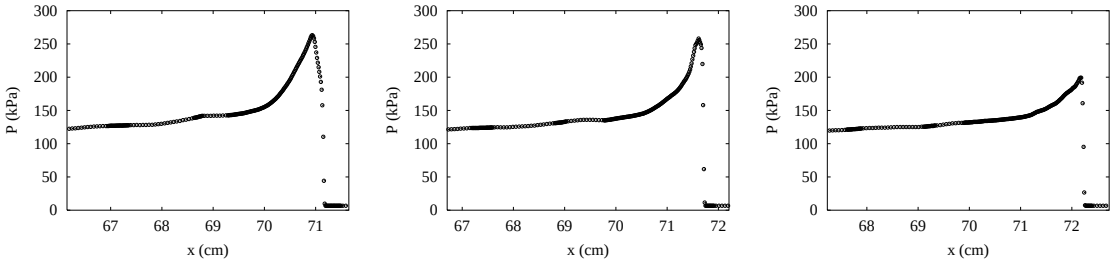

$t = 440.1$ μs 442.9 μs 445.7 μs

Figure F.1: Cross-sections of pressure for a two-dimensional CJ detonation in stoichiometric H_2–O_2 with 70% Ar dilution, initially at 6.67 kPa and 298 K.

(a) Numerical schlieren–type images

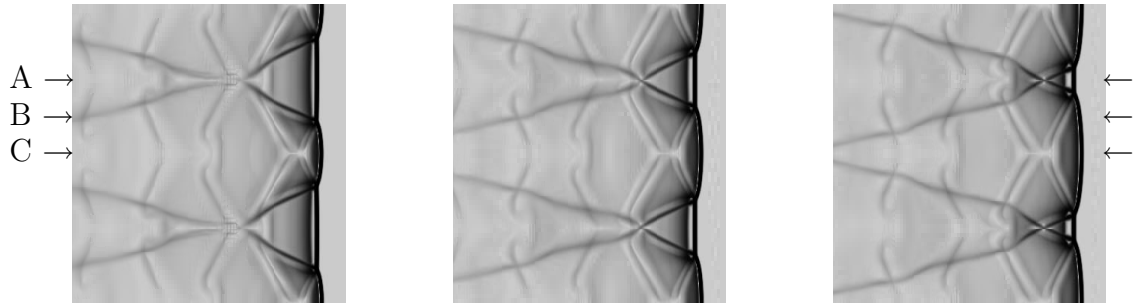

(b) Cross-section A

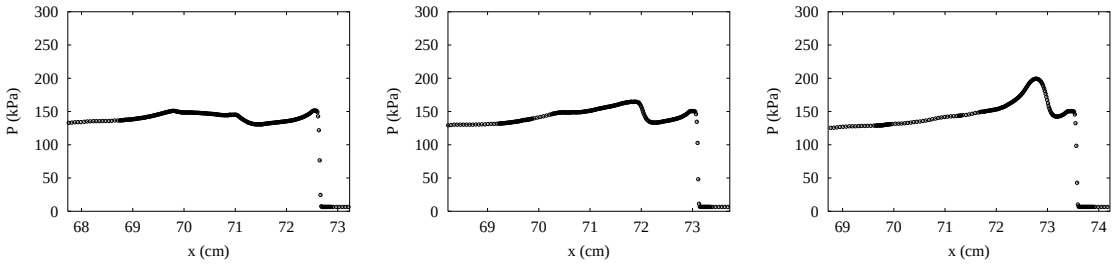

(c) Cross-section B

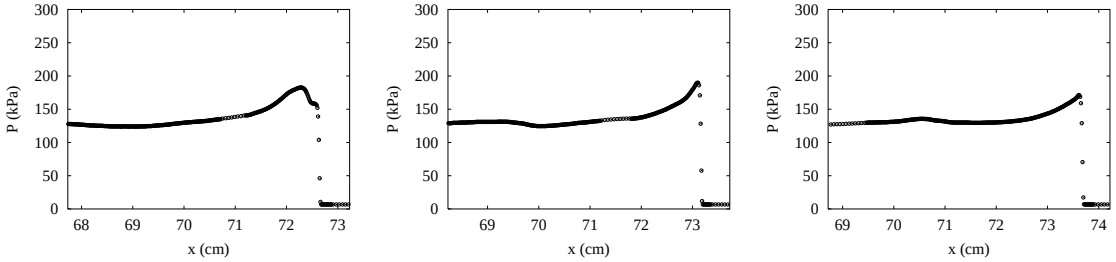

(d) Cross-section C

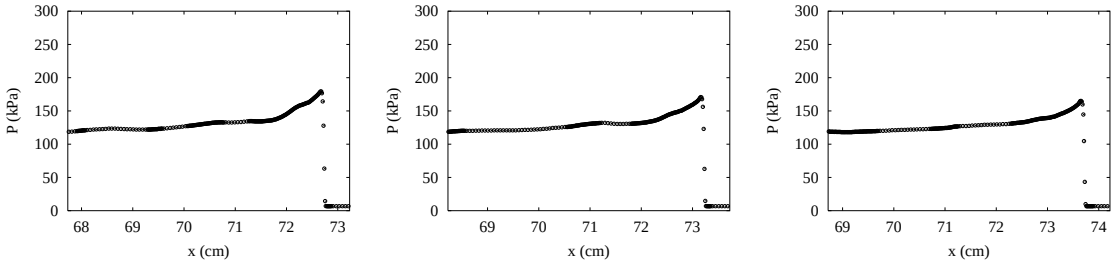

$t = 448.7\ \mu$s 451.7 μs 454.7 μs

Figure F.2: Cross-sections of pressure (cont.).

(a) Numerical schlieren–type images

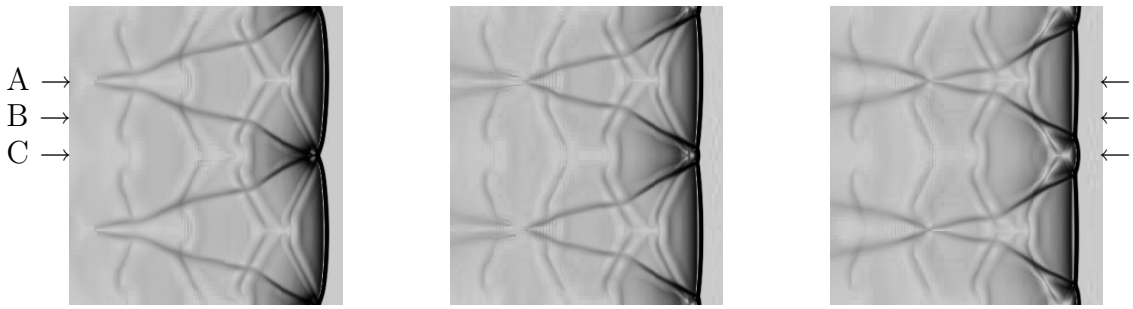

(b) Cross-section A

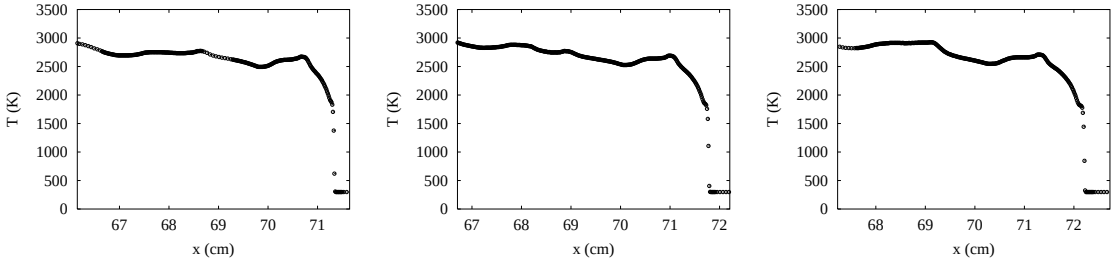

(c) Cross-section B

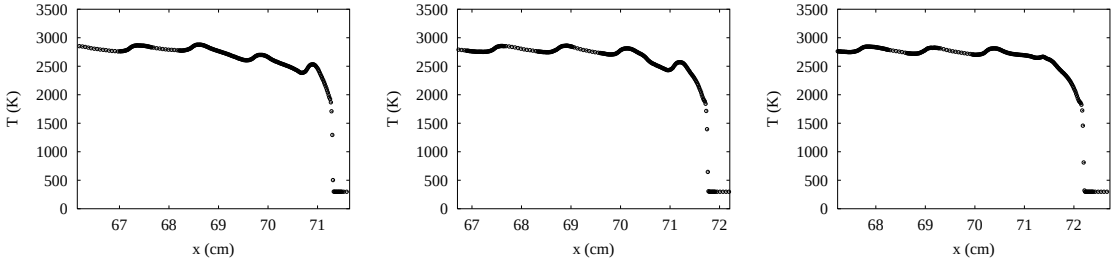

(d) Cross-section C

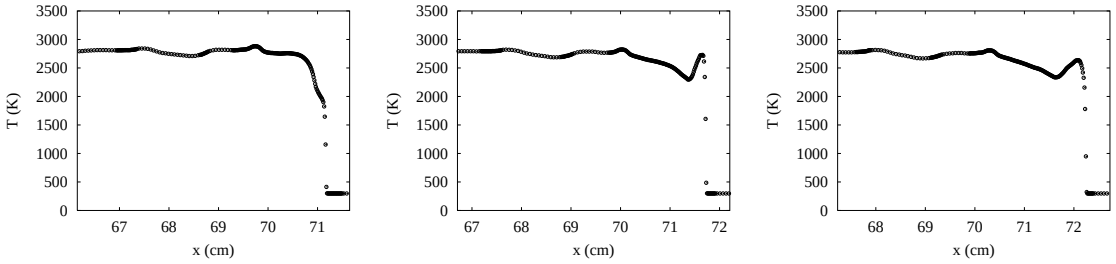

$t = 440.1$ μs 442.9 μs 445.7 μs

Figure F.3: Cross-sections of temperature.

(a) Numerical schlieren–type images

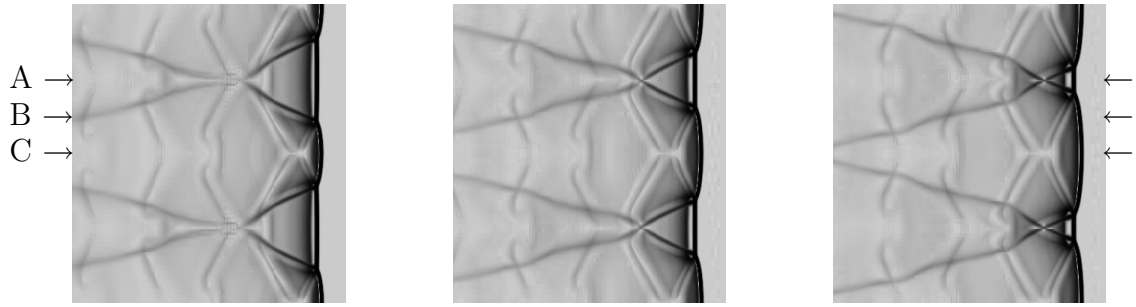

(b) Cross-section A

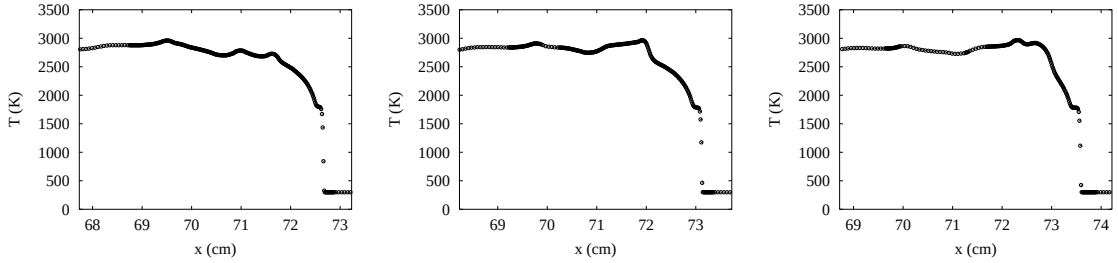

(c) Cross-section B

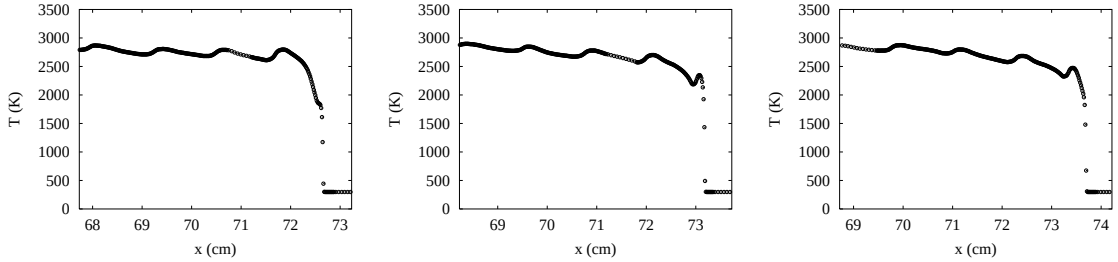

(d) Cross-section C

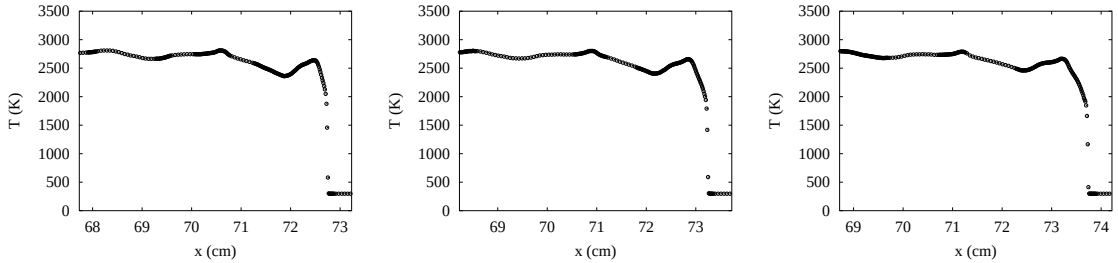

$t = 448.7$ μs 451.7 μs 454.7 μs

Figure F.4: Cross-sections of temperature (cont.).

(a) Numerical schlieren–type images

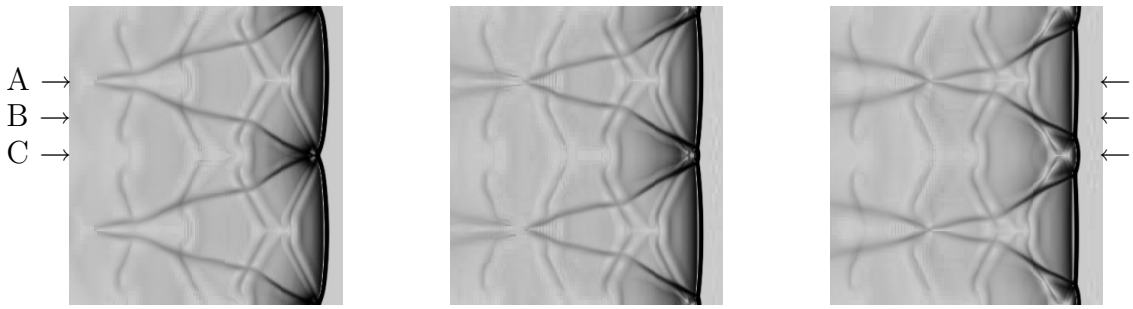

(b) Cross-section A

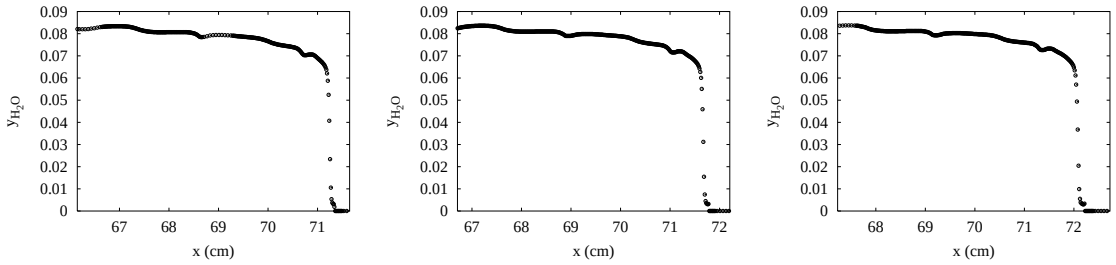

(c) Cross-section B

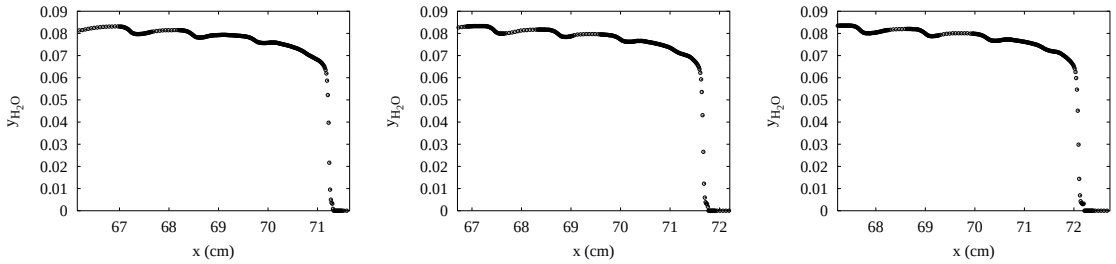

(d) Cross-section C

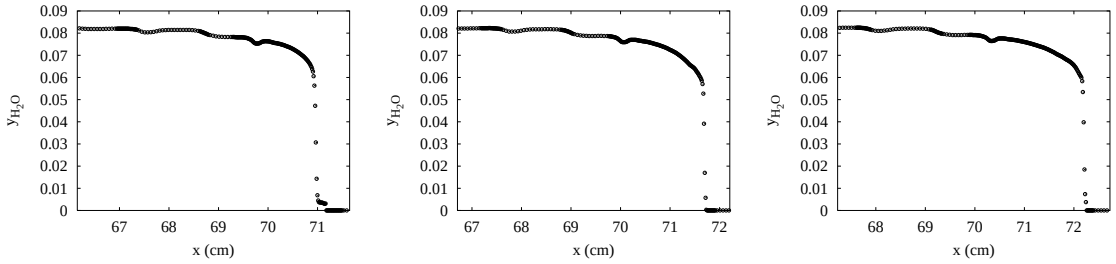

$t = 440.1$ μs 442.9 μs 445.7 μs

Figure F.5: Cross-sections of H_2O mass fraction.

(a) Numerical schlieren–type images

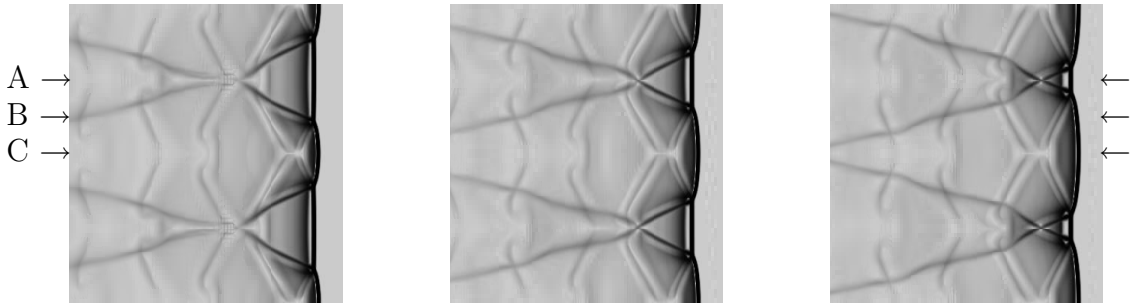

(b) Cross-section A

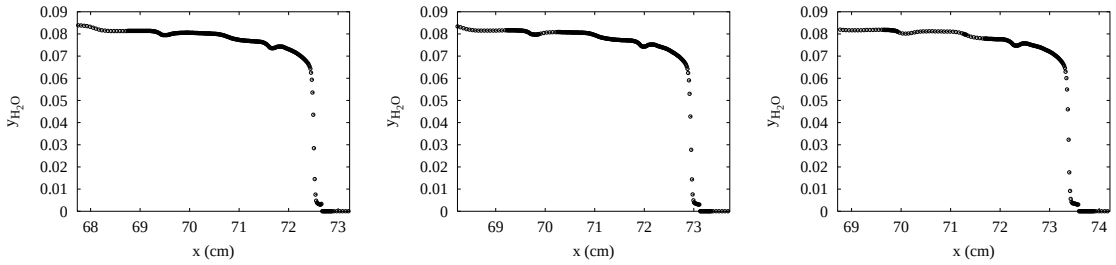

(c) Cross-section B

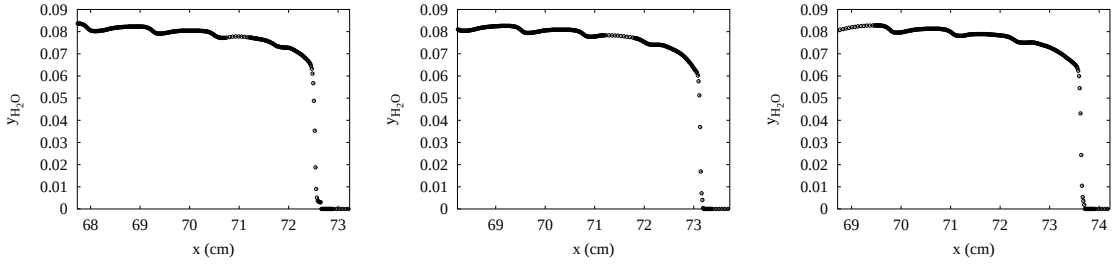

(d) Cross-section C

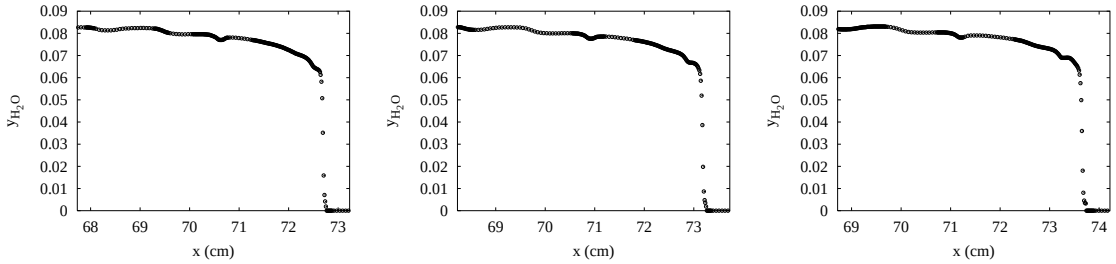

$t = 448.7$ μs 451.7 μs 454.7 μs

Figure F.6: Cross-sections of H_2O mass fraction (cont.).